Multi-scale Population Balance Modelling and Controllability of Granulation Processes

by

Rohit Ramachandran

December 2008

A thesis submitted for the degree of
Doctor of Philosophy of the University of London
and Diploma of Membership of Imperial College

Centre for Process Systems Engineering
Department of Chemical Engineering
Imperial College London
United Kingdom

Abstract

Many continuous granulation plants operate below their design capacity, suffering from high recycle rates and instabilities. Thus, there is an immediate economic incentive for effective operation and control of granulation units. The overall granulation process is integrated and interacting, with limited manipulated variables available (e.g. binder addition, nozzle locations and mixing rate). Hence, the complex process dynamics and operational challenges presented warrant a fundamental model-based strategy for design, operation, control and scale-up that is well supported by experimental analyses. A realistic model of the granulation process has to account for the granule size, the binder content, and the porosity (or related parameter bulk density), thereby necessitating a three-dimensional population balance model to yield a good representation of the process. While this multi-dimensional population balance model is warranted by the physics of the problem, it is a bigger challenge to derive kernels (rate laws) for the key granulation mechanisms. Most kernels in the literature are empirical and/or semi-empirical and provide little insight into the intricacies of the granulation mechanisms. This effectively results in an inability to make the necessary engineering decisions to improve control of the granulation process. Hence, this thesis is concerned with a more systems-centric approach to enhance the design, control and scale-up of granulation processes.

Experimental studies on a lab-scale batch drum granulator for a Calcite/PVOH-H_2O system were performed to assess granulation kinetics and model development of the granulation process. Effects of process/material properties and liquid binder distribution on granule properties, illustrating the non-homogeneity of key particle attributes and which justify the need for multi-dimensional population balances, were studied. Process sensitivities, manipulations and potential disturbances were identified, formulating a comprehen-

sive control configuration for granulation processes, with application seen in a continuous drum granulation of limestone. While carrying out experiments, multiple granule attributes were characterised and this presents a challenge, which this research addresses accordingly.

A population balance model incorporating nucleation, aggregation, breakage and consolidation was developed in this research. Novel aspects are the mechanistic formulations of the nucleation, aggregation and breakage kernels which are derived from first-principles. Such mechanistic descriptions of the rate processes lend themselves to a more in-depth understanding of the granulation process, contributing fundamental knowledge to the design, control and scale-up of these processes. A sensitivity analysis of the model was then performed to ascertain the influence of model parameters on the particle density distribution. Continuing from this, a compartmentalised version of the combined population balance model was developed, for the purpose of controllability analysis. Results obtained were used to identify suitable control-loop pairings to facilitate enhanced control-loop performance.

Experimental validation of the population balance model is an integral part of this research. The model was quantitatively validated using lab-scale experimental data for granule size, binder content and porosity. The tuned model was then able to predict evolutions and distributions of granule attributes for different operating conditions and formulations. The model was also validated for different granulation systems. This illustrates the robustness and flexibility of the model and these results are promising toward the longer-term step of a first-principles based predictive model for the granulation process that can help alleviate the need for large number of experiments.

As an alternative to deriving the above-mentioned mechanistic kernels, a discrete element modelling (DEM) approach was also undertaken in this thesis. Based on a Volume of Fluid (VOF) method, the analysis carried out provided useful information to help understand the effect of primary particle morphology on granulation kinetics making it possible to establish relationships between material and process/design properties and granulation process behaviour.

Acknowledgements

This section is a tribute to the numerous people who have contributed to the culmination of this thesis in one way or another, during my time at Imperial College London.

I express my deepest gratitude to my principal supervisor, Dr. Charles Immanuel for providing me the opportunity to work on this project. Charles has injected tremendous energy into the project and his keen eye for detail and thorough supervision has led immensely to the quality of this thesis. My sincere thanks also goes out to my co-supervisor, Dr. Frantisek (Ferry) Stepanek. Ferry could always be counted on for helpful suggestions and friendly advice. His door was always open and i could just drop in whenever i wanted to discuss research, which was extremely productive. Both Charles and Ferry spared no expense pertaining to my research and thanks to them i have traveled overseas to several conferences and even spent three months in Australia. I have also had the pleasure of working with a wonderful group of collaborators such as Prof. James Litster from Purdue University (formerly from The University of Queensland), Prof. Francis Doyle III (from University of California at Santa Barbara), Prof. Ian Cameron and Dr. Fu-Yang Wang, (both from The University of Queensland). Jim has played an instrumental part in shaping my research and has provided excellent feedback especially in relation to the experimental work i have done. Frank also played a major role in my research work and his expertise in the process control area augmented the quality of my work. Both Ian and Fu-Yang provided useful feedback toward my work and along with Jim were excellent hosts when i visited them in Australia. I must also acknowledge the help of Constantijn Sanders and Thomas Glaser. Together with Jon, my colleague from Imperial, we worked on a pilot-plant granulation facility and we had some lovely times during the course of our three months in Brisbane, Australia, which till date is one of the prettiest cities i have

seen.

I am fortunate to have had a group of exceptional colleagues and friends in Drs. Jonathan Poon, Mark Pinto, Nicola Bianco and Stephen Sweetman with whom i have worked alongside over the course of these 3 years. Jon, thanks for always answering my call for help anytime of the day and night. Undoubtedly, you made my initial foray into the deep dark recesses of population balance modelling and granulation a whole lot easier. Mark, thank you for being super intelligent and allowing me to pick your brains as and when required, which was quite often! Nicola, thanks for being the way you are and showing me never to take life too seriously. No matter what, you always have a smile on your face and it invariably always rubbed off. Steve, you are the comedian of our group and thanks for always keeping us in good humour and spirits, especially on those cold, dreary, wintery London mornings. Thanks guys for all the good times we have had in pubs, office, Australia, the spas in Harrison Hot springs and the wonderful pub where we played pool and ate those ridiculous yummy buffalo wings, New York city, Salt Lake city and so many other places. We have certainly traveled a lot together, especially you and me Jon. I think we have been almost all the over world together right from the west coast of Canada to the east coast of Australia. I can tell you that my girlfriend is quite envious of you :).

I also extend my gratitude to several other people from the department. Dr. Mansoor Ansari, currently a post-doc was very helpful when i joined and helped me overcome any inertia associated with performing fluid-bed granulation experiments. I'm happy to say that although we have graduated, we still keep in touch professionally and personally. Dr. Jerry Heng, now a lecturer took time of his busy schedule to help me on miscellaneous matters when i was just about to move to London and join Imperial. We had met when he gave a seminar at NUS, when i was a masters student and ever since then we have kept in touch. I also thank Sarah Everall, who was very patient and sent me many an email in response to any queries i had regarding my application to the department.

I would be remiss if i did not acknowledge the friendship and support of all my good friends from Singapore and UK namely Sara, Selva, Mags, Zahira, Pam, Lavina, Pavi, Pallavi, Rupa, Kavitha, Dharini, Manas, Manju and Murthy. You all have known me for

many years and although we are all scattered in different corners of the globe. we still keep in touch as best we can. Special mention goes to Murthy who i've known for several years now and in my opinion is not only a cartoon :). but one of the most remarkable and sincere persons I've ever known.

My family have played a huge role in all this and no amount of words can express how grateful i am to all of them. I am truly blessed to have wonderful parents in my Mom and Dad, who have showered me with unconditional love and support. My sister, Pooja and Brother-in-Law, Nimesh have helped me out so much over the years, providing me with all the care and comfort one could possibly need. My nephew, Rheansh who is truly adorable spurred me onto to complete my PhD as soon as possible so that i could go back earlier and see him. My uncle and aunt in UK, Shoban mama and Sumathi aunty deserve special mention for making my stay in UK feel as if i were home. My other uncle and aunt in India, Deepak mama and Shalini aunty always go out their way to make my stay with them such an enjoyable one. I've also had some great times with my cousins who i'm extremely close to. Rahul, Rohan, Ash and Pran, let's toast to all the good times we have had right from playing cricket in Bamrauli to sipping single malt in Peterborough.

I would like to thank Hiral Sanghvi, the special someone in my life :). She truly has been a pillar of support over the last few years putting up with all my weird habits especially during the thesis writing stage. Babe, for all this and so much more you have done for me, i am truly indebted. I love you.

Finally, i would like to dedicate this thesis to my late grandparents. Thata and Ammama, not a day goes by where i don't think of you. I miss you both very much.

Contents

List of Tables

List of Figures

Chapter 1

Introduction

1.1 Process Modelling

Process modelling is the attempt to present systematic methods that are useful in the development and application of mathematical models and is a key component of process systems engineering (Denn, 1986; Hangos and Cameron, 2001). A mathematical model of a process (a.k.a. process model) is a system of equations whose solution, given specified input data, is representative of the response of the process to a corresponding set of inputs (Denn, 1986). The concept of representing process behaviour with mathematical expressions has several advantages. These are namely investigating the process response(s) rapidly and inexpensively without necessarily interfering with the physical process; and analysis and/or design of the control system of the process (Ogunnaike and Ray. 1994). There are several ways of classifying process models. Each of these results in various model characteristics which have an impact on solution techniques and the application areas where they potentially can be used. Table 1.2 in Hangos and Cameron (2001) provides a good overview of the common model types and their basic characteristics. This research is concerned with distributed parameter systems, details of which are provided in the following section.

1.2 Distributed Parameter Systems

Many industrial processes are such that their constituents are distributed with respect to one of more of their characteristics, called internal attributes. Such processes come under the class of distributed parameter systems (DPSs). DPSs are the most natural and generic systems existing today. Dynamic characteristics of most natural structures, manufacturing processes, particulate processes, fluids, heat transfer, control, etc.. all come under this DPS category (Tzou and Bergman, 1998). This thesis concerns particulate processes which are essentially distributed systems described by population balances (e.g. size distribution of crystals, emulsion polymers and granules; and age distribution of microbial cells). In general, the dynamics or responses of these distributed processes are functions of space and time, and these systems are normally modelled by partial differential equations (PDEs). This is in contrast to lumped parameter systems (LPSs), in which any dependent variable can be assumed to be a function of only time and all constituents of a population are considered alike. While lumped parameter models are usually used to describe processes, many important processes are inherently distributed in nature, thus necessitating the study of DPSs. However, researchers often were constrained to treat these distributed processes as lumped processes, mainly because of the following reasons.

- Lack of understanding of mechanisms governing the distributed nature of the processes.
- Lack of suitable process instrumentation to monitor distributed process characteristics.
- Lack of computational tools to handle increased complexity of the distributed problem.

As a result, there is a loss in applicability and performance of the model in neglecting the distributions. Moreover, the identification and control of entire distributions (as opposed to the control of a lumped property) results in substantial improvement in the operational and economical benefits. Continuing from this, there is a growing awareness in industries of the need to reduce fluctuations in process variables by considering control of entire distributions. Within the research community, it is widely accepted that acknowledging the

distributed attributes of the process would result in substantial improvement in product quality (Christofides, 2002).

Gay and Ray (1995) were one of the first researchers who were concerned with developing effective and readily implementable techniques for identification and control of distributed parameter systems, and they accomplished this by means of singular value decomposition (SVD). They demonstrated that their technique was a sound and convenient basis for feedback control system designs. This work was extended several years later by Chakravarthi and Ray (1999) who showed a systematic means of identification and control of distributed systems through the use of boundary inputs, using the same technique. Along these lines, Zheng and Hoo (2004) were successful in implementing a quadratic dynamic model-based controller on a lower order model that was identified using a nonlinear distributed parameter system. In the polymerisation literature for example, Semino and Ray (1995b) demonstrated successful control of the particle size distribution (PSD) of emulsion polymers, based on their research on the controllability of distributions in various population balance systems (Semino and Ray, 1995a). In later work, Immanuel and Doyle III (2003b) highlighted the importance of feedback control in control of PSD in semi-batch emulsion polymerisation. In another study, an on-line multi-variable model predictive control (MPC) was formulated to control PSD and molecular weight distribution (MWD) by manipulating the flow rates of monomers, surfactant, initiator and temperature of the reactor (Alhamad et al., 2005). The applicability of MPC in distributed systems was also illustrated in the work of Dokucu et al. (2008a) who considered an in-batch closed-loop control of the full PSD in a semi-batch emulsion copolymerization system. Within the same system in another study, Dokucu et al. (2008b) developed feedback control strategies for the regulation of PSD that could also be applicable for regulation of distributions in other particulate systems governed by population balances. Even in other areas such as crystallisation and aerosol processes, significant advances have been made in the control of size distributions (Shi et al., 2005; Yu et al., 2007; Kalani and Christofides, 2002; Kostoglou et al., 2006). However, in granulation (which this research deals with), which by-and-large operates in a highly inefficient manner due to poor control, there have been very few studies that have successfully addressed the control of distributions and other

related issues. This point will be discussed in more detail in the following sections.

1.3 Problem Statement and Motivation

Granulation is the generic term for particle size enlargement of fine powders. Many continuous granulation plants operate well below their design capacity, suffering from high recycle rates and even instabilities induced by disturbance amplification effects (Zhang et al., 2000; Wang and Cameron, 2002; Immanuel and Doyle III, 2005). In batch operation for instance, it is of interest to develop a systematic strategy for scale-up of high value products. However, scale-up is poorly understood and more often that not, unacceptable outcomes at the larger scale are obtained (Leuenberger and Betz, 2007). Further advanced control objectives of granulation include the granule size distribution (GSD) which finds correlation with several end-use properties spanning various process industries including delivery rates of drugs/fertilisers/detergents and taste of products. Thus there is an immediate economic incentive for better understanding and for effective control and scale-up of granulation units. However, the overall granulation process is highly integrated and interacting; comprising of drying, classification and crushing units and recirculation loops; with limited manipulated variables available for operation and advanced control. Current state of granulation research also shows significant gaps between the microscopic particle-level physics and plant-scale modelling. As a result, there is a large amount of empiricism in granulation modelling, which provide little insight into the intricate mechanisms of the granulation process. This effectively results in a lack of knowledge to make appropriate engineering decisions to improve the control and scale-up of the granulation process.

Each of these factors, motivate a first-principles model-based strategy for design, control and scale-up that is well supposed by experimental studies/analyses/validation. Furthermore, although granulation research is relatively in its infancy compared to other particulate processes, research advances in granulation can potentially enhance the control of other distributed particulate processes. Prior to formulating specific thesis objectives, it is imperative to address the existing gaps and challenges in granulation research in more detail. This is discussed in the next section.

1.4 Existing Gaps and Challenges in Granulation Research

In order to improve the efficiency of the overall operation of the granulation process, it is necessary to consider the aspects of (1) experimental studies and validation; and characterisation of multiple granule attributes; (2) model development and solution techniques; (3) sensitivity studies and controllability analysis; (4) instrumentation and monitoring; (5) optimisation and control; and (6) scale-up (typically for batch granulation). These aspects are outlined below. For the purpose of this thesis, the distributions considered are granule size, fractional binder content and porosity (details of which are provided in chapter 2).

1.4.1 Experimental Studies and Validation; and Characterisation of Multiple Granule Attributes

Experimental studies assume importance and pose a challenge in granulation because of the potential uncertainties in the granule mechanisms. Therefore, suitable experiments have to be designed and carried out for three main reasons.

- Firstly to isolate various mechanistic parameters in the models.
- Secondly to compare model predictions of evolutions and distributions of granule attributes with those measured. In doing so, these models can be deemed valid to be used for further analysis, optimisation, control and scale-up. Comparing experimental data with model predictions, requires the characterisation of multiple important granule attributes (for a realistic characterisation). Obtaining these average and distributed properties pose an entirely different challenge due to measurement conflicts.
- Thirdly to identify process sensitivities and important process manipulations for feedback control.

In the current granulation literature, there are no studies that have validated time evolutions of distributions for multiple granule properties. Also, there have been no studies that have characterised multiple granule properties (both average and distributed) for granulation systems described in this thesis. In addition, there is no research that has studied

process sensitivities and related them to feedback control. Details of the above will be discussed in chapters 2-7.

1.4.2 Model Development and Solution Techniques

The development of models describing the intricate granulation mechanisms is a non-trivial task. The modelling of distributions in granulation processes involves population balance equations and relies on mesoscopic phenomena that can be broadly classified as birth, growth and death. Difficulties arise in the mathematical representations of these potentially uncertain phenomena as well as the modelling of kinetic and thermodynamic parameters that drive the mechanisms. Another big challenge in the development of these models for granulation is the solution technique for these complex models. These models comprise of integro partial differential equations, ordinary differential equations and algebraic equations. Furthermore, for multi-dimensional models of granulation (which this thesis deals with) analytical solutions do not exist. Standard numerical techniques also render these models of reduced utility even for off-line applications, let alone on-line applications. Thus, effective models and efficient custom-built numerical solution techniques need to be developed. However, in the current granulation literature, many of the existing models are empirical in nature and offer no realistic insight into the intricate mechanisms of the granulation process. Furthermore, the models considered under-represent the granule characteristics (e.g. a one-dimensional population balance model that models only GSD and is unable to account for distributions with respect to binder content and porosity). To date, there exist no studies that have successfully modelled and numerically solved multi-dimensional population balances that incorporate fundamental process physics and chemistry. Further details are provided in chapters 2 and 4-6.

1.4.3 Sensitivity Studies and Controllability Analysis

Effective control of any process depends on two pre-requisites. Firstly the identification of sensitivities of the process and secondly the controllability of the process. Sensitivity studies are important because of the need to ascertain the ability of input parameters to influence the distributions, in combination with other macroscopic lumped variables.

This in turn enables the development of effective and efficient control strategies. While this analysis is intuitive in lumped systems, in the case of distributed systems the analysis is not so straightforward. This is mainly due to the fact that distributed properties are intimately related and cannot be controlled independently (Pottman et al., 2000; Glaser et al., 2008).

The second pre-requisite is the controllability of the process. This aspect entails identifying the potentials and limitations of the overall system. While a complete theory of controllability exists for lumped parameter systems, such is not the case for distributed systems (which are described by partial differential equations). This is mainly because the properties of partial differential equations depend so much on their characteristics, and initial and boundary conditions. As a result, controllability theory has evolved for very specific cases (Semino and Ray, 1995a). Furthermore, distributions result in an infinite-dimensional system with respect to the outputs and in contrast, dimensions of the inputs are small. As a result, the distributions that can be practically achieved are limited. In addition, for multi-variable systems, the attainable regions of the variables of interest are normally correlated, limiting the control of distributions. Hence, the above aspects need to be properly understood to arrive at efficient control strategies. Groundwork has been laid by Semino and Ray (1995a) who performed detailed controllability analysis on distributed systems such as human population, emulsion polymerisation and crystallisation. Furthermore, a simulation-based controllability analysis on a first-principles based granulation process model (for aggregation only) was undertaken by Fevotte and Doyle III (2005). However, a more in-depth sensitivity study and controllability analysis of the overall granulation process (considering most of the key mechanisms) should be undertaken and to date, no work on this exists. Further details will be discussed in chapter 7.

1.4.4 On-line Instrumentation and Monitoring

The primary factor that determines the success of the control of entire distributions, is the availability of good on-line instrumentation and sensors for monitoring purposes. Feedback control necessitates the measurement of granule size distribution (GSD), fractional binder content distribution and porosity distribution, at a sufficiently high frequency. There-

fore, having an on-line (or a quick at-line) analyser tracking a significant process variable increases process understanding. Furthermore, responses to changes in the variable of interest can be made more rapidly and to a greater effect. The caveat is that acquiring data from distributed processes (e.g. granulation) is not as straightforward and routine as is the case for typical chemical processes (Pottman et al., 2000). In addition, any real-time measurements from sensors have to be integrated with control hardware and software to ensure that the signal is used in feedback calculations. There exist few studies that have demonstrated the use of on-line particle analysis for monitoring and control. These are discussed below.

To characterise GSD, several methods have and can be used. Sieve analysis is the most conventional method, however it cannot be conducted in real time and this precludes it from on-line monitoring and control. Similarly, there exist many other off-line and at-line instruments that work on the principle of laser diffraction, image analysis and light scattering. In comparison, developing on-line methods for size analysis that are (1) able to monitor distributions, (2) tested for its validity and (3) gone on to be applicable to control of granule size, are significantly more challenging. With regards to this, Watano and Miyanami (1995) and Watano (2001) were two such studies that successfully demonstrated the use of a novel image processing system to monitor and control granule growth in fluid-bed granulation.

To characterise fractional binder content, a moisture analysis of the granule has to be undertaken. Similar to the size analysis, various off-line methods exist and these include thermo-gravimetry, spectrophotometry, electrical conductivity and infra-red. Converting these technologies to enable on-line monitoring is however a non-trivial task, and two studies have successfully managed this. In the first study, Gradinarsky et al. (2006) demonstrated *in situ* monitoring and control of moisture content using an open-ended coaxial probe and in the second study, Portoghese et al. (2008) demonstrated continuous on-line measurement of solid moisture content in fluid bed granulation, using triboelectric probes.

The third granule attribute to be characterised is porosity (or related parameter bulk density). Once again, off-line and at-line methods such as mercury intrusion and pycnometry

exist. Hitherto, there are no direct *in-situ* methods to monitor porosity in real-time to facilitate on-line control.

1.4.5 Optimisation and Control

From the optimisation and control perspective, a blind strategy based on the detailed process model will be less effective due to the non-convexity and computational intensity of the problem. Therefore, a strategy that explicitly exploits the problem physics along with the process model should be considered, analogous to the work of Immanuel and Doyle III (2003b), for the case of emulsion polymerisation. Till date however, there have only been few studies that have attempted to tackle the issues of optimisation and control in granulation. Wang (2006) have investigated process optimisation and optimal control of batch and continuous drum granulation processes. The main foci of their work have been the construction of control relevant population balance models, the investigation of optimal operating conditions and the development of optimal control algorithms. In a later study, Wang (2007) demonstrated a multi-form modelling approach to drum granulation which resulted in significant reduction in computational times. Since both open-loop optimal control and closed-loop MPC rely on iterative dynamic simulation and optimisation, overall reduction of computational time makes on-line application possible. This could imply a big step toward the industrial applications of model-based control for granulation processes. However, these studies have considered empirical-based granulation processes and to date, there have been no works reported on the optimisation of first-principle based granulation processes.

With regards to control of distributions in granulation, only few studies have successfully demonstrated suitable control strategies to control distributions. Zhang et al. (2000) presented a useful study whereby the recycle size distribution (RSD) was regulated with a proportional-integral (PI) controller by manipulating water addition to the feed slurry. Their results also showed that the RSD was heavily correlated with average granule size and moisture content and as a result, they were controlled indirectly. In another study, Pottman et al. (2000) applied a model-based MPC to a specific granulation system. Their results showed that they were successful in regulating the bulk density variable to

its set-point whilst maintaining the granule size distribution within specified upper and lower limits. This work was subsequently extended by Gatzke (2001) who went on to propose two additional extensions to traditional MPC controllers. Aside from regulatory controllers (e.g. PI) and MPC, fuzzy logic controllers have also been used in the control of granulation processes (Watano, 2001; Watano et al., 2001). However, these studies have implemented these strategies for specific systems and operating conditions. Therefore, a more general process model (based on the underlying mechanisms of the granulation process) would be a useful aid in formulating more robust control strategies that can accommodate deviations from nominal conditions. To date, there has been no work on this.

1.4.6 Scale-up

One of the new trends in granulation research is the issue of scale-up. The implicit objective of scale-up is to improve the economy of production. Typically in the pharmaceutical industry, dosages have been manufactured in small batches. However, production costs have escalated and the whole production process has to be investigated to ascertain if there is a chance to reduce costs and increase productivity by scaling up (Leuenberger and Betz, 2007). Granulation processes are intrinsically complex and are influenced by several process variables. As a result, scale-up of granulation processes from small scale to production scale is often done empirically in the pharmaceutical industry, often yielding unacceptable results (Rambali et al., 2003). Faure et al. (2001) and Mort (2005) have provided an excellent review on the types of scale-up strategies that would be applicable to granulation processes. There strategies can be grouped into

- Methods based on monitoring one representative parameter, by relating the representative parameter to one or more properties of the granule via empirical relations. These methods have seen application in the works of Faure et al. (1999) and Rambali et al. (2003).

- Modelling the process using experimental design: Once established, the models can estimate granule attributes at changing operating conditions and scale. These methods have seen application in the works of Wehrle et al. (1993) and Ogawa et al.

(1994).

- Using first-principle models such as population balance models. To date. there have been no reported work(s) that use these models for scale-up.

Although the first two methods have been used successfully for scale-up, they are essentially based on either heuristics, empirical relations or empirical models. They are also potentially tedious and require large amounts of experimentation to establish linkages between material properties and process/design parameters with granule properties. Moreover, they are specific to particular systems and ranges of operating conditions. Population balances however, offer the potential to circumvent these issues by providing the necessary meso-scale links between material properties and process/design parameters with granule properties with reduced experimentation and time. In principle, a good understanding of the granulation process on the micro-scale and a working realistic model of the population balance is required. In practise, there are still large gaps to be addressed in the population balance modelling of granulation processes (as previously discussed in section 1.4.2).

1.5 Thesis Scope and Objectives

In summary, the discussion in the above section has identified the significant gaps and challenges in the existing granulation literature. This logically lends itself to the following discussion, where the scope of this thesis is defined and the specific objectives of this thesis are formulated.

In light of the discussions in sections 1.3 and 1.4, it clear that to address the granulation problem in an effective manner and improve upon the current state-of-the-art, there are eleven major areas to further research. Summarising from section 1.4, these are namely (1) on-line instrumentation and monitoring, (2) model development, (3) solution techniques, (4) experimental studies, (5) experimental validation, (6) characterisation of multiple granule attributes, (7) sensitivity studies, (8) controllability analysis. (9) optimisation. (10) control and (11) scale-up. As put forward by Cameron et al. (2005), this thesis is concerned with a more systems-centric approach to the granulation problem which could

significantly enhance the design, control and scale-up of granulation processes. Quantitative contributions of this thesis will be made in the areas of (2), (3), (4), (5), (6), (7) and (8) with qualitative insight in the areas of (10) and (11). A summary of the overall objectives is given below:

- **Experimental Studies:** Firstly, to study the granulation kinetics of a typical granulation recipe and investigate the effect of material and process parameters on granule properties. Secondly, to investigate process sensitivities and important process manipulations, to form a control configuration for both batch and continuous granulation processes.

- **Characterisation of multiple granule properties:** To measure the average and distributed properties of granule size, binder content and porosity which accounts for a realistic characterisation of a granule. This is firstly to be used for validation purposes and secondly, to justify the need for multi-dimensional population balance models by investigating the heterogeneity/homogeneity of the distributions.

- **Model development:** Firstly to formulate an effective multi-scale, multi-dimensional population balance model for the granulation process. This model should account for the distributions across granule size, binder content and porosity and also account for the multi-scale character of the process. Furthermore, this model should be based on first-principles (i.e., based on the underlying physics and chemistry of the important granulation mechanisms.) Secondly to investigate alternative means (e.g. via discrete element models) of obtaining relationships between fundamental solid and liquid properties with granulation dynamics.

- **Solution technique:** To reduce computational time of the current solution technique used in this research, making the model more amenable to on-line control.

- **Experimental validation:** Firstly, to validate the first-principles based models at the batch scale for different granulation systems (i.e., high-shear, fluid-bed and drum) illustrating the robustness and flexibility of the model. Secondly, to ensure that the valid models can be used for further analysis.

- **Sensitivity studies:** To perform a detailed sensitivity analysis of the population balance model, to identify the influence of adjustable model parameters on the particle density distribution.

- **Controllability analysis:** To develop a compartmentalised version of the combined PBM, for the purpose of a detailed controllability analysis. To further identify optimal control-loop pairings in a granulation process to potentially enhance control-loop performance of key controlled variables.

1.6 Thesis Structure

Having presented the objectives of the thesis, the rest of the thesis is organised as follows. A specific review/critique of the existing literature pertaining to the different objectives will be provided at the beginning of each chapter.

- Chapter 2 provides a detailed review of the fundamentals and population balance modelling of granulation processes.

- Chapter 3 presents the experimental studies on distributions of granule size, binder content and porosity in batch drum granulation; and the methodology for characterising multiple granule properties.

- Chapter 4 presents the experimental validation studies on a multi-scale and multi-dimensional population balance model in drum granulation, that incorporates mechanistic descriptions of granule nucleation and aggregation. A parallel programming framework to alleviate simulation time of the model is also presented.

- Chapter 5 presents the theoretical kernel development and model validation of granule breakage in high-shear mixer granulation.

- Chapter 6 presents the development and validation of a combined mechanistic population balance model for fluid-bed granulation, under low shear conditions.

- Chapter 7 presents a controllability analysis and identification of optimal control-loop pairings in a multiple-input multiple-output (MIMO) granulation process.

- Chapter 8 an alternative approach to obtaining links between fundamental material properties and process/design parameters with end granulation behaviour, by studying the distribution and accessibility of binder in wet granules via discrete element modelling.
- Chapter 9 presents the conclusions and contributions of this thesis with indications to future work.

Chapter 2

Fundamentals and Population Balance Modelling of Granulation Processes

The purpose of this chapter is to present to the reader a broad but detailed review of the fundamentals and population balance modelling aspects of granulation, which forms the basis of this research work. This includes an introduction to granulation, the granulation process, mechanisms of granulation, and granulation equipment. This is followed by an introduction to the population balance equation, multi-dimensional population balance models, identification of kernels and solution techniques. Lastly, the multi-scale aspects of granulation and a summary of the chapter are presented.

2.1 Granulation Fundamentals

Granulation, also known as agglomeration, is the generic term for particle size enlargement of fine powders. Granules are larger, semi-permanent aggregates in which the original particles can still be distinguished (Ennis and Litster, 1997). Granulation is a particle design process whereby the desired attributes are controlled by a combination of formulation parameters (e.g. solid and liquid properties) and process parameters (e.g. type of granulator and operating conditions). Some of the advantages granules offer over fine powders are

described below:

- Better flow properties: Granules flow easily compared to fine powders. Improved flow properties result in granules being easier to dispense and disperse uniformly.
- Increased bulk density: This reduces storage volume and also transportation costs.
- Segregation: Granules of similar size are able to co-mix together. preventing segregation.
- Dusting behaviour: Granules unlike powder. do not have a tendency to release airbone dust which can be potentially harmful.
- Controlled release of active ingredients: Often in the pharmaceutical industry. granules are produced that consist of an active pharmaceutical ingredient (API) and an excipient. This facilitates the controlled release of active ingredients into the body.
- Improved solubility: Granules dissolve more easily compared to powders which tend to form lumps.

As a result of the numerous advantages granulated products have to offer. granulation is ubiquitous in a wide range of industries. These include pharmaceuticals, mineral processing, agricultural products, foodstuffs, detergents and speciality chemicals. Moreover, granulation is a key step in these industries and improper granulation can cause problems in downstream unit operations of milling and tabletting, for instance in the case of a pharmaceutical manufacturing process (Iveson et al.. 2001).

2.1.1 The Granulation Process

Figure 2.1 presents a schematic representation of a typical continuous granulation process. During the granulation process, the liquid binder (from the spray nozzles) wets the dry powder (feed stream) and together, they are agitated in the granulator. Granules that are formed are then dried and classified. Products that meet the appropriate size specifications are withdrawn and off-specification material (e.g. those that are oversized or undersized) are recycled back into the granulator. Prior to this, oversized granules are crushed. Aside

from size, granules may have to adhere to certain bulk density specifications. In the next section, the key mechanisms that govern the granulation process will be introduced.

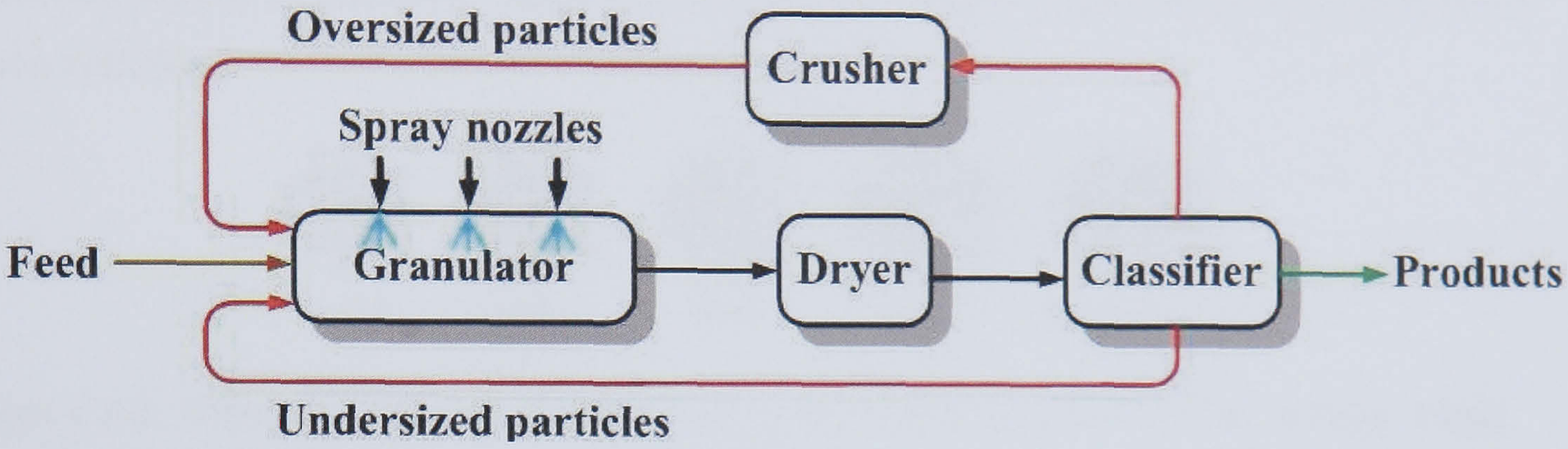

Figure 2.1: A schematic of a continuous granulation process (Cameron et al., 2005).

2.1.2 Physics and Mechanisms

Research on granulation mechanisms has been underway since the work of D. M. Newitt (1958), till the present day. D. M. Newitt (1958) mainly focussed on how the internal structure of the granules affect their behaviour. They reported that granulation occurred only when the moisture content was between certain limits. Below a minimum value, excessive caking was observed and large and weak granules were formed. Above a maximum value, the growth rate was excessive. Aside from moisture content, they observed that drum rotation speed, drum loading and the initial particle size distribution had an impact on granule growth. They then proceeded to explain these phenomena by studying the granule structures and determined that granules can exist in a number of different states (see Figure 2.2). In the pendular state, particles are held together by liquid bridges at their contact points (pendular bonds). The capillary state occurs when a granule is saturated implying that all the voids are filled with liquid and the surface liquid is drawn back into the pores under capillary action. The funicular state is a transition between the pendular and capillary state, where the voids are not fully saturated with liquid. The droplet state occurs when the particles are held within or at the surface of a liquid drop. The pseudo-droplet state occurs when unfilled voids remained trapped inside the droplet. From the granule structures, they concluded that granules had to be compacted from the pendular/funicular state to the capillary state to result in growth. They postulated that

granules coalesce (aggregate) when they are surface wet (i.e., pores are saturated and liquid has been squeezed out onto the surface). When the granules are surface wet, they have a certain degree of plasticity which allows them to deform (resulting in a contact area) upon collisions.

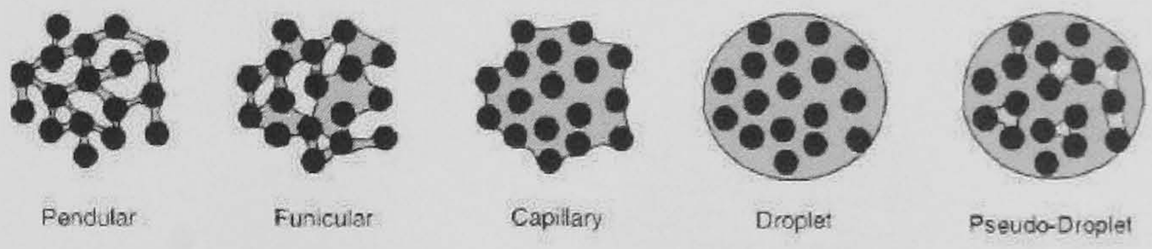

Figure 2.2: Different states of saturation of liquid bound granules (D. M. Newitt, 1958).

Based on the work of D. M. Newitt (1958), research on granule formation has continued with granulation behaviour been described in terms of a number of different mechanisms (Sastry and Fuerstenau, 1973). These are namely nucleation, layering, coalescence, abrasion transfer, crushing and layering. However, having numerous mechanisms to elucidate the behaviour of granule formation is a daunting task and some of these processes tend to overlap, resulting in an unclear demarcation between the various mechanisms (Iveson et al., 2001). Therefore, it is becoming more common to view the granulation mechanisms as a combination of only three sets of rate processes (Ennis and Litster, 1997; Iveson et al., 2001). These are,

1. *Wetting and nucleation*, where the liquid binder is brought into contact with a dry powder bed and is distributed through the bed resulting in a distribution of nuclei granules. See Figure 2.3a.

2. *Consolidation and growth*, where collisions between two granules, granules and feed powder, or granules and the equipment lead to compaction and growth. See Figure 2.3b.

3. *Attrition and breakage*, where wet or dried granules break due to impact, wear or compaction in the granulator or during subsequent product handling. See Figure 2.3c.

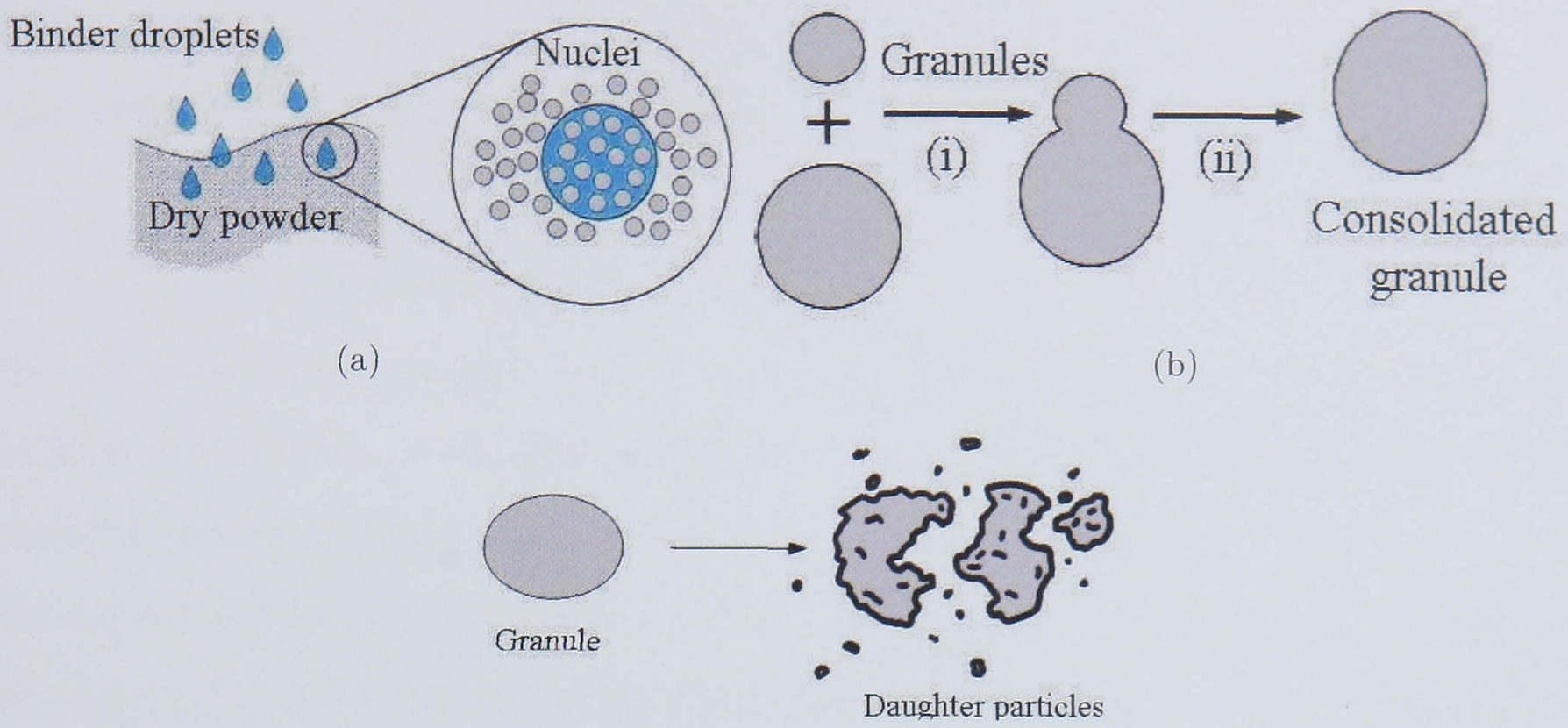

Figure 2.3: Granulation mechanisms of (a) wetting and nucleation, (b) aggregation and consolidation, (c) attrition and breakage.

2.1.2.1 Wetting and Nucleation

Wetting and nucleation is the process of bringing the liquid binder into contact with dry powder and attempting to distribute this liquid evenly throughout the powder. It is regarded as an important stage in granulation processes but is rarely identified and separated from other granulation mechanisms (Mort and Tardos, 1999). Wetting and nucleation can subsequently be envisioned as consisting of three different stages which are

- Wetting: The stage in which the binder and powder first come into contact and the binder spreads over the powder.
- Nuclei formation: The actual nuclei are formed.
- Binder dispersion: The stage in which the binder is further distributed throughout the powder due to mechanical forces.

Wetting is determined by thermodynamic properties, such as the contact angle between the binder and the powder, and the surface tension of the liquid as well as by kinetic properties such as droplet size, binder viscosity and porosity of the powder bed. The wetting stage can be quantified with the use of the theoretical penetration time (τ_{CDA}),

which describes the time required to penetrate a powder bed for single droplet (Denesuk et al., 1993), and is defined in Equation 2.1 as,

$$\tau_{CDA} = \frac{2V_0^2}{\pi^2 \varepsilon_s^2 r_d^4 R_{pore}} \frac{\mu}{\gamma_{LV} cos\theta} \tag{2.1}$$

where V_0 is the total droplet volume, ϵ_s is the surface porosity, r_d is the radius of the footprint of the drop on the powder surface, R_{pore} is the effective pore radius based on cylindrical pores, μ is the liquid viscosity, γ_{LV} is the liquid surface tension and θ is the solid-liquid contact angle. Nuclei formation is determined by the spreading behaviour of the binder which is controlled by the contact angle and surface tension. Binder dispersion is controlled by mechanical forces in the granulator such as the rotating speed of impellers in a high shear mixer, or the fluidising velocity in a fluid-bed granulator.

A number of different nuclei formation mechanisms have been proposed in the literature. Schaefer and Mathiesen (1996) performed experiments with a laboratory scale high-shear mixer using lactose and molten polyethylene glycol as a binder. Based on their results, they proposed two possible mechanisms for nuclei formation, namely the distribution mechanism and the immersion mechanism. In the distribution mechanism, the nuclei formed tend to be porous with low liquid saturation levels resulting in slow growth rates (due to liquid binder being squeezed out slowly). In the immersion mechanism, the growth rates tend to be higher due to less porous nuclei with higher liquid saturation levels. The relative size of the binder droplets with respect to the particle size determines which mechanism the nuclei formation obeys. When the binder droplets are small compared to the particles, the distribution mechanism is followed and vice versa. The general trend is for low shearing forces, large binder droplets and high binder viscosity to shift the nuclei formation mechanism from distribution to immersion. In another study, Vonk et al. (1997) proposed the destructive nucleation mechanism based on experiments conducted in a high-shear mixer. The initial nuclei formed (known as the primary nuclei) were characterised by high porosity and low tensile strength that were prone to fragmenting after undergoing some growth. The particles that resulted from the fragmentation were known as the secondary nuclei and these nuclei were characterised by lower porosity and higher tensile strength.

In order to develop a more generalised version of nucleation and to quantify the influence of process parameters, Litster et al. (2001) proposed a dimensionless spray flux and Hapgood (2000) and Hapgood et al. (2002) constructed the nucleation regime map. The dimensionless spray flux is an equipment independent parameter that describes how the binder droplets interact with the dry powder. In the spray zone, which is the zone where binder and powder are brought into contact, the projected area of drops by the nozzle per unit time equals

$$a_d = \frac{3V}{2d_d} \tag{2.2}$$

Here, a_d is the projected area of drops by the nozzle per unit time. V is the volumetric spray rate and d_d is the droplet diameter. Combining Equation 2.2 with the rate at which the surface of the dry powder bed is renewed, yields

$$\psi_a = \frac{3V}{2Ad_d} \tag{2.3}$$

where ψ_a is the dimensionless spray flux and A is the powder flux through the spray zone. The dimensionless flux can be used as an indicator of how well dispersed the binder droplets are. Litster et al. (2001) conducted experiments and their results showed that for $\psi_a < 0.1$, nucleation is in the drop controlled regime and for $\psi_a > 0.5$, caking of the bed surface occurs. However, a low value of ψ_a does not necessarily imply drop controlled granulation as the time a droplet of binder requires to penetrate the powder bed also determines the type of nucleation mechanism. Hapgood (2000) and Hapgood et al. (2002) constructed the previously mentioned nucleation regime map, which included both these parameters (See Figure 2.4). The nucleation regime map features the dimensionless spray flux ψ_a as the y-axis and the drop penetration time t_p (made dimensionless by the particle circulation time, t_c) as the x-axis. When the dimensionless spray flux is small, ($\psi_a < 0.1$) and the penetration time is short, nucleation occurs within the drop controlled regime where each droplet of binder liquid forms one individual granule. When either the penetration time is too long or the dimensionless spray flux is large, nucleation occurs within the mechanical dispersion regime, where mechanical forces are mainly responsible for the size distribution of the nuclei. The regime map distinguishes between the type of nucleation but not the rates at which it occurs, negating its use in a modelling framework.

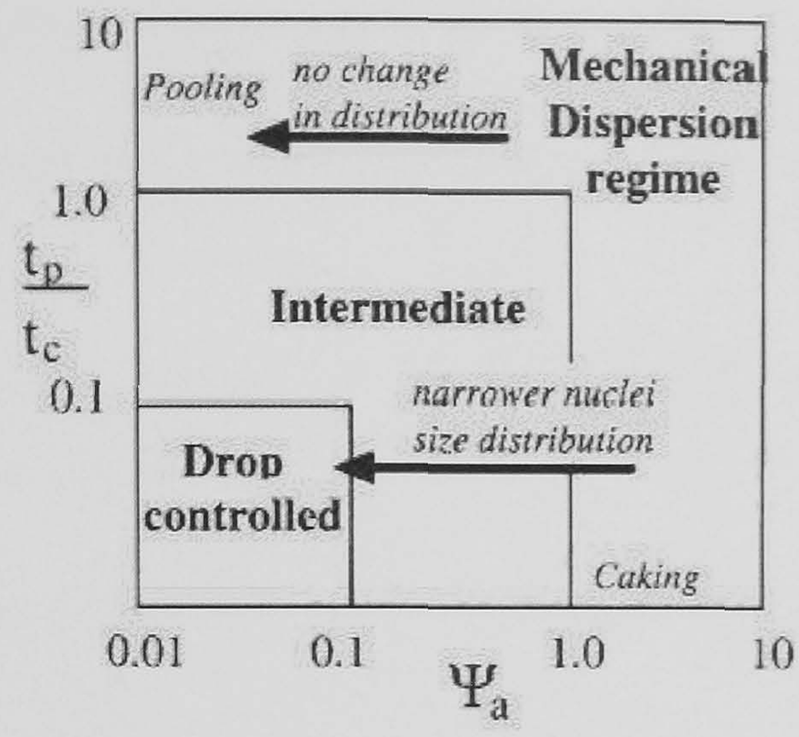

Figure 2.4: Nucleation regime map (Hapgood, 2000).

2.1.2.2 Consolidation and Growth

Granule growth (aggregation and consolidation) occurs when material in the granulator collides and sticks together. In an early study, Kristensen et al. (1985) considered aggregation to have occurred when plastic granules deform on impact and a contact area is created. In another study, Ennis et al. (1991) considered aggregation to occur when the liquid bridge layer at the surface of the granules is able to dissipate the relative kinetic energy of the two colliding granules. As granules collide with one another and/or the interior surfaces of the granulator, they gradually undergo consolidation. This serves to squeeze out trapped air and liquid which in turn results in a reduction of size and porosity. Granule consolidation also affects growth behaviour. There are two main regimes of granule growth: 1) steady growth and 2) induction type growth.

Weak deformable granules form a large contact area upon collisions and these tend to exhibit steady growth behaviour. This is marked by a steady increase of the particle size with time. Strong granules on the other hand exhibit induction type growth. During the induction time, granules consolidate slowly until they are surface wet (i.e., liquid binder is squeezed out onto the surface). During this period of consolidation, the growth rate is negligible but upon the granules being surface wet, rapid growth results due to aggregation. Aside from these two types of growth, Iveson and Litster (1998a) defined five other growth regimes which are,

- Dry: Free-flowing powder at low liquid contents such that no nuclei will be formed.
- Nucleation only: Insufficient binder for the nuclei that have already been formed to further aggregate.
- Crumb: Granules are too weak to withstand the shearing forces in the granulator. No stable granules produced.
- Rapid growth: Large amounts of binder present. Growth rate is high and uncontrollable.
- Slurry: Excessive binder is present. A slurry is produced.

In an attempt to derive quantitative expressions for the boundaries that separated these regimes, Iveson and Litster (1998a) derived two dimensional numbers. The first (De) is the deformation number and is a measure of the deformability of the granules as is defined in Equation 2.4.

$$De = \frac{\rho_g U_c^2}{Y_g} \tag{2.4}$$

Here, ρ_g is the granule density, U_c is representative collision velocity and Y_g is the dynamic yield stress. The second dimensionless number, (s_{max}) is the maximum pore saturation, which is a measure of the amount of binder within the granule and is defined in Equation 2.5.

$$s_{max} = \frac{\omega \rho_s}{\rho_l \epsilon_{min}} \tag{2.5}$$

Here, ω is the amount of liquid binder (kg/kg), ρ_s is the skeletal density of the particles, ρ_l the liquid density and ϵ_{min} the minimum granule porosity. In a subsequent study, Iveson (2002) used the Stokes' deformation number ($St_{def} = 0.5De$) in place of De. From batch experiments performed by Iveson and Litster (1998a) who used various grades of glass ballotini and binder viscosities, the boundaries between the different regimes were identified (see Figure 2.5). This regime map continues to be a useful tool in understanding granule behaviour and the effects of binder content, process agitation intensity, binder viscosity, binder surface tension and particle size on the St_{def} and s_{max}. However, a limitation of

the regime map is that it only provides information about the type of growth and not the rates of growth which is necessary to incorporate the mechanisms of aggregation and consolidation into a modelling framework.

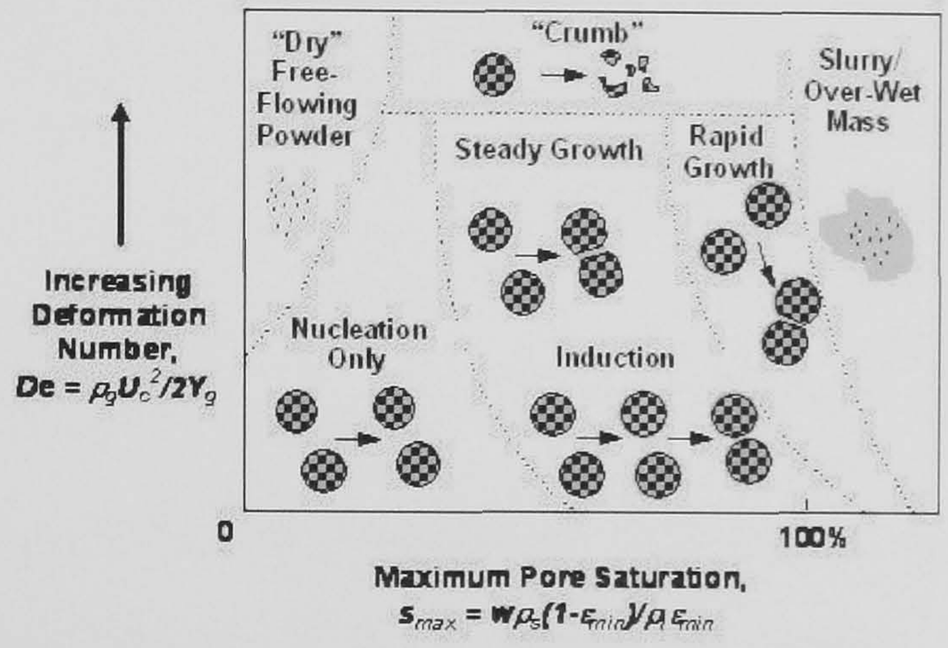

Figure 2.5: Growth regime map (Iveson et al., 2001).

2.1.2.3 Breakage and Attrition

Breakage of granules can occur as a result of impact force between granules and/or with the interior surfaces of the granulator. There are very few studies that have attempted to describe breakage in granulation processes. Several of these studies have shown via experiments that increasing the agitation intensity (impeller speed) reduces the overall mean size of granules (Schaefer et al., 1990; Watano and Miyanami, 1995; Knight et al., 2000). However, reduction of mean size with increased agitation could also be explained as a result of loss of aggregation efficiency. Hence, changes in the size distribution on their own are insufficient evidence to confirm the occurrence of granule breakage. In other studies, Vonk et al. (1997), Ramaker et al. (1998) and Pearson et al. (1998) identified wet granulation breakage in high-shear mixer experiments, by using coloured tracer granules/liquid. For instance, in the work of Pearson et al. (1998), the tracer granules were broken, leaving coloured fragments in the smaller size classes, indicating granule breakage. In the literature, there is limited quantitative theory to predict conditions for granulation breakage and the effect of formulation properties on breakage. To date, Tardos et al. (1997) and Kenningley et al. (1997) present the two main attempts in predicting and understanding granule breakage.

Tardos et al. (1997) present that granules will deform and break in their shear fields if there is sufficient externally applied kinetic energy. This leads to a Stokes' deformation number criteria for breakage (parameters previously defined in Equation 2.4) as defined in Equations 2.6 and 2.7.

$$St_{def} > St^*_{def} \tag{2.6}$$

$$St_{def} = \frac{\rho_g U_c^2}{2Y_g} \tag{2.7}$$

Tardos et al. (1997) measured granule deformation and break up under shear in a fluid-bed granulator. Granules first elongated under shear and then broke at a Stokes' deformation number of approximately 0.2. However, there are some limitations to this work. For example, in a high shear granulator, granules are more likely to break on impact with the impeller as opposed to shear. Hence more information is required and has to be suitably incorporated in wet granule breakage mechanism to aptly describe the breakage phenomenon. Kenningley et al. (1997) developed a relationship for breakage in a high shear mixer granulation by equating the kinetic energy of impact to energy absorbed by plastic deformation of granules. Granule yield strength is assumed to be due to viscous pressure loss for fluid flow between particles by the Kozeny-Carman equation. The amount of strain (ε_m) is given by,

$$\varepsilon_m^2 = \frac{1}{540}\frac{\varepsilon^3}{(1-\varepsilon)^2}\frac{\rho u d_{32}}{\mu} \tag{2.8}$$

where d_{32} is the Sauter mean size of the granules' constituent particles, ε is the granule porosity, u is the granule velocity, μ is the liquid binder viscosity and ρ is the solid particle density. Increasing particle size or decreasing viscosity will increase the amount of impact deformation. Granules will subsequently break for a strain value that is more than 0.10 and Kenningley et al. (1997) have reported that it shows reasonable agreement with their experimental data. The approaches of Tardos et al. (1997) and Kenningley et al. (1997) show reasonable promise as a foundation for measuring granule breakage but more data and information are still needed to measure granule breakage for granules with a wide range of mechanical properties. Moreover, their studies on breakage serve as qualitative

indicators for breakage without supplying any information regarding rates of breakage. Attrition of granules, which can occur during subsequent product handling, is out of the scope of this thesis and will not be reviewed.

2.1.3 Granulation Equipment

A gamut of granulator designs exist in industry depending on the required characteristics of the granulated product. A detailed review of the designs and typical operating conditions can be found in Ennis and Litster (1997). There are generally three main types of granulating equipment, classified by the way the material is agitated: tumbling granulators (e.g. drum), fluid-bed granulators, and mixer granulators. A brief introduction to each type is given below.

2.1.3.1 Drum Granulators

Drum granulators produce mostly spherical granules between $1-20\,mm$ in diameter and are particularly popular in the production of fertilisers, agricultural chemicals and in the iron-ore industry (Ennis and Litster, 1997). Drum granulators are large rotating cylinders, $0.5-4\,m$ in diameter, usually inclined up to 10^0 to the horizontal. Fine powder enters and tumbles towards the exit whilst being mixed with finely atomised binder liquid. They are usually operated in closed circuit, with a set of screens at the exit removing and recycling undersized and oversized material

2.1.3.2 Fluid-Bed Granulators

A fluid-bed granulator is a tall cylindrical or rectangular vessel containing a bed of particles. Air is forced through a distributor at the base which fluidises and agitates the powder. A binding fluid (a solution, suspension or a melt) is added by spraying from above, below, or within the powder bed. These binder drops collide with the powder particles and form liquid bridges, which hold them together by capillary suction. Nucleation and growth mechanisms tend to dominate fluid-bed granulation as the forces in the bed are relatively low compared to other granulators. By heating the fluidising air, the product can be granulated and dried simultaneously, which is particularly useful in the specialty

chemical, and pharmaceutical industries (Ennis and Litster, 1997). Fluid-bed granulation has many controlling process variables including air flowrate, air temperature, solids bed height, binder spray rate, humidity, drop size, and the position of the nozzle relative to the bed surface. These variables are often inter-related which makes controlling fluid-bed granulation more complex.

2.1.3.3 Mixer Granulators

Mixer granulators (also known as high-shear granulators) use an impeller to vigorously agitate the powder and produce high-density granules usually less than $2\,mm$ in size (Ennis and Litster, 1997). They are commonly found in the pharmaceutical, agrochemical and detergent industries because of their ability to handle difficult feed formulations, including high viscosity binder fluids and fine cohesive powders. Impellers rotate at high speed (between $100 - 1500$ rpm) on either a vertical or horizontal axis to create the agitation required for granulation. Many impeller designs are available but there is little demonstrated scientific support for the designs or their effect on granulation. A second smaller impeller, called the chopper, rotates at much higher speeds (around 1500 rpm); the role of the chopper in granulation is currently a matter of debate. It either fractures larger agglomerates or causes growth of smaller agglomerates, depending on the feed, operating conditions and the geometry of the mixer, impeller and chopper. Mixer granulation allows the binder to be added as a liquid by pouring or spraying, or by a third process where the binder is added as a solid and mixed with the powder while the granulator temperature is increased above the binder melting point. This type of granulation is called melt granulation.

2.2 Population Balance Modelling of Granulation Processes

As seen from the first chapter, the essence of modelling is to construct a mathematical description of a system which subsequently can be used for analysis, simulation, control or optimisation, based on the objective of the model. There are several approaches to model granulation processes. At one end, there is mechanistic modelling that aspires to elucidate the dynamic behaviour of a system by incorporating the fundamental physics

and chemistry into the model. Such models are generally complex although they are valid over a wide range of operating conditions and can be used for predictive purposes. At the other end of the spectrum, there are black-box models (empirical models) that merely serve to mimic the system behaviour via means of input-output data. Such models are less complex and easier to incorporate in control schemes but tend to be valid only at certain operating conditions due to their empirical nature. Furthermore, they cannot be used for predictive purposes. Ideally, a combination of the two models (known as grey box model) that incorporates the detail of the mechanistic model with the data fitting attributes of the empirical model is suitable to depict the behaviour of the granulation process. The precursor of this is to develop a first principle model of the granulation process which is an important step. There have been several studies that have reported the underlying phenomena that represent the granulation process (Iveson et al., 2001; Adetayo et al., 1995; Liu et al., 2000). A suitable methodology to model these granulation mechanisms is through population balance models (Ramkrishna, 2000).

Population balances are mathematical models that describe changes in populations in which each member of the population is distributed with respect to one or more properties. In particle technology (e.g. granulation), the most obvious property is particle size and population balances have often been applied to model changes in the size distribution. Since particle size is one of the important parameters and correlates with end usage, the need for the population balance models are clear.

2.2.1 The Population Balance Equation

In its most general form, the population balance equation (PBE) is written as shown below (Ramkrishna, 2000):

$$\frac{\partial F(\mathbf{x},t)}{\partial t} + \frac{\partial}{\partial \mathbf{x}}\left[F(\mathbf{x},t)\frac{d\mathbf{x}}{dt}\right] = \Re_{formation}(\mathbf{x},t) - \Re_{depletion}(\mathbf{x},t) \tag{2.9}$$

Here $\mathbf{x}$ is the vector of state variables used to characterise the distribution and $F(\mathbf{x},t)$ is the population distribution function. In granulation for example, a single variable, size is often employed; and the resulting distribution is called the granule size distribution. The

term $\frac{\partial}{\partial \mathbf{x}}\left[F(\mathbf{x},t)\frac{d\mathbf{x}}{dt}\right]$ accounts for growth processes. Specifically, the term $\frac{d\mathbf{x}}{dt}$ accounts for growth of a particle with respect to each state variable. Thus, in granulation, the term $\frac{d\mathbf{x}}{dt}$ could represent the rate at which granules compact due to collisions (*i.e.* the rate of consolidation); $\frac{\partial}{\partial \mathbf{x}}\left[F(\mathbf{x},t)\frac{d\mathbf{x}}{dt}\right]$ would then account for the rate at which the distribution evolves due to this rate of consolidation. $\Re_{formation}(\mathbf{x},t)$ accounts for formation of particles due to nucleation, aggregation and breakage phenomena, and $\Re_{depletion}(\mathbf{x},t)$ accounts for depletion of particles by the same phenomena.

2.2.2 Multi-Dimensional Population Balance Models

One-dimensional models have been well exploited in particulate processes for model-based analysis (Christofides, 2001; Ma et al., 2002; Immanuel and Doyle III, 2003a). They are often adequate for processes where the effect of key mechanisms (such as nucleation, aggregation and breakage) on the process dynamics can be accounted for through the consideration of a single particle characteristic (e.g. size distribution of emulsion polymers). However, the accurate modelling of granulation processes warrants the consideration of multiple particle characteristics. Aside from granule size, binder content has an important effect on granule growth with many studies concurring that the amount of binder correlates directly with the rate of granule growth, due to a larger availability of surface-wet granules (Knight, 1993; Kristensen, 1996). As a direct result of this, induction time decreases promoting steady growth (Iveson and Litster, 1998a; Wauters, 2000; Knight et al., 1998; Hoornaert et al., 1998). Intuitively as well, it is clear that improper liquid distribution (which often occurs in granulation) will promote different granule growth rates (Reynolds et al., 2004). Granule porosity is an essential parameter that has a profound effect on granule growth behaviour. Below a certain critical porosity, pore saturation is low and binder liquid remains within the granule resulting in surface-dry granules. Above the critical porosity, pores are saturated and liquid is squeezed on the surface resulting in surface-wet granules and higher growth rates. Porosity also has an effect on deformability and strength and as a result it can have a pronounced effect on growth and breakage. For instance, in the work of Annapragada and Neilly (1996) it was observed that porous granule when initially formed, go onto break quickly (resulting in higher breakage rates) and thereafter aggregate to form stronger denser granules (resulting in lower breakage rates).

As a result of the above discussion, the granulation process should be described by a three-dimensional population balance model, which accounts for granule size, binder content and porosity. The potential heterogeneity of the population distribution with respect to all three attributes is such that lumping in any of these dimensions would result in considerable model errors (Iveson, 2002). In formulating the three-dimensional population balance, the three particle attributes are recast in terms of their individual volumes of solid (s), liquid (l) and gas (g) (Verkoeijen et al., 2002). The purpose of modelling the granulation process in terms of its individual volumes enables decoupling of the individual meso-scopic processes (i.e., aggregation, consolidation etc.). This essentially offers two advantages. Firstly, one could model a single rate process at a time. Secondly, the mutually exclusive character of the internal coordinates substantially improves the solution of the model as rate processes with differing time constants are segregated. This point will be discussed in more detail in section 2.2.4.1. The resulting three-dimensional population balance equation is then given by

$$\frac{\partial}{\partial t}F(s,l,g,t) + \frac{\partial}{\partial g}(F(s,l,g,t)\frac{dg}{dt}) + \frac{\partial}{\partial s}(F(s,l,g,t)\frac{ds}{dt}) + \frac{\partial}{\partial l}(F(s,l,g,t)\frac{dl}{dt}) = \Re_{nuc} + \Re_{aggre} + \Re_{break} \tag{2.10}$$

where $F(s,l,g,t)$ represents the population density function such that $F(s,l,g,t)ds\,dl\,dg$ is the moles of granules (adopting a number-based population balance instead of mass or volume-based) with solid volume between s and $s+ds$, liquid volume between l and $l+dl$ and gas volume between g and $g+dg$. The partial derivative term with respect to s, accounts for the layering of fines onto the granule surfaces; the partial derivative term with respect to l accounts for the drying of the binder and the re-wetting of granules; the partial derivative with respect to g accounts for consolidation which due to compaction of the granules, results in an increase of pore saturation and decrease in porosity. In this thesis, layering and drying are neglected. The formation and depletion terms associated with the aggregation phenomenon ($\Re_{aggre}$) are defined in Equations 2.11-2.13 (Ramkrishna, 2000; Immanuel and Doyle III, 2005). In these equations, s_{nuc} is the solid volume of nuclei

(assumed fixed), and $\beta(s\prime, s-s\prime, l\prime, l-l\prime, g\prime, g-g\prime)$ is the size-dependent aggregation kernel that signifies the rate constant for aggregation of two granules of internal coordinates $(s\prime, l\prime, g\prime)$ and $(s-s\prime, l-l\prime, g-g\prime)$. β is essentially a measure of how successful collisions between two particles resulting in a larger granule are. See section 2.2.3.1 for more details.

$$\Re_{aggre}(s,l,g,t) = \Re_{aggre}^{formation} - \Re_{aggre}^{depletion}. \tag{2.11}$$

where

$$\Re_{aggre}^{formation} = \frac{1}{2}\int_{s\prime=s_{nuc}}^{s-s_{nuc}}\int_{l'=0}^{l}\int_{g'=0}^{g}\beta(s\prime, s-s', l', l-l', g', g-g')\times F(s\prime, l', g', t)F(s-s', l-l', g-g', t)ds'dl'dg' \tag{2.12}$$

$$\Re_{aggre}^{depletion} = F(s,l,g,t)\int_{s\prime=s_{nuc}}^{s_{max}}\int_{l'=0}^{l_{max}}\int_{g'=0}^{g_{max}}\beta(s\prime, s, l', l, g', g)\times F(s\prime, l', g', t)ds'dl'dg' \tag{2.13}$$

The breakage term ($\Re_{break}$) is mathematically described in two parts; the breakage kernel (k_{break}) and the breakage function (b). The former describes the rate at which a particle of size s, l and g breaks into a fragments of size s_1, l_1 and g_1. The latter describes the sizes of these fragments formed. Therefore, $\Re_{break}$ is defined in Equations 2.14 to 2.16.

$$\Re_{break}(s,l,g,t) = \Re_{break}^{formation} - \Re_{break}^{depletion} \tag{2.14}$$

$$\Re_{break}^{formation} = \int_s^{\infty}\int_l^{\infty}\int_g^{\infty}k_{break}(s',l',g')b(s,l,g,s',l',g')\times F(s',l',g',t)ds'dl'dg' \tag{2.15}$$

$$\Re_{break}^{depletion} = k_{break}(s,l,g)F(s,l,g,t) \tag{2.16}$$

Similar to the formation and depletion terms associated with $\Re_{aggre}$ and $\Re_{break}$. the nucleation is described by the rate of formation of nuclei and the rate of depletion of primary particles and is defined in Equations 2.17 to 2.19 (Poon et al.. 2008).

$$\Re_{nuc}(s,l,g,t) = \Re_{nuc}^{formation} - \Re_{nuc}^{depletion} \tag{2.17}$$

$$\Re_{nuc}^{formation} = \int_{s\prime=s_{min}}^{s_{max}} \int_{l\prime=l_{min}}^{l_{max}} \int_{g\prime=g_{min}}^{g_{max}} k_{nuc}(s\prime,l\prime,g\prime)F(s\prime,l\prime.g\prime,t)ds\prime.dl\prime.dg\prime \tag{2.18}$$

$$\Re_{nuc}^{depletion} = k_{nuc}(s\prime.l\prime,g\prime)F(s\prime,l\prime.g\prime.t)Nx(s\prime.l\prime,g\prime) \tag{2.19}$$

where N is the number of primary particles in the nucleus and $x(s\prime.l\prime.g\prime)$ is the fraction of primary particles with characteristic $s\prime, l\prime, g\prime$ that are present in the nucleus (Poon et al., 2008). More details will be presented in chapter 4.

The consolidation model is represented by an empirical exponential decay relation and is shown in Equation 2.21. The porosity of granules is defined by Equation 3.3 and substituting Equation 3.3 into Equation 2.21 gives a formal expression explicitly in terms of the three independent internal coordinates (see Equation 2.22), which can then be used in Equation 2.10.

$$\varepsilon = \frac{l+g}{s+l+g} \tag{2.20}$$

$$\frac{d\varepsilon}{dt} = -c\left(\varepsilon - \varepsilon_{min}\right) \tag{2.21}$$

$$\frac{dg}{dt} = -c\frac{s+l+g}{s(1-\varepsilon_{min})}\left[l - \frac{\varepsilon_{min}s}{1-\varepsilon_{min}} + g\right] \tag{2.22}$$

Here ε_{min} is the minimum porosity of the granules and c is the compaction rate constant.

2.2.3 Identification of Kernels

A primary challenge in the development of the population balance models is the identification of appropriate kernels (rate constants) that describe the individual mechanisms. While the development of a multi-dimensional population balance model is motivated by the physics of the problem, it is a tougher task to obtain three-dimensional kernels that account for the dependence of the rates on the particle traits (i.e., size, binder content and porosity).

2.2.3.1 Aggregation Kernel

The aggregation kernel β is a very important parameter in the population balance model, as ideally it should provide the functional dependency of the aggregation rate on the process and material variables (Adetayo and Ennis, 2000; Abberger, 2001). These process parameters could include rotational speed of a drum or mixer, fluidisation air velocity and geometry of the granulator. Material parameters on the other hand would include initial particle size distribution, amount of binder, binder viscosity, interfacial tension and contact angle.

The aggregation kernel is essentially a measure of how successful a binary collision of two particles v and u of volumes $(s\prime, l\prime, g\prime)$and $(s - s\prime, l - l\prime, g - g\prime)$ is, assuming that $F(v)F(u)$ is a measure of the total number density of all possible binary collisions that can occur. This is a reasonable assumption if the system is assumed to be free-in-space, implying that any given particle can collide with all other particles as the paths to other particles are not hindered (Sastry and Fuerstenau, 1973; Wauters, 2000). In the event that the system is restricted-in-space (i.e., particles can only collide with neighbouring particles), the number of possible binary collisions is significantly less than $F(v)F(u)$ (Sastry and Fuerstenau, 1973; Wauters, 2000). To compensate for this, Sastry and Fuerstenau (1973) introduced a means to correct this error by stating that the number of possible binary collisions would reduce to $\frac{F(v)F(u)}{N_{tot}}$, where N_{tot} is the total number of particles (in terms of number density) in the system. For granulation, the decision to ascertain if the system is free-in-space or restricted-in-space is fairly arbitrary with some studies adopting the correction factor (Liu and Litster, 2002; Adetayo and Ennis, 2000; Wauters, 2000) and others choosing not to (Hounslow, 1998; Biggs et al., 2003; Madec et al., 2003; Darelius et al., 2005; Tan et al., 2005).

In view of the importance of the aggregation kernel, it is no surprise that there are many studies that have focussed on the development and usage of the aggregation kernel. However, despite their increasing use, the aggregation kernel and process is poorly understood (Madec et al., 2003). A full modelling of the kernel should take into account all the parameters (discussed above) that would influence the aggregation rates. However, this is

usually not the case.

The aggregation kernel $\beta(u, v)$ can be subdivided into two parts and is defined by (Sastry, 1975),

$$\beta(u, v) = \beta_0 \beta^*(u, v) \tag{2.23}$$

where β_0 is the rate constant, which is dependent on the operating conditions of the granulator. $\beta^*(u, v)$ illustrates the dependency of the kernel on the size of the aggregating granules and determines the shape of the resultant granule size distribution (Adetayo et al., 1993; Smit et al., 1995; Adetayo and Ennis, 1997). Due to the complexities of the aggregation mechanism, the initial aggregation kernels that appeared in the literature were empirical expressions that evaluated the kernel metric as a function of particle size (e.g. constant, sum and product kernels). Many forms of these empirical kernels exist and a comprehensive summary of them are provided in Ennis and Litster (1997), Liu and Litster (2002) and Cameron et al. (2005). The disadvantages of these kernels are 1) they have no physical basis, 2) they have several empirical parameters that need to be tuned to provide the best fit to experimental data, and 3) they are unable to account for the effects of process parameters and material properties on the end granule properties/distributions. The advantage of these kernels are in its simplicity and ease of use in population balance models.

As the understanding of the aggregation process improved, Madec et al. (2003) proposed a multi-dimensional phenomenological kernel that would model the evolution of the aggregation process against size as well as binder composition. The advantage of their kernel was that firstly, it resulted in a better physical representation of the effect of size and binder content on the aggregation rate and secondly, it was easily implementable in a population balance model. The disadvantage is that it still did not account for the effect of material (solid and liquid) properties and process parameters.

Developments in this area also have seen the emergence of two other aggregation kernel forms; the equi-partition of kinetic energy (EKE) kernel described by Hounslow (1998) (based on the kinetic theory of gases) and the kinetic theory of granular flow (KTGF)

kernel (Rajniak et al., 2006). Both these kernels make use of a collision success factor (ψ) which calculate the probability of aggregation of two colliding granules. The advantages of these kernel forms is that firstly, detailed discrete element modelling (DEM) simulations can be undertaken to obtain accurate values of ψ that account for the effects of solid and binder properties, as seen in the works of Stepanek et al. (2006) and Stepanek et al. (2008) (also see chapter 8). Secondly, they can be easily incorporated into population balances. The disadvantage of these kernel forms is that obtaining accurate forms of ψ from DEM simulations is time consuming. To compensate for this, simpler forms of ψ may be used (e.g. a constant factor as employed by Tan et al. (2005)). However,this has the further disadvantage of relegating the kernel forms to purely empirical expressions.

Alongside the above mentioned developments, theoretical kernels have been appearing in the literature to predict the probability of aggregation from the physical properties of the solid and binder. The general idea of these models is to use a force or energy balance to predict whether granules will aggregate or not. Examples of these theoretical kernels include the work of Ennis et al. (1991), who described the aggregation mechanism as a function of a dimensionless Stokes' number. This number is essentially a measure of the ratio of granule collisional kinetic energy to the viscous dissipation brought about by interstitial binder. Subsequently, Liu et al. (2000) extended this model to include the possibility of plastic deformation during granulation. Both these models however, were static descriptions of the micro-scale physics and were not incorporated into the population balance model. Liu and Litster (2002) was the first to extend the work of Liu et al. (2000) and incorporate the kernel into a population balance framework. Their method was based on assigning constant kernels to three different regimes of aggregation (i.e., type 1 or type 2 aggregation with no plastic deformation; type 2 aggregation with plastic deformation; and rebound). For the first two cases, a finite constant is assigned and in the third case, a value of zero is assigned. While their method was an improvement to previous kernels formulated, it was disadvantageous in the sense that it simplified the simulations by assuming a representative aggregation rate for the same aggregation type. Immanuel and Doyle III (2005) however, have managed to improve upon this drawback by using the mechanisms of Ennis et al. (1991) and Liu et al. (2000) and converting them to dynamic

kernels that are incorporated into the PBM, without assuming constant aggregation rates for each aggregation type. Details of this method will be presented in chapter 4, with application seen in chapters 4 and 6.

2.2.3.2 Breakage Kernel

Compared to the aggregation kernel, research on breakage kernels is still in its infancy. Sanders et al. (2003) and Biggs et al. (2003) attempted to model breakage as a negative aggregation rate process, essentially reporting a reduced aggregation rate constant. However, there are problems with this approach as aggregation is a second order rate process and breakage is a first order rate process. Therefore, trying to incorporate breakage in an aggregation kernel is fundamentally flawed and will not succeed with any physical basis (Reynolds et al., 2005). In other studies, complexity of breakage models extend from empirical models based on experimental observations of breakage (Van den Dries et al., 2003; Salman et al., 2003), to binary breakage functions (Tan et al., 2004, 2005) that describe how a granule breaks into large and small fragments. These models however, do not explicitly account for any process parameters or material properties to determine breakage rates. More recently, Dhanarajan and Bandyopadhyay (2007) presented an energy-based model for high-shear granulation processes, whereby the extent of granule breakage was considered to be directly proportional to the impact-energy and inversely proportional to granule strength. While their model showed a close correspondence between the predicted and experimental results for a particular granulation recipe, it lacked a rigorous physical basis in the following ways. Firstly, it assumed that kinetic energy was a function of only mass (neglecting velocity) and that all collisions were elastic (neglecting loss of kinetic energy due to inelasticity). Secondly, it assumed that granule strength was primarily a function of binder content, without considering the effect of binder properties such as viscosity, surface tension and contact-angle. To date, there is no comprehensive breakage kernel in the literature that has sound physical basis and does not make any simplifying assumptions.

2.2.3.3 Nucleation Kernel

Similar to the research on breakage kernels, there is very limited research on the development of nucleation kernels that have a sound physical basis. Moreover, the representation of the nucleation kernel in population balances is fairly poor. The traditional approach to model nucleation has been to add nuclei of a specific size at a constant rate to the process, where the rate constant is used as a fitting parameter. Advancing from this, Hapgood (2000) have developed a nucleation regime map that demonstrates the effect of binder addition and powder flow on the resulting nuclei size distribution. However, their work has not been incorporated into population balances to predict nuclei size distributions and neither does it describe the effects of solid/liquid properties on the size distribution. Subsequently, Wilderboer (2002) extended the work of Hapgood (2000) by developing a DEM of nucleation which describes the effects of various design and operating parameters on the nuclei size distribution. Their model could also be incorporated into the 1-D population balance models for predictive purposes. More recently, Poon et al. (2008) developed a more comprehensive nucleation model that can be applied to multi-dimensional population balance models. Their kernel is based on the wetting kinetics and thermodynamics that govern nucleation and also accounts for the effects of material properties (solid and liquid) on the final nuclei size distributions. Details of the kernel will be discussed in chapter 4 with applications seen in chapters 4 and 6.

2.2.4 Solution Techniques

As seen from the above discussions, multi-dimensional population balances and kernels are warranted for the granulation process. As a result, the challenges lie not only in the development of these models/kernels but also in their applications which require efficient techniques for their solution. The population balance equation used to model the granulation process, results in complicated hyperbolic integro-partial differential equations. Furthermore, the multi-time scales in the process render the model equations with a large stiffness, substantially complicating the numerical integration. The multi-scale nature of the spatial coordinates in the partial differential equations makes it a challenge to develop a suitable discretisation of the spatial coordinates. The multi-number scales represented

by the different states of the models (the particle versus the lumped quantities) also complicate numerical integration. Lastly, the multi-dimensional distributions (along multiple spatial coordinates) add to the computational complexity as well as to the memory needs in the computers. Hence, it is of interest to develop a robust, realistic and efficient solution technique for multi-dimensional population balance equations (Ma et al., 2002; Mantzaris et al., 2001).

Several numerical solution techniques have been applied in solving the population balance equations (PBEs) such as discretisation techniques (eg. finite difference and method of weighted residuals), wavelet based methods and Monte-carlo methods. The finite difference method approximates the partial derivatives by a truncated series expansion (eg. Taylor's series) and this results in a system of ordinary differential and algebraic equations. A limitation of this technique is that there tends to be inherent oscillations or dispersions in the numerical solution which is due to approximating the derivatives with finite differences. The second type of discretisation technique is the method of weighted residuals (MWR). Here, the solution within the sub-domain of interest (r_{min}, r_{max}) is approximated in terms of basis functions and weighting functions. The weighted sum of the residuals of the population balance equation at certain points are forced to zero. This ensures that the approximated solution of the PBE tries to make the PBE valid at those colloquation points. Some of the sub-classes of MWR include (but not limited to) the collocation technique and Galerkin's method. The essential difference between these two sub-methods lies in the choice of the chosen form of the weighting function. The computational requirements of the MWR and its sub-classes are substantial and moreover, the ability of these methods to handle steep moving profiles, which arise due to growth and aggregation, has not been suitably demonstrated (Liu and Cameron, 2003). These problems coupled with the limitations of the finite difference technique have led to the emergence of a relatively new numerical scheme for solving the PBE, classified as wavelet based methods. Volume-based population balance equations with particle volume as the internal coordinate are used to show the main traits of the wavelet methods. The most important advantage of these methods is their ability to circumvent the issue of steep moving profiles. The above techniques discussed so far are deterministic in nature. In the

case of the finite difference technique and MWR, the main problem lies in the integro-differential nature of the PBE which requires the discretisation of the size distribution. This discretisation is tedious as the features of the distribution may change during growth and they are not known ahead of time (Smith and Matsoukas, 1998). This difficulty can be dealt with through the use of Monte Carlo methods. These methods use probabilistic tools which essentially incorporate the stochastic behaviour of the particles with particle events occurring at random. The probability of a particle proceeding from its current state to a new state is determined by the Markov conditional probability (Immanuel and Doyle III, 2003a). Monte Carlo methods can be further divided into time-driven and event-driven simulations. In the former approach, the time interval Δt is chosen and events within this interval are determined stochastically. In the latter approach, Δt is determined based on the rates of the processes. Furthermore, the event-driven method can be sub-divided into constant volume (total volume is conserved) and constant number methods (total particles are conserved). The main advantage of the constant number method as opposed to its constant volume counterpart is that the population of particles remain large enough for accurate Monte Carlo simulations. A comprehensive review of existing solution techniques can be found in Cameron et al. (2005) and Pinto (2008).

2.2.4.1 Hierarchical Two-tier Algorithm

A two-tier hierarchical solution technique has previously been presented for one-,three-, and six-dimensional population balance models (Immanuel and Doyle III, 2003a, 2005; Pinto et al., 2007). In this technique, the particle population is first discretised into sub-populations and the population balance is formulated for each of these semi-lumped sub-populations. This is obtained by the integration of the population balance equation (see Equation 2.10) over the domain of the sub-populations and re-casting the population into finite volumes. In this finite volume scheme, Equation 2.10 may be re-written in a discrete form as shown in Equation 2.24.

$$\frac{dF'_{i,j,k}}{dt} + \frac{F'_{i,j,k}}{\triangle g_k}\frac{dg}{dt}\Big|_{g_k} - \frac{F'_{i,j,k+1}}{\triangle g_{k+1}}\frac{dg}{dt}\Big|_{g_{k+1}} = \Re_{nuc} + \Re_{agg} + \Re_{break} \tag{2.24}$$

Here $F'(i,j,k) = \int_{s=s_i}^{s_{i+1}} \int_{l=l_j}^{l_{j+1}} \int_{g=g_k}^{g_{k+1}} F(s,l,g)\, ds\, dl\, dg$, s_i is the value of the solid volume at the upper end of the i^{th} bin along the solid volume axis, l_j is the value of the liquid volume at the upper end of the j^{th} bin along the liquid volume axis, g_k is the value of the gas volume at the upper end of the k^{th} bin along the gas volume axis. $\triangle g_k$ is the size of the k^{th} gas bin with respect to the gas volume axis. The particle population is assumed to be uniform within each of the finite volumes. Thus, by this technique, the partial-differential integral equation as represented by the population balance equation, is reduced to a system of ordinary differential equations in terms of the rates of nucleation, aggregation and breakage.

The schematic depiction of the hierarchical two-tier solution technique is shown in Figure 2.6. This two-tier formulation is essentially a decomposition strategy whereby the various rate processes of nucleation, aggregation, breakage and consolidation are computed in the first tier of the algorithm (at each time step) and the particle population is updated in the second tier. A first order Euler predictor-corrector technique is utilised for the information exchange between the two tiers. The two-tier solution strategy enables reduction in computational time partly due to the reduction of the stiffness of the system equations by the above-mentioned decomposition strategy. The other major factor that contributes to the improvement in computational time is the off-line semi-analytical solutions for the aggregation and breakage terms (Immanuel and Doyle III, 2003a, 2005; Pinto et al., 2007). This results in casting the complex triple integrals in simpler addition and multiplication terms, major portions of which are computed once a-priori to the start of the simulation. These semi-analytical solutions are derived based on the assumption of uniform particle density within each finite volume (bin). Refer to Immanuel and Doyle III (2003a) for the detailed derivations. Applications of the two-tier technique are seen in chapters 4-7. See Appendix C for more details on the two-tier algorithm.

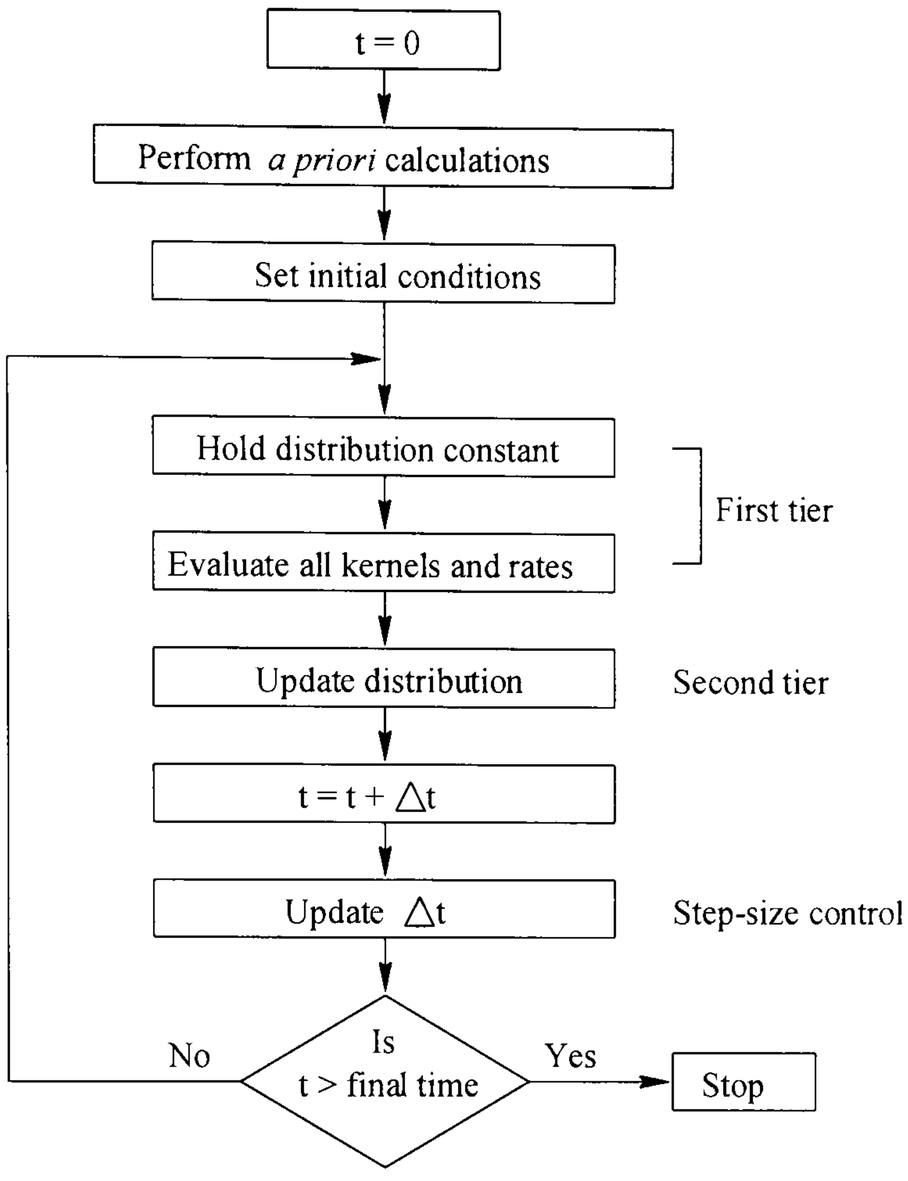

Figure 2.6: Schematic representation of the hierarchical two-tier algorithm (Immanuel and Doyle III, 2003a).

2.3 Multi-scale Aspects of Granulation Processes

Figure 2.7 shows a scale map from Ingram et al. (2004) which considers the key granulation mechanisms as represented by the differing time and length scales within the granulation process. It can be seen that the granulation process is essentially a multi-scale operation where the final granule attributes are determined by the physics and chemistry at the micro-scale (particle level) through to the macro-scale equipment level. Traditionally in granulation, research has focussed on either the macro-scale (black-box using input/output data) behaviour or the micro-scale (particle-level) behaviour. In general, the micro-scale behaviour is better understood than the macro-scale, with the meso-scale (the scale between the micro- and macro-scale) essentially being ignored (Micheals, 2003). Meso-scale models such as population balances are useful in providing the explicit linkages to predict macroscopic properties using the microscopic information. Currently, this is an open area

of research and is one of the objectives of this thesis.

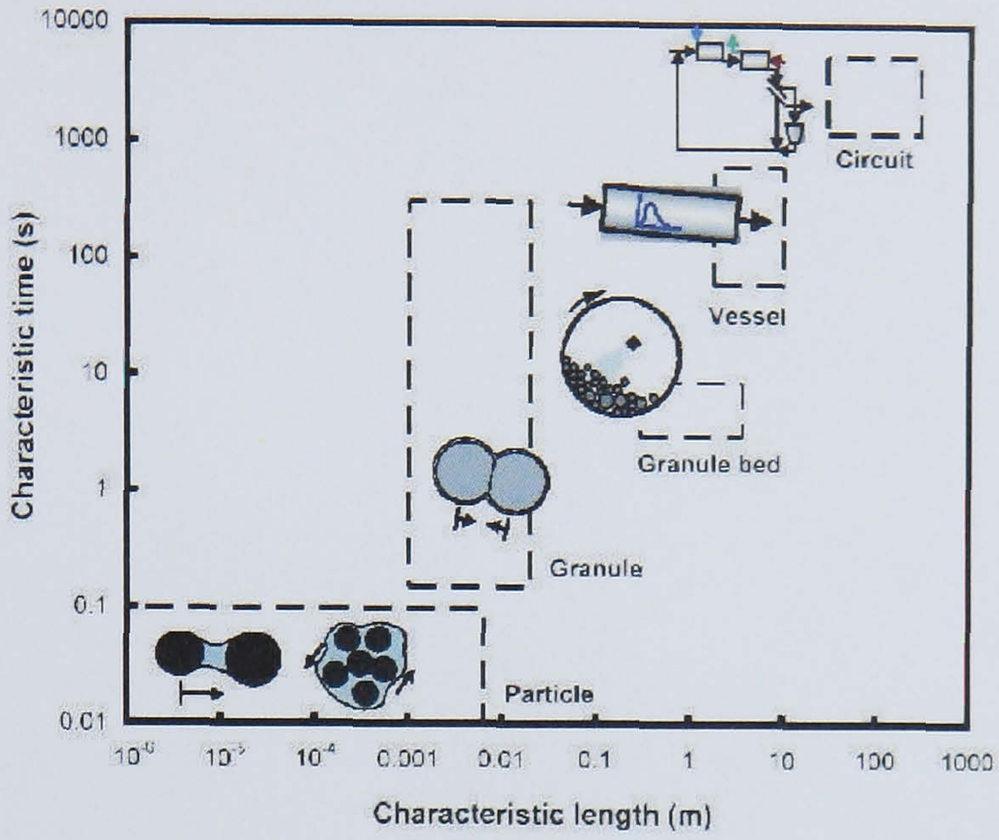

Figure 2.7: Multi-scale nature of granulation processes (Ingram et al., 2004).

2.4 Summary

In this chapter, one of the key areas of granulation research that was reviewed was the physics and mechanisms of the granulation process. It could be seen that although substantial research has been carried out in understanding granulation behaviour, there are still enormous opportunities that present themselves in granulation research. For instance, in modelling the granulation rate processes, fundamental kernels that are based on the underlying physics of the granulation process are required to be identified. However, this is a non-trivial task and many of the existing kernels (particularly for nucleation and breakage) are empirical and do not account explicitly for process/design parameters and material properties that directly influence granule properties. Another limitation of most of the existing kernels is that their rates are a function of granule size but not liquid content and/or granule porosity. With regards to population balance models that are warranted for granulation processes, many of the current models are one-dimensional and do not account for distributions of multiple granule properties. Multi-dimensional population balances on the other hand require novel solution techniques for their efficient solution and one such technique is presented. The multi-scale nature of the granulation process also requires a

synergetic approach in modelling, using micro-scale particle-level information to predict macroscopic properties via meso-scale linkages. In the next chapter, the experimental studies undertaken on distributions of granule size, binder content and porosity in batch drum granulation will be presented.

Chapter 3

Experimental Studies on Multiple Granule Distributions in Batch Drum Granulation

Batch granulation experiments on a lab-scale drum granulator for a Calcite/Polyvinyl alcohol in water (Calcite/PVOH-H_2O) system are presented in this chapter. Experimental studies were carried out to study the aggregation kinetics and mechanism for this granulation recipe, whilst investigating the effects of binder-to-solids ratio and drum load on the granule size, binder content and porosity distributions. In particular, the effect of formulation properties and the granulation operating conditions on the batch process dynamics and the end-granule properties were studied. The formulation properties considered included liquid surface tension, powder-liquid contact angle, dynamic yield stress, powder shape and liquid viscosity. The operating variables included the binder-to-solids ratio, binder addition duration and the binder addition mode. The sensitivity in the process and the non-homogeneity of key particle attributes (size, binder content, and porosity) were evident. The important process manipulations for feedback control and potential disturbances were identified, formulating a comprehensive control configuration for batch

[1]Part of this chapter is based on, R. Ramachandran, J. M. -H. Poon, C. F. W. Sanders, T. Glaser, C. D. Immanuel, F. J. Doyle III, J. D. Litster, F. Stepanek, F. Y. Wang and I. T. Cameron. "Experimental studies on distributions on granule size, binder content and porosity in batch drum granulation: inferences on process modelling requirements and process sensitivities", Powder Technology, 188 (2), 89-101, 2008.

granulation. The importance of multi-scale process models that link fundamental material properties with the granulation mechanisms and end-granule properties was also evident from the experiments. A three-dimensional population balance equation structure in terms of the particle size, binder content and porosity was confirmed to be an ideal framework for the process model.

3.1 Introduction and Objectives

In recent years, granulation has been studied extensively. Granulation processes are operated in a highly inefficient manner, with large recycle ratios within the process (3-5:1, recycle/product) (Mort et al., 2001; Iveson et al., 2001). A key control objective in granulation is to maintain specific size ranges for the granules. Granules that do not conform to the stringent size ranges and are either smaller or larger, are recycled to the process. In view of the importance of size control, most of the recent studies on granulation have placed emphasis on granule size alone (Adetayo et al., 1995; Hoornaert et al., 1998; Knight et al., 1998; Mort et al., 2001; Andreani et al., 2003; Saleh et al., 2003; Heinrich et al., 2003; Liu and Cameron, 2003; Sanders et al., 2003; Bardin et al., 2004; Moura et al., 2005; Darelius et al., 2005; Subero-Couroyer et al., 2006; Tan et al., 2004). However, the higher than desired recycle ratios could be due to improper distribution of the liquid binder resulting in unwetted fines and large granule chunks and hence the wider size distribution than desired. Furthermore, bulk density (related parameter, porosity) could be a further contributing factor to the large recycle ratios, as granules have to satisfy a certain bulk density tolerance. Taking these factors into consideration, it is clear that granule size, binder content and bulk density/porosity are all important particle traits that need to be monitored.

Traditionally, granulation processes have been modelled using one-dimensional population balance equations based on distribution of size alone (Iveson, 2002). The common assumption was that size is the only variable that characterises a granule. In the literature, there exist several studies that examine the effect of different parameters on granule growth with respect to granule size (Hemati et al., 2003; Tan et al., 2006; Walker et al., 2006).

Recent modelling efforts attempt to account for each of size, binder content and porosity, to better represent the granulation process. To complement such modelling efforts, experimental efforts seek to measure distributions along each of the three particle traits with granule size and porosity being accounted for (Annapragada and Neilly, 1996; Yu et al., 2003; Zou et al., 2003; Hogekamp and Pohl, 2003). Biggs et al. (2003) performed granulation experiments in a high shear mixer for both calcium carbonate/polyethylene glycol (PEG) and lactose/hydroxy propyl cellulose (HPC) systems, with PEG and HPC as the binder in their respective cases. In these experiments both the granule size distribution (GSD) and the binder size distribution (BSD) were determined. Sieve analysis was used to determine the GSD. For the determination of the binder distribution, thermogravimetric analysis was employed for the granulation recipe using PEG as the binder whilst a near infrared spectroscopy method was used for determining the HPC binder content. In another study, Reynolds et al. (2004) adopted a melt-in technique for binder introduction for granulating a calcium carbonate/PEG system. An average binder content was then determined for each size class using thermogravimetric analysis (oven drying) in addition to the GSD acquired through sieve analysis. Their study revealed that samples collected at the beginning of the granulation comprised of granules with varying binder compositions. In addition, from single granule analyses for a particular time instance and size class, a wide distribution for the binder composition was observed more so at early granulation times.

Evidence of non-uniformity of binder distribution in wet high shear granulation has been studied by several authors (Knight et al., 1998; Scott et al., 2000; Johansen and Schaefer, 2001). A study performed by Knight et al. (1998) concluded that the method of binder delivery (i.e. melt-in, pour-on, spray-on) influenced the growth behaviour and final size distribution of the granules. A lone study exists wherein each of size, binder content and porosity were characterised (Scott et al., 2000). In their study, poly-ethylene glycol (PEG) with a molecular mass of 1500 was used as the binder, which is a solid at temperatures less than 45°C. Upon the culmination of the granulation process, the dry granules (comprising of calcium carbonate and solid PEG) were sieved into various size classes. A representative porosity for granules in each size class was determined through porosimetry using a pore

size analyser to determine the volume of air contained within the granules. Similarly, each sample was subjected to thermo-gravimetric analysis in which they were heated to a temperature above 45°C until the PEG evaporated and an average binder content in each size class was determined. This presents a complication to the situation. Obtaining the binder content distribution requires the granules to be dried (thermo-gravimetric method) after sieving. An accurate GSD requires the granules to be dried before sieving. At best, size and porosity are the two granule attributes that could be measured. Therefore, in such cases, it is a challenge to characterise all three granule attributes. In this chapter, a methodology for characterising granule size, binder content and porosity is presented.

The present study goes on to investigate, for the spray-on method of binder delivery, the effect of optimal and non-optimal binder distribution on granule growth. Broader objectives of this study include firstly, identifying a suitable granulation recipe and operating conditions to produce rich granulation data; and to characterise the time evolution of these particle traits of size, binder content and porosity. Secondly, to identify suitable population balance model formulations from the measured three-dimensional data (i.e., size, binder content and porosity). Thirdly, to identify sensitivities in the process leading to better understanding in the control of the granulation process. Section 3.2 details the experimental procedures for carrying out the batch granulation experiments on a laboratory scale drum granulator. Section 3.3 presents the experimental findings and relates these to the widely accepted granulation mechanisms. Section 3.4 draws together the implications of the findings from these batch granulation experiments and relates them to granulation process control.

3.2 Materials and Methods

3.2.1 Materials

For the drum granulation experiments, calcite (limestone) was used with a volume mean diameter (d_{30}) of $130\,\mu m$ and with 95% of the mass less than $250\,\mu m$. The measured skeletal density of calcite was $2.743\,kg\,m^{-3}$. Polyvinyl alcohol in water (PVOH-H_2O) (2.5% concentration by mass) was used as the liquid binder. Hereafter, 2.5% concentration

by mass is implicit in the notation of PVOH-H_2O unless otherwise stated.

3.2.2 Granulation Experiments

The granulation experiments were performed using a stainless-steel rotating drum with a diameter of $0.3\,m$ and a length of $0.2\,m$. It was equipped with six wedge-shaped cardboard lifters of $5\,mm$ in height to promote tumbling motion. Approximately $1.5\,kg$ of dry powder was used for each experiment. The size distribution of the powder was analysed to confirm that almost identical initial distributions were used for all experiments. The experimental protocol is set out below:

1. The drum is operated at $25\,rpm$. A drum speed of $25\,rpm$ is chosen as this results in an optimal flow pattern (cascading/tumbling motion) based on visual inspection.

2. Liquid binder is prepared 24 h beforehand by dissolving 2.5% by mass of polyvinyl alcohol (PVOH) in water at 85°C. The solution is then filtered to ensure no suspended solids are present in the solution. Thereafter, the solution is allowed to equilibrate to ambient temperature.

3. The liquid binder is placed in a pressure pot which is used for binder delivery into the drum. The pressure pot is then calibrated and set at the desired spray rate(s). The pressure pot is tested prior to spraying, to ensure smooth and continuous binder delivery into the drum.

4. A total of $1.5\,kg$ (nominal case) of calcite is weighed out and loaded into the drum. The powder is then evenly spread out to ensure optimal tumbling motion.

5. The granulation process commences at $t = 0\,min$ and the binder is sprayed into the drum at the designated time.

6. Samples are taken out at time instances of 3, 5, 7, 10, 15 and $30\,min$, by scooping approximately $150\,g$ of sample from several fixed locations in the drum (see section 3.2.3). The experiment is then stopped at $30\,min$ (granulation end time).

7. The samples are then dried and subject to further characterisation.

3.2.3 Method of Sampling

The sampling method employed in this study is known as scoop sampling. The method involves plunging a scoop into the powder and removing the sample. This method may be prone to error since the whole of the sample does not pass through the entire powder bed, and since the sample is taken from the surface, it may not be representative of the mass as a whole (Allen, 1997). In order to test the suitability of the scoop sampling method, one experiment was performed where the granulator was stopped after 15 $mins$. Then six sub-samples were withdrawn to form a single representative sample of the entire powder bed (see Figure 3.1). Each sub-sample was scooped from several fixed drum locations to minimise any sampling bias. This was because, it was observed that different sized granules congregated in different locations in the drum. Large granules tended to move to the periphery of the drum interior and smaller granules tended to stay in the middle. By comparing the first sample to the rest of the samples, it was possible to test the reproducibility of the sampling method. In Figure 3.2, the GSDs of the nominal experiment (i.e. binder-to-solids ratio = 0.12 and drum load = 1.5 kg) for three distributions are shown. It can be seen that the differences in the samples are marginal. It was concluded that the first sample was representative of the entire size distribution in the drum. Therefore, this sampling technique was considered suitable for this study.

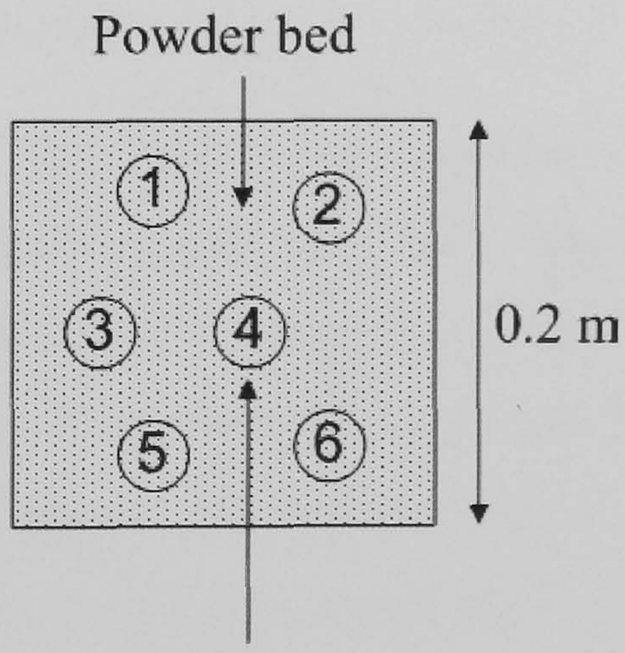

Figure 3.1: Plan view of the powder bed showing the locations of the six sampling areas.

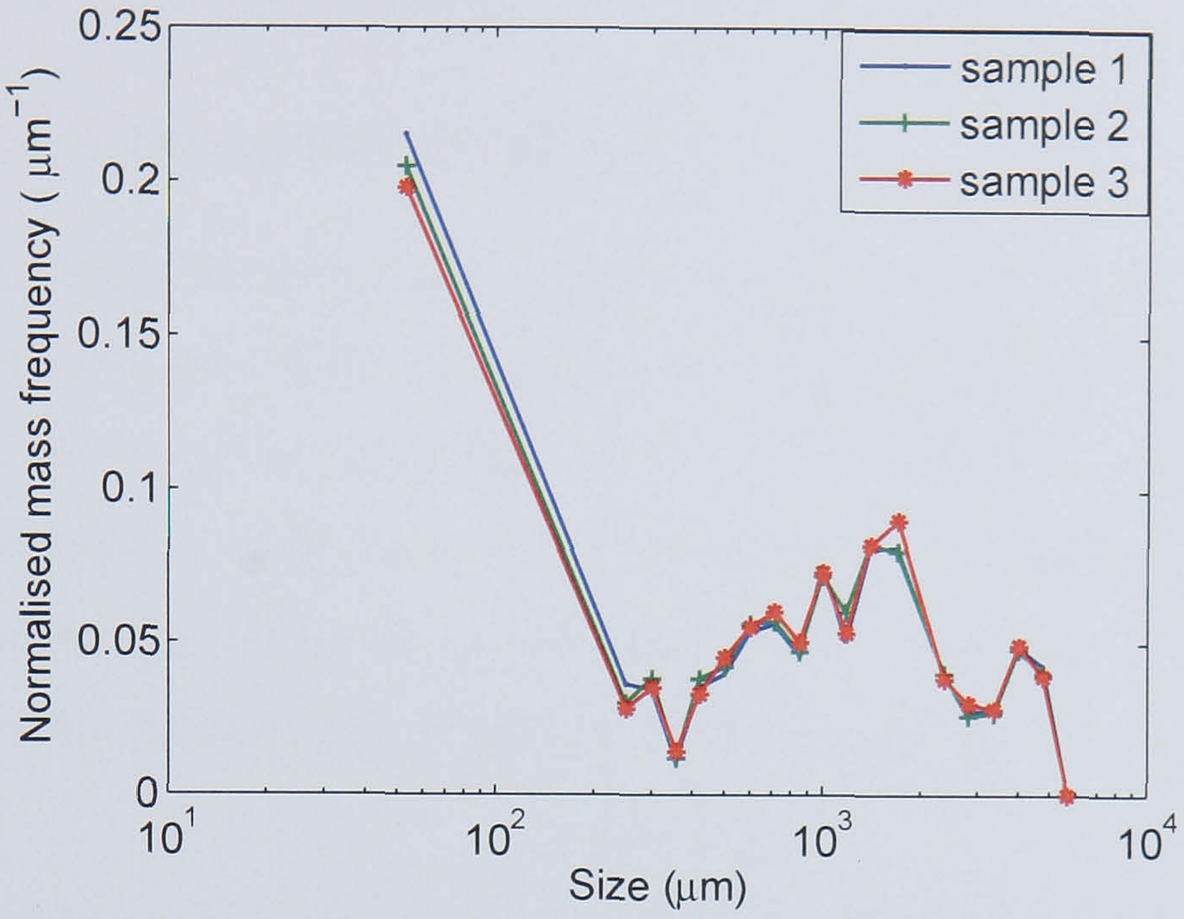

Figure 3.2: Granule size distributions of three samples taken at the same time instant, to study the effectiveness of the scoop sampling method.

3.2.4 Size Analysis

Two types of size analysis were performed in the course of this work:

1. The determination of the particle size distribution (PSD) of the initial primary powder (fines).

2. The determination of the granule size distribution (GSD) evolving with time.

The PSD was determined by laser diffraction methods using the Malvern Mastersizer E. Water was used as the dispersing medium. The GSD was determined by means of sieve analysis, using a fourth-root-of-two progression series using sieves (Endecotts Ltd.) ranging from $250\,\mu m$ to $8.0\,mm$. For sieve analysis, it was imperative that an optimal time for the sieve shaker was determined. Too short a time would result in not all granules moving down the sieves and too long a time could result in breakage and attrition of the granules. Therefore, to determine an optimal time, the sieve shaker was stopped every one minute from $t = 1\,min$ to $t = 10\,min$ and the mass on each sieve was weighed. It was observed that there was negligible change in mass between $t = 5\,min$ and $t = 6\,min$. Hence, $5\,min$ was determined to be the optimal time for sieving. After size analysis, the sieved samples from each size range were subjected to binder content and porosity analysis

as discussed in section 3.2.5 and 3.2.6.

3.2.5 Binder Content Measurements

Obtaining the binder content distribution requires the granules to be dried (thermo-gravimetric method) after sieving. An accurate GSD requires the granules to be dried before sieving. At best, size and porosity are the two granule attributes that could be measured. Therefore, in such cases, it is a challenge to characterise all three granule attributes. Therefore in order to circumvent this situation, blue dye was used as a means of inferring the binder composition of the granule samples using spectrophotometry which is detailed below.

Blue dye (Queen Fine Foods, Australia) was included in the formulation of the final liquid binder by mixing the dye with PVOH-H_20 prior to spraying the liquid binder into the drum granulator. The concentration of the dye in PVOH-H_2O was 8.9 g/L for all cases. The binder content was then indirectly inferred using spectrophotometry by measuring the absorbance of the blue dye. The following protocol was used in carrying out the measurements for the binder content of the granule samples.

1. A working standard was prepared with a blue dye concentration of $8.9\,g/L$. Other standard solutions were prepared with a concentration range between $0.1\% - 2\%$ by diluting the working standard using de-ionised water. The working standard with a dye concentration of $8.9\,g/L$ represents 100% solution strength. De-ionised water was used as the diluent in all cases when preparing the solutions.

2. A preliminary scan was performed across the absorption spectrum between ($300\,nm - 1000\,nm$) using the standard solution with a solution strength of 2% and the absorption peak corresponding to the dye component was identified at $630\,nm$. Subsequent absorption measurements were performed at this wavelength (See Figure 3.3).

3. The absorbance of the dye component was measured for the standard solutions previously prepared with a solution strength in the range of $0.1\% - 2\%$. A linearity curve was generated relating the absorbance to the solution strength containing the

blue dye component. Repeatability measurements were carried out with a percentage relative standard deviation of 0.7 %. The equation for the linear curve is given below.

$$AU = 0.3181 \times [C]_{dye}. \tag{3.1}$$

where, AU is the measured absorbance at $630\,nm$ and $[C]_{dye}$ represents the solution strength (in %) of the standard containing the blue dye component in solution (See Figure 3.4).

4. Approximately $1\,g$ of granule sample was dissolved in $10\,mL$ of de-ionised water. The mixture is subjected to shaking to ensure thorough mixing, allowing the blue dye component to be extracted from the solids and into the solution.

5. The dissolved sample was centrifuged at $5000\,rpm$ for $5\,mins$. The supernatant was carefully extracted for subsequent absorbance measurements.

6. The binder content of the granule sample is determined from the measured absorbance of the sample and the sample mass using the absorbance-concentration relationship given in Equation 3.1 and Equation 3.2 (expressed as a percentage, L:S%).

$$\text{L:S\%} = \left(\frac{1}{100}\right)\left(\frac{AU}{0.3181}\right)\left(\frac{\rho_l}{M_s}\right) \tag{3.2}$$

In addition to the above spectrophotometric analysis, representative portions of each sample were reserved for thermo-gravimetric analysis. The granules were dried in an oven for a duration of $2\,h$ at 110°C and the resultant change in mass (due to the loss of PVOH-H_2O) was recorded. This change in mass was used for calculating the average binder content.

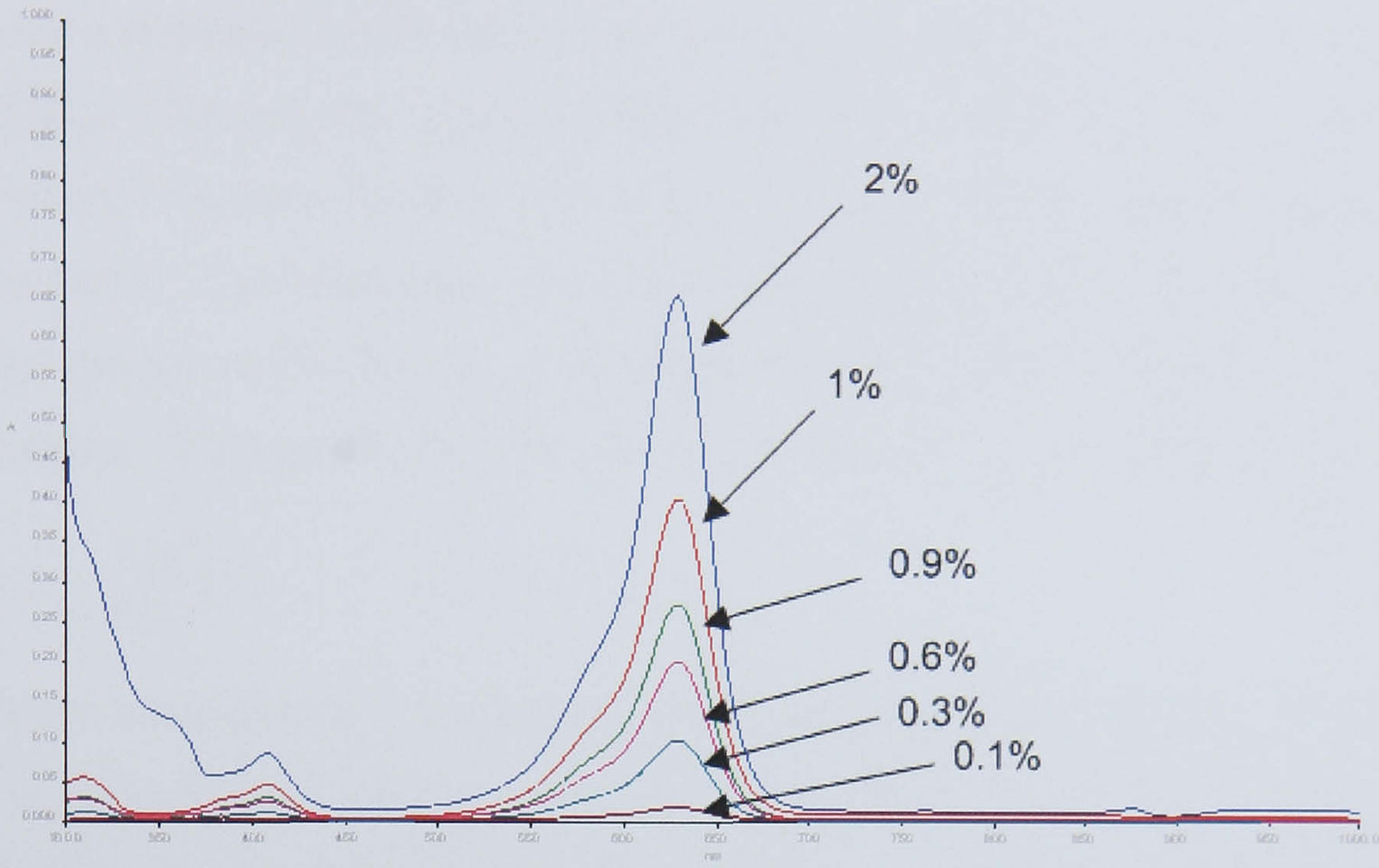

Figure 3.3: Absorption spectrum for the dye component at 630 nm for solution strengths varying from 0.1% to 2%.

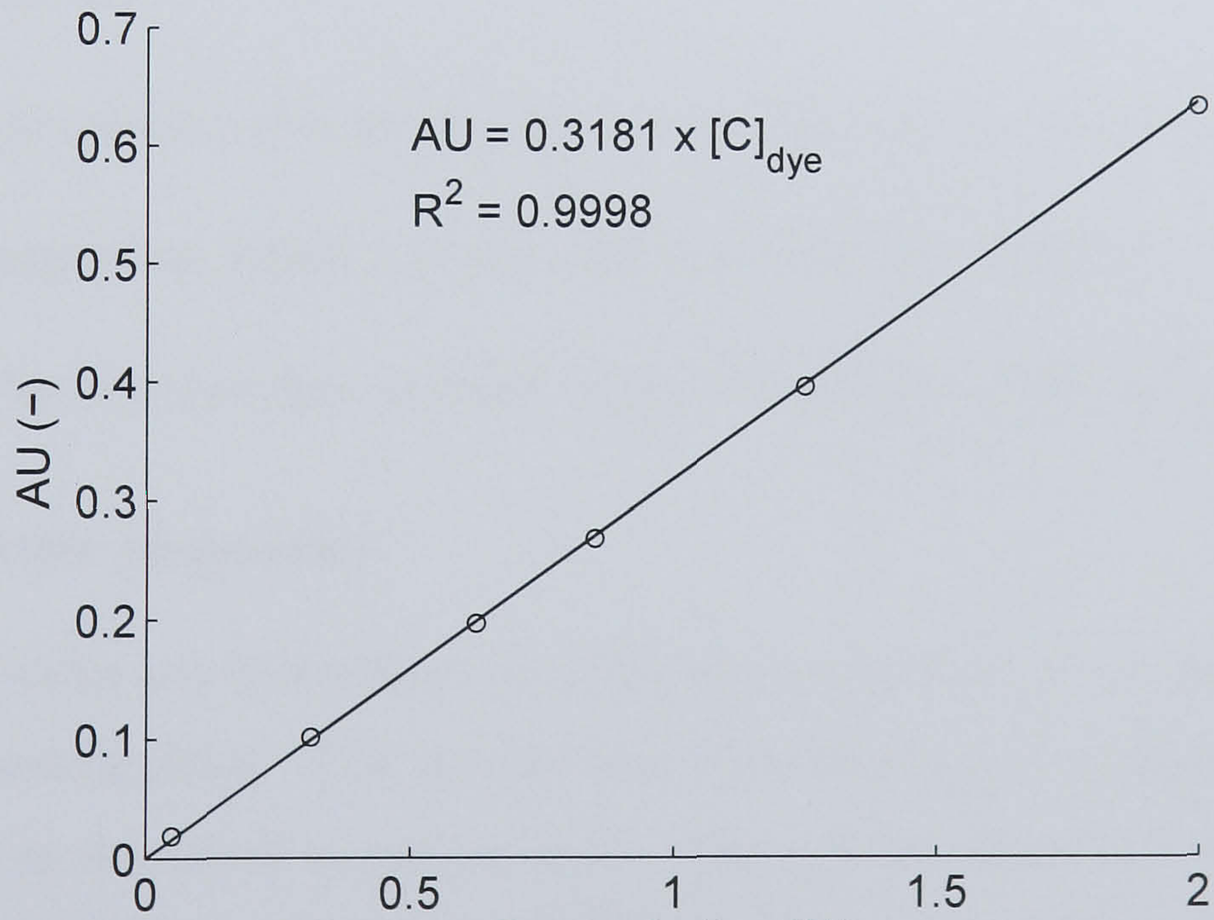

Figure 3.4: Calibration curve generated from standard solutions with known dye concentrations.

3.2.6 Porosity Measurements

The porosity ϵ is defined as the ratio of the volume of liquid and pores to the total volume ($\epsilon = \frac{V_l+V_g}{V_s+V_l+V_g}$). The porosity of the granules were determined in each of the size fractions of the granules. The true density (ρ_a) of each sample was measured using the Accupyc 1330 Pycnometer (Micromeritics). The bulk density (ρ_b) which is the mass of an object divided by volume (including the pore volume) was measured using the GeoPyc 1360 (Micromeritics). The porosity is then determined using Equation 3.3 given below.

$$\epsilon = 1 - \left(\frac{\rho_b}{\rho_a}\right) \tag{3.3}$$

Ten repeated measurements of absolute and bulk density were performed on the same sample. It was observed that the standard deviation for both measurements were less than 0.01. The measured absolute density for calcite was 2.743 $kg\,m^{-3}$, which is typically on the higher side.

3.2.7 Formulation Properties

The formulation properties identified in this study for the Calcite/PVOH-H_2O system are organised as follows:

- Powder properties: powder density, powder size distribution and powder shape.
- Liquid properties: liquid viscosity and liquid surface tension.
- Powder-liquid properties: contact angle and dynamic yield stress.

3.2.7.1 Powder properties

The powder density was determined using helium pycnometry (Accupyc 1330), which was described in section 3.2.6. The powder size distribution was obtained by the Malvern Mastersizer E as described in section 3.2.4. The powder shape was determined using a scanning electron microscope (SEM). SEM images provides a three-dimensional view of the primary particles, which were useful for assessing the surface structures of the powder (primary) particles. In this study, a magnification of $\times 200$ was used.

3.2.7.2 Liquid Properties

- *L*iquid viscosity: The viscosity was determined using the AR-G2 magnetic bearing rheometer (TA Instruments). The instrument was fitted with $8\,mm$ stainless steel parallel plates. All experiments were performed at ambient temperature ($22^{\circ}C$). Samples were loaded in-between the parallel plates with a gap of $1000\,\mu m$ and were initially subjected to a strain sweep ($0.01\% - 10\%$ strain at $1\,Hz$ frequency). All samples were found to be within their linear viscoelastic region in the applied strain limits. The same sample was then subjected to three frequency sweeps ($0.1 - 10\,Hz$) at 1% strain and then the viscosity was determined.

- *L*iquid surface tension: Surface tension is governed by thermodynamic variables and primarily by the chemical nature of the components present in the surface phase. In this study, the liquid surface tension was obtained from the literature (Bhattacharya and Ray, 2004)(see Figure 3.5).

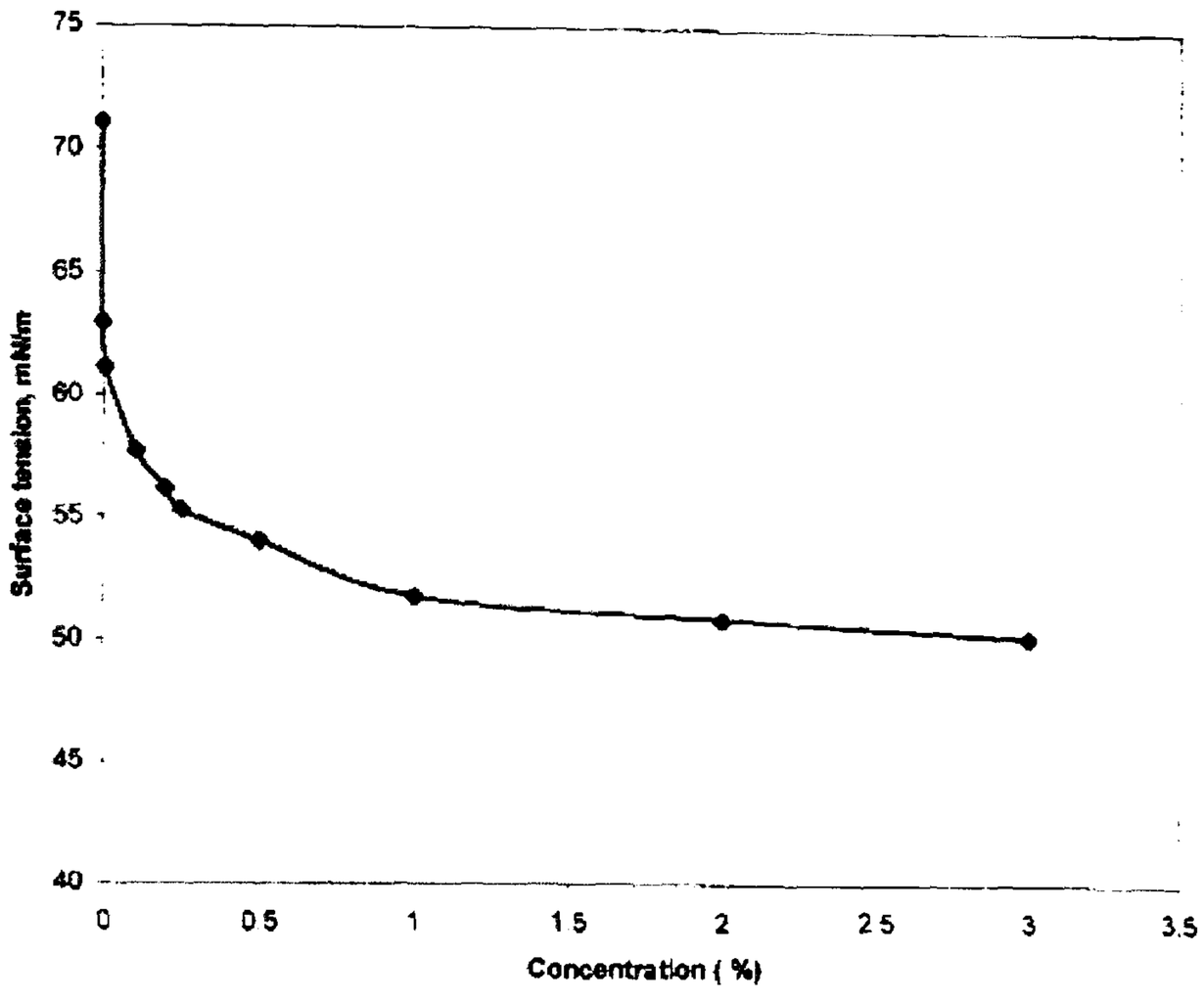

Figure 3.5: Profile showing the variation of the surface tensions of poly vinyl alcohol with concentration (Bhattacharya and Ray, 2004).

3.2.7.3 Powder-liquid Properties

- *C*ontact angle: The powder-liquid contact angle is determined using the contact anglometer (Model 1501, Micromeritics). The anglometer permits measuring the maximum height a drop or a small pool of liquid can attain on a horizontal surface. The primary powder (fines) is first compressed to form a cake of powder. A precision micrometer is then used to ascertain the distance (d_1) between the lower and upper surfaces of the powder cake. Thereafter, the liquid is added onto the surface in increments with a hypodermic syringe until there is no further increase in liquid height. The distance (d_2) between the lower surface of the powder cake and the upper liquid surface is determined. The greatest height that the liquid can maintain is then calculated as $d_2 - d_1$. When the contact angle θ is between 0° and 90°, i.e., when the liquid wets and spreads, θ is calculated using Equation 3.4.

$$cos\ \theta = 1 - \sqrt{\frac{Bh^2}{3(1-\epsilon)(1-\frac{Bh^2}{2})}} \tag{3.4}$$

When θ is greater than 90°, i.e., when the liquid does not spread. the relationship is given in Equation 3.5.

$$cos\ \theta = -1 + \sqrt{\frac{4 - 2Bh^2}{3(1-\epsilon)(Bh^2)}} \tag{3.5}$$

In these equations, $B = \frac{\rho g}{2\gamma}$ where ρ is the liquid density. g is the acceleration due to gravity, γ is the liquid surface tension, $h = d_2 - d_1$ is the maximum measured liquid height and ϵ is the porosity of the surface given by Equation 3.6,

$$\epsilon = \frac{(d^2\pi t/4) - w/\rho_s}{(d^2\pi t/4)} \tag{3.6}$$

where d is the diameter of the powder cake, $t = d_1$ is the thickness of the powder cake, w is the weight of the powder composing the cake and ρ_s is the absolute density of the powder.

- *D*ynamic yield stress: Iveson (2002) and Iveson and Page (2005) developed a technique for measuring the dynamic strength of a granule using compression tests on cylindrical pellets of the granule formulation at medium to high strain rates. The peak flow stress was measured and this parameter was used as a key predictor for granule deformation, consolidation and coalescence as will be explained in section 3.3.4.

Axial compression experiments were performed using an Instron Dynamite load frame (Model 8841). Prior to this, cylindrical pellets were formed from a premix (with known binder-to-solids ratio) of calcite powder and PVOH-H_2O, using a metal pellet press of height $25\,mm$ and diameter $20\,mm$. Platen speeds ranging from $0.1\,mm/s$ to $200\,mm/s$ were chosen to simulate particle velocities in typical drum granulators. Each formulation was tested at these compression velocities. Data obtained from the compression tests are in the form of normal force (N) against platen position (mm). This data is then converted to a stress-strain curve for the compression, where the natural strain is given by Equation 3.7.

$$\epsilon = ln\frac{H}{h} \tag{3.7}$$

Here H is the initial height of the pellet ($25\,mm$) and h is the height of the pellet at any point of time. Assuming volume is conserved and each pellet deforms as a perfect cylinder, the cross-sectional area of the pellet at any point of time is defined in Equation 3.8 as

$$A = \frac{H}{h}\frac{\pi D^2}{4} \tag{3.8}$$

where D is the original pellet diameter. Thus the applied stress at any point of time is defined in Equation 3.9 as

$$\sigma = \frac{F}{A} \tag{3.9}$$

where F is the applied force. Subsequently, the peak flow stress (σ_p) of each data set (corresponding to the various platen speeds) is recorded as the maximum point in the stress-strain curve and the corresponding strain rate (ϵ) is calculated in Equation 3.10 as

$$\dot{\epsilon} = -\frac{1}{h_p}\frac{dh}{dt} = \frac{\nu_{platen}}{h_p} \tag{3.10}$$

where h_p is the pellet height at the peak flow stress point and ν_{platen} is the velocity of the platen with values ranging from 0.1 to $200mm/s$. It was shown that by dimensionalising the peak flow stress and strain rate, data for many formulations could be collapsed onto a single curve. Strain rate is represented by the capillary number which is a ratio of the relative effects of viscous to capillary forces and is defined in Equation 3.11 as

$$Ca = \frac{\mu\dot{\epsilon}d_p}{\gamma cos\theta} \tag{3.11}$$

where μ is the liquid binder viscosity, d_p is the specific surface mean particle size of the primary powder measured using the Malvern Mastersizer E, γ is the liquid surface tension and θ is the powder-liquid contact angle. The peak flow stress is made dimensionless with respect to the capillary bond strength and is defined in Equation 3.12 as

$$Str^* = \frac{\sigma_p d_p}{\gamma cos\theta} \tag{3.12}$$

3.2.8 Experimental Design

A series of structured tests were designed in which deliberate perturbations were introduced into the input variables of the process with the intent of observing the effects on the pre-defined outputs. The first step is to identify the inputs and outputs. In this study, the inputs were the binder-to-solids ratio and the drum load. The outputs were granule size, binder content and porosity. Tan et al. (2006) showed that by conducting experiments in a small scale fluid-bed granulator, the selection of different input variable(s) influenced the granule growth behaviour, size distribution and in some cases the morphology of the granules produced. Selecting an input regime to obtain suitable granules that may be adequately characterised is not a trivial task. Therefore, prior to any factorial experimental design, a nominal set of inputs has to be identified from which one parameter may be varied at a time whilst holding the others constant. For the purpose of this study, the binder-to-solids ratio and the drum load were varied. The nominal experiment is that of binder-to-solids ratio $= 0.12$ and a drum load $= 1.75\,kg$. Liquid viscosity was also altered to understand its effect on granule strength and this will be explained in section 3.3.4. All other formulation properties and operating conditions were kept constant.

3.2.9 Liquid Binder Distribution

Successful modelling of the granulation process necessitates detailed understanding of parameters and variables on the microscopic and mesoscopic scales. In particular for wet granulation, binder content of granules is an important property that also influences coalescence along with the material properties and the primary powder characteristics that were discussed above. In one-dimensional models that consider only size, a batch averaged binder content can be obtained and this ratio applied to all granules in the batch. Such models assume that the liquid binder is well mixed among the powder bed and that granules in all size classes have identical binder content. This assumption is not realistic as studies have shown that there can be significant variation in the binder content among granules in various size classes (Knight et al., 1998; Scott et al., 2000; Johansen and Schaefer, 2001; Reynolds et al., 2004). The present study aims to consider the effects (if any) of different binder delivery methods on (a) granule size distribution and (b) binder

content in each size class. Three binder delivery methods were used in this study, namely, the optimal spray method, the pre-mix method and the point-wise method. A detailed description on the implementation of each method is provided below:

- ***Optimal spray method*** In this method (See Figure 3.6a), the drum is loaded with the initial powder mass. Then, the batch drum granulator is run for 20 s after which, the binder is sprayed for the required duration in accordance to the target binder-to-solids ratio. Samples are then extracted at designated time instances.

- ***Pre-mix method*** This method is carried out in two stages (See Figure 3.6b). Firstly, the drum is loaded with two-thirds of the initial powder mass. The batch drum granulator is run for 20 s prior to turning on the liquid binder spray. When the required binder volume has been sprayed, the binder spray is turned off and the remaining one third of the powder mass is introduced into the drum and continued to granulate until the granulation end time has been reached. Samples are extracted at designated time instances.

- ***Point-wise method*** In this method a syringe is used to mimic the localised wetting effect on the powder bed. The syringe is loaded with the required volume of binder solution and introduced manually into the drum granulator at a steady rate. The position of the syringe remains fixed thereby constraining the spray zone to a narrow area on the powder bed surface. Granulation continues and samples are extracted at designated time instances. (See Figure 3.6c).

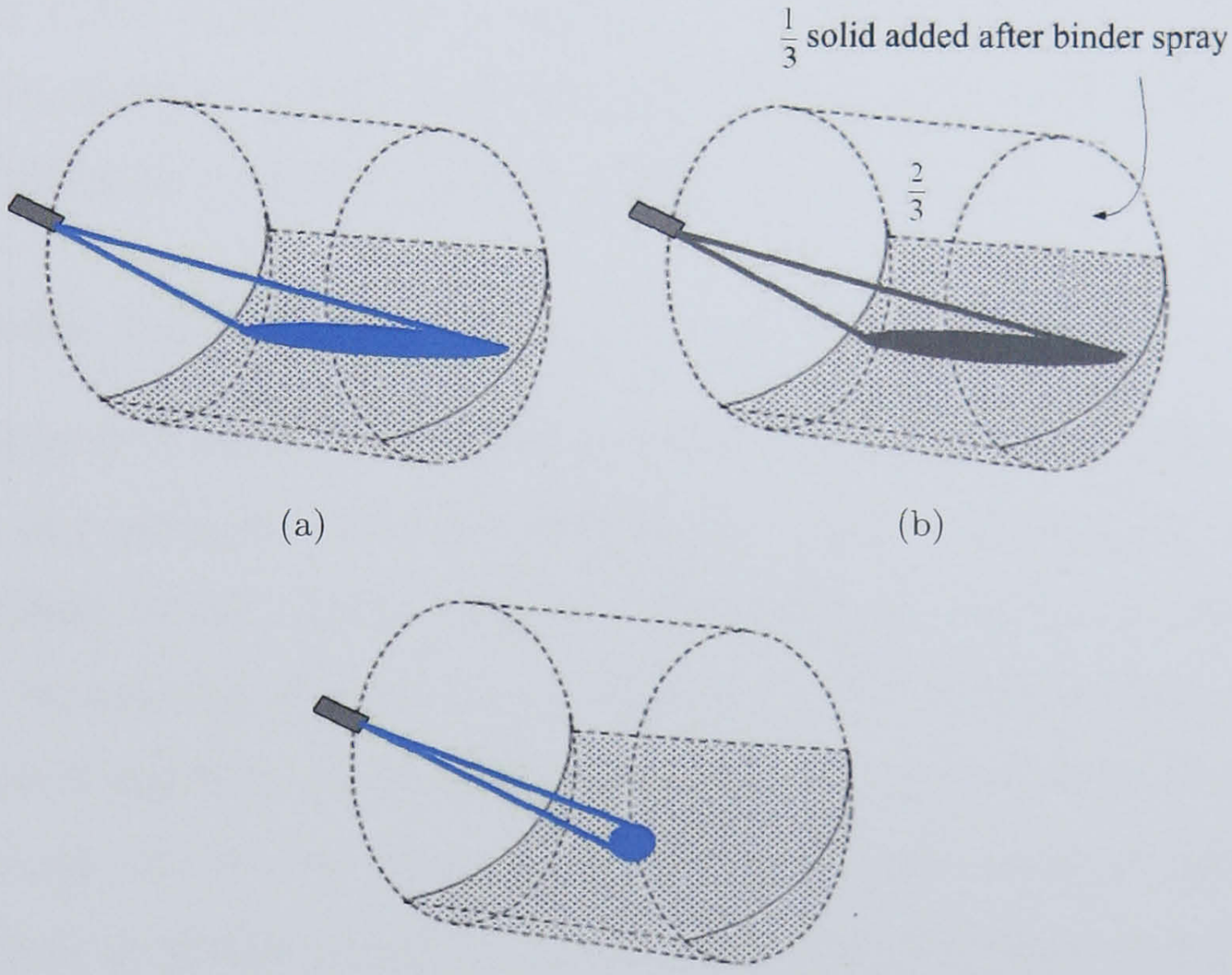

(a) (b)

(c)

Figure 3.6: Binder distribution studies on the method of liquid binder delivery carried out for (a) optimal spray, (b) pre-mix, (c) point-wise delivery.

3.3 Results and Discussion

3.3.1 Recipe Identification

Calcite (limestone) was chosen for this study due to its many uses as fertiliser, chalk, cement and building stone. Polyvinyl alcohol was chosen as the additive in water as it is non-toxic and odourless. Calcite has various applications in the industry which include fertilisers, chalk, cement and building stone to name a few. This material is ideally suited to this study as it will serve to demonstrate the coupling of the population balance model with a realistic process application of direct relevance to the industry. The binder additive employed in this study, polyvinyl alcohol, is both odourless and non-toxic thereby facilitating its handling and preparation.

3.3.2 Powder Properties

Random samples of limestone (i.e., different lots of the same grade/supplier) were analysed to determine the variation in the size distribution between the samples. In Figure 3.7, the PSDs of three of the random samples of limestone are shown. It can be seen that the variation between the distributions are minimal. This indicates that to maintain an almost identical initial distribution, random sampling of primary powder is sufficient. *From Figure 3.7, it can also be seen that primary particle size distribution is fairly wide. This has ramifications on granule growth in the following ways. Firstly, as a result of the broad PSD, the resulting GSD would be broad and possibly multi-modal.* This is due to the fact that there exist many different combinations of particles of different sizes coalescing, thus forming granules in various size ranges. Secondly, a broad PSD with a mixture of small and large primary particles would result in a larger extent of granulation. This is attributed to the fact that a large and small particle are more likely to coalesce as opposed to two large particles. This factor is reflected in the aggregation kernel formulations by (Wauters, 2000; Immanuel and Doyle III, 2005). In other kernel formulations such as the one in Madec et al. (2003), a large and small particle have a higher chance of coalescing than two small particles, again suggesting higher aggregation rates in a broad seed. As further support, it has also been experimentally observed that large granules comprise more of smaller primary particles whilst smaller granules are comprised mainly of larger primary

particles (Scott et al., 2000).

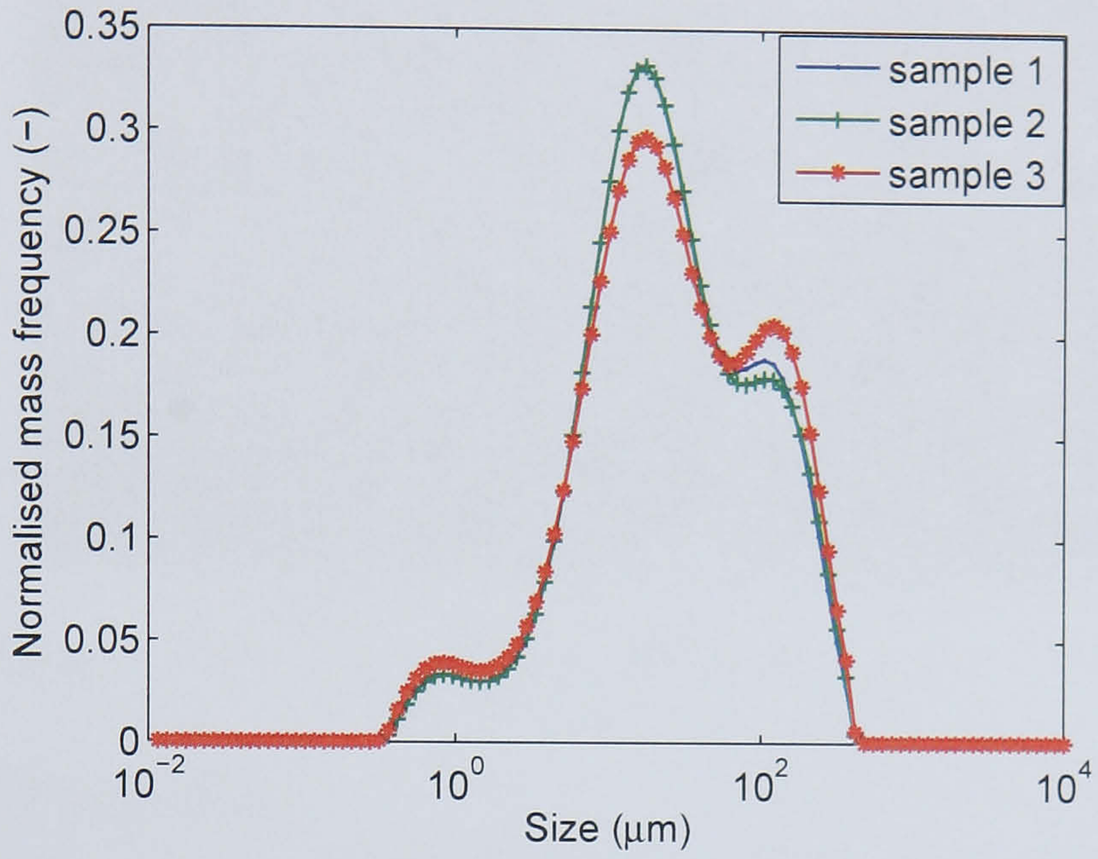

Figure 3.7: Primary particle size distribution .

Furthermore, the broad PSD of the primary particles might cause the powder bed to be fairly dense, and might cause difficulty in the liquid binder to penetrate through the layers and wet any particles embedded in the lower layers. For this particular case, how well the binder is distributed would largely depend on the tumbling motion of the drum which should ensure a constant circulation of the particles, provided the motion is optimal (Litster et al., 2001). A sub-optimal distribution of liquid binder in the powder bed could lead to preferential growth of high liquid content granules, resulting in very large granules and unwetted primary particles (see section 3.3.6). *This suggests that in drum granulation processes, the drum rotation speed could be another possible control handle to ensure optimal binder distribution.* In this manner, the controlled variable (e.g. average granule size) is regulated via the redistribution of binder as well as the breakup of particles from mechanical dispersion, by the continuous or discrete adjustment of drum speed.

Figure 3.8 depicts images of the particles as seen in an SEM at a magnification of $\times 200$. It can be observed that the particle surfaces are rough and non-spherical. This could be a contributing factor to the strength of the granules (see section 3.3.4) due to particle interlocking, where the strength of the granule is increased as particles cannot easily slide past one another.

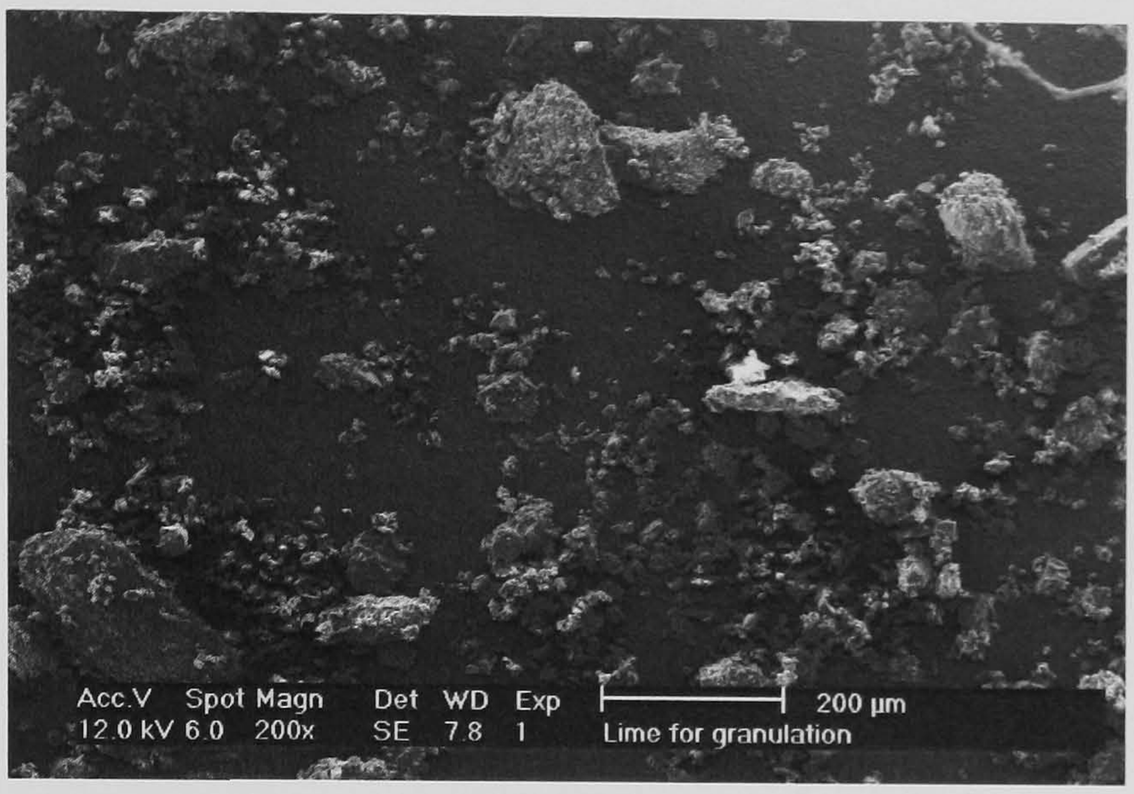

Figure 3.8: Primary particle shape, as seen through an SEM at $\times 200$ magnification.

3.3.3 Liquid Properties

Many researchers have postulated that the viscosity of the binder has a significant effect on the granulation process (Hapgood et al., 2002; Van den Dries et al., 2003; Walker et al., 2006). Iveson and Litster (1998a) had also indicated that the variation in binder viscosity may change the dominant granule growth mechanism. Viscosity affects the viscous forces that can dominate in determining the granule-granule interactions (Reynolds et al., 2007). In this study, water was initially used as the liquid binder and it was observed that there was an accumulation of wall buildup of fine primary particles with time. Weak and friable granules were formed with layering (sticking of the fine powder that was accumulated on the walls, on granules) being the predominant mechanism for granule growth. Subsequently, PVOH was employed as an additive to increase the viscosity of the liquid binder. The viscosity of the binder was measured to be $0.0052\,Pa.s$, approximately five times that of water at room temperature. It was immediately observed that the increase in viscosity resulted in strong and surface wet granules that did not fragment easily. Furthermore, the average granule size was also increased but minimal layering was observed. This implies that due to the increase in viscosity, the predominant mechanisms were now coalescence (increase in average granule size) and consolidation. This phenomenon was also observed in the work by (Hoornaert et al., 1998). The primary particle size will also influence the minimum binder viscosity required for granule growth. A higher viscosity is required to promote coalescence and consolidation (Iveson et al., 1996) and to minimise breakage

when the primary particle size is larger, which is the case for this study.

A literature value of $52\,mN/m$ was obtained for the surface tension of PVOH-H_2O (Bhattacharya and Ray, 2004) which is approximately seven-tenth the surface tension of water at ambient temperature. A key finding from Capes and Danckwents (1967) suggested that due to the strength of the capillary bond in drum granulation, the ratio of liquid surface tension to particle size needs to exceed a minimum value in order for granules of sufficient strength to be formed. Iveson and Litster (1998a) investigated the effect of liquid binder surface tension on the dynamic yield strength of granules and concluded that a decrease in binder surface tension decreased the dynamic yield stress of granules. Based on this, water would be a good choice of binder as it has a higher surface tension. However, the viscosity of water was not high enough to form strong liquid bridges as discussed previously. Furthermore, Iveson and Litster (1998a) observed that *for a more viscous binder, the binder viscosity dominated the yield-stress behaviour as opposed to the surface tension.* Thus, the PVOH-H_2O solution was chosen in this study, despite its lower surface tension compared to water.

3.3.4 Powder-liquid Properties

The powder-liquid contact angle determined for this system using the contact anglometer (Micromeritics) was 43.2°. Low contact angles imply that the liquid wets the surface and will spread readily across it, whereas high contact angles imply that the liquid does not wet the surface and will tend to form beads (Iveson et al., 2000). In an earlier study, Iveson and Litster (1998a) noted that coverage of porous powders (such as the one in this study) had a maximum as contact angle was decreased. Based on the experimental studies, it was deduced that the contact angle resulted in a high coverage (at or near the maximum) such that it increased the probability of a particle coming into contact with the wetted portion of another particle, resulting in potentially higher rate of coalescence.

Figure 3.9 demonstrates the typical strain rate dependent behaviour of the Calcite/PVOH-H_2O system. The peak flow stress versus strain rate is depicted for three different binder-solids-ratio of 0.10, 0.12 and 0.14. At low strain rates, the peak flow stress is strain rate-

independent. Above some critical strain rate, the peak flow stress increases with increasing strain rate. This suggests that at low strain rates, the granule strength is dominated by capillary forces and at high strain rates, viscous dissipation dominates (Iveson and Page, 2005). Iveson and Page (2005) also noted the transition between brittle and plastic behaviour with strain rate. Low strain rates resulted in brittle behaviour and high strain rates in plastic behaviour. In this work, it was experimentally observed that at lower strain rates, the pellets showed large cracks leading to brittle failure. At higher strain rates, the pellets tended to deform plastically upon compression. Furthermore, it can be seen that for a higher binder-to-solids ratio, the peak flow stress increases across all strain rates.

Figure 3.10 shows the peak flow stress and strain rate plotted in dimensionless form. At a Capillary number (Ca) below 10^{-5}, the dimensionless peak flow stress (Str*) is insensitive to changes in Ca. Ca is defined in Equation 3.13 where μ is the viscosity of the binder, $\bar{\varepsilon}$ is the strain rate, d_p is the particle diameter, θ is the contact angle and γ is the liquid-vapour surface tension. Str* is defined in Equation 3.14 where σ_p is the peak flow stress.

$$Ca = \frac{\mu \bar{\varepsilon} d_p}{\gamma cos\theta} \tag{3.13}$$

$$Str^* = \frac{\sigma_p d_p}{\gamma cos\theta} \tag{3.14}$$

Above this value, Str* increases with Ca. At low Ca, the predominant mechanism is layering and at higher Ca, coalescence is more predominant. This is consistent with what was experimentally observed. With water as the liquid binder, the capillary forces were relatively higher than the viscous forces resulting in a low Ca, leading to layering. With the addition of PVOH, the viscous forces were now increased and the capillary forces decreased. This resulted in a higher Ca (calculated to be approximately of the order of 10^{-4}), thus prone to increased coalescence and consolidation. Hence, this regime is more suitable for model validation studies at the first stage, as coalescence and consolidation are more important compared to other rate processes. The effects of viscosity on granule strength were also investigated (see Figures 3.11 and 3.12). At comparable strain rates, it

was observed that there was increased coalescence and consolidation. For all Figures 3.9 to 3.12 the shapes are consistent with the shapes seen in Iveson and Page (2005). Standard errors were also calculated and reported to be approximately 0.003. This indicates that the data are statistically significant and that instrumentation error is negligible.

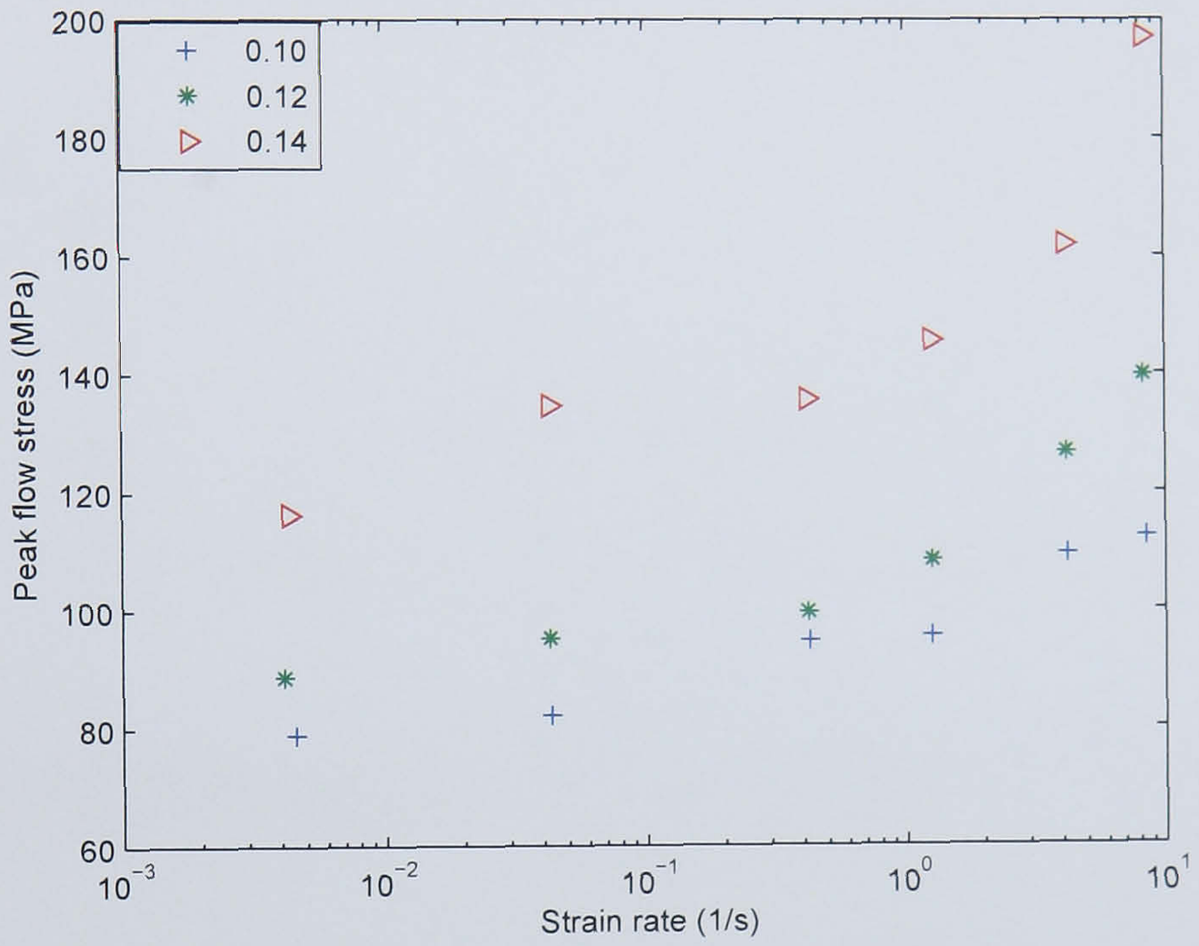

Figure 3.9: Peak flow stress against strain rates for various binder-to-solids ratio for 2.5% PVOH-H_2O.

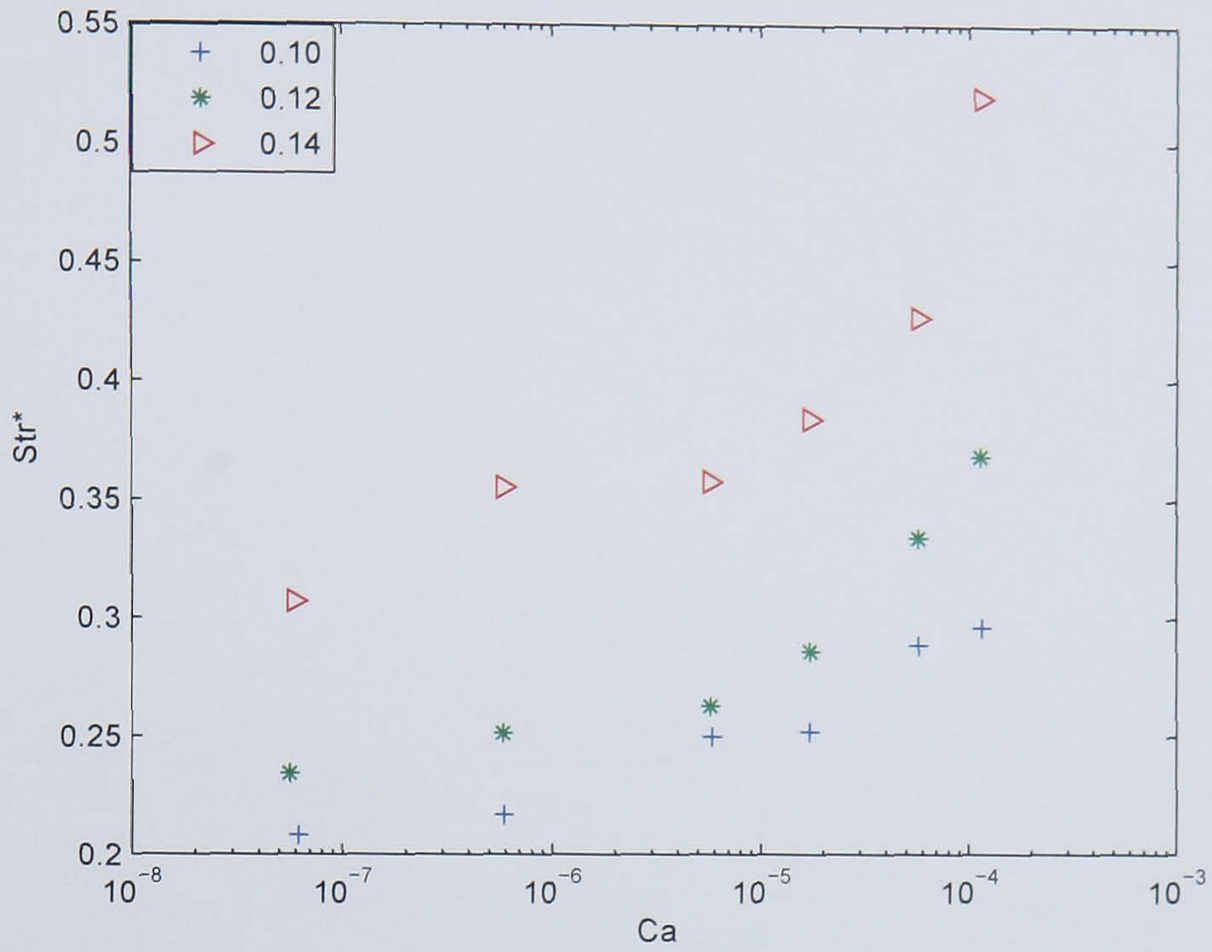

Figure 3.10: Dimensionless peak flow stress against capillary number for various binder-to-solids ratio for 2.5% PVOH-H_2O.

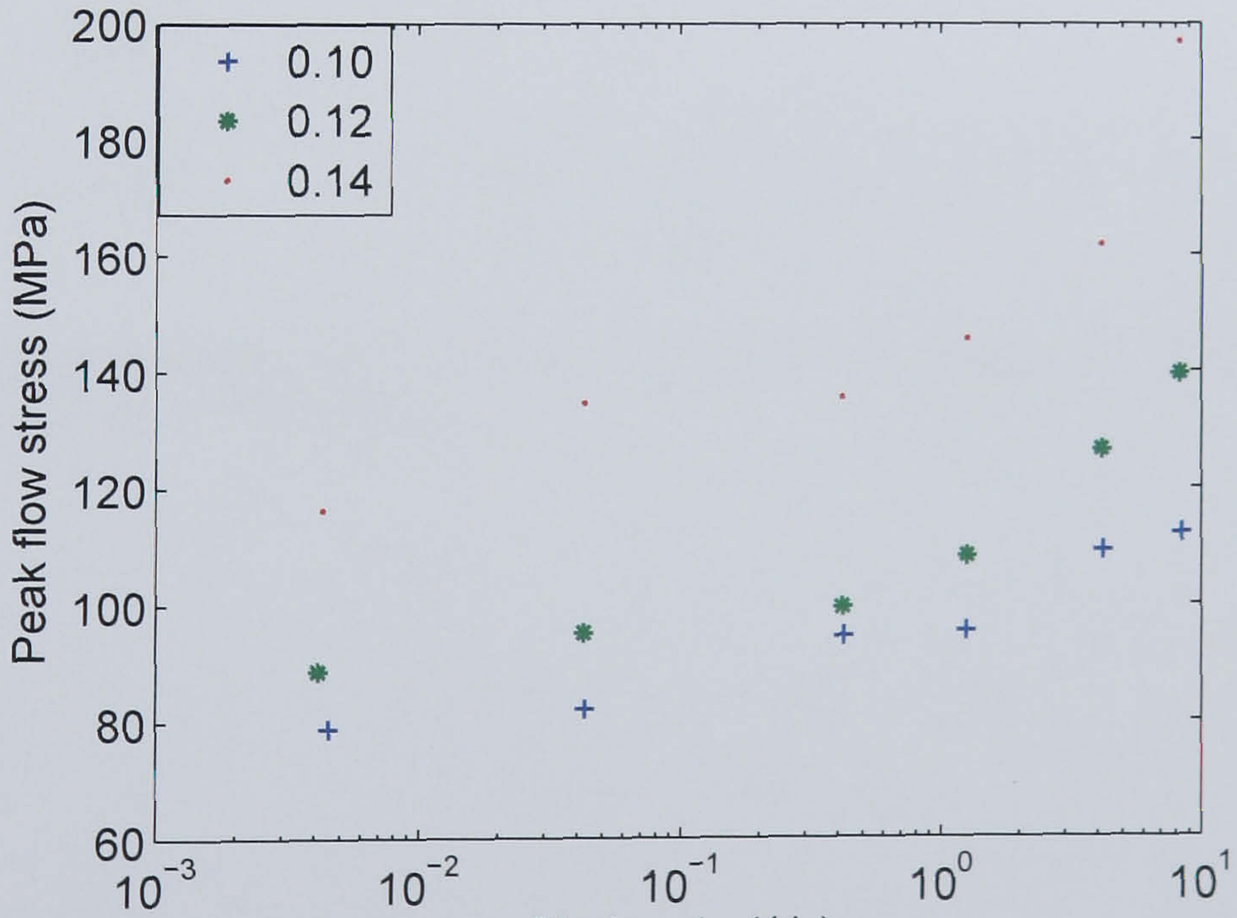

Figure 3.11: Peak flow stress against strain rates for various binder-to-solids ratio for 5% PVOH-H_2O.

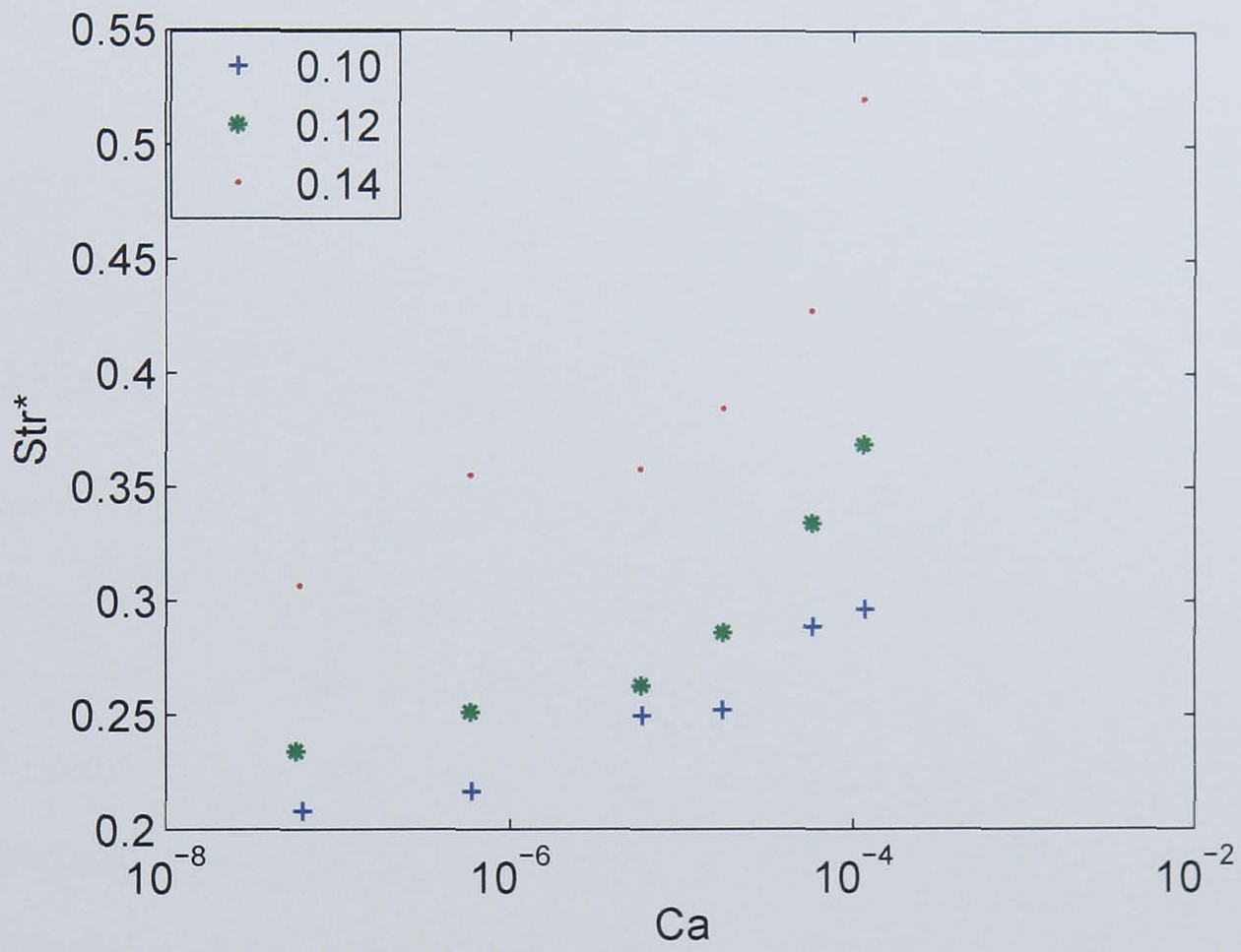

Figure 3.12: Dimensionless peak flow stress against Capillary number for various binder-to-solids ratio for 5% PVOH-H_2O.

3.3.5 Growth Behaviour

In Figure 3.13, the GSD profiles corresponding to a drum load of $1.75\,kg$ are plotted. In these figures, the binder-to-solids ratio is varied from 0.10 to 0.14. The GSDs display a multi-modal distribution and as time progresses, there is a general shift toward large size granules. Furthermore, it can be seen that granule size is very sensitive to binder-to-solids ratio. At a lower binder-to-solids ratio of 0.11 most of the particles remain ungranulated. This is in contrast to a binder-to-solids ratio of 0.14 where a large proportion of granules are in the largest size ranges. Binder-to-solids ratio of $0.12-0.13$ produce a broad distribution of granules from fines to large sized granules. When the drum load was decreased to $1.5\,kg$, it was observed that the average granule size decreases (as seen in Figure 3.14). Repeat experiments were carried out to ensure that this difference in average size was not a result of experimental errors. Therefore, this illustrates the effect of the bed density on the consolidation and aggregation rates, the effect being attributed possibly to an influence on the flow pattern and liquid distribution.

To further characterise the formulation and to understand the granulation dynamics, it is important to plot the relationship between growth behaviour, and pore saturation and deformation number on a regime map (see Figure 2.5 in Chapter 2). Iveson and Litster (1998a) and Iveson et al. (2001) postulated that the type of granule growth that a system exhibits is a function of only the pore liquid saturation and the amount of granule deformation upon impact. Granule pore saturation is defined to be the maximum granule pore saturation (S_{max}) as defined in Equation 3.15.

$$S_{max} = \frac{w\rho_s(1-\epsilon_{min})}{\rho_l \epsilon_{min}} \tag{3.15}$$

Here w is the binder-to-solids ratio, ρ_s is the solid density, ρ_l is the liquid density and ϵ_{min} is the minimum porosity. The Stokes' deformation number is defined in Equation 3.16. where ρ_g is the granule density, U_c is the particle velocity and Y_g is the yield stress of the granule. Y_g was obtained from the stress strain relationships (of various formulations with different liquid to solids ratio) which were measured using the Instron Dynamite load frame.

$$St_{def} = \frac{\rho_g U_c^2}{2Y_g} \tag{3.16}$$

The initial hypothesis about the growth behaviour is that the system is in the induction growth regime with reasonable nucleation and binder distribution. There is reasonable distribution of the liquid, with some inevitable rewetting of some powder leading to a relatively broad starting GSD but with a few huge clumps. At low binder contents (0.11 and 0.12), there are considerable unwet fines. The granules grow slowly as they consolidate and layer onto some additional fines. Within the time of the experiment. the granules do not become sufficiently surface wet for coalescence to predominate. This observation can be verified from the results obtained in Table 3.1 for binder-to-solids ratio of 0.11 and 0.12. The relatively low values obtained for St_{def} and S_{max} prove that a portion of the particles remain in the *nucleation only* regime where granule nuclei form, but there is insufficient binder to promote further granule growth. Remaining granules may lie in the *induction growth* regime where there is a long period of little or no growth in which granules undergo compaction causing internal binder to be squeezed out onto the granule surfaces. However, due to the long induction period, the internal liquid does not rise to the surface fast enough for coalescence to take place. At an intermediate binder content of 0.13, similar behaviour is observed but after 15 minutes, most of the unwet fines are used up and the beginning of coalescence is seen. Based on St_{def} and S_{max} values, it is likely the the granules are in the *induction and rapid growth* boundary. The increased binder content reduced the induction period which is expected for highly consolidating systems such as the present system and after 15 minutes, the surface wet granules move into the *rapid growth* stage resulting in fast coalescence. At high binder contents (0.14) all the fines are used up in the initial wetting stage and there is fast coalescence immediately. As seen from the St_{def} and S_{max} values, this shows that the induction period is very short and the granules have moved into the rapid growth regime.

Table 3.1: Stokes' deformation number and maximum pore saturation for different formulations.

No.	**Binder-to-solids ratio**	St_{def}	S_{max}
1	0.11	$1.80e^{-4}$	0.415
2	0.12	$1.79e^{-4}$	0.484
3	0.13	$1.59e^{-4}$	0.575
4	0.14	$1.38e^{-4}$	0.699

The typical duration of the binder spray was $120\,s$ and from the average diameter versus time plot (see Figure 3.15), the apparent time constant (τ) of the system to be approximately $180\,s$ ($3\,min$). *This implies promise for feedback control, as the system seems to have the potential to respond fast when there is a change in the manipulated variable (binder flow rate).* Had the time constant been much greater than the binder duration. this would imply that the process is sluggish, with implications on the economy (long batch times, for instance) and a possible need for aggressive control settings to obtain the best performance from the process. Alternatively, if the time constant was faster than the binder duration, this would imply that the process is extremely sensitive and this could result in instabilities and difficult control.

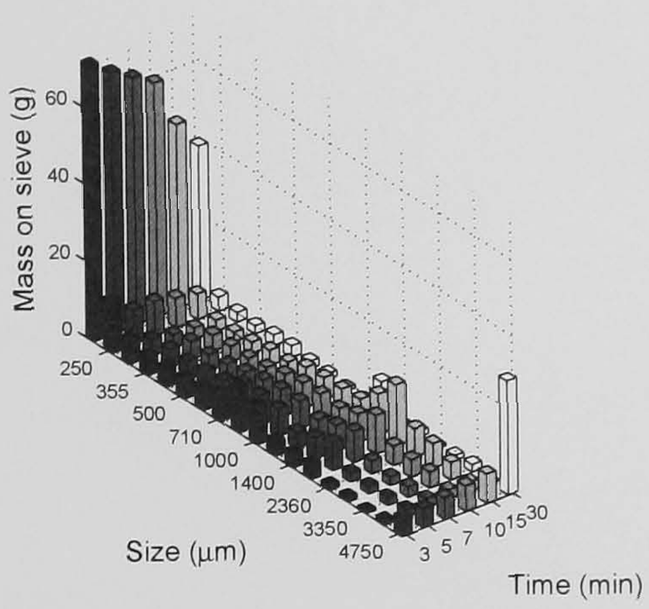

(a) binder-to-solids ratio = 0.11

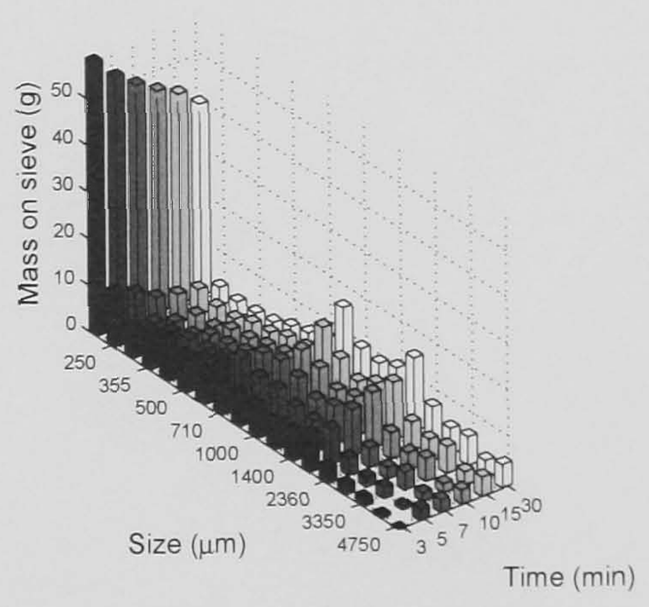

(b) binder-to-solids ratio = 0.12

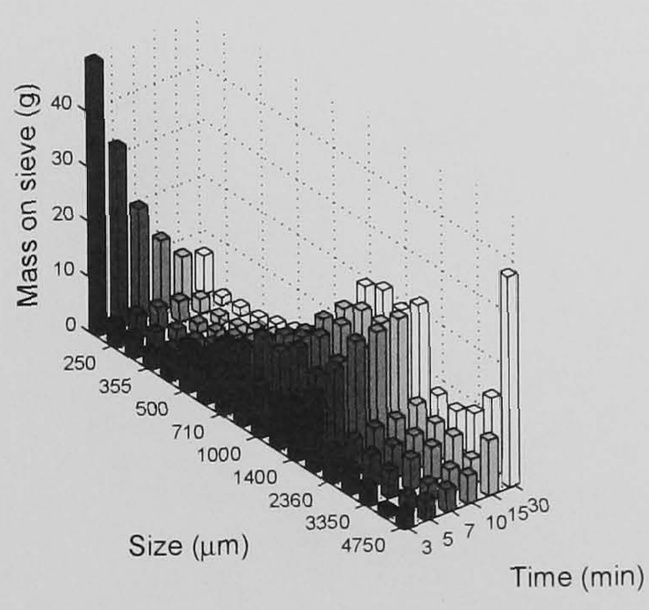

(c) binder-to-solids ratio = 0.125

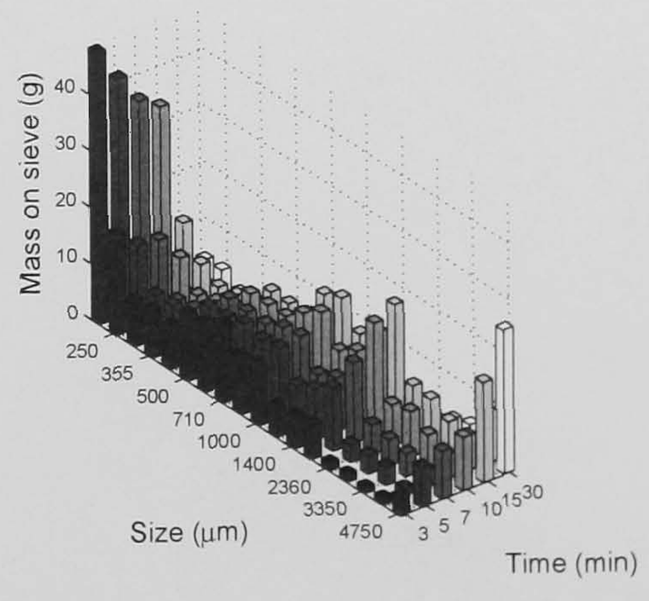

(d) binder-to-solids ratio = 0.13

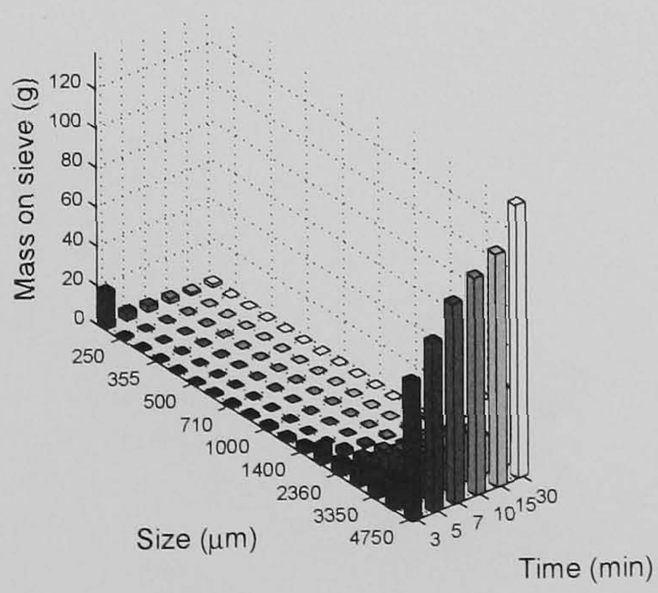

(e) binder-to-solids ratio = 0.135

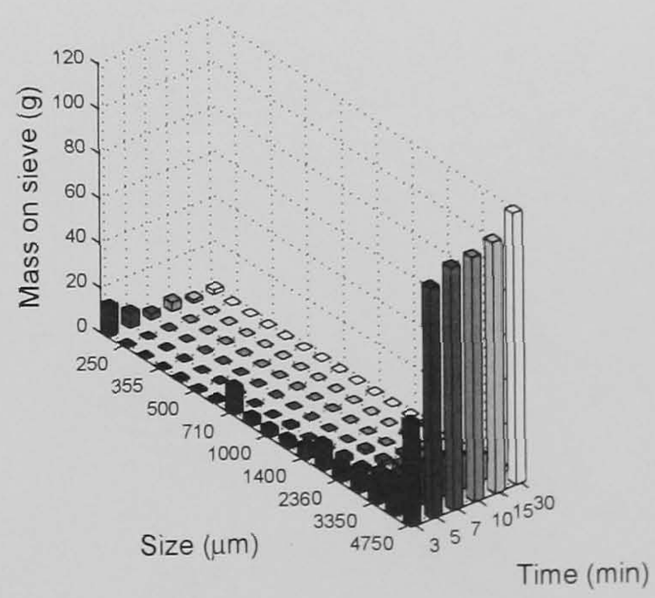

(f) binder-to-solids ratio = 0.14

Figure 3.13: GSD profiles for drum load of 1.75 kg. Optimal binder distribution (Fig 3.6a) where binder is sprayed for approximately 2 min and sampling commences at 3 min.

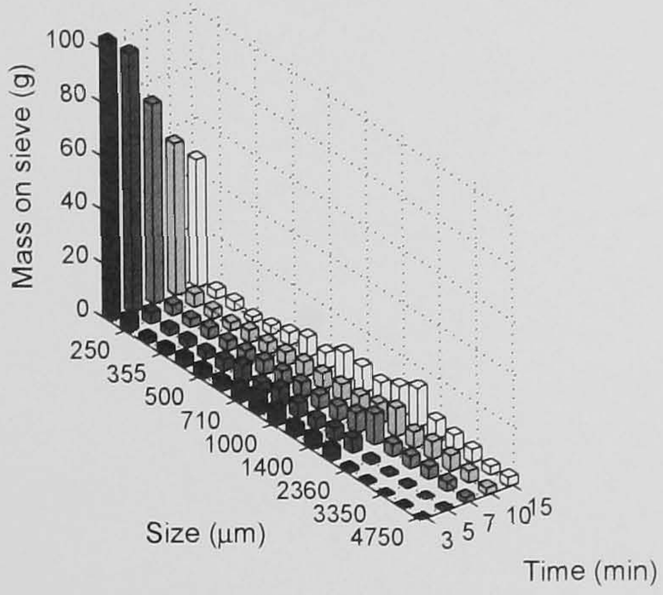

(a) binder-to-solids ratio = 0.11

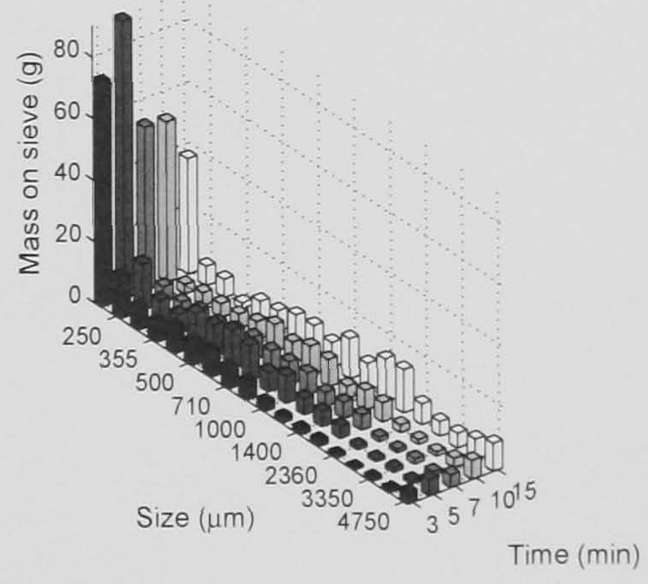

(b) binder-to-solids ratio = 0.12

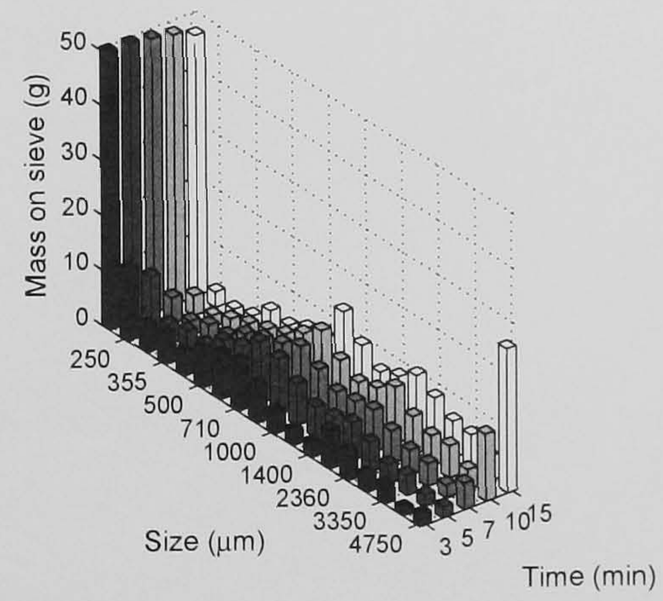

(c) binder-to-solids ratio = 0.125

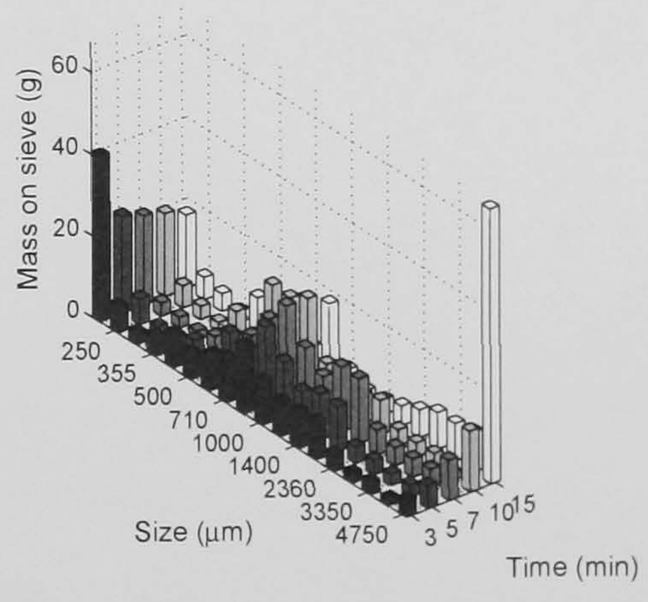

(d) binder-to-solids ratio = 0.13

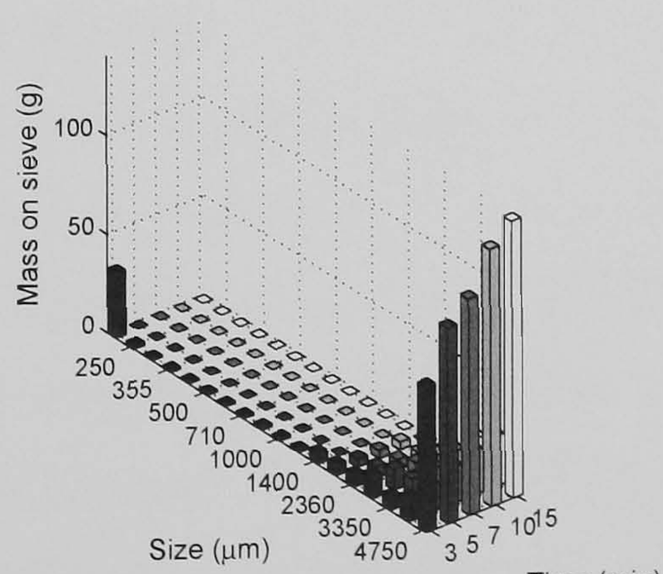

(e) binder-to-solids ratio = 0.135

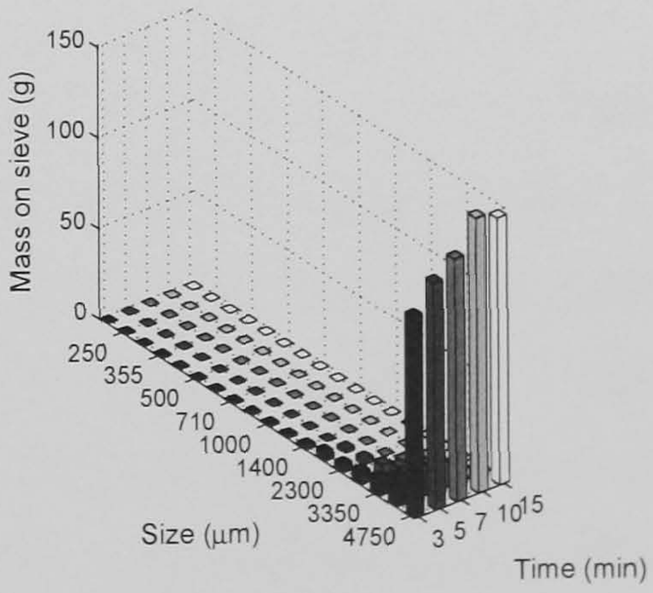

(f) binder-to-solids ratio = 0.14

Figure 3.14: GSD profiles for drum load of $1.5\,kg$.

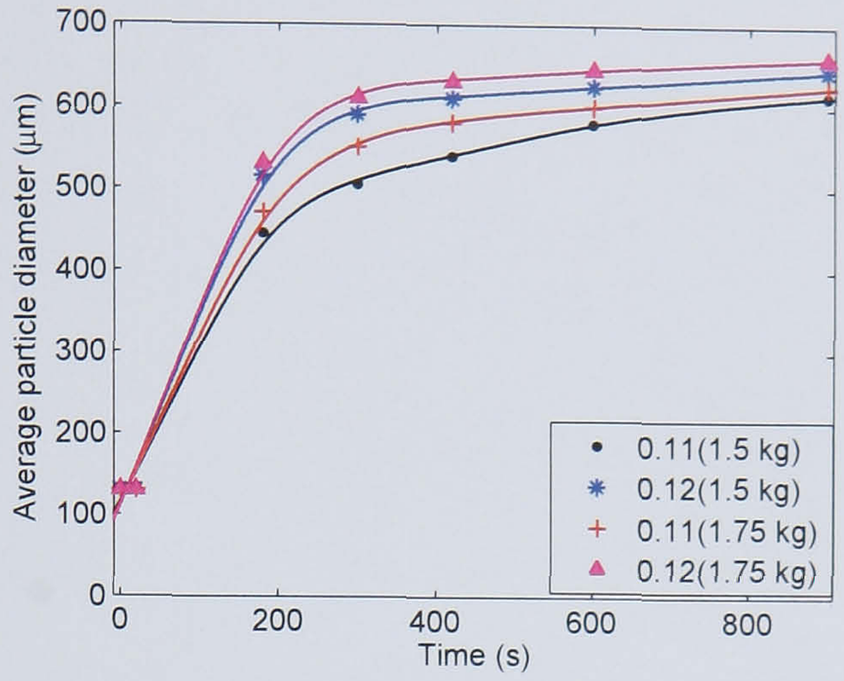

Figure 3.15: Plot of average diameter versus time for different binder-solid ratio and drum loadings.

Figure 3.16a depicts the binder content distribution across the different size ranges, for a binder-to-solids ratio of 0.12 and a drum load of $1.75\,kg$, at three time instances during the batch. The binder content is defined as:

$$\text{L:S} = \frac{V_l \rho_l}{V_s \rho_s} \tag{3.17}$$

where V is the volume, ρ is the density and the subscripts s and l denote solid and liquid respectively. The trends observed in the figures complement those of other studies (Knight et al., 1998; Scott et al., 2000; Johansen and Schaefer, 2001; Reynolds et al., 2004). For all the time samples studied, there is a clear trend of small granules containing relatively less binder content. Granules in the mid-range have relatively the highest binder content. The assumption is that binary coalescence is the predominant growth mechanism and coalescence will only occur if one of the granules contain more than a critical binder content. This implies that the resultant larger granules (upon successful coalescence) must have come from original granules that contained a binder content that is higher than the critical amount. Smaller granules on the other hand do not have this critical binder content and subsequent collisions are unlikely to lead to successful coalescence. The trends seen in the $15\,min$ and some of the $10\,min$ data are below the theoretical binder content of 0.12 and 0.125. This is attributed to loss of binder over time.

The influence of binder-to-solids ratio and drum load on the binder content distribution is shown in Figures 3.16b and 3.16c respectively. The trends observed are comparable to that

in Figure 3.16a. This shows firstly that inhomogeneous binder distribution results irrespective of the binder-to-solids ratio. and secondly that a different flow pattern (as a result of a different drum loading) does not result in homogenous distribution of binder. *These observations present a compelling argument for multi-dimensional population balance models that explicitly account for non-uniform binder distribution in addition to non-uniform size distribution.* Binder content values inferred from the absorbance measurements are reproducible as indicated by the error bars in Figure 3.16b.

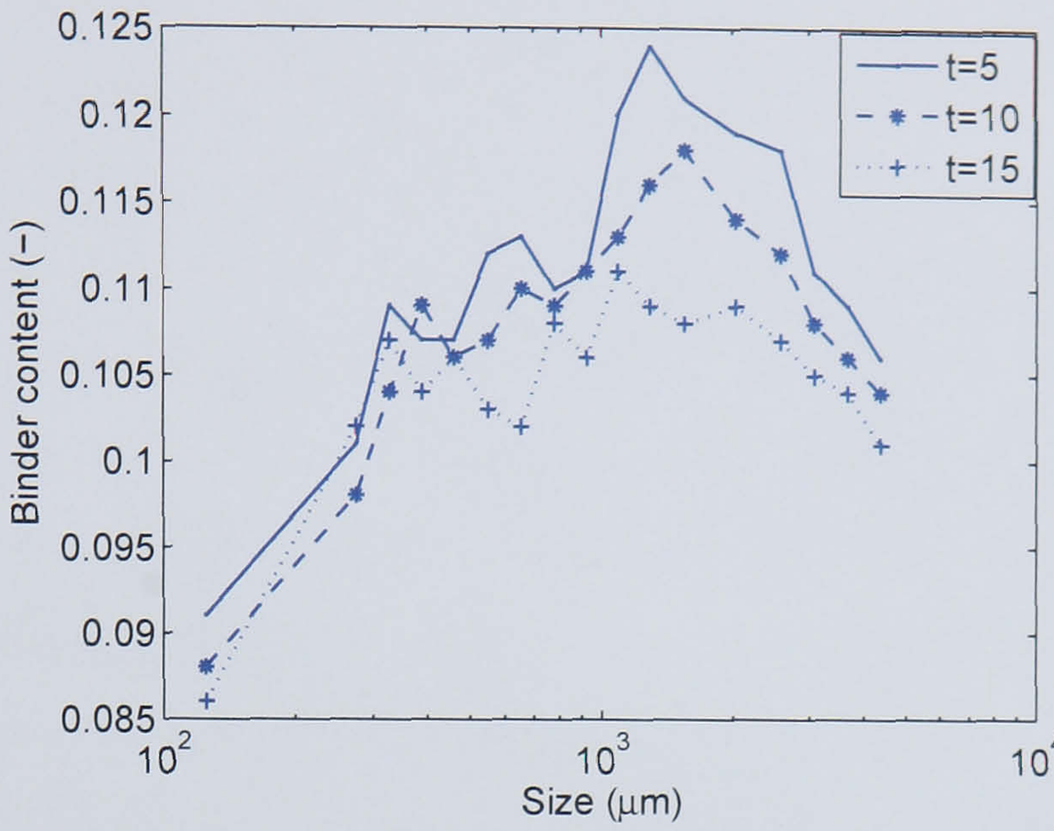

(a) binder-to-solids ratio = 0.12 and drum load = 1.75 kg

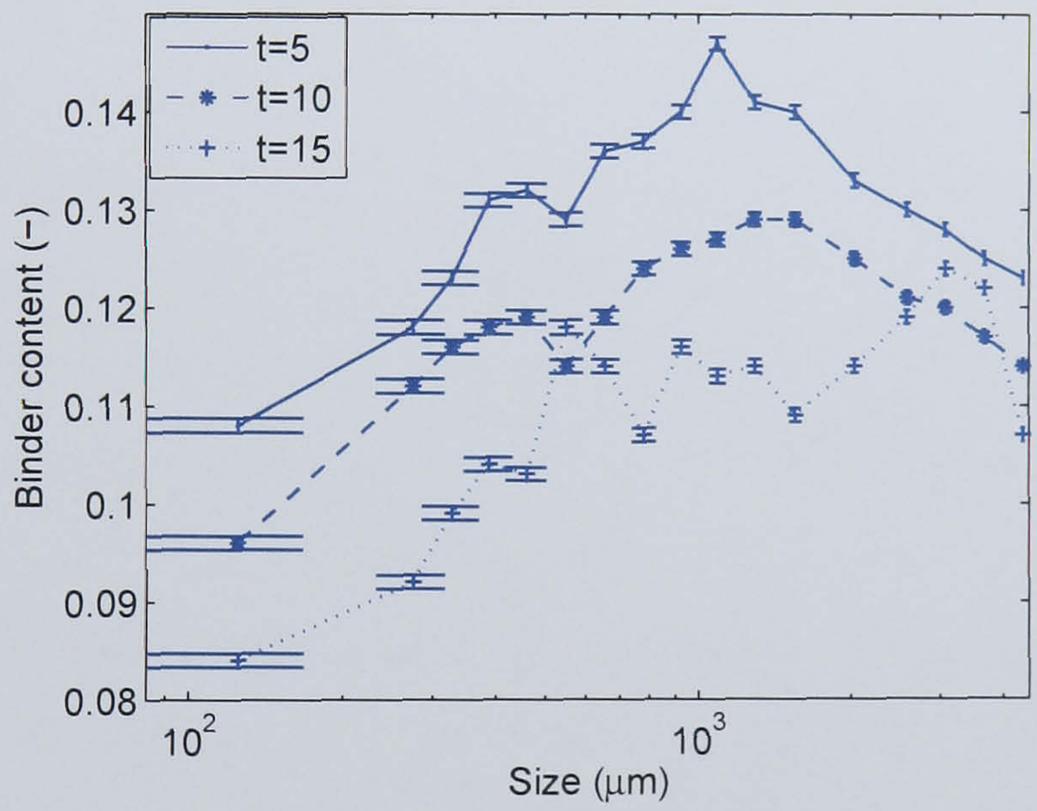

(b) binder-to-solids ratio = 0.125 and drum load = 1.75 kg

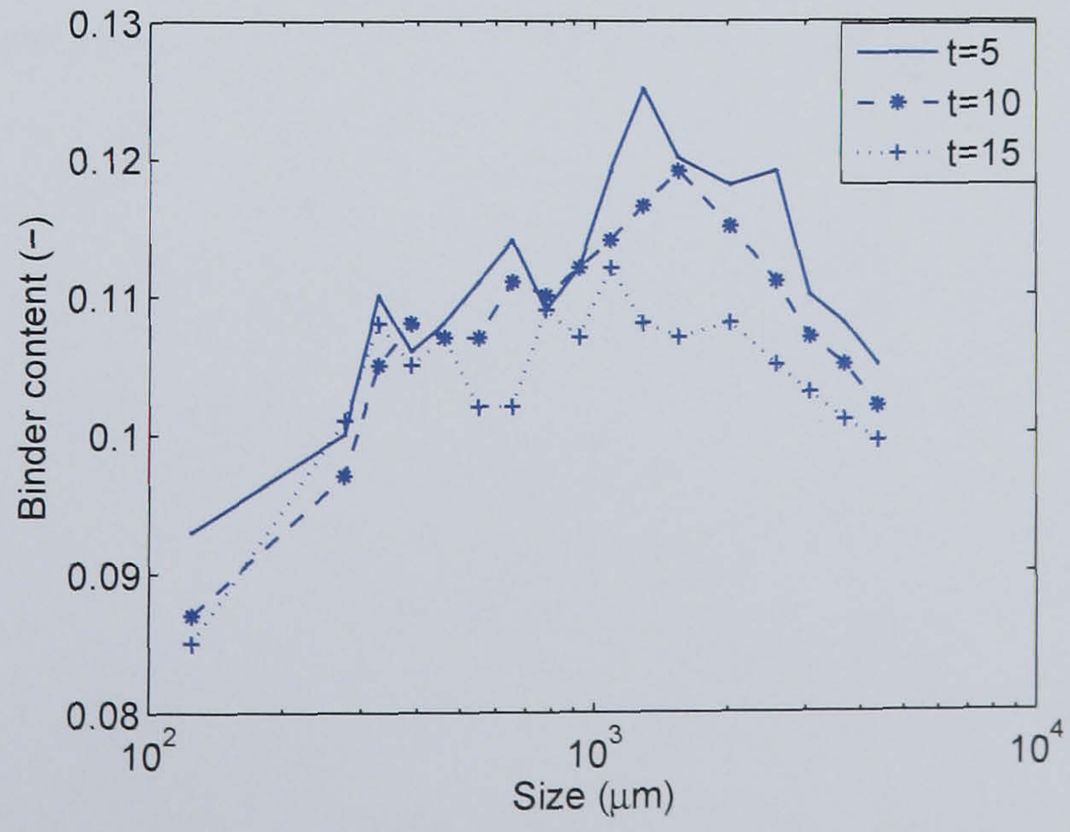

(c) binder-to-solids ratio = 0.125 and drum load = 1.5 kg

Figure 3.16: Distribution of binder content across different size ranges.

Figure 3.17 depicts the porosity distribution across the different size ranges, for a binder-to-solids ratio of 0.12 and 0.125 and a drum load of $1.50\,kg$ and $1.75\,kg$. The influence of binder-to-solids ratio and drum load on porosity is shown in Figures 3.17b and 3.17c respectively. It can be seen that larger sized particles tend to be less porous. This is because larger particles generally consist of smaller fines Scott et al. (2000) and as a result of the closely packed nature of the granule structure, the pore volume is smaller. It can also be seen that for a higher binder-to-solids ratio (See Figure 3.17b) the porosity across the size classes reduces. This could happen as a result of the higher binder-to-solids ratio leading to increased coalescence which in turn results in larger and more compact granules. Comparing Figures 3.17b and 3.17c, it was observed that the drum load also has an effect on porosity and at the higher drum load of $1.75\,kg$, the porosity across the size classes is marginally lower. This suggests that due to the different flow pattern (caused by the larger drum load), more compact granules were now formed. Furthermore, over time a general trend in the reduction of porosity was observed. This accentuates the effect of consolidation and compaction of the granules over time. Overall, it can be seen that the porosity of the granules varies significantly across the size classes. Also, binder-to-solids ratio and drum load influence the intermediate and end-point porosity distribution. *Once again, this supports the need for multi-dimensional population balance models that account for heterogeneous porosity distribution.* Porosity values inferred from the granule density measurements of the GeoPyc are reproducible as indicated by the error bars in Figure 3.17b. However, the absolute porosity values may be an overestimate as the GeoPyc instrument reports inter- and intra-granule porosity. The assumption is that the granules are compacted substantially such that inter-granule porosity is considered negligible.

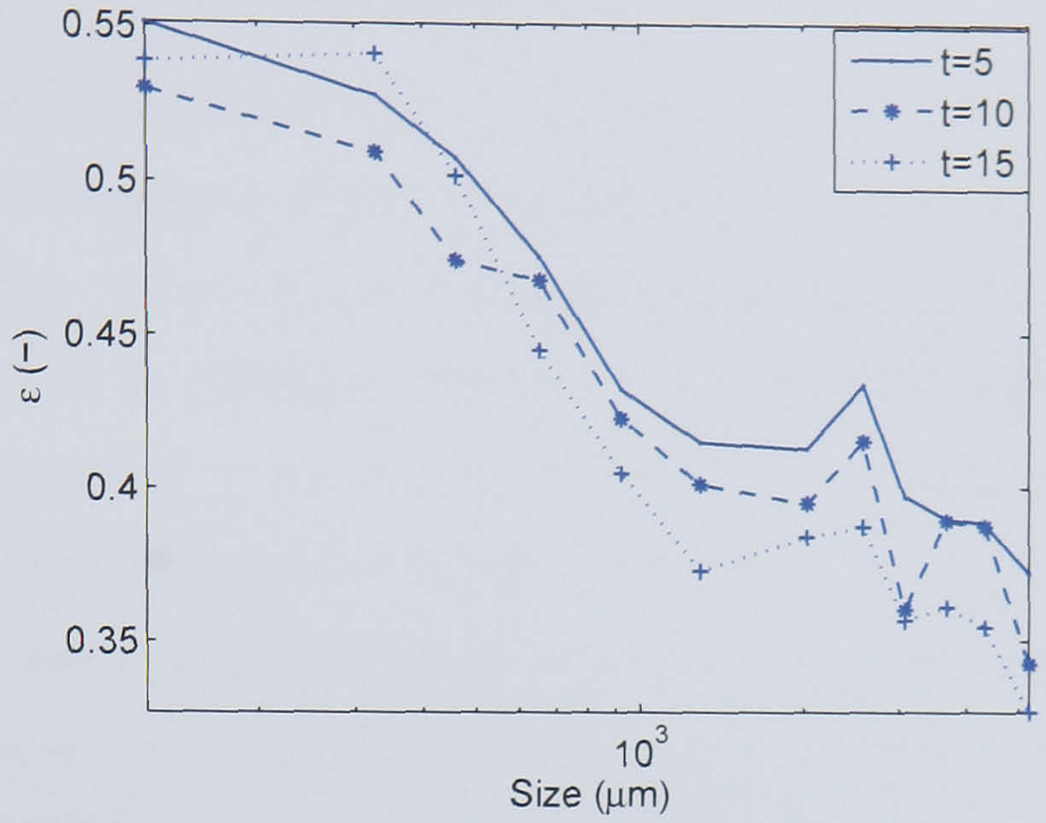

(a) binder-to-solids ratio $= 0.12$ and drum load $= 1.75\,kg$

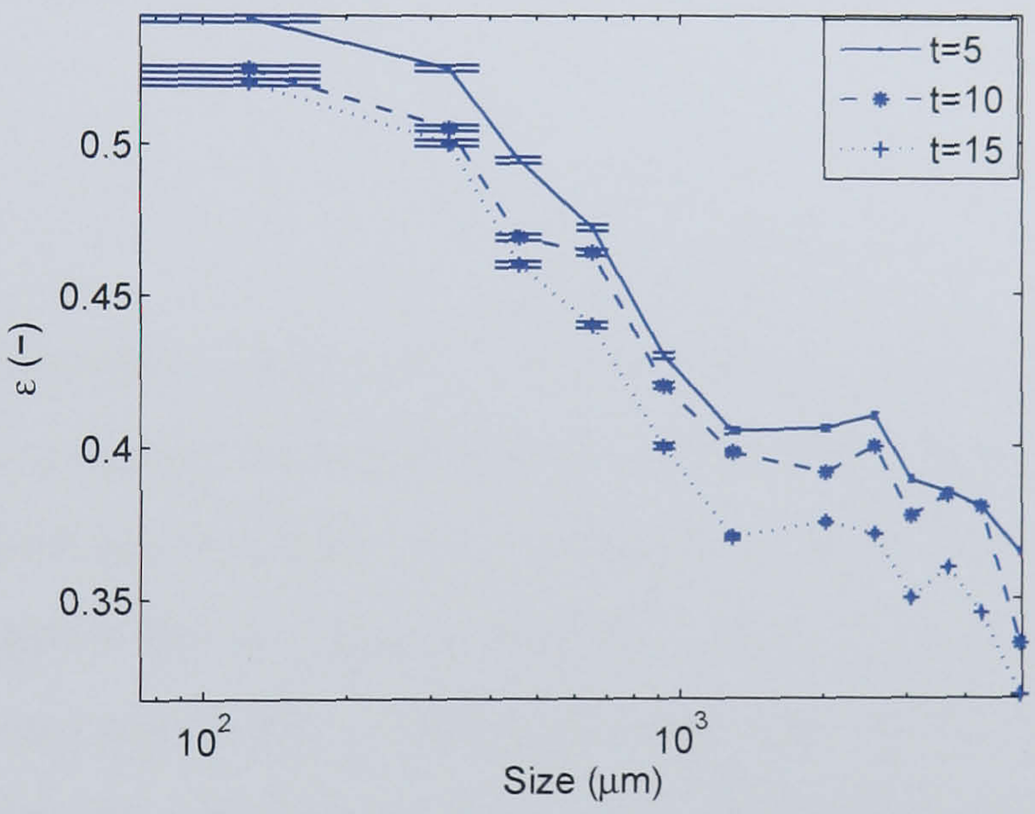

(b) binder-to-solids ratio $= 0.125$ and drum load $= 1.75\,kg$

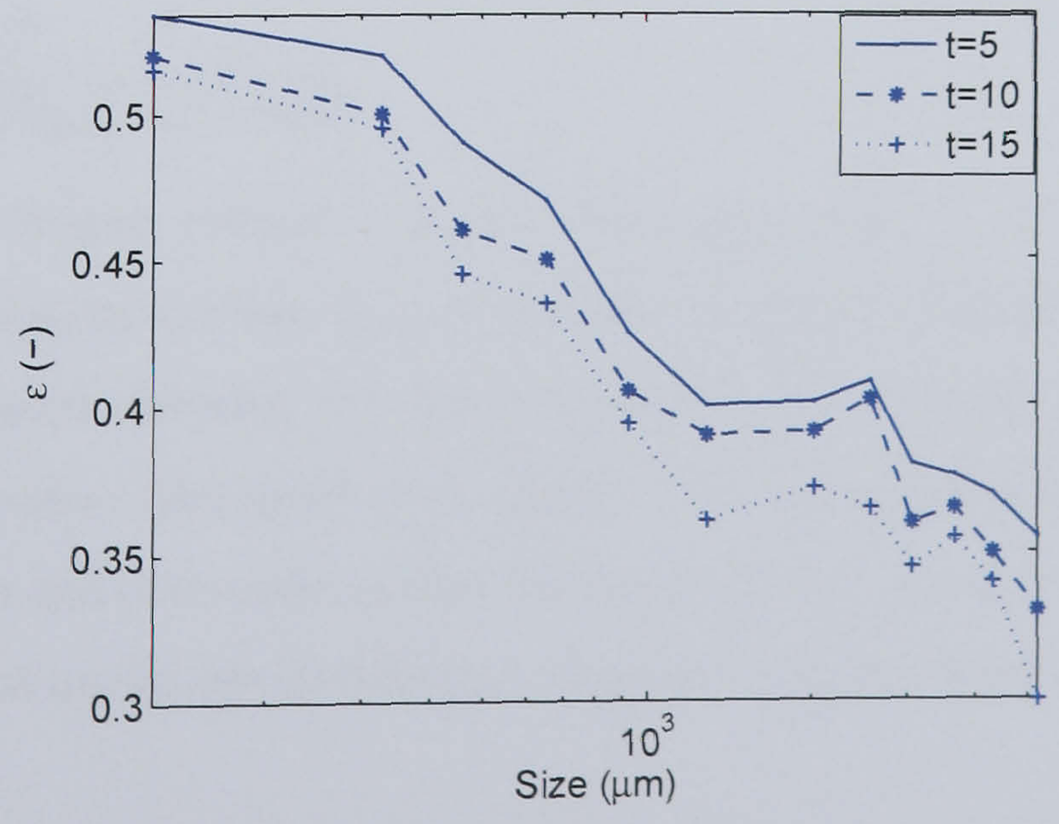

(c) binder-to-solids ratio $= 0.125$ and drum load $= 1.5\,kg$

Figure 3.17: Porosity distribution across size class.

3.3.6 Liquid Binder Distribution

The GSDs for the pre-mix (see Figure 3.18a) and point-wise (see Figure 3.18b) binder delivery methods are shown in Figure 3.18 for a target binder-to-solids ratio of 0.125 and drum load of 1.75 kg. It can be seen that granules are preferentially formed in the largest size classes of 7000μm to 11000μm. This is in contrast to the GSD of the optimal spray method (see Figure 3.13c) in which a broad distribution of granules of various sizes were observed, for the same binder-to-solids ratio and drum load. These results clearly depict the importance of the initial nuclei size distribution. These observations can be explained using the concepts of (a) the dimensional spray flux (Ψ_a) first proposed by Litster et al. (2001) and (b) the binder-to-solids ratio.

The dimensionless spray flux, Ψ_a is a measure of the binder density on the powder surface and is defined as

$$\Psi_a = \frac{3\dot{V}}{2\dot{A}d_d}, \tag{3.18}$$

where V is the volumetric spray rate, A is the area flux of powder passing through the spray zone and d_d is droplet diameter (Litster et al., 2001). In the optimal method, Ψ_a is calculated to be 0.16 which is fairly small such that each droplet is expected to form one nucleus. This is known as the droplet controlled regime. It must be noted that a low Ψ_a is a necessary but not a sufficient condition for drop controlled nucleation. The drop must also wet the powder and have a small penetration time. Drop penetration time is defined to be:

$$t_p = \frac{2V_0^2}{\pi^2\varepsilon^2 r_d^4 R_{pore}} \frac{\mu}{\gamma_{LV}\cos(\theta)} \tag{3.19}$$

where V_0 is the droplet volume, ϵ is the surface porosity, r_d is the radius of the drop footprint on the powder surface, R_{pore} is the effective pore radius on the basis of cylindrical pores, μ is the liquid viscosity, θ is the solid-liquid contact angle, and γ_{LV} is the liquid-vapour surface tension (Hapgood et al., 2002). The t_p for this system is estimated to be much less than 1 s and this confirms that nucleation occurs mostly in the droplet controlled regime. The initial nuclei size distribution goes on to impact the final GSD. In the droplet

controlled regime, the nuclei formed are sufficiently small to ensure a rich and varied GSD as observed in Figure 3.13c.

In the point-wise method, it can be seen that the area of the powder surface in the spray zone is comparatively less than that of the optimal spray method. Furthermore, the binder spray rate and the droplet size is larger. This results in an increased Ψ_a of 1.14. As Ψ_a increases, the probability of droplets overlapping to form larger agglomerate nuclei increases. If Ψ_a is sufficiently large, the surface of the bed will cake in the spray zone. In such an instance, mechanical forces in the drum are required to break the cake and disperse the binder. Having moved out of the droplet controlled regime, very large granules from wet clumps are formed very early in the process resulting in an almost instantaneous bimodal distribution. However, through time, the fines disappear almost completely. The implication is that the larger and wetter granules quickly densify, are continually surface wet and sweep up the unwet fines resulting in a layering phenomenon. The low shear forces inherent in the drum are unable to break up these large granules.

In the premix method, Ψ_a is approximately the same as that of the optimal spray method although the GSD profiles are significantly different. Subero-Couroyer et al. (2006) showed that above a certain binder-to-solids ratio, excessive granule growth is promoted and granules are prone to form chunks. In the premix method, due to the binder-to-solids ratio initially being higher than the optimal spray method (prior to the remaining one-third of the powder being added), granules in the largest size class are preferentially formed. Subsequent decrease in the binder-to-solids ratio (upon addition of the remaining powder) merely resulted in layering of the fine powder onto the existing large and wet granules.

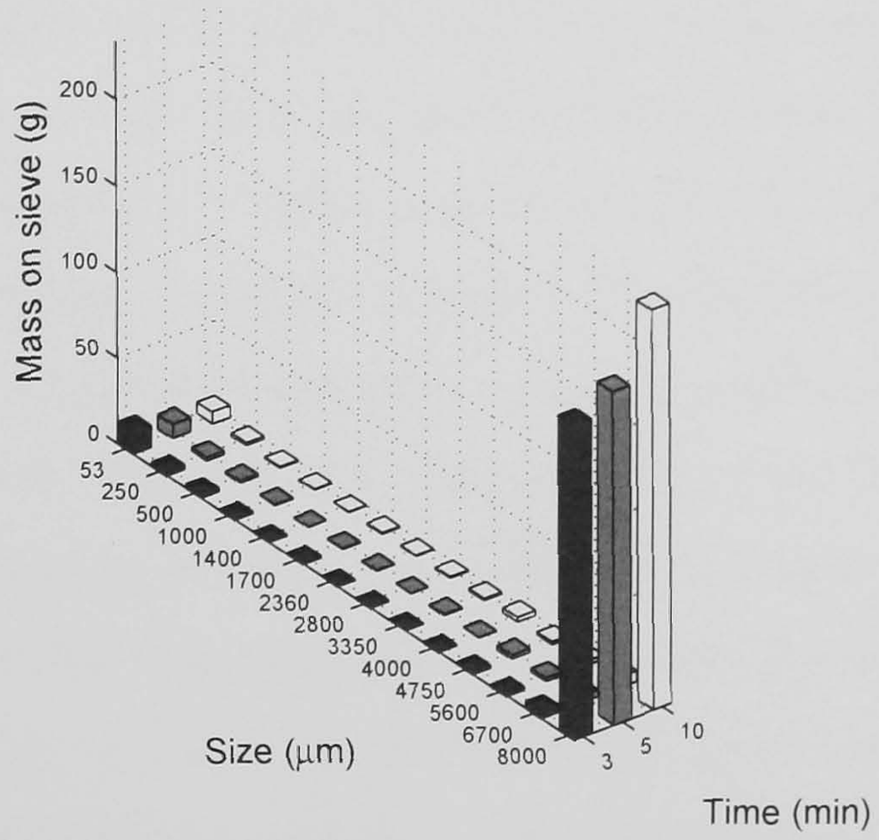

(a) Premix

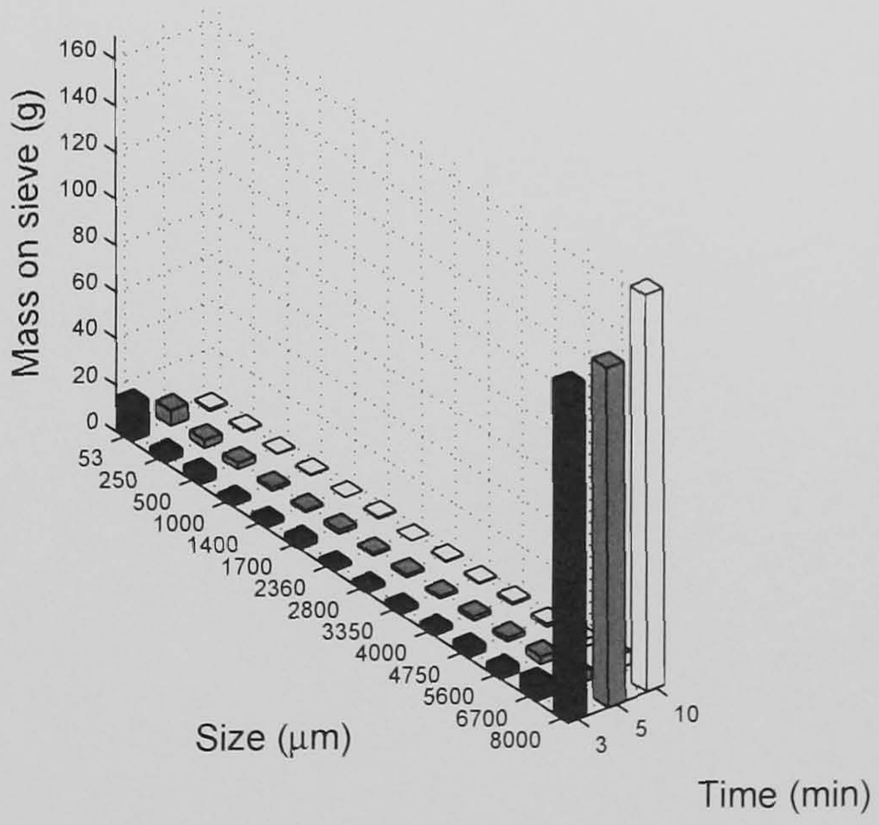

(b) Pointwise

Figure 3.18: GSD profiles for pre-mix and point-wise binder addition, for comparison against Figure 3.13c for the optimal binder addition method.

Figure 3.19 depicts the binder content distribution across size classes for the optimal spray, pre-mix and point-wise methods at $t = 5\,mins$, $t = 10\,mins$ and $t = 15\,mins$. For all three time instances, it can be seen that there is a much higher variation in the binder content for the premix and pointwise methods compared to the optimal spray method. This increase in heterogeneity of the binder distribution is attributed to sub-optimal binder delivery methods which are unable to distribute the binder evenly across the size classes. An interesting phenomenon is observed in the premix for all three time instances. The binder content in the smaller size classes are relatively higher than that in the larger classes. This is converse to the optimal spray method and other trends reported in the literature (Knight et al., 1998; Scott et al., 2000; Johansen and Schaefer, 2001; Reynolds et al., 2004). This highlights the effect of the layering phenomenon in contrast to coalescence, or the complete lack of both growth phenomena. Layering results in dry fine powder sticking to surface wet smaller granules resulting in a gradual decrease in the binder content as granule size increases. The higher binder content reported in the small size classes could be a result of small and wet granules that did not undergo layering or coalescence.

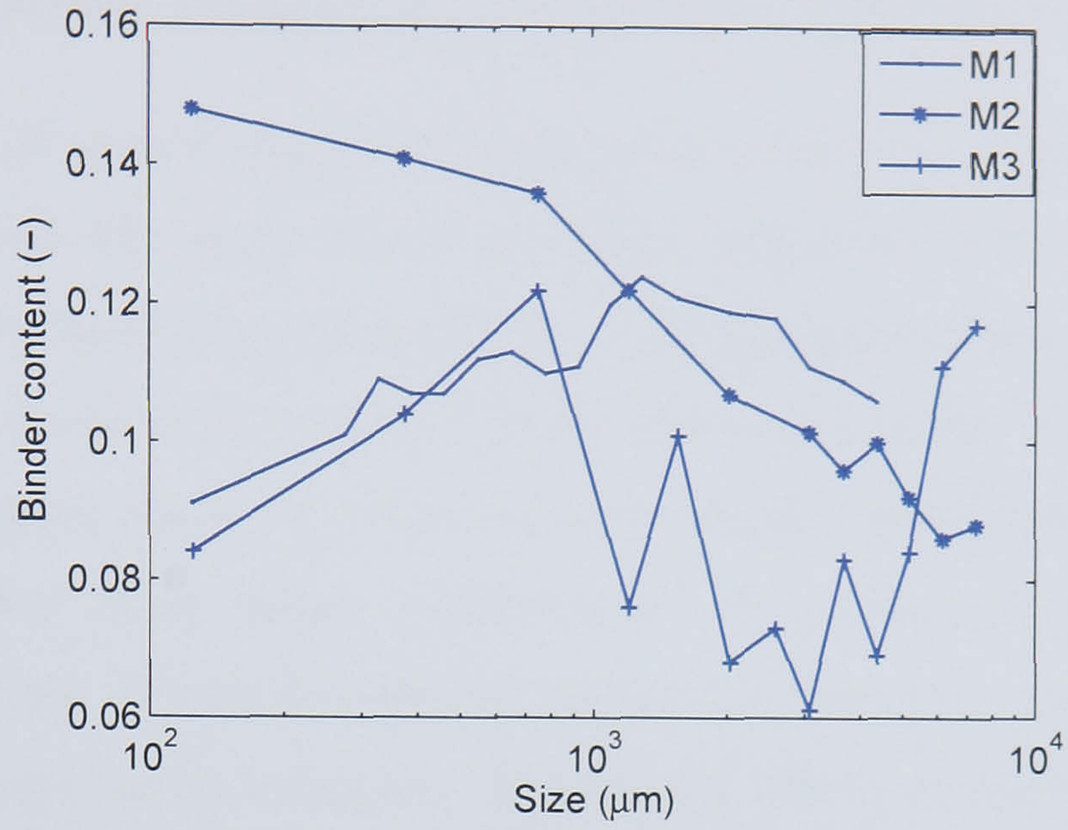

(a) Comparison of binder content distribution at $t = 5\,min$

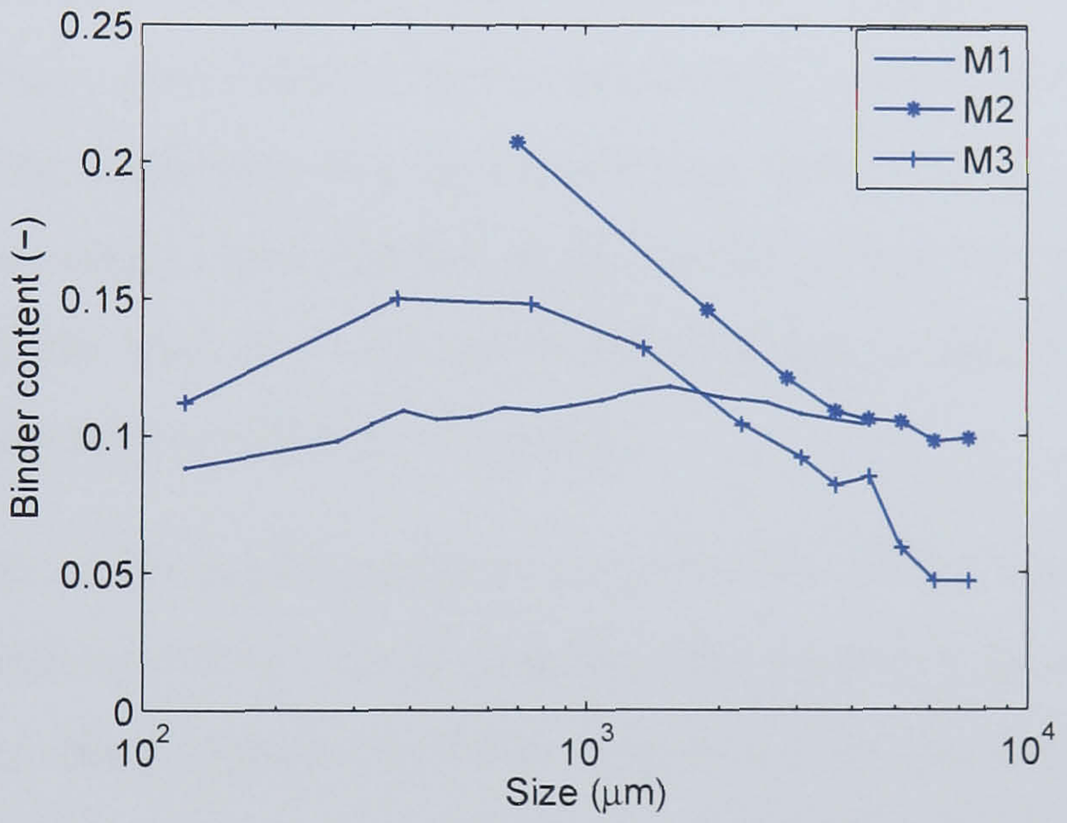

(b) Comparison of binder content distribution at $t = 10\,min$

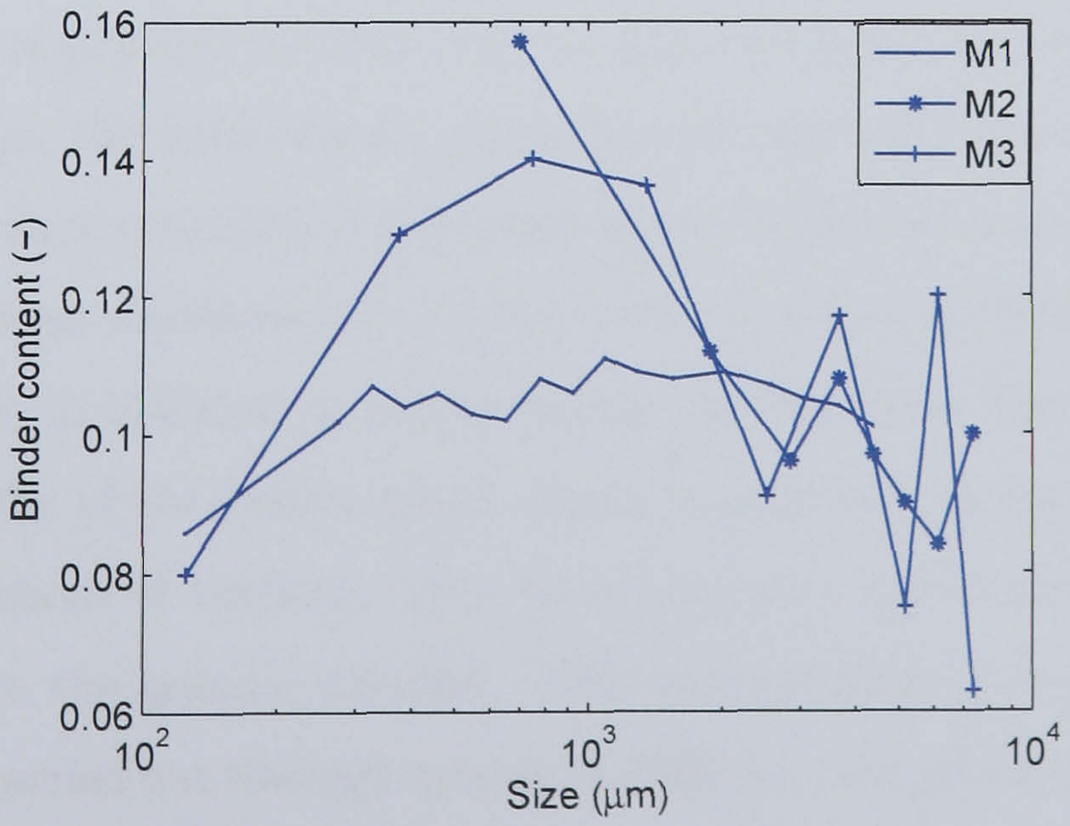

(c) Comparison of binder content distribution at $t = 15\,min$

Figure 3.19: Binder content distribution for optimal spray (M1), pre-mix (M2) and point-wise (M3) methods.

3.4 Conceptual Analysis of a Control Structure Formulation

The strong effect of several important formulation properties on the granulation mechanisms were evident in this study. These properties include the solid properties and powder characteristics, the liquid properties, and the solid-liquid properties. The results illustrate the disturbance character of several of these properties in the granulation process, although some of these could be exploited for feedback control purposes. Secondly, the equally strong effect of operating conditions on the granulation mechanisms were also evident in this study. These include the binder-to-solids ratio, binder spray times and methods, and binder spray locations. The strong effects of these operating conditions were particularly manifested in the liquid "mal-distribution" studies. The pre-mix and point-wise methods symbolise cases where optimal binder distribution is not obtained. In this study coalescence, consolidation and to some extent layering were predominant. In the next step, operating conditions may be chosen such that breakage is predominant. This would enhance the overall controllability of the process to make it more amenable to feedback control along the lines of a segregated and hierarchical control approach undertaken in the work of Immanuel and Doyle III (2003b).

Figure 3.20 depicts an integrated systems representation of the various formulation properties and the operating and/or design variables that could influence both the granulation process and the resultant granule attributes. Figure 3.21 is a conceptual representation of an overarching structure of a feedback control configuration for the granulation process. Powder feed rate, nozzle position, multiple nozzles, binder flow rate and the mixing rate are all important manipulations that may be adjusted to ensure target attributes are attained. In addition, the liquid binder properties can also be utilised for feedback control purposes, subject to practicality of implementation. Both the viscosity and surface tension effects have also been mentioned as playing a role in some respects towards the strength of granules. Thus, in addition to manipulating the flow rates individually through each nozzle, the viscosity of the binder could also be a manipulated variable for GSD control (through combinations of binders), while simultaneously paying attention to the effect of binder viscosity on the granule strength. This manipulation of the viscosity and surface tension could be carried out through mixing of different concentrations of binder solutions.

Depending upon the operating conditions, it is entirely possible (as shown in this chapter) that there exists a clear shift in granulation mechanisms (e.g.coalescence to layering, droplet-controlled nucleation to lump formation, etc.). This in turn exemplifies the extreme sensitivity in the process, and the need for advanced model-based control. The model should of necessity take a multi-scale structure, including the effects of the important formulation material properties in addition to those of the operating variables. It is also confirmed that a three-dimensional population balance equation is the necessary basic structure for batch granulation, so as to account for the heterogeneity in particle size, binder content and porosity. This population balance model structure is indeed well-suited also for the incorporation of multi-scale information through appropriate mechanistic kernels for the particle rate processes (Immanuel and Doyle III, 2005; Poon et al., 2008).

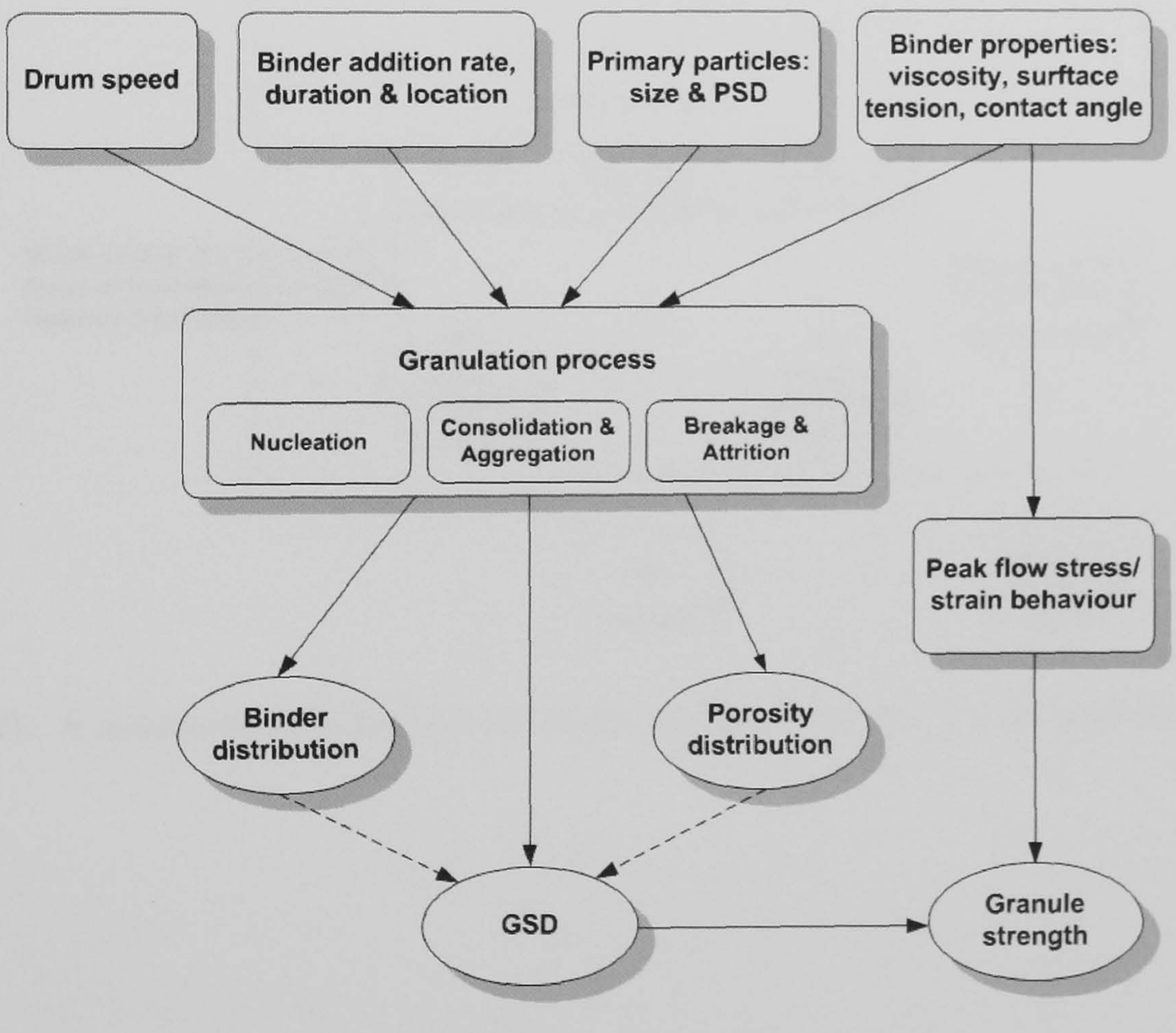

Figure 3.20: A comprehensive systems-wide representation of the granulation process.

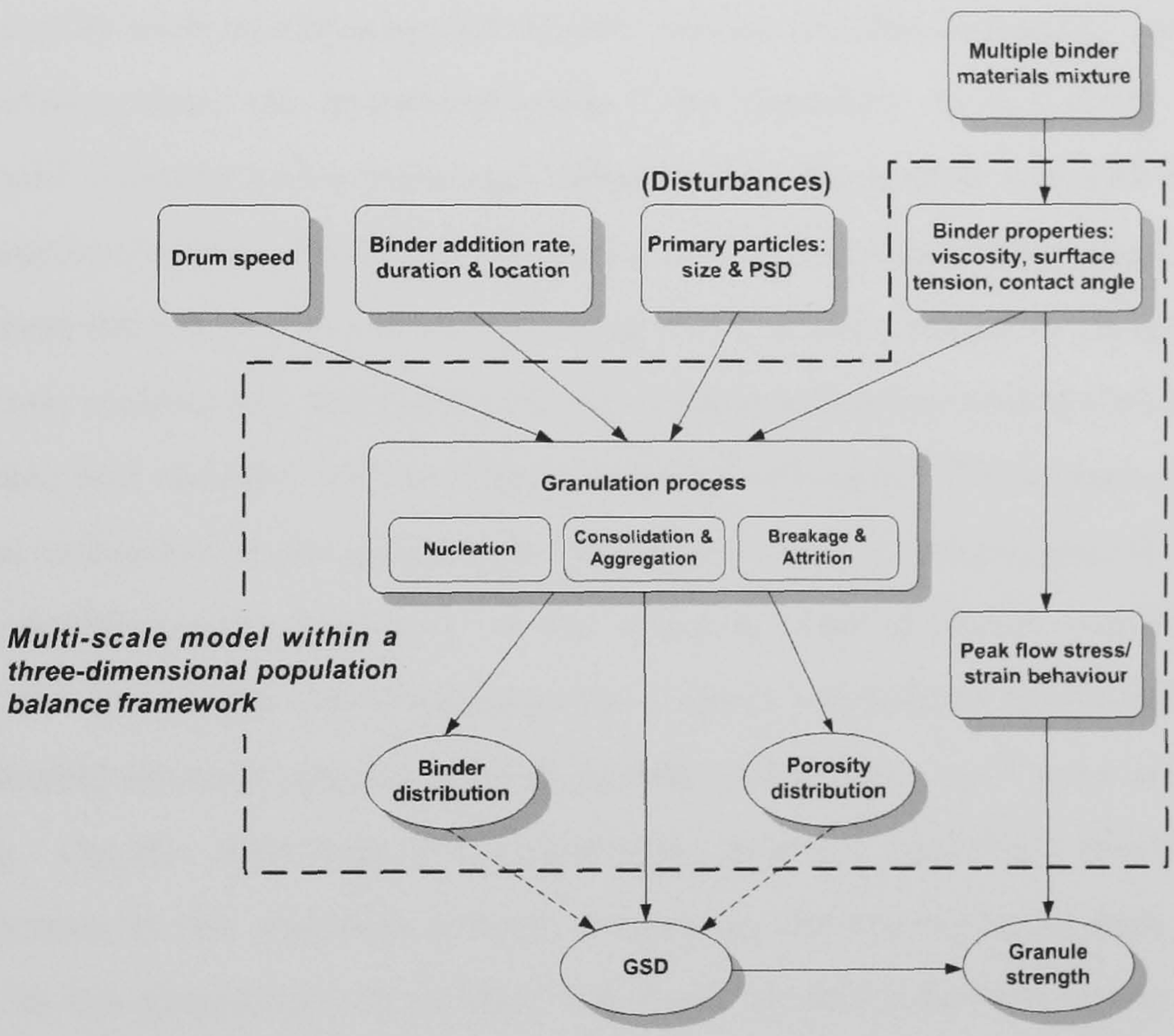

Figure 3.21: A schematic of a proposed control configuration for the granulation process.

3.5 Conclusions

In this study, for the first time, three granule attributes (i.e.. size. binder content and porosity) were characterised for batch granulation using spray-on liquid binder. This is an extension to typical data gathered (e.g. size and either binder content or porosity) for such systems. Various formulation properties and operating conditions were examined in detail. Powder properties such as powder size, powder density and particle shape play an important role in the final size distribution as well as the strength of the granules formed. Liquid properties such as viscosity and surface tension are also important, and further. a trade-off between these two properties needs to be identified. In this study. it was seen that the liquid viscosity had a prominent influence over the granule strength compared to the liquid surface tension. Powder-liquid properties such as the contact angle are vital as well, and these determine the extent of wetting which in turn relates to the probability of nucleation and coalescence. Dynamic yield stress measurements revealed that both binder-to-solids ratio and viscosity had an effect on granule strength. These measurements also provided an indication of the mechanism that would likely dominate granule growth (i.e. layering, consolidation, coalescence) for the different cases of binder-to-solids ratio and viscosities. For instance at low strain rates the granules will exhibit brittle behaviour with poor mechanical strength suggesting that growth under these conditions are dominated by layering. On the other side of the spectrum, granules exhibiting plastic behaviour with coalescence as the prevalent growth mechanism corresponding to high strain rates conditions in the granulator. It is thus important to determine the strain rate (drum speed) of relevance inside the granulator in order to effectively model the granulation behaviour (Iveson et al., 2003).

The process dynamics of Calcite/PVOH-H_2O granulation was observed for different binder-to-solids ratios and drum load. The GSDs indicated a rich distribution over the different size ranges, and showed that size is very sensitive to the binder-to-solids ratio and to a lesser extent on the drum load. Porosity was also measured (for different binder-to-solids ratio and drum load) across the various size ranges depicting the effects of consolidation and porosity variation across the size classes. Two cases of liquid binder mal-distribution were compared with a case of optimal binder distribution. It was clearly seen in the

GSD and binder content profiles that sub-optimal methods of binder delivery result in very different size and binder content distributions. This partly indicates a shift in the predominant granulation mechanisms of nucleation and growth (e.g. from coalescence to layering, and a shift in nucleation regime). Overall, the binder-to-solids ratio and drum load not only influenced the GSD but also the binder content and porosity distributions. This clearly illustrates the limitations of one-dimensional population balance models that consider only size. Hence, multi-dimensional population balance models that account for binder content and porosity variations are required to adequately model the granulation process.

An integrated view of the granulation process, taking into consideration the granulator operating variables as well as the feed properties, has provided indications towards an overarching configuration for feedback control. It should be mentioned that this overarching configuration is compatible with the recent Process Analytical Technologies (PAT) initiatives (Barrett et al., 2005). In view of this configuration, it is seen that a multi-scale model that accounts for both the material properties and the operating conditions as inputs that determine the granulation mechanisms and the granule end-use properties would be a crucial aid for process control. This could be elegantly formulated within the multi-dimensional population balance framework, thereby also accounting for the heterogeneity in the granule traits. Such modelling and control studies are underway in chapters 4, 5, 6 and 7 of this thesis.

Chapter 4

Model Validation Studies in Batch Drum Granulation

In this chapter, a dynamic model is presented for the granulation process, employing a three-dimensional population balance framework. As a first attempt to account for the multi-scale character of the process, the nucleation and aggregation kernels used in the population balance model are derived using mechanistic representations of the underlying particle physics such as wetting kinetics and energy dissipation effects. Thus, the fundamental properties of the powder and the liquid were used as parameters in the model to predict the granulator dynamics and granule properties. The population balance model is validated against experimental data from a Calcite/PVOH-H_2O recipe obtained using a lab-scale drum granulator for granule size, fractional binder content and porosity. A reasonably good agreement between experimental and simulation results were obtained for the granule size distribution under different experimental conditions. In addition, accurate model predictions were made for the evolution of the average properties (i.e., size, fractional binder content and porosity) for various operating conditions.

---

[1]Part of this chapter is based on, J. M. -H. Poon, R. Ramachandran, C. F. W. Sanders, T. Glaser, C. D. Immanuel, F. J. Doyle III, J. D. Litster, F. Stepanek, F. Y. Wang and I. T. Cameron, "Experimental Validation Studies in Batch Drum Granulation", Chemical Engineering Science, 2008, *In Press*.

4.1 Introduction and Objectives

Granulation processes have been ubiquitous in the industry for many years, with significant research undertaken to gain insight into the underlying phenomena occurring during the process. However, industrial granulation processes are by-and-large operated in a highly inefficient manner with large recycle ratios within the process (3-4:1, recycle/product) (Iveson et al., 2001; Mort et al., 2001; Wang and Cameron, 2002). This motivates the need to provide an integrated process model, which will be a crucial aid for a more efficient operation of the process (Litster, 2003; Bardin et al., 2004; Knight, 2004; Mort, 2005). A comprehensive model of the process will enable an analysis of the system dynamics and the formulation of a suitable control strategy, which will in turn contribute to a more efficient operation of the process (Litster et al., 2001; Knight, 2004). This model-based approach is substantiated by the fact that plant-level experiments can be labour and capital intensive, making an experiment-based approach less suitable for investigating all facets of this complex dynamic system. With current improvements in computer technology, computer simulations are becoming more amenable and provide a greater rationale for developing models that would facilitate the design of granulation processes (Heinrich et al., 2003).

The granulation process is an example of a multi-scale problem and the multi-scale nature of this process was summarised in Figure 3.21 of Chapter 3. Micro-scale phenomena such as the wetting kinetics and energy dissipation effects (which are reflected in binder addition and mixing rates) directly influence the meso-scale phenomena (nucleation, aggregation, consolidation and breakage), which in turn directly determine the macroscopic properties such as granule size. The micro-scale properties themselves are influenced by fundamental material properties, both of the solid and the liquid. Detailed experimentation was performed in order to verify the link between the fundamental properties and operating variables on the one hand and the end-granule properties on the other hand (see Chapter 3). This was carried out by performing batch granulation experiments for a Calcite/Polyvinyl alcohol in water (Calcite/PVOH-H_2O) recipe. Three-dimensional data of granule distribution across size, binder content and porosity were measured. These experimental studies lend clear support for the development of multi-scale process models. Thus,

an integrated framework is needed. to accommodate models of different length and time scales pertaining to the various sub-processes and to account for fundamental material properties. The models should capture the dynamics depicted in Figure 3.21, traversing from fundamental material properties and operating conditions, to the granulation process mechanisms and dynamics, to the granule properties (granule size distribution, binder content and porosity). The multi-scale modelling approach adopted is based on the transformation of the micro (particle-level) model such that it may be used within a macro (process-level) model. Ingram et al. (2004) discuss various other multi-scale integration frameworks that link micro-scale models with macro-scale models within a unified framework.

4.2 Proposed Model with Mechanistic Kernels

The present study is restricted to modelling of the phenomena of nucleation, aggregation and consolidation, and the population balance equation reduces to the following:

$$\frac{\partial}{\partial t}F(s,l,g,t) + \frac{\partial}{\partial g}\left(F(s,l,g,t)\frac{dg}{dt}\right) = \Re_{nuc} + \Re_{aggre}. \tag{4.1}$$

The multi-scale link to the fundamental material properties appears in the form of kernels that are used to describe the particle rate processes. In previous studies, the implementation of mechanistic kernels for both the aggregation and nucleation phenomena has been presented (Immanuel and Doyle III, 2005; Poon et al., 2008). However, a quantitative experimental validation of the model predictions was not presented. The aim of this study is to extend on the previous works, by providing experimental validation of the integrated three-dimensional population balance model employing mechanistic representations for the aggregation and nucleation kernels, and an empirical exponential decay relation representing granule consolidation (Iveson et al., 1996). The porosity of granules is defined in Equation 4.2 and the consolidation first order model is shown in Equation 4.3. During the consolidation process, the volume of solid and liquid remain unchanged i.e., $\frac{ds}{dt} = \frac{dl}{dt} = 0$. Substituting Equation 4.2 into Equation 4.3 gives a formal expression explicitly in terms of the three independent internal coordinates, which can then be used in Equation 4.1.

$$\varepsilon = \frac{l+g}{s+l+g} \tag{4.2}$$

$$\frac{d\varepsilon}{dt} = -c\left(\varepsilon - \varepsilon_{min}\right) \tag{4.3}$$

$$\frac{dg}{dt} = -c\frac{s+l+g}{s(1-\varepsilon_{min})}\left[l - \frac{\varepsilon_{min}s}{1-\varepsilon_{min}} + g\right] \tag{4.4}$$

Here ε_{min} is the minimum porosity of the granules and c is the compaction rate constant. A brief description of the mechanistic kernels used in this study will be provided next. Further details pertaining to the kernel development may be found elsewhere (Ennis et al., 1991; Liu et al., 2000; Immanuel and Doyle III, 2005; Poon et al., 2008).

4.2.1 Nucleation Model

At the onset of granulation, the nucleation process is considered to be crucial as the initial nuclei size distribution obtained will influence the resulting granule size distribution. Nucleation occurs at the first instant when the fine powder makes its first contact with the liquid binder. Nuclei formation occurs when the binder droplet penetrates the powder mass and nucleates particles in its immediate vicinity to form a granule nucleus. This process is influenced by the ability of the liquid binder to spread over the solid as determined by the spreading coefficient, which indicates whether this spreading process is energetically favourable or not. This spreading coefficient is related to the works of adhesion and cohesion of solid and liquid used in the granulation recipe (see Equation 4.6). Furthermore, the nature of the nucleation regime (e.g., drop controlled, intermediate, mechanical dispersion; see Hapgood (2000)) will also be dependent on the operating conditions of the granulator, including the spray rate of the liquid binder and the mixing intensity. These dependencies are captured by the simple, first version of the nucleation kernel given in Equation 4.5 (Poon et al., 2008):

$$k_{nuc}(s_{nuc}, l_{nuc}, g_{nuc}) = A_0 Q e^{\lambda/RT}. \tag{4.5}$$

Here s_{nuc}, l_{nuc} and g_{nuc} are the nuclei particle traits representing the volume of solid, the volume of liquid and the volume of gas in the nuclei particle, A_0 is an adjustable parameter.

Q is the liquid binder spray rate, λ is the spreading coefficient. R is the ideal gas constant and T is the operating temperature of the granulator. The spreading coefficient is defined in Equation 4.6 for two possible scenarios. The first case considers the solid particles to be of equivalent size to the binder droplet whilst the other considers the binder droplet to be significantly larger than the solid particles.

$$\lambda = \begin{cases} W_A - W_{CL} \ , \ D_d \approx D_p, \\ W_A - W_{CS} \ , \ D_d \gg D_p. \end{cases} \tag{4.6}$$

Here, W_A is the work of adhesion, D_p is the diameter of the particle, D_d is the diameter of the binder droplet, W_{CS} and W_{CL} are the works of cohesion for a solid and liquid respectively. Both the works of cohesion are dependent on the respective surface energies of the solid and binder used in the formulation.

The volume of the nuclei V_n is given by Equation 4.7, where V_0 is the volume of a droplet, V_{up} is the volume of the portion of the droplet that is unavailable for particle nucleation (see Figure 4.1), l_{sat} is the liquid saturation level of the nuclei, ε_{eff} is the effective porosity of the nucleus, $V_{p,l}$ is the average liquid volume of the primary particles and $V_{p,s}$ is the average solid volume of the primary particles.

$$V_n = \frac{V_0 - V_{up}}{l_{sat}\,\varepsilon_{eff} - (1 - \varepsilon_{eff})\frac{V_{p,l}}{V_{p,s}}}. \tag{4.7}$$

The parameter V_{up} depends upon the operating conditions, and in particular upon the time available for the droplets to penetrate into the bed. The time required to allow for complete drop penetration can be determined using the drop penetration model developed by Hapgood et al. (2002). The theoretical study performed by Hapgood et al. (2002) also allows for the determination of the volume of binder that remains at the surface (unpenetrated). The individual volumes of the solid, liquid and gas in the nucleus (s_{nuc}, l_{nuc} and g_{nuc}; in Equation 4.5) can be computed from the total volume of the nucleus V_n, e.g., $s_{nuc} = V_n\,(1 - \varepsilon_{eff})$ (see Poon et al. (2008) for derivation and details).

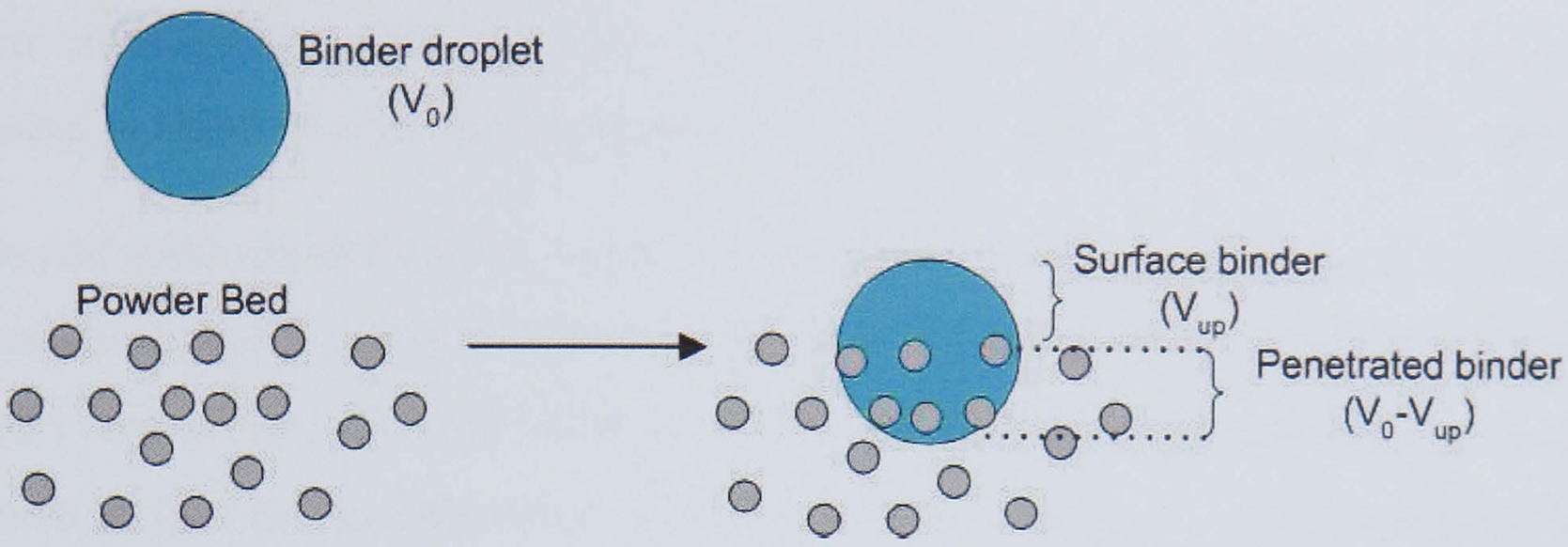

Figure 4.1: Schematic of the nucleation mechanism.

4.2.2 Aggregation Model

An important mechanism during granulation is the aggregation phenomenon. The aggregation term is comprised of two terms, the formation and depletion of particles as shown in Equations 2.11 - 2.13. As previously mentioned the aggregation kernel represents an important parameter for the growth phenomenon, as it is a measure of the rate at which two particles will successfully aggregate forming a single larger particulate entity. In the case of Equations 2.12 and 2.13, it is a measure of success for particles p_1 and p_2 with characteristics (s', l', g') and $(s - s', l - l', g - g')$, respectively, coalescing to form a new particle with characteristics (s, l, g).

Previous attempts to represent the aggregation kernel in the form of empirical kernels, with particle size as the main contributing factor predominating aggregation, have been used with varying degrees of success, coupled with parameter fitting to experiments. However, it has been long recognised that collision between particles resulting in successful coalescence is dependent upon other factors in addition to the sizes of the participating particles, such as the binder content of the particles, binder viscosity, the initial distribution of the seed particles (primary particles). In addition, equipment level parameters such as the rate of mixing, binder flow rate, powder flux under the spray zone and the geometry of the granulator will impart a significant influence with respect to the granule growth mechanisms. An overview of mechanistic kernel for aggregation is introduced, which is based on the previous works of Ennis et al. (1991) and Liu et al. (2000). Immanuel and Doyle III (2003a) applied this micro-level model for aggregation from an energy dissipation perspective, by computing the net attractive potentials (based on energies) between various

particle combinations with each other. This approach was later adopted for granulation modelling in three-dimensional population balances (Immanuel and Doyle III, 2005).

The model used prescribes two conditions in which coalescence can occur and these are designated as type I and type II coalescence and is schematically depicted in Figure 4.2. In type I coalescence, the initial kinetic energy of the approaching particles are completely overcome by the viscous dissipation in the liquid layer, leading to coalescence prior to their surfaces making direct contact with each other. The relative velocity of the particles as a function of their separation distance is defined in Equation 4.8.

$$\begin{aligned} u(h) &= u_0, \quad h > h_0 \\ u(h) &= u_0 \left[1 - \frac{1}{St_v} \ln\left(\frac{h_0}{h}\right)\right], \quad h < h_0 \end{aligned} \tag{4.8}$$

Where, u_0 is the initial approach velocity of the particles (based on the mixing intensity within the granulator), h is the separation distance between the colliding particles, u represents the relative velocity of the particles as they approach each other and is a function of the separation distance between the two particles, h_0 represents the thickness of the liquid binder layer that forms around each particle. The net attractive potential (ψ) between the particles is calculated using Equation 4.9, based on the relative velocity of the particles as determined from Equation 4.8.

$$\psi\left(p_1, p_2, h\right) = \frac{1}{2} m (2u(h))^2. \tag{4.9}$$

Type II coalescence involves two sequential stages prior to coalescence - the forward path and the reverse path (see Figure 4.2). The path with the higher energetics is taken as the rate-determining step. The forward path is represented by the approach stage, with the initial kinetic energy being dissipated by the viscous liquid layer. The elastic energy that is released upon particle deformation following collision leads to the rebound stage (reverse path). The energy lost during the impact and particle deformation may be calculated using Equation 4.10. At this particular instant, the particles will either coalesce if the

elastic energy is fully dissipated by viscous dissipation, or particle separation (rebound) will occur. The velocity of the particles corresponding to the retraction phase is given in Equation 4.11 with δ'' representing the permanent plastic deformation of the particles defined in Equation 4.12. The net attractive potentials corresponding to the forward path and the reverse path are given in Equations 4.13 and 4.14, respectively.

$$E_c = \frac{1}{2} m (2u_1)^2. \tag{4.10}$$

$$\begin{aligned} u'(h) = u_2 - \frac{3\pi\mu\tilde{\mathrm{D}}^2}{16\tilde{\mathrm{m}}h^2} \Bigg[(\delta'')^2 \left(\frac{h^2}{h_a^2} - 1 \right) + 2h\delta'' \left(\frac{h}{h_a} - 1 \right) \\ + 2h^2 \ln \left(\frac{h}{h_a} \right) \Bigg], \quad 0 < h < h_0 \\ u'(h) = u'(h_0), \quad h > h_0 \end{aligned} \tag{4.11}$$

$$\begin{aligned} \delta'' = \left(\frac{8}{3\pi} \right)^{\frac{1}{2}} (St_{def})^{\frac{1}{2}} \tilde{\mathrm{D}} \left[1 - \frac{1}{St_v} \ln \left(\frac{h_0}{h_a} \right) \right] \left[1 - 7.36 \frac{Y_d}{E^*} (St_{def})^{-\frac{1}{4}} \right. \\ \left. \times \left[1 - \frac{1}{St_v} \ln \left(\frac{h_0}{h_a} \right) \right]^{-\frac{1}{2}} \right] \end{aligned} \tag{4.12}$$

$$\psi_{forward}(p_1, p_2, h) = \frac{1}{2} m \left[2u(h) \right]^2 - E_c \tag{4.13}$$

$$\psi_{reverse}(p_1, p_2, h) = -\frac{1}{2} m (2u')^2 \tag{4.14}$$

Thus, the kinetic energy of the particles, suitably corrected for viscous dissipation, constitutes the major factor in modelling the aggregation phenomenon. These steady state forces are then employed for the dynamic calculation in the Smoluchowski formulation (Immanuel and Doyle III, 2005), drawing a parallel with the DVLO theory (transition state theory that is well established in the emulsion polymerisation literature Immanuel

and Doyle III (2003a). The Fuch's stability ratio for type I coalescence is given by Equation 4.15.

$$W(p_1,p_2) = (r_1+r_2)\int_{D=(r_1+r_2)}^{\infty} \frac{\exp\left(\frac{\psi(p_1,p_2,D)}{kT}\right)}{D^2} d(D) \tag{4.15}$$

Where, ψ is the net attractive potential (calculated from the kinetic energies of the particles corrected for viscous dissipation), r_i is the radius of particle p_i. For type II coalescence, there are two definitions for the Fuch stability ratio, corresponding to the forward path and the reverse path, with the higher energetic pathway as the rate-limiting step. and is given in Equation 4.16. Here, the $\psi_{forward}$ is the net attractive potential driving the approach phase and $\psi_{reverse}$ is the net attractive potential driving the retraction phase.

$$\frac{W(p_1,p_2)}{r_1+r_2} = max\left(\int_{D=(r_1+r_2)}^{\infty} \frac{\exp\left(\frac{-\psi_{forward}(p_1,p_2,D-r_1-r_2)}{kT}\right)}{D^2} d(D),\right.$$
$$\left.\int_{D=(r_1+r_2)}^{\infty} \frac{\exp\left(\frac{-\psi_{reverse}(p_1,p_2,D-r_1-r_2)}{kT}\right)}{D^2} d(D)\right) \tag{4.16}$$

The energy dissipation calculations for type I and type II coalescence and the modelling of the steady state forces at the particle level are subsequently used in the calculation of the aggregation kernel using the Smoluchowski formulation given in Equation (4.17). Here, k is the Boltzmann constant, T is the temperature and c_1 is an adjustable constant accounting for errors arising from model lumping assumptions.

$$\beta(p_1,p_2) = c_1 \frac{4\pi u_0 (r_1+r_2)^2}{W} \tag{4.17}$$

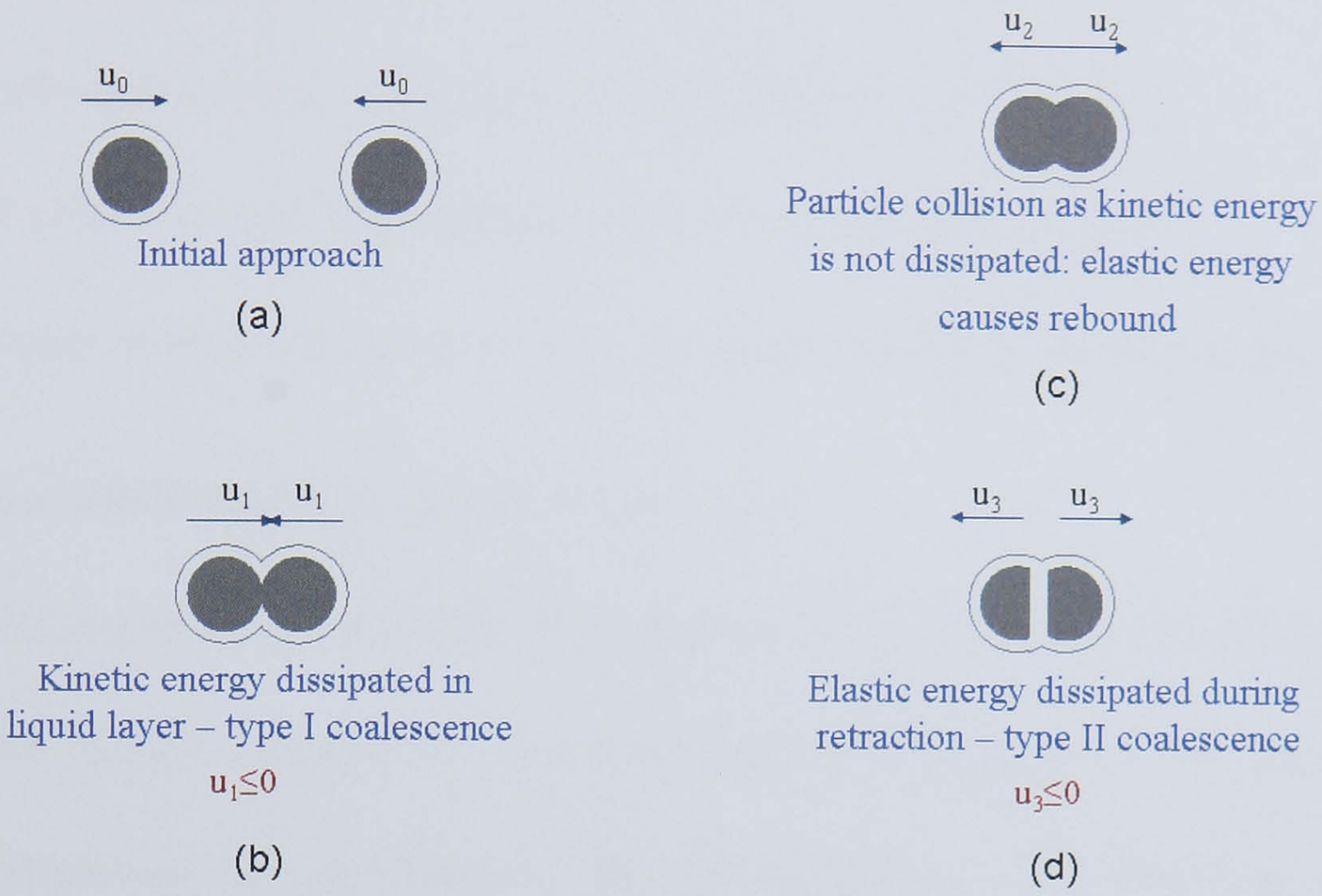

Figure 4.2: Schematic representation of the two types of aggregation phenomena reproduced from Immanuel and Doyle III (2005). u_0 is the approach velocity at infinite separation; u_1 is the velocity at impact; u_2 is the initial rebound velocity; u_3 is the velocity at the separation of binder layers.

4.2.3 Model Inputs under Mechanistic Kernels

By virtue of the mechanistic description of the granulation process, the model now incorporates the material properties of the solid and binder and also the process operating conditions in an explicit manner. The incorporation of the former would not be easily possible from an empirical modelling approach. In the following, model inputs pertaining to the nucleation kernel and the aggregation kernel are specified. These model inputs are classified into (i) fundamental material properties, (ii) process manipulations and (iii) adjustable parameters.

Fundamental material properties (either measured in this study or obtained from literature):

- Binder viscosity (μ) - determined through measurements.

- Liquid binder surface tension (γ) - obtained from literature.
- Solid-liquid contact angle (θ) - determined through measurements.
- Particle density (ρ_s) - determined through measurements.
- Solid yield strength (Y_d) - determined through measurements.
- Diameter of primary particles (d) - determined through measurements.

Process manipulations(measured in this study):

- Liquid binder spray rate (Q) - set according to experimental conditions.
- Binder droplet volume (V_0) - set according to experimental conditions.
- Initial particle size distribution - determined through measurements.

More-Sensitive Adjustable parameters:

- Consolidation frequency factor (c) in Eq.(4.4).
- Aggregation kernel frequency factor (c_1) in Eq.(**??**).
- Adjustable constant for the nucleation kernel (A_0) in Eq.(4.5).
- Granule size upper limit for aggregation (D_{upper}).

Less-Sensitive Adjustable parameters:

- Effective porosity of the bed mass (ε_{eff}).
- Critical liquid content for surface film formation (l_{min}).
- Mixing rate, which is reflected by the relative collision velocity of the particles in the granulator (u_0).
- Volume of unpenetrated binder (V_{up}).
- Height of particle surface asperity (h_a).

4.2.4 Numerical Solution and Parallel Programming

In solving the three-dimensional population balance model, the hierarchical solution strategy described in Chapter 2 was utilised. In addition, a parallel programming framework was implemented to aid the solution of the model by reducing computational time. These results are presented in the following sections.

4.2.4.1 LAM/MPI

Message passing interface (MPI) is a communications protocol. It is the de facto standard for communication among different nodes running a parallel program in a distributed memory system. MPI implementation consists of a library of routines from Fortran, C or C++. LAM (local area multicomputing) is an MPI programming environment and development system for many computers on a network. With LAM/MPI, a dedicated computer cluster can act as a single parallel computing resource.

4.2.4.2 Results

The hierarchical two-tier technique has proven to be an efficient solution technique in solving one-dimensional population balance equations (Immanuel and Doyle III, 2003a). For the multi-dimensional case, the solution technique is also able to achieve similar levels of efficiency and accuracy as shown by (Immanuel and Doyle III, 2005; Pinto et al., 2007; Pinto, 2008; Pinto et al., 2008). However, due to the exponential increase in the number of finite elements (associated with multiple dimensions) execution time for a typical simulation (1 hour granulation time and grid size of 35 by 15 by 12 bins) is approximately 294 minutes.

In implementing the parallel programming framework, part of the population balance equation needs to be split amongst the different processors. The bulk of the computational time results from solving the triple integrals present in Equation 2.12 in chapter 2. In a single-processor job, the triple integrals present in the population balance equation (see Equation 2.12) are solved for by entirely one processor. This entails discretising the particle population into sub-populations and the population balance is formulated for each of the

semi-lumped sub-populations. For a typical simulation, this would mean integration of the PBE over the domain of the sub-populations, totalling approximately 6300 finite volumes (i.e., 35 by 15 by 12 bins). In a multi-processor job, the computational burden is split among the different N processors whereby each processor integrates the PBE over $\frac{6300}{N}$ finite volumes, where N is the total number of processors.

Table 4.1 presents the computational time and parallel speedup (S(N)) of single- and multi-processor jobs. Parallel speedup is defined to be the ratio of the rate at which work is done (the power) when a job is run on N processors to the rate at which it is done by just 1 processor. Let T(N) be the time required to complete the task on N processors. The speedup is the ratio

$$S(N) = \frac{T(1)}{T(N)} \tag{4.18}$$

Table 4.1: Parallel processing times/speeds.

Number of processors	**Time (min)**	**Parallel Speedup (-)**
1	294	1.00
2	210	1.40
4	98	3.00
8	60	4.90
10	57	5.16

Ideally, a computational job that is split up among N processors would be completed in $\frac{1}{N}$ of the time, leading to an N-fold increase in power. However, any given piece of parallelised work to be done will contain parts of the work that must be done serially, one task after another, by a single processor. This part does not run any faster on a parallel collection of processors. Only the part that can be parallelised runs as much as N-fold faster. Furthermore, amongst two or more processors that perform different parts of the same task (parallelising the task), the slowest processor among them is the rate determining step. This means that the fastest processor has to wait for the slowest processor before the data is compiled as a whole, prior to moving on to the next task. Therefore, it is highly impossible that any parallel job performs N times faster using N processors. Results in Table 4.1 show that this is indeed true and with 10 processors. a

parallel speedup of 5.16 is achieved. However, the overall speedup 5.16 is still a substantial reduction in computational time and this could prove to be a useful feature. It must be noted that although parallel processing has been shown to be efficient, the data resulting from it should still be compared with that of the single processor. This is to ensure that there are no numerical inconsistencies associated with parallel processing. From Figures 4.3a and b, we can see that the profiles generated from each of the N processors are congruent with one another. Checking the bulk variables such as total particle density and average particle volume, lends credence that no significant numerical errors arise due to parallel processing.

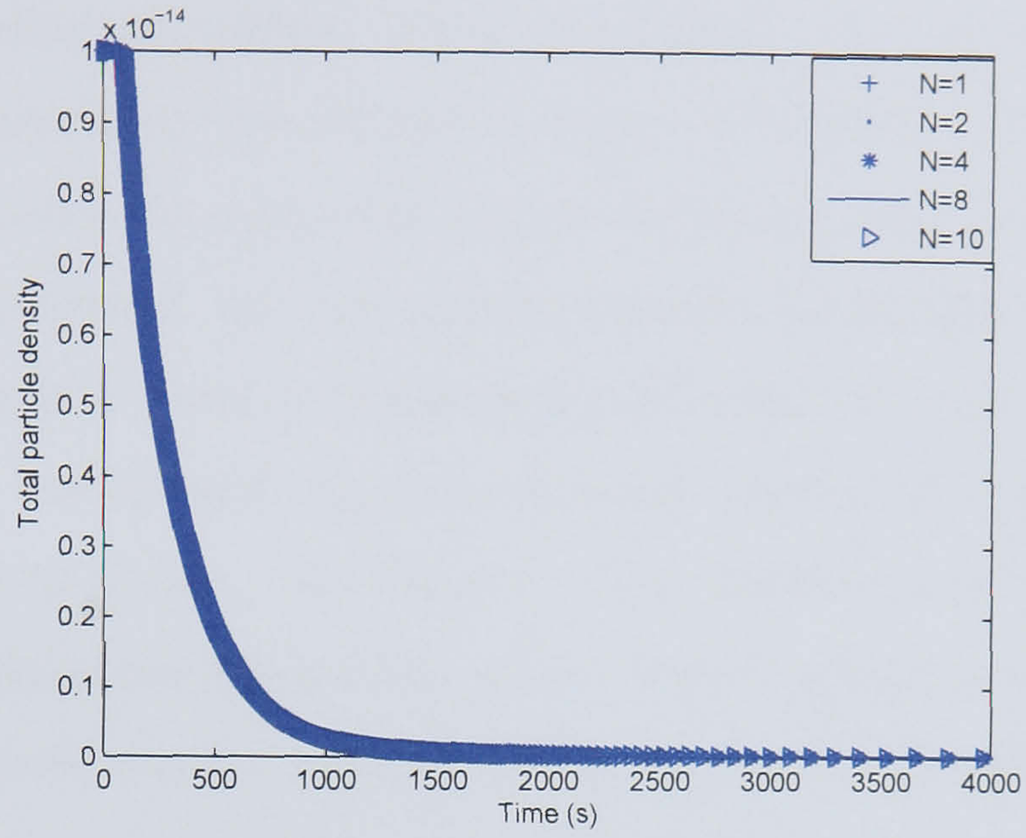

(a) evolution of total particle density

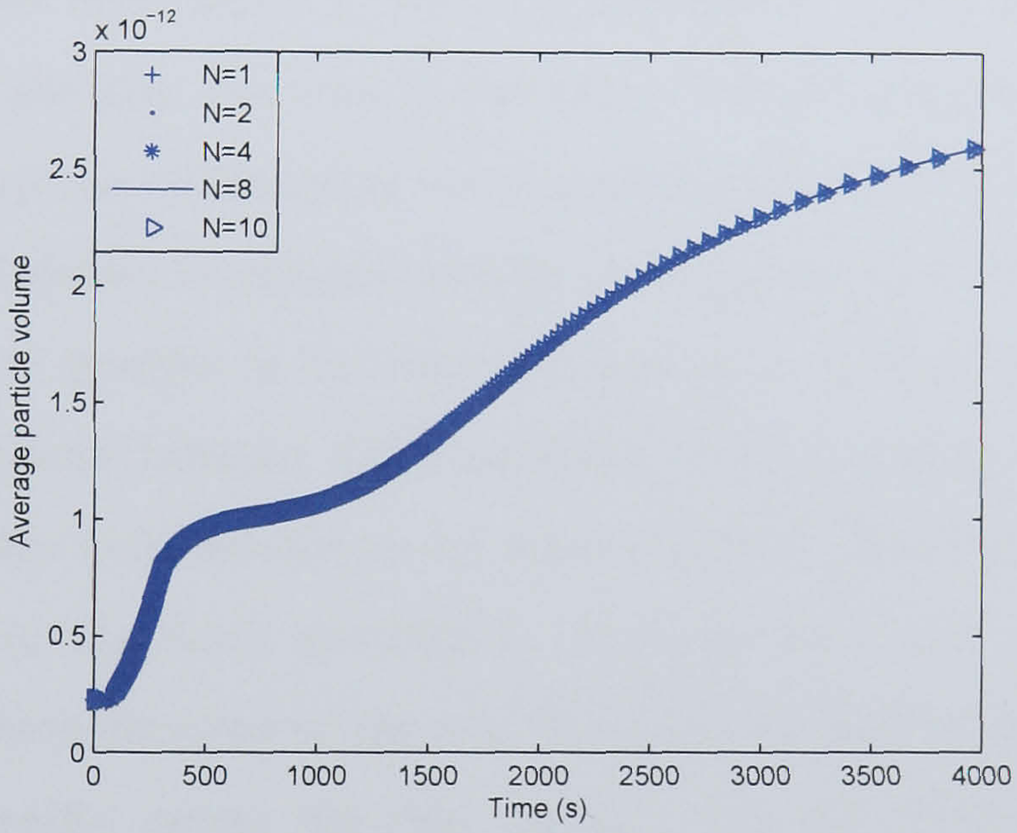

(b) evolution of average volume of particle

Figure 4.3: Profiles of total particle density and average volume against time

.

4.3 Experimental Details

For the drum granulation experiments, calcite (Aglime, Landmark, Australia) was used with a volume-mean diameter (d_{30}) of 130 μm and with 95% of the mass less than 250 μm. d_{30} is defined to be the ratio of the total volume of particles (i.e., the third moment of the moment distribution) to the total number of particles (i.e., the zeroth moment

of the moment distribution) (Allen, 1997). Henceforth, d_{30} used in the thesis signifies volume-mean diameter. Polyvinyl alcohol in water (PVOH-H_2O, Elvanol T66, Du Pont. USA) (2.5% concentration by mass) was used as the liquid binder. Semi-batch granulation experiments were performed, with the powder mass placed initially in the drum, and the binder spray rate set at $1.72\,mL/s$, commencing $20\,s$ after the start of the batch (start of drum rotation) and lasting until the predetermined amount of binder is delivered. The drum speed was set to $25\,rpm$. A laboratory scale stainless steel drum granulator was used, comprising a liquid binder spraying nozzle (flat-fan spray pattern) pointing directly at the powder bed mass, using a pressure pot (pressurised at 500 kPa).

In this study, the results from three granulation experiments are reported. For case 1 the target binder-to-solids ratio was 0.11 with a drum load of $1.5\,kg$ charged into the drum prior to the start of the run. For case 2, the experimental conditions remain identical to case 1 with the exception of changing the target binder-to-solids ratio to 0.12. Finally, for case 3 the experimental conditions remain the same as for case 1 with the exception of varying the mass of powder in the drum granulator to $1.75\,kg$. Thus, case 1 and case 2 allow for a comparison between different liquid binder-to-solids content whilst case 1 and case 3 will enable comparisons to be made between the effects on different initial powder mass loads in the drum granulator. Samples were collected at different times and subjected to a measurement of the size distribution, and the distributions of binder content and the porosity across the size classes. The size distribution was measured by sieving using a fourth-root-of-two progression series of sieves (Endecotts Ltd.) ranging from $250\,\mu m$ to $8\,mm$. Subsequently, a representative portion of each sample was subjected to binder content measurement through thermo-gravimetry and porosity measurement using pycnometry. See chapter 3 for more details.

4.4 Model Validation Results

The model simulations were carried out on a 2GHz Intel Dual Core processor desktop computer with 2GB RAM using the intel FORTRAN compiler. The total discretised domain for the simulation comprised of 50, 20 and 10 bins along the solid, liquid and gas internal coordinate axes, respectively. The width of the bin along the solid volume

is $\Delta R_s = 1.07 \times 10^{-5}\, m$, the width of the bin along the liquid volume ranges between $\Delta R_l = 3.35 \times 10^{-7}\, m$ to $\Delta R_l = 2.68 \times 10^{-5}\, m$ and the width of the bin along the gas volume is $\Delta R_g = 1.5 \times 10^{-6}\, m$. A first order Euler predictor-corrector method was employed for the integration of the system of ODEs. The computation time required for the simulation of the population balance model accounting for nucleation, aggregation and consolidation was approximately $1.5\, hrs$ for the nominal case (case 1).

The population balance model was validated by comparing the simulated variables with experimental measurements. Granule samples were taken out from the drum granulator at the time instances of $180\, s$, $300\, s$, $420\, s$, $600\, s$ and $900\, s$. The primary particles were monodispersed with a volume-mean diameter of $130\, \mu m$. It must be noted that although the initial distribution in the model was unimodal (unlike the experimentally measured bimodal distribution, see Figure 3.7), the average diameter in both cases were the same. This was based on the assumption that final granule properties are not very sensitive to the initial PSD as seen in the simulated findings of Poon (2008). Other model inputs such as the initial number/mass of seed particles, volume of the binder droplet, duration of binder addition, and binder flow rate were set as per actual experimental conditions. Table 4.2 provides the operating information for the batch granulation.

Table 4.2: Batch granulation variables.

	Case 1	**Case 2**	**Case 3**
Initial powder mass (kg)	1.5	1.5	1.75
Rate of binder spray $(mL\ s^{-1})$	1.72	1.72	1.72
Duration of binder spray (s)	96	104	112
Volume of binder droplet (m^3)	1.15×10^{-11}	1.15×10^{-11}	1.15×10^{-11}

A sensitivity analysis around the nominal operating regime was performed to determine the influence of the adjustable model parameters on the particle density distribution. The first set of data (Section 4.4.1) was used to tune the model i.e., determine the values of the adjustable parameters listed in Section 4.2.3. Subsequently, the tuned model was used to predict the GSD, fractional binder content and porosity at other operating conditions. The parameters were tuned by varying some of the sensitive parameters in the simulation mode, to provide an acceptable match via visual inspection between the model output and

the experimentally obtained PSDs. The more-sensitive adjustable parameters that were tuned in this manner were parameters in the nucleation kernel (A_0), the aggregation kernel (c_1) and the consolidation kernel (c), and the maximum granule size limit for aggregation (D_{upper}). The less-sensitive adjustable parameters that remained fixed at nominal values were the height of the surface asperity of the particles (h_a), the critical binder content required prior to surface film formation (l_{min}), the effective porosity of the powder bed mass (ϵ_{min}), the relative approach velocity of the two coalescing particles (u_0) and the volume of droplet that remains unpenetrated (V_{up}) (see Section 4.2.3). Table 4.3 lists the fundamental material properties that were either measured or obtained from the literature, and the nominal values of the less-sensitive adjustable parameters. Table 4.4 lists the more-sensitive adjustable parameters.

Table 4.3: Fundamental material properties and less sensitive adjustable parameters from Section 4.2.3.

No.	Property	Value
1	μ	$5.20 \times 10^{-3}\ Pa\,s$
2	ρ_s	$2.74 \times 10^{3}\ kg/m^3$
3	Y_d	$1.591 \times 10^{-4}\ Pa$
4	E	$8.20 \times 10^{6}\ Pa$
5	h_a	$5.0 \times 10^{-5}\ m$
6	l_{min}	0.99 (-)
7	d_{50}	130 μm
8	γ_{LV}	$5.2 \times 10^{-2}\ N/m$
9	γ_{SV}	$4.0 \times 10^{-2}\ N/m$
10	θ	43.2°
11	ϵ_{eff}	0.20 (-)
12	u_0	$5.0 \times 10^{-3}\ m/s$
13	V_{up}	$0\ m^3$

Table 4.4: The more-sensitive adjustable parameters from Section 4.2.3.

No.	Property	Value
1	c	5.0×10^{-5} (-)
2	c_1	3.0×10^{7} (-)
3	A_0	$4.0 \times 10^{-20}\ mol/m^3$
4	D_{upper}	740 μm

4.4.1 Case 1

Case 1 corresponds to a binder-to-solids ratio of 0.11 and a drum load of 1.5 kg. Figure 4.4a depicts the simulated time evolution of the total particles in the system, which reduces due to the combined effects of nucleation and aggregation. It can be seen that from $0-2\,min$ there is a rapid decrease in particles and from $2-15\,min$ there is a decline in the rate of decrease of particle numbers. This trend is expected as the binder is being sprayed approximately in the first two minutes, which results in a sharp decrease in total particles (sum of granules and fines). Thereafter, the nucleation event stops and only aggregation occurs as a result of the residual binder within the particles. Figures 4.4(b)-4.4(d) show the change in average particle diameter, fractional binder content and average porosity with time respectively. The plots show a good agreement between the simulated profiles and the experimentally-measured data. Fractional binder content is defined as $LS = \frac{l}{s+l+g}$ and average porosity was previously defined by Equation 4.2.

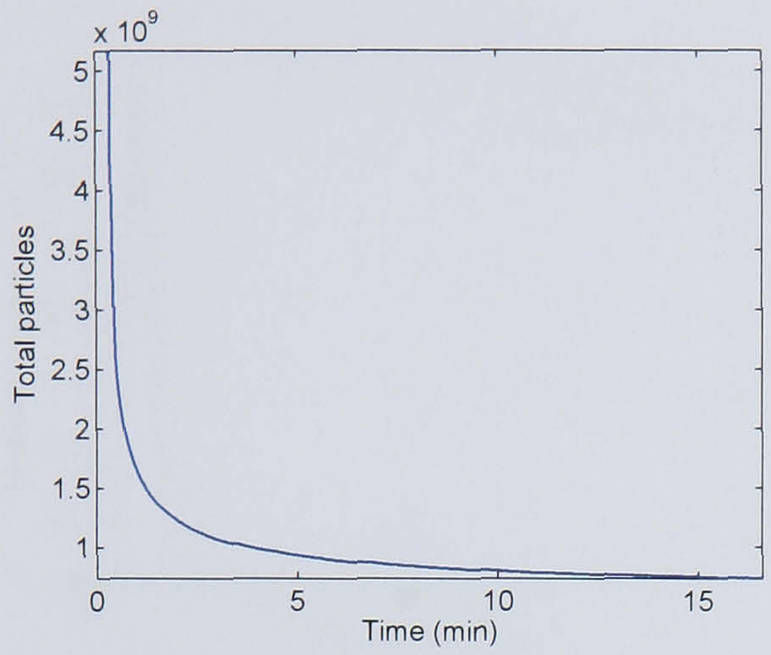

(a) simulated output for total particles

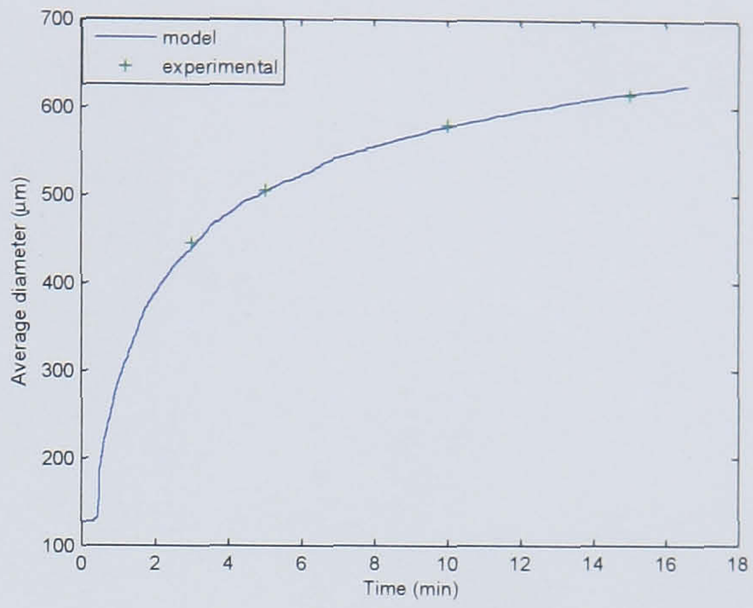

(b) comparison between model output and experimental data for the evolution of average particle diameter

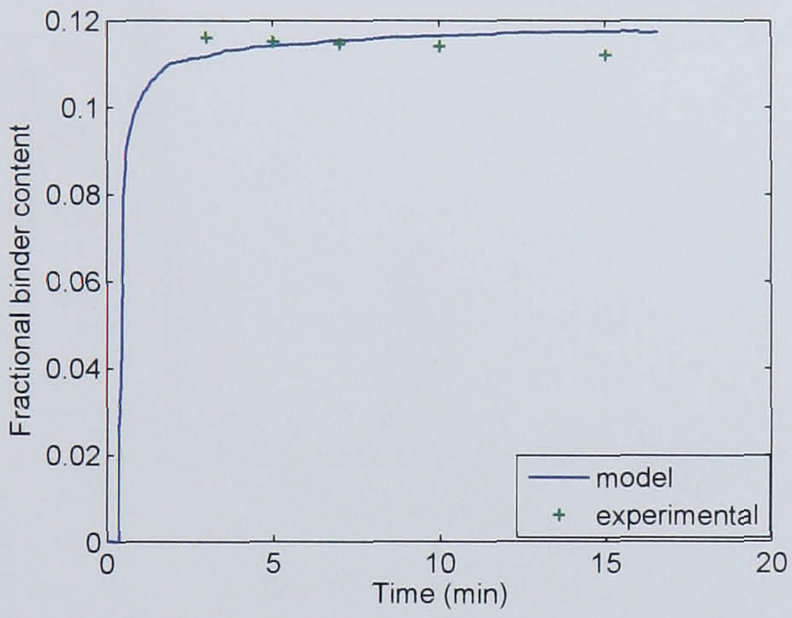

(c) comparison between model output and experimental data for the evolution of fractional binder content

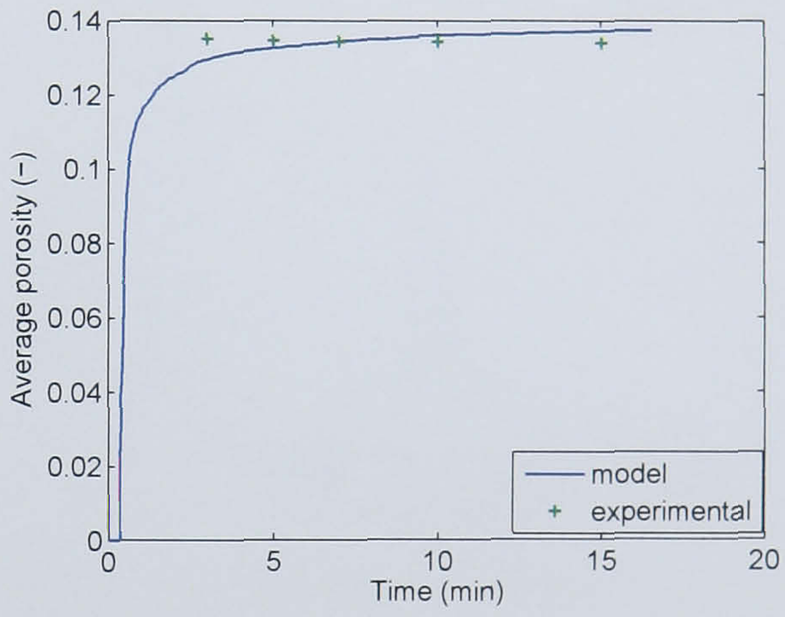

(d) comparison between model output and experimental data for the evolution of average porosity

Figure 4.4: Time profiles for total particles, average diameter, average fractional binder content and average porosity for binder-to-solids ratio = 0.11 and drum load = $1.5\,kg$ (case 1).

The GSD profiles at the intermittent sampling times during the experiment (i.e. $180\,s$, $300\,s$, $420\,s$, $600\,s$ and $900\,s$) are compared with those obtained from sieve analysis as seen in Figure 4.5. The GSDs are represented as the normalised number frequency of granules with respect to granule size. A clear progression is observed during the course of granulation whereby particles agglomerate together forming larger sized granules, which is depicted by the gradual reduction in the peak spanning $0-250\,\mu m$ and a corresponding growth in the peak spanning $700-1000\,\mu m$ (note the change in the range of the y-axis).

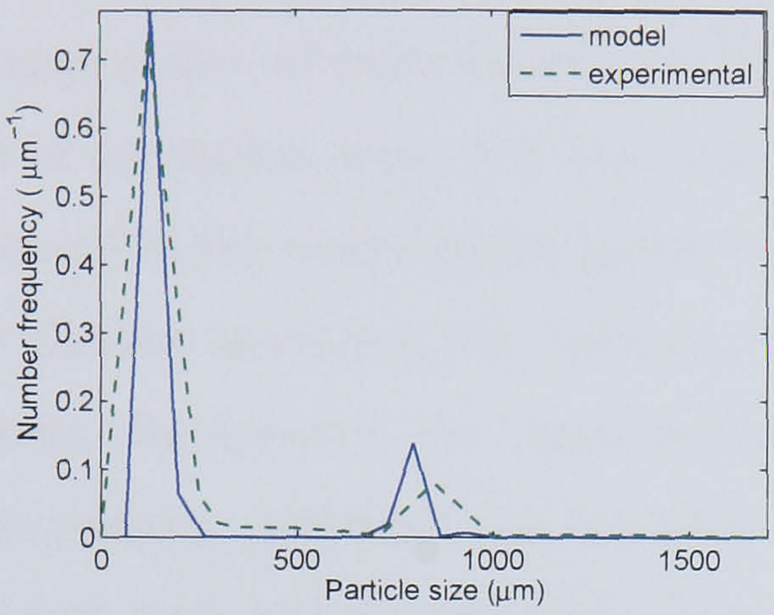

(a) time $= 3\,min$

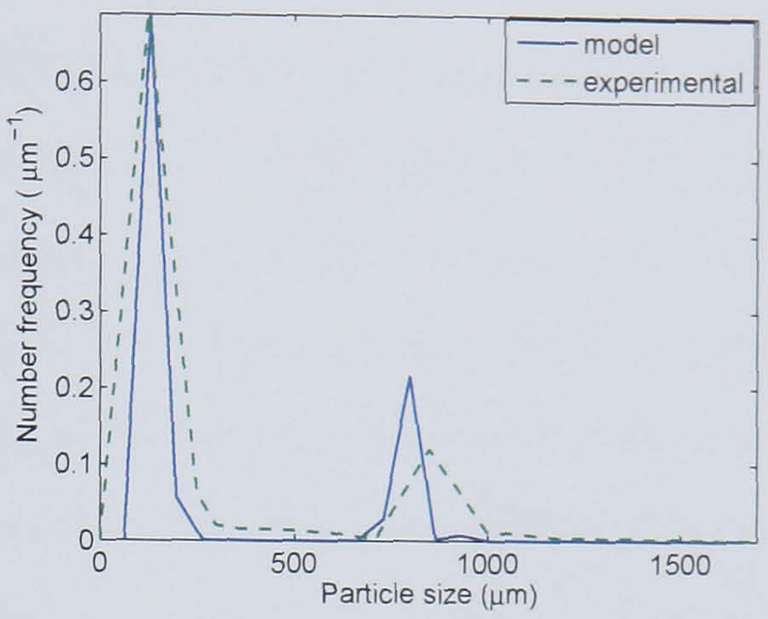

(b) time $= 5\,min$

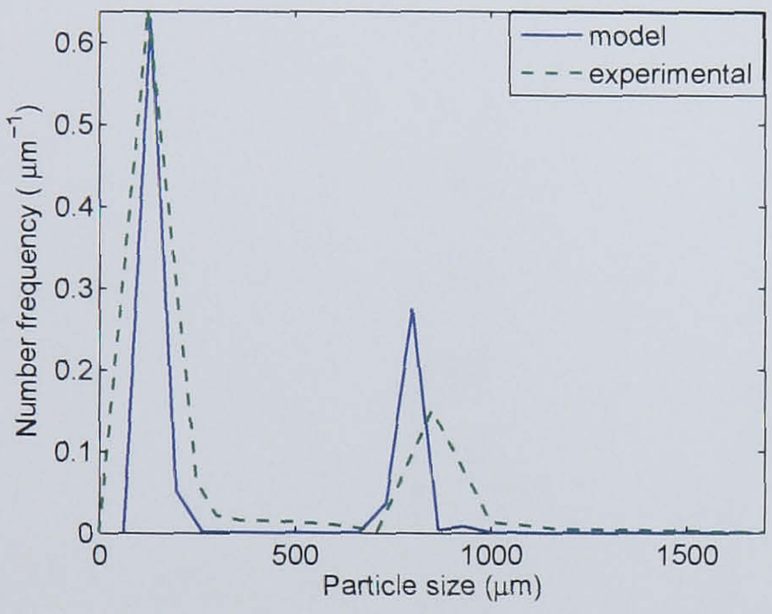

(c) time $= 7\,min$

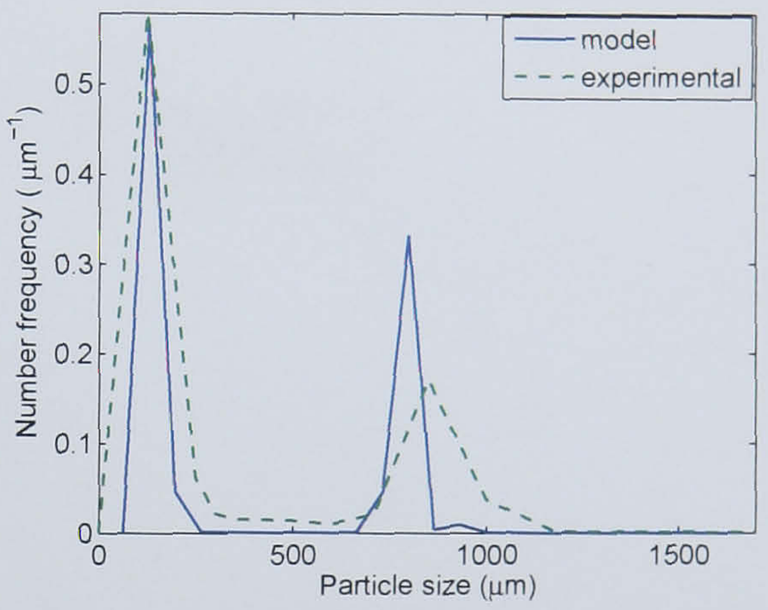

(d) time $= 10\,min$

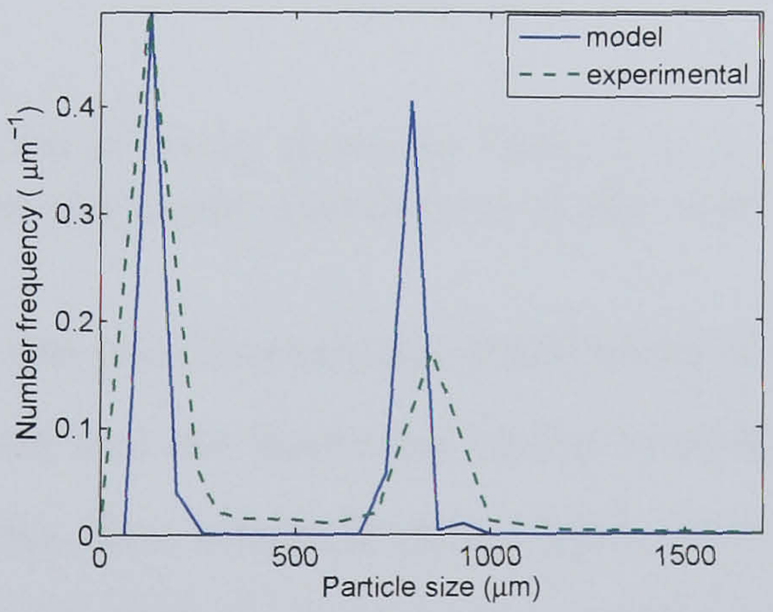

(e) time $= 15\,min$

Figure 4.5: Comparison of simulated and experimentally-measured granule size distribution at various time instances for binder-to-solids ratio $= 0.11$ and drum load $= 1.5\,kg$ (case 1).

Figure 4.6 shows an early distribution obtained from, the model simulations for the formation of nuclei particles 1×10^{-2} s after the binder has begun spraying with the number

of primary particles that constitute towards the formation of a granule nucleus varying in the range of $40-47$ primary particles for each nuclei formed. The figure shows that at the onset of nucleation, there is a narrowing of the particle size distribution. This is possibly attributed to the consolidation phenomenon, causing the newly formed nuclei to compact more thereby increasing the likelihood of continuing future growth forming larger sized granules. Furthermore, the nuclei particles formed falling into larger particle size classes is also present. Although, the proportion of newly formed nuclei is dwarfed by the more dominant peak corresponding to the smaller sized particles. Thus, this makes it difficult to see in Figure 4.6.

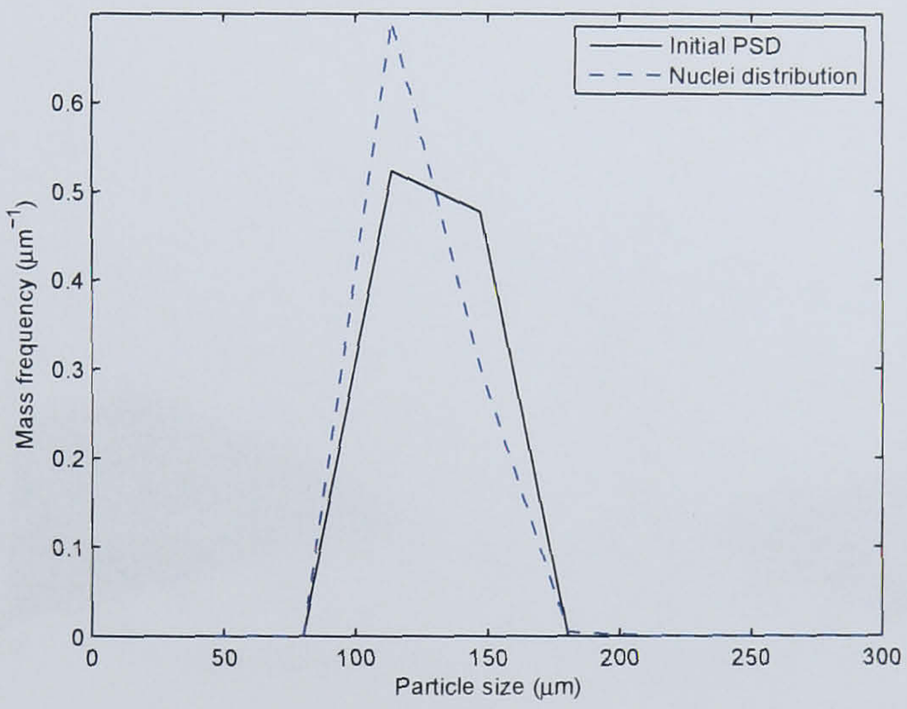

Figure 4.6: The distribution of nuclei particles formed, at 1×10^{-2} s after the start of the binder spray, as seen from the model simulations under case 1 conditions.

Figures 4.7(a)-(f) depict the two-dimensional distribution of the particle population with respect to particle diameter and the fractional binder content. The initial seed of primary particles is shown at $t = 0\,s$. The binder is sprayed into the system after $20\,s$, which initiates the granulation process, with the initial seed particles beginning to nucleate rapidly as shown through Figures 4.7(b)-(d). The emergence of the second mode of larger size particles is the cumulative effect of nucleation and aggregation. At $t = 100\,s$ granulation is well underway with particles growing via consolidation and aggregation. At this point in time the particle population is bimodal and continues to persist until the end of the granulation time. Such emergence of bimodal granule size distribution has also been observed in previous studies (Knight et al., 1998).

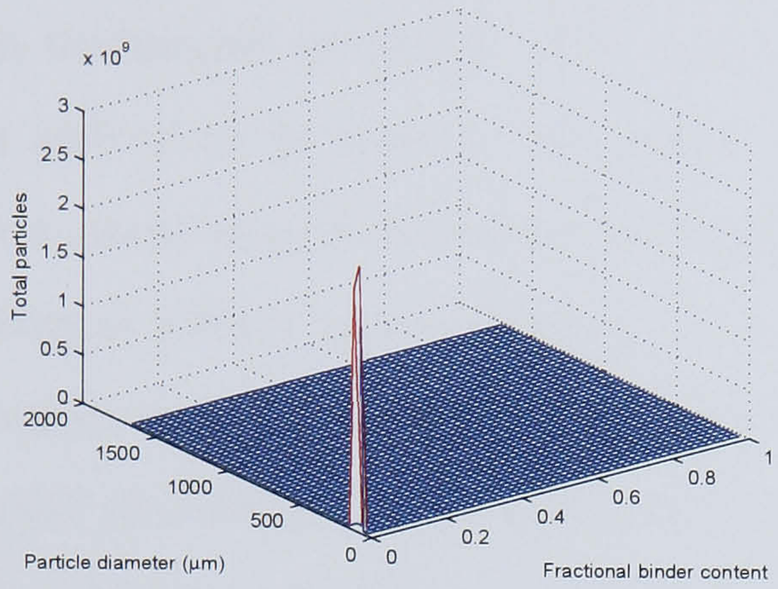

(a) time $= 0\,s$

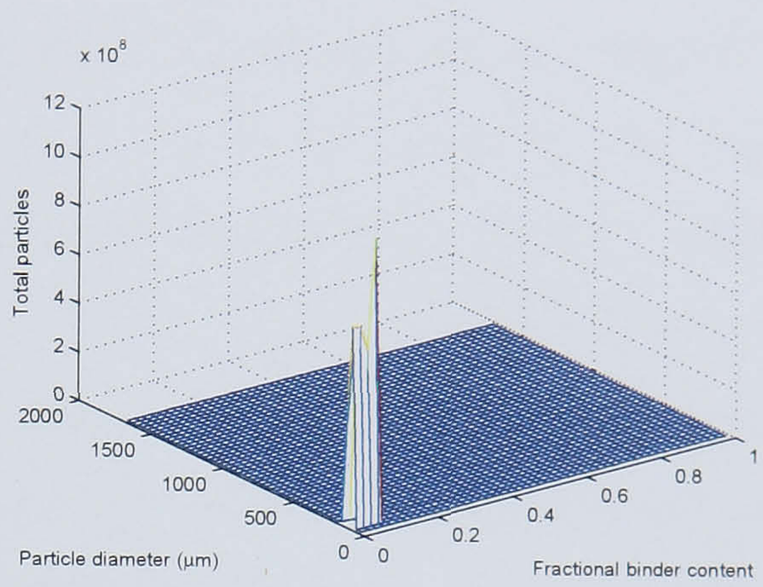

(b) time $= 20.01\,s$

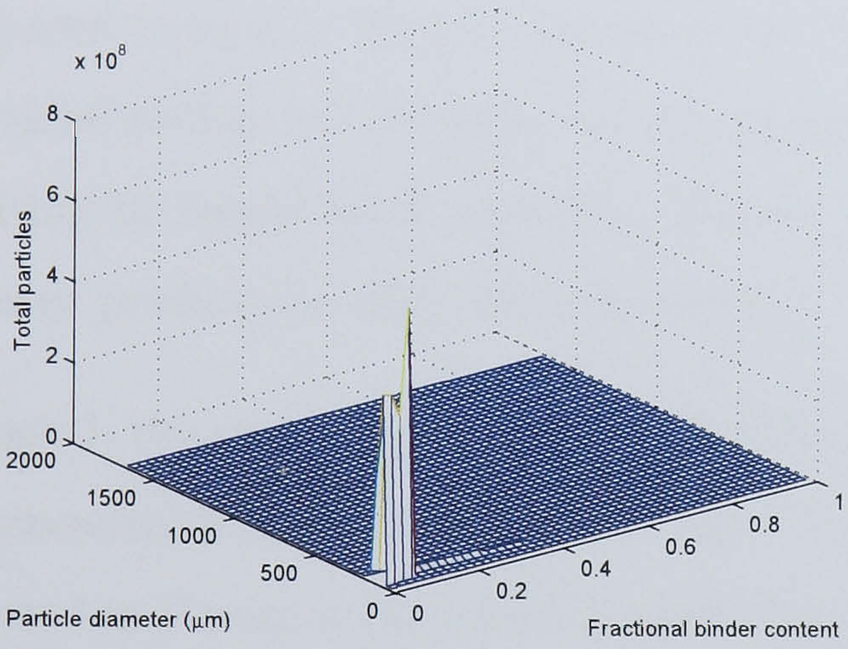

(c) time $= 25\,s$

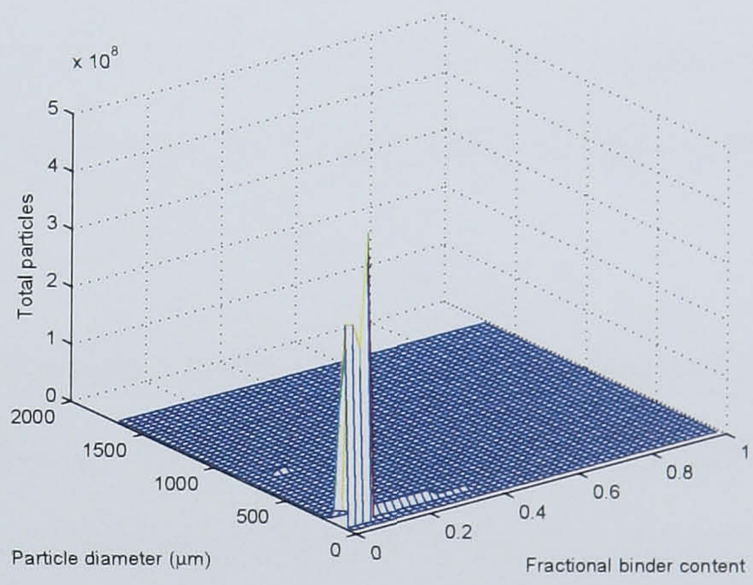

(d) time $= 30\,s$

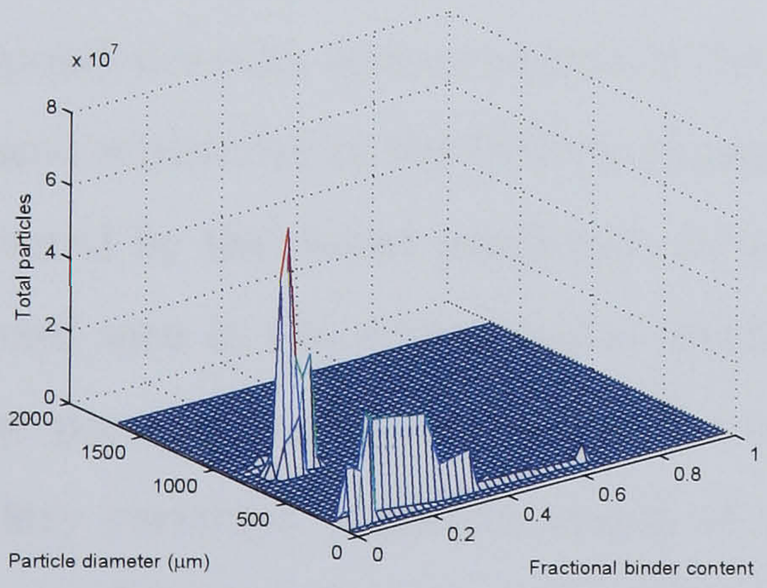

(e) time $= 180\,s$

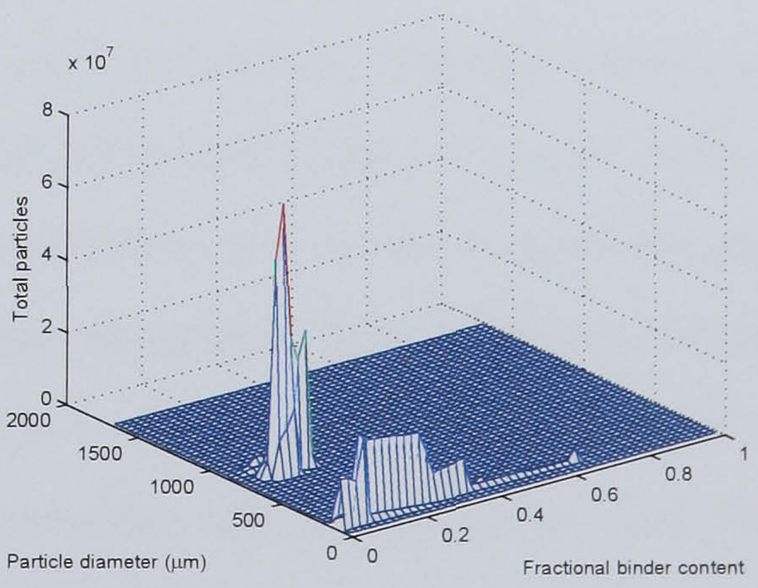

(f) time $= 900\,s$

Figure 4.7: Time instances of the evolution of granule population distribution across size and fractional binder content for binder-to-solids ratio $= 0.11$ and drum load $= 1.5\,kg$ (case 1).

4.4.2 Cases 2 and 3

Case 2 pertains to a binder-to-solids ratio of 0.12, while the other operating conditions remain unchanged as case 1. The various adjustable parameters are maintained at the values arrived at in case 1. Intuitively, the mean granule diameter and the fractional binder content should increase compared to the nominal conditions in case 1 which was operating at a lower binder-to-solids ratio. The simulated GSDs, fractional binder content and average porosity were compared with their experimental counterparts. In Figure 4.8. the model predictions for the GSD with the experimental data show a close correspondence between the two sets of data. Further, it is confirmed in Figures 4.9a and 4.9b respectively that the average granule size and the average fractional binder content are higher for case 2 compared to case 1. This is consistent with the theory that a higher binder-to-solids ratio (provided it does not exceed a certain upper bound) promotes nucleation and aggregation resulting in larger sized particles. Figure 4.9c shows a good match also of the average porosity predictions with the experiments.

In Case 3, the operating conditions were identical to those used in case 1 with the exception of increasing the drum load to $1.75\,kg$. The ability of the model to predict the GSD is reflected in Figure 4.10, where a good alignment is achieved with the experimental data. The evolution of average granule diameter, fractional binder content and average porosity are shown in Figures 4.9a, 4.9b and 4.9c respectively. Model predictions provide a good correspondence with measurements of these averaged properties. The experiments indicate a reduced sensitivity in the GSD to change in the drum load from $1.5\,kg$ to $1.75\,kg$, which is captured by the model prediction as well. In addition, the model adequately captures the trend seen in the experimental results for the average fractional binder content and average porosity among cases 1-3. The fractional binder content and the porosity being secondary variables, a perfect match of these variables was not essential, and therefore not pursued during the parameter adjustment. The goal of parameter adjustment was to ensure a good match of the GSD and the average granule size. However, to ensure the predictive capability of the model under other operating conditions, it is important for these secondary variables to capture the non-linear trends shown by the experiments. The model structure clearly exhibits this ability and thereby preserves internal stability.

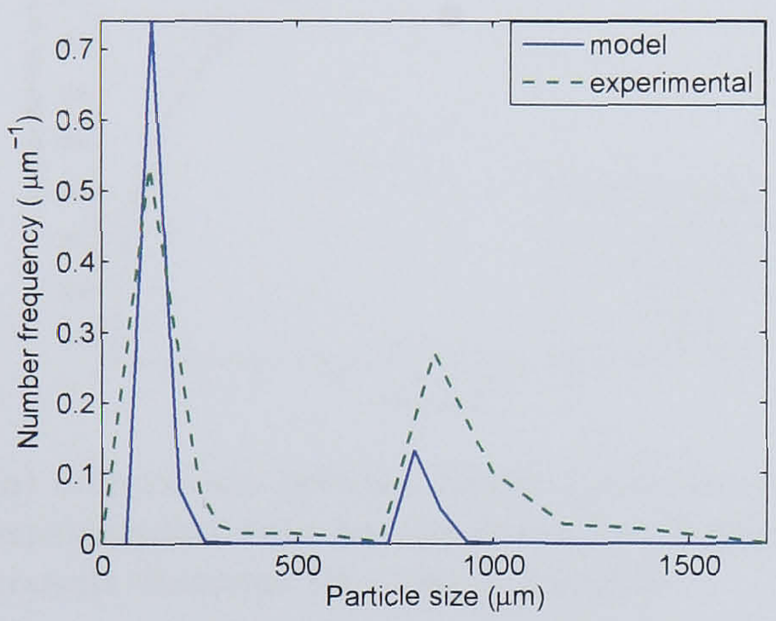

(a) time $= 3\,min$

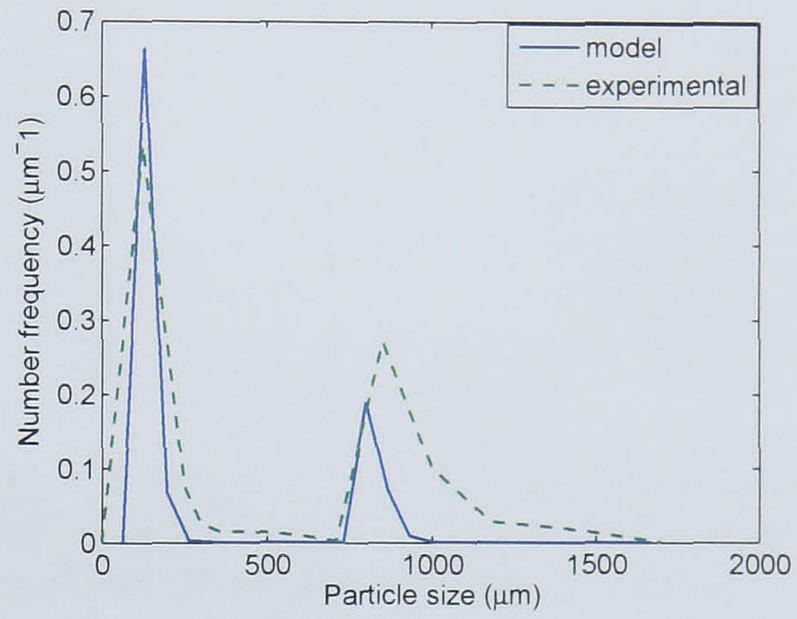

(b) time $= 5\,min$

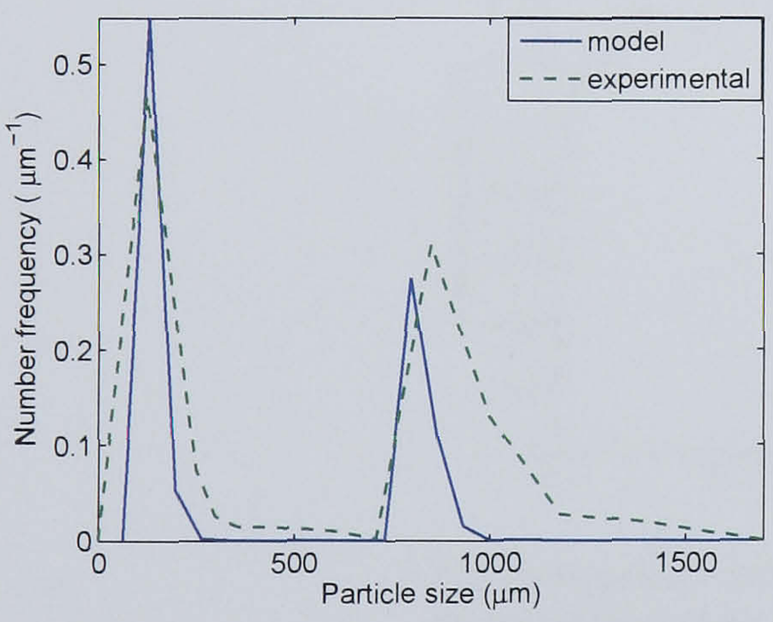

(c) time $= 10\,min$

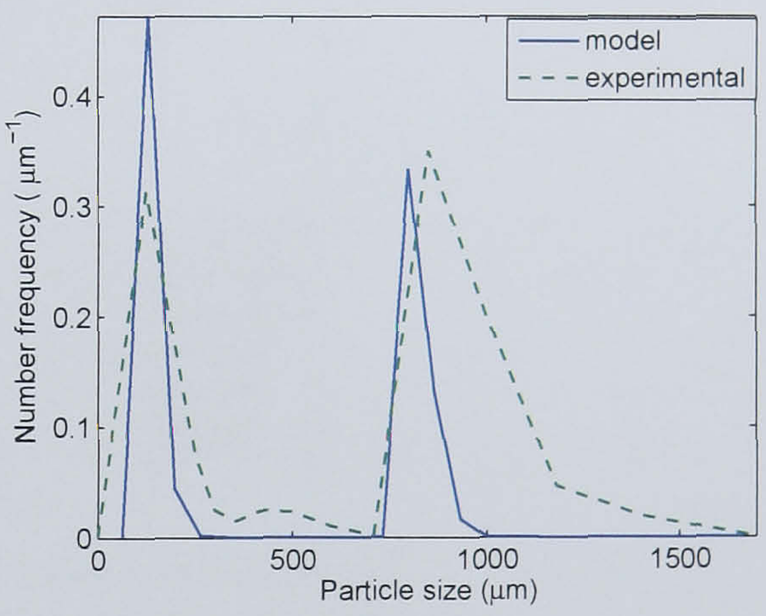

(d) time $= 15\,min$

Figure 4.8: Comparison of simulated and experimentally-measured granule size distribution at various time instances for binder-to-solids ratio = 0.12 and drum load = $1.5\,kg$ (case 2).

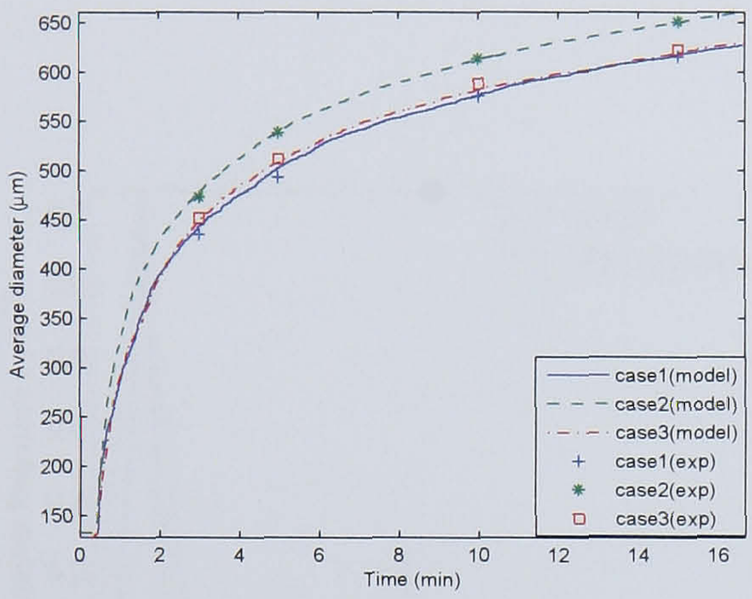

(a) comparison between model predictions and experimental data for the evolution of average granule diameter for cases 1, 2 and 3

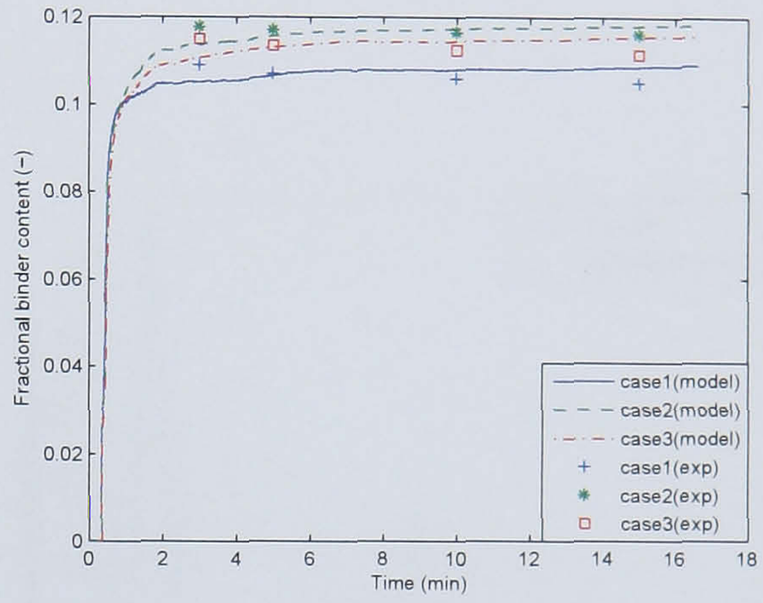

(b) comparison between model predictions and experimental data, for the evolution of fractional binder content for cases 1, 2 and 3

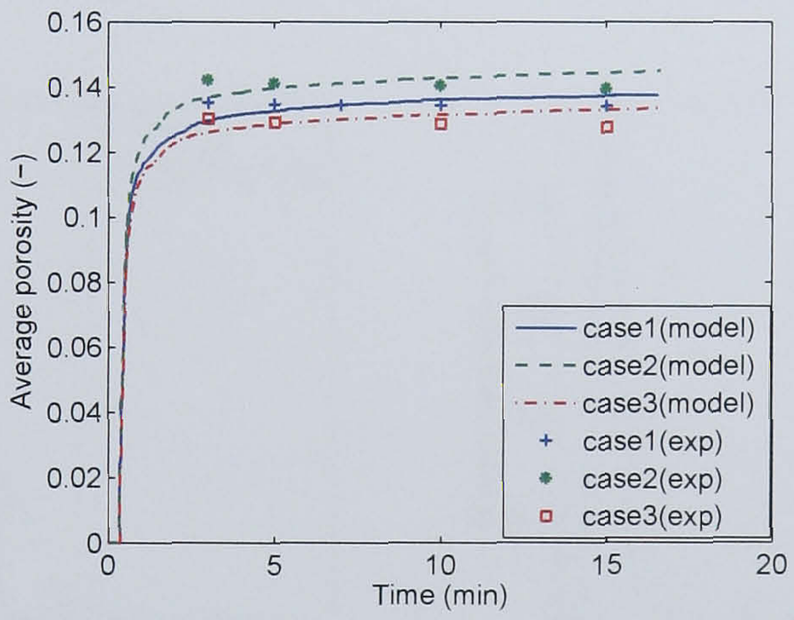

(c) comparison between model predictions and experimental data, for the evolution of average porosity distribution for cases 1, 2 and 3

Figure 4.9: Time profiles for the average granule diameter, fractional binder content and average porosity for cases 1, 2 and 3 with comparisons made between model simulated predictions and experimental measurements. Cases 1 and 2 correspond to a target binder-to-solids ratio of 0.11 and 0.12 respectively, and an initial drum load of $1.5\,kg$. Case 3 corresponds to a target binder-to-solids ratio of 0.11 with an initial drum load of $1.75\,kg$ of powder.

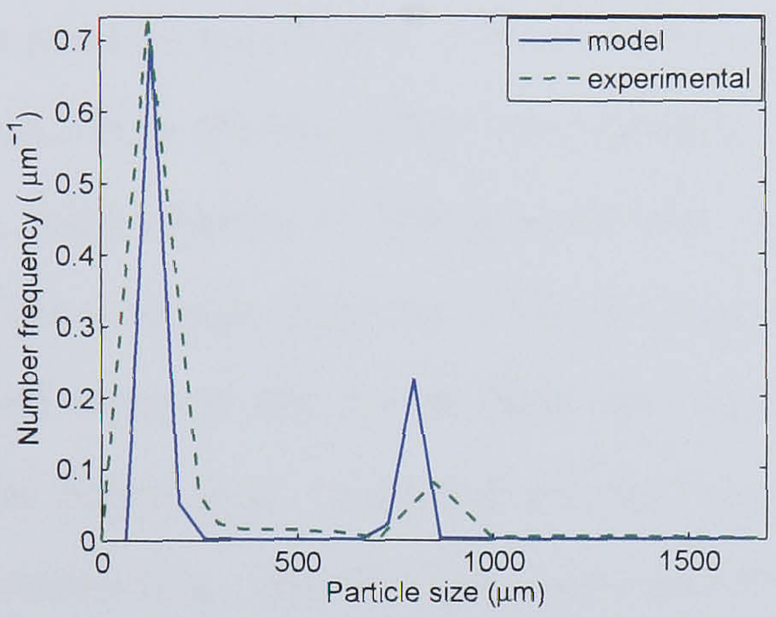

(a) time $= 3\,min$

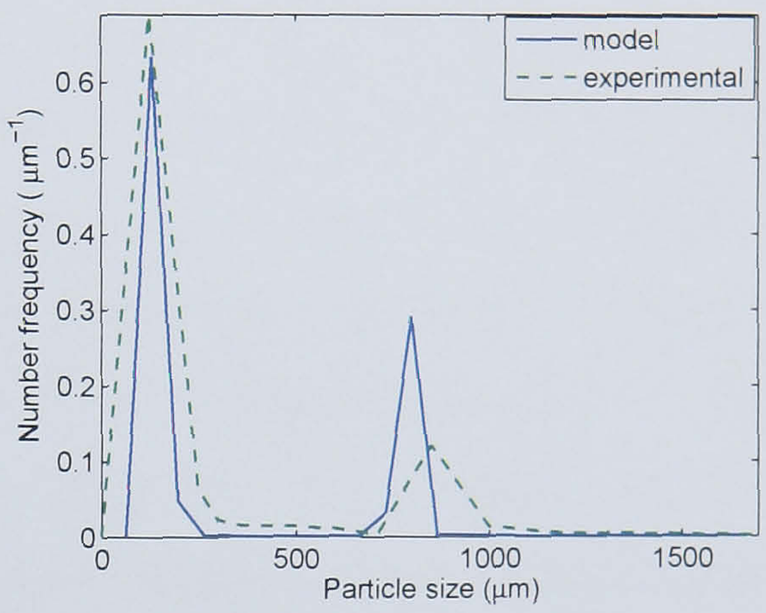

(b) time $= 5\,min$

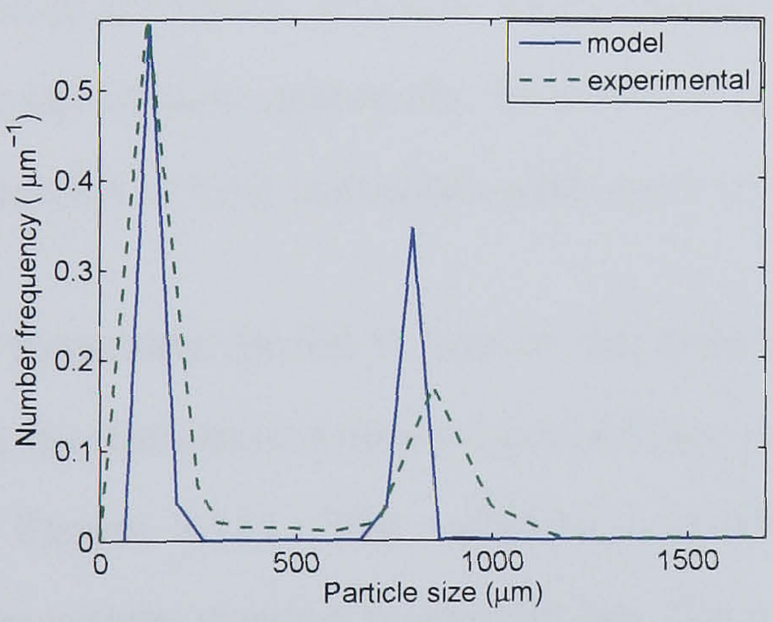

(c) time $= 10\,min$

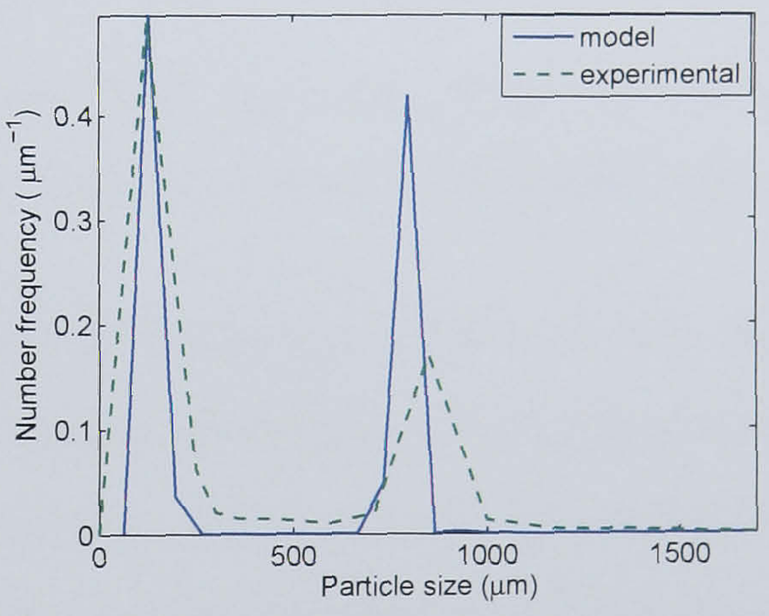

(d) time $= 15\,min$

Figure 4.10: Comparison of simulated and experimentally-measured granule size distribution at various time instances for binder-to-solids ratio $= 0.11$ and drum load $= 1.75\,kg$ (case 3).

4.5 Conclusions

In this study, a three-dimensional population balance model of a granulation process employing mechanistic representations for the nucleation and aggregation phenomena was validated for a Calcite/PVOH-H_2O recipe. Laboratory scale experiments were performed to obtain data on granule distribution across size, binder content and porosity. This study was one of the first attempts to measure granule population distribution across all these three granule attributes. The comparison of the model with the batch granulation experimental data showed close correspondence between model simulations and experimental data, with respect to the granule size distribution, the average fractional binder content and the average porosity. These early studies under the experimental conditions considered support the thesis that the incorporation of fundamental properties of both the binder liquid (e.g. viscosity, surface tension, solid-liquid contact angle), and the powder properties (e.g., density, size and size distribution) into mechanistic kernels for the underlying granulation phenomena will enable an improved tracking of the dynamic behaviour of the granulation process. Once validated, such a model will be particularly valuable for scale-up of new materials, in predicting the granulator operation given the fundamental properties of new materials with only a reduced number of carefully-designed experiments.

The proposed model is one of the first attempts to bridge the multi-scale gap traversing from fundamental material properties, to granulation operation, to end granule properties (see Figure 4.11). The validation of this model with batch granulation experiments are encouraging, serving to strengthen the role of mechanistic kernels of the different rate processes in providing a more accurate description of the dynamics of the process. However, only a portion of the rich features of the model was validated in this study, particularly the effects of a few operating conditions of the granulator. Similar validation studies need to be performed using different liquid binders and different powder materials, in addition to the validation of the effects of the other operating variables such as the mixing rates. The parallel programming results are also encouraging and combined with the hierarchical two-tier technique, highlights the potential of the full 3-D PBE model to be used for feedback control purposes.

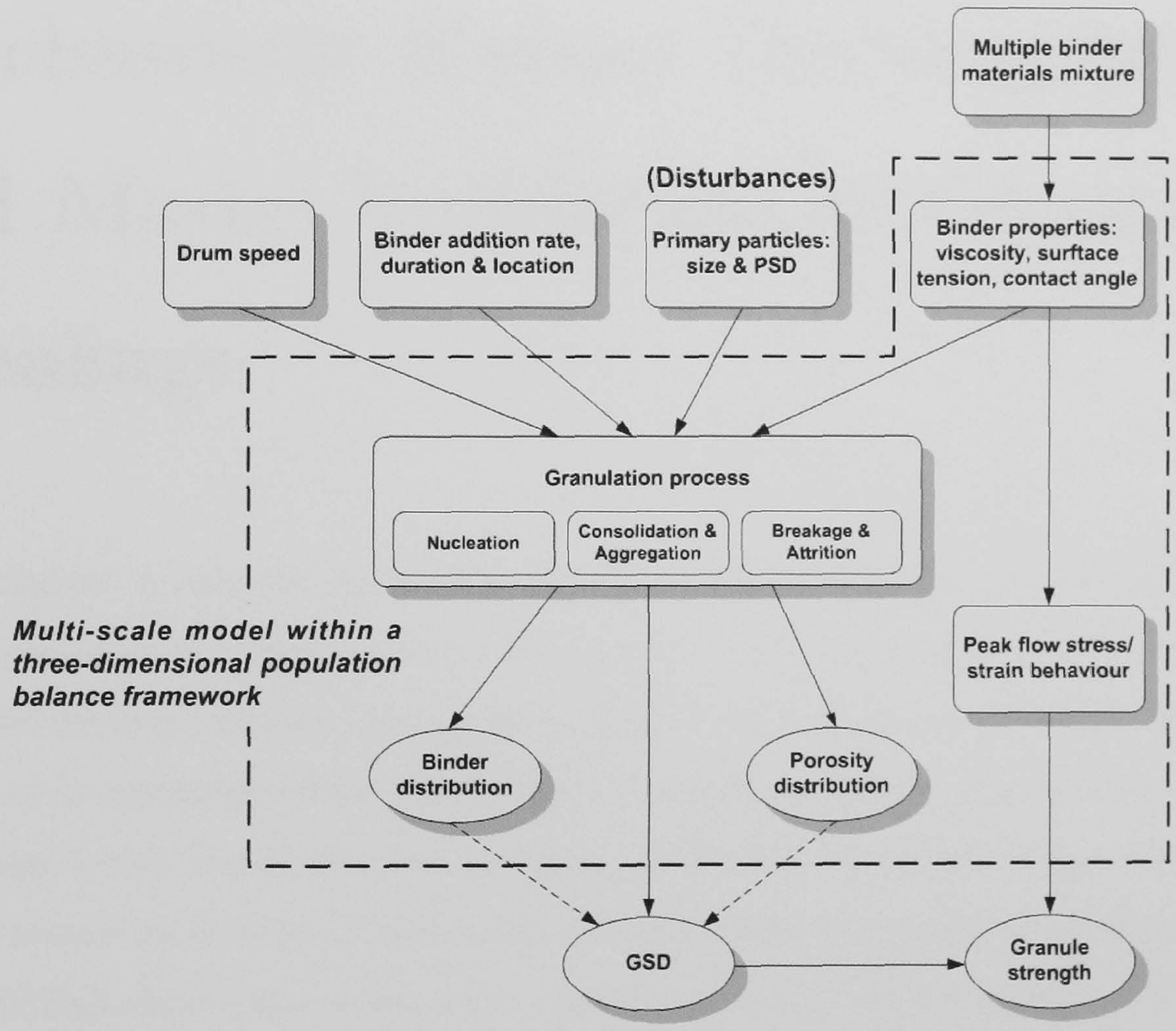

Figure 4.11: The experimentally-confirmed multi-scale links in the granulation process, as presented in chapter 3.

Chapter 5

Mechanistic Kernel Development and Model Validation of Granule Breakage

In this chapter, a dynamic model is presented for the granulation process, employing a three-dimensional population balance framework. The major focus of this work is the theoretical development and experimental validation of a novel mechanistic breakage kernel that is incorporated within the population balance equation. Qualitative validation of breakage kernel/model was first performed and trends of lumped properties and distributed properties show good agreement with the expected phenomenological behaviour. Successful high-shear mixer granulation experiments using a Ballotini/PVOH-H_2O recipe were then carried out to mimic predominantly breakage-only behaviour whereby the rate of breakage was greater than the rates of nucleation and aggregation. Good agreement between experimental and simulation results were obtained for the granule size distribution under different operating conditions. In addition, accurate model predictions were obtained for the evolution of the lumped properties.

---

[1]Part of this chapter is based on, R. Ramachandran, C.D. Immanuel, F. Stepanek, J.D. Litster and F.J. Doyle III, "A Mechanistic Model of Granule Breakage in Population Balances of Granulation: theoretical kernel development and experimental validation", Accepted in Chemical Engineering Research and Design.

5.1 Introduction and Objectives

In granulation, it is now generally accepted that three rate processes are sufficient to elucidate its behaviour. These are namely wetting and nucleation; consolidation and growth; and breakage and attrition (Litster and Ennis, 2004). In the recent years, significant research on the understanding of granulation has been carried out. This has resulted in many research advances with regard to accurate modelling of the granule mechanisms, especially in the case of granule growth (e.g. aggregation) (see Chapter 2, section 2.2.3.1). Based on the literature reviewed in chapter 2 (see section 2.2.3), it can be inferred that granule breakage, like nucleation is less understood compared to granule growth. This inference has been reported by Liu et al. (2008) in their work on wet granule breakage. However, understanding breakage behaviour is of importance as breakage of wet granules will influence and control the final granule size distribution, especially in high-shear granulators (Iveson et al., 2001; Liu et al., 2008). Breakage can also be used to limit maximum granule size or help distribute a viscous binder, which would lead to an increase in the aggregation efficiency. As can be seen from the discussions in chapter 2, many of the existing breakage models/kernels are empirical and do not explicitly account for the dependance of material properties; and process and design parameters. In other cases, studies have neglected breakage altogether, lumping the breakage mechanism in their aggregation model. Given the importance of breakage and the lack of suitable breakage models, this chapter is concerned with regards to the qualitative and quantitative development and validation of a novel multi-dimensional mechanistic breakage model that can explicitly account for the dependence of key material properties and process/design parameters on multiple granule properties. A detailed sensitivity analysis will also be undertaken to quantify effects of key properties/parameters on end granule properties.

5.2 Background

At the process scale, breakage is important in enhancing the product distribution and eventual strength of the product granules. For instance, Vonk et al. (1997) observed that secondary nuclei (that were fragments of larger particles) had a higher tensile strength

(see Chapter 2, section 2.1.2.1). Knowledge of accurate rates of breakage will improve modelling and prediction of granule properties which in turn will facilitate a better understanding of the granulation process. At the micro-scale, extensive studies have been performed to characterise granule strength and behaviour, under static and dynamic conditions (Reynolds et al., 2004). This has the potential to improve understanding of breakage at the process scale, by incorporating the micro-scale physics in the form of a breakage kernel into population balances. The first step in deriving such a kernel is to understand how different variables (material properties and process/design parameters) affect breakage behaviour.

5.2.1 Effect of Variables on Granule Breakage

Variables that influence granule breakage can be grouped into material properties (e.g. powder/solid and liquid properties) and process/design parameters. The former has a direct consequence on the granule strength which in turn determines the rate and extent of granule breakage. The latter has an effect on the impact forces/stresses on the granule which also influences the rates and extent of granule breakage.

5.2.1.1 Material Properties

The material properties that influence granule breakage can be grouped as follows:

- **Binder viscosity**: Binder viscosity affects granule strength by determining the viscous forces in liquid bridges between primary particles. It was observed that a higher binder viscosity correlated with stronger granules and resulted in lower breakage rates (Eliasen et al., 1998; Van den Dries et al., 2003).

- **Binder surface tension**: Binder surface tension determines granule strength by causing capillary forces (via the liquid bridge) between primary particles. It was observed that increased surface tension resulted in stronger capillary forces thus reducing the propensity of granule breakage (Ennis et al., 1991; Tardos et al., 1997; Iveson et al., 1998; Iveson and Litster, 1998b).

- **Contact angle between binder and primary particle**: Contact angle affects the wetting behaviour of the binder on the powder surface. Knight (2001) reported

that larger contact angles (resulting in poor wetting) tended to lead to granules with lower strength.

- **Primary particle size and shape**: Van den Dries et al. (2003) showed that higher granule strength (reduced breakage) is associated with smaller primary particle size. Johansen and Schaefer (2001) showed that rounding of the primary particle shape (higher sphericity) reduces granule strength due to a reduction in particle interlocking.

5.2.1.2 Process and Design Parameters

Similarly, the process and design parameters that influence granule breakage can be grouped as follows:

- **Binder content**: It has been shown that increasing binder content results in decreased porosity as a result of the pores being filled with liquid (Iveson et al., 1996). Typically this reduction in porosity leads to an increase in granule strength and hence a higher resistance to breakage.

- **Binder addition method**: It is generally assumed that the method of binder addition (e.g. spray, pour-on, melt) has a considerable effect on granule properties and will influence rate processes (e.g. breakage) (Knight et al., 1998; Wauters, 2000)

- **Agitation intensity**: The general consensus is that increased agitation intensity (due to increased impeller speed) results in increased granule breakage (Eliasen et al., 1998; Knight et al., 2000).

- **Granulation time**: Schaefer (2001) reported that granule strength increases by gradual densification as the granulation process time is extended.

5.2.2 Deriving the Breakage Function

As seen from Equations 2.14 and 2.15 in chapter 2, breakage is described by the breakage function (b) and the breakage kernel (K_{break}). The breakage function describes how fragments, resulting from the breakup of granules, are distributed in terms of their volume.

There are several possible functional forms for this distribution, given either by continuous (e.g. normal or lognormal distribution) or discrete (e.g. binary) distributions. The breakage function used in this thesis is based on the work of Pinto et al. (2007); Pinto (2008); Pinto et al. (2008). Based on the probabilities of particles in a particular finite volume breaking to form daughter particles in one or more smaller finite volumes in the three-dimensional space, they performed a numerical operation that was able to describe the distribution of these fragments. Using these probabilities. semi-analytical solutions were derived for the triple integrals present in $\Re_{break}^{formation}$ (see Equation 2.14). thus eliminating the integrals altogether and aiding the numerical solution. In the next section, the development of the breakage kernel is described.

5.3 Mechanistic Kernel Development

A granule will break if the external stress during an impact exceeds the intrinsic strength of the granule. This is analogous to the Stokes' deformation number criteria for breakage whereby a granule will break if the applied kinetic energy during an impact is greater than the energy required for breakage (Iveson et al., 2001). Therefore the proposed kernel form is defined in Equations 5.1 and 5.2.

$$K_{break}(s,l,g) \propto \frac{external\,stress}{intrinsic\,strength} \tag{5.1}$$

$$K_{break}(s,l,g) = A \times \frac{external\,stress}{intrinsic\,strength} \tag{5.2}$$

where K_{break} is the breakage kernel, A is a proportionality constant and s, l, g are the respective volumes of solid, liquid and gas pertaining to individual finite volumes (bins). Units are dimensionless. If K_{break} is less than one, $K_{break} = 0$, as the external stress applied is less than the intrinsic strength of the granule and the granule does not break.

5.3.1 External Stress

To calculate the external stress (σ_{ext}), external forces (F_{ext}) acting on a granule and their area of contact (A_c) need to be evaluated. External stress is then defined in Equation 5.3.

$$\sigma_{ext}(s,l,g) = \frac{F_{ext}(s,l,g)}{A_c(s,l,g)} \tag{5.3}$$

5.3.1.1 Forces

The external forces on the granules/particles can occur via the following ways:

- **Case 1:** Forces due to fluid flow.
- **Case 2:** Forces due to particle-particle collisions.
- **Case 3:** Forces due to particle-wall collisions.
- **Case 4:** Forces due to particle-impeller collisions.

Case 1: Forces due to fluid flow

The force (F_{flu}) on a particle in laminar flow is defined in Equation 5.4.

$$F_{flu}(s,l,g) = 6\pi\mu r v \tag{5.4}$$

where r is the radius of the particle, v is the velocity of the particle relative to the fluid and μ is the viscosity of the fluid. The force (F_f) on a particle in turbulent flow is defined in Equation 5.5. Although Equation 5.5 is a simplistic representation of turbulent forces, it is sufficient for the purposes of this work due to the fact that the overall forces of fluid flow are negligible compared to the other forces (as will be discussed in the following sections).

$$\begin{aligned} F_f(s,l,g) &= \frac{1}{2}\rho C_d A v^2 \\ &= \frac{1}{2}\pi\rho C_d r^2 v^2 \end{aligned} \tag{5.5}$$

Here ρ is the density of the fluid and C_d is the drag coefficient which for a spherical particle is 0.47. C_d increases as non-sphericity increases. Reynold's number (Re) which is defined

in Equation 5.6 is calculated to determine if conditions are either laminar (see Figure 5.1a) or turbulent (see Figure 5.1b). L is the characteristic length.

$$Re = \frac{\rho v L}{\mu} \tag{5.6}$$

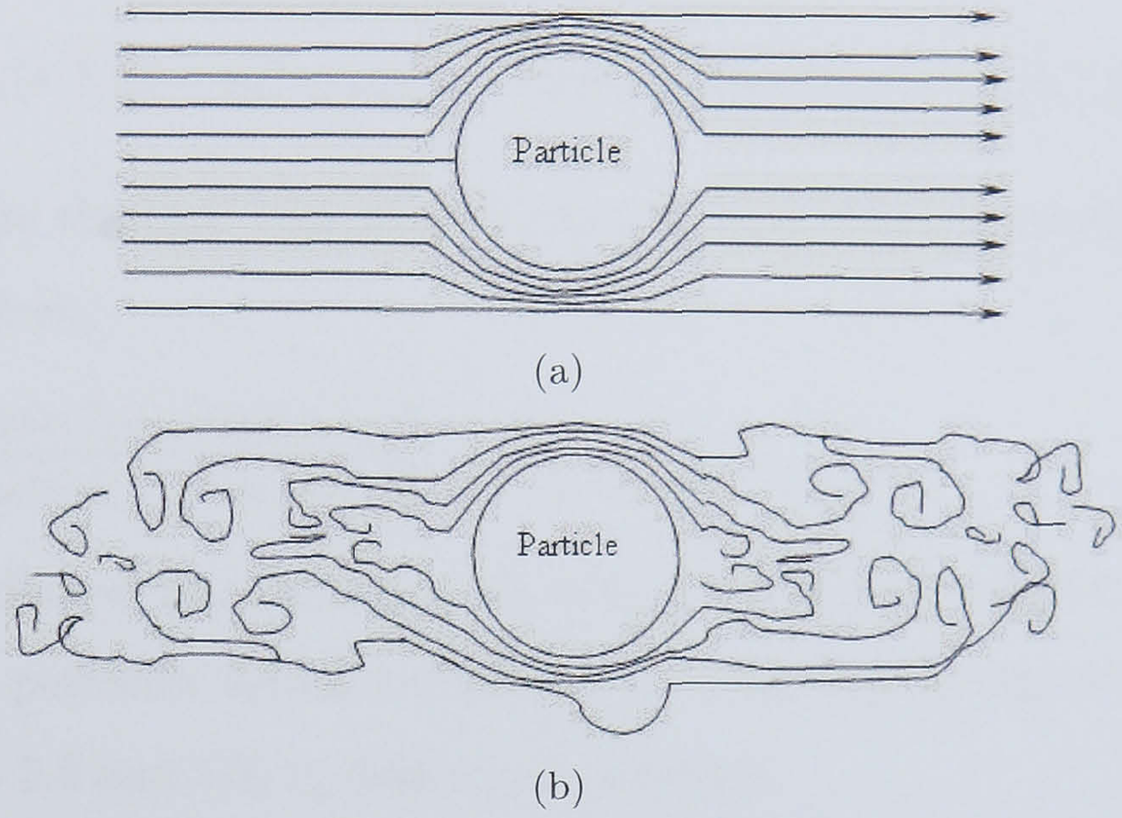

Figure 5.1: (a) laminar flow consists of isolated layers of air with different velocities, (b) turbulent flow consists of unorganised motions of air molecules which often change their velocities due to interactions with one another.

Case 2: Forces due to particle-particle collisions

In the case of particle-particle collisions, a particle with mass m_a and initial velocity u_a collides head-on with another particle of mass m_b and initial velocity u_b (see Figure 5.2).

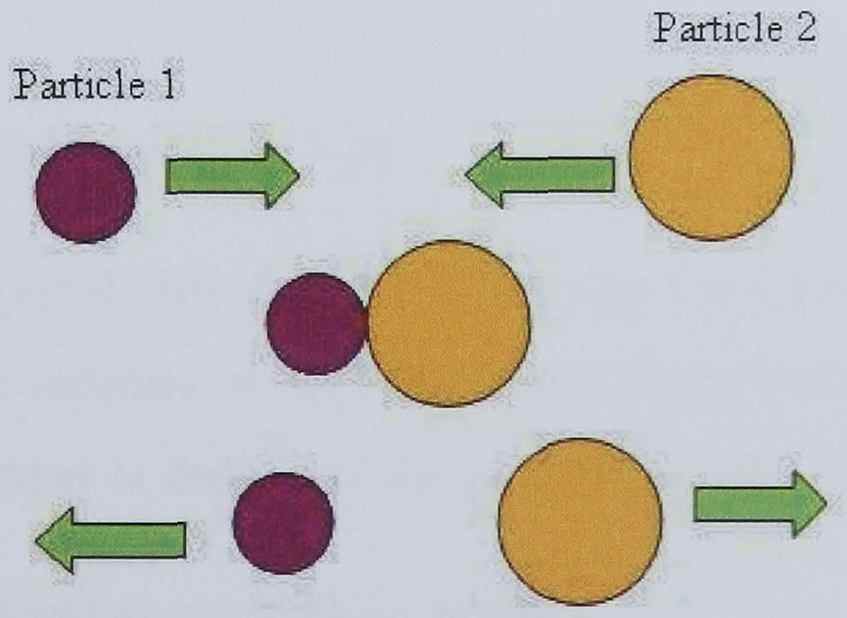

Figure 5.2: Schematic representation of 1-dimensional particle-particle collisions.

Based on the conservation of momentum, momentum before impact $\equiv$ momentum after impact. Assuming that the total energy input into the system is constant, $u_{a,b}$ (initial

velocities of either particle) can be defined in Equation 5.7 as

$$u_{a,b}(s,l,g) = \left(\frac{1}{m_{a,b}(s,l,g)}\right)^{0.5} \tag{5.7}$$

where m is the mass of either particle. Therefore,

$$m_a(s,l,g)(v_a(s,l,g) - u_a(s,l,g)) = m_b(s,l,g)(v_b(s,l,g) - u_b(s,l,g)) \tag{5.8}$$

where v_a and v_b are the final velocities of particles a and b respectively. which are yet to be determined. Given,

$$e(s,l,g) = \frac{v_b(s,l,g) - v_a(s,l,g)}{u_a(s,l,g) - u_b(s,l,g)} \tag{5.9}$$

where e is the coefficient of restitution whereby $e = 1$ denotes perfectly elastic collisions and $e = 0$ denotes perfectly inelastic collisions. e is material specific and is known apriori. Solving Equations 5.8 and 5.9, v_a and v_b are obtained.

Once v_a and v_b are obtained, there are many approaches to modelling the collision interactions between particles. In this work, a harmonic spring model that is realistically able to model collisions between particles is used (Luding et al., 1994). Two particles interact when their relative distance $r_{ab} = |\mathbf{r}_{ab}|$ (where r_{ab} points from the centre of a to the center of b) is smaller than the sum of their radii (the radius of the particles R_a and R_b). In this regime, $R_a + R_b > r_{ab}$, an elastic restoration force (F_{el}) can be defined as seen in Equation 5.10.

$$F_{el}(s_a, l_a, g_a, s_b, l_b, g_b) = -k[(R_a + R_b) - r_{ab}]\mathbf{n}_{ab} \tag{5.10}$$

where $\mathbf{n}_{ab} = \frac{\mathbf{r}_{ab}}{r_{ab}}$ is the normal direction of contact and k is a force constant. s_a, l_a, g_a, s_b, l_b, g_b are the component volumes of particles a and b respectively. Secondly, a frictional force in the normal direction is defined as seen in Equation 5.11

$$F_{fric}(s_a, l_a, g_a, s_b, l_b, g_b) = -\gamma_N \tilde{m}[\mathbf{v}_{ab} \cdot \mathbf{n}_{ab}]\mathbf{n}_{ab} \tag{5.11}$$

where $\mathbf{v}_{a,b}$ is the relative velocities of particles a and b, $\tilde{m}$ is twice the reduced mass of particles a and b (i.e., $\frac{2m_a m_b}{m_a + m_b}$), $d = R_a + R_b$, γ_N is the damping coefficient. $\mathbf{r}_{a,b}$ is then defined in Equation 5.12, where x_{max} is the maximum depth of penetration and considering

nonlinear interactions between particles, is defined in Equation 5.13 (Luding et al., 1994). Based on the Hertz interaction law, $\beta = 0.5$ (Luding et al., 1994). $\bar{E} = \frac{E}{[3(1-\sigma^2)]}$. where E is the Young's modulus and σ is the Poisson ratio. d is the sum of the radii R_a and R_b. Both E and σ are material specific and are known apriori.

$$\mathbf{r}_{ab} = R_a + R_b - x_{max} \tag{5.12}$$

$$x_{max} = \left[1 + \frac{\beta}{2}\right]^{\frac{1}{2+\beta}} \left[\frac{m_a}{\bar{E}d^{1-\beta}}\right]^{\frac{1}{2+\beta}} (u_a)^{\frac{2}{2+\beta}} \tag{5.13}$$

Similarly, the collision time (t_c) is defined in Equation 5.14

$$t_c = I(\beta)\frac{x_{max}}{u_a} \tag{5.14}$$

where $I(\beta) = 2.94$ (Luding et al., 1994). Subsequently, k and γ_N are obtained as follows:

$$k = \frac{m_a}{2}\left(\frac{\pi}{t_c}\right)^2 \tag{5.15}$$

$$\gamma_N = \frac{-2lne}{t_c} \tag{5.16}$$

The total external force as a result of particle-particle collisions is then obtained as seen in Equation 5.17.

$$F_{ext}(s_a, l_a, g_a, s_b, l_b, g_b) = F_{el}(s_a, l_a, g_a, s_b, l_b, g_b) + F_{fric}(s_a, l_a, g_a, s_b, l_b, g_b) \tag{5.17}$$

Case 3: Forces due to particle-wall collisions

In the case of particle-wall collisions, a particle a collides with the wall (interior surfaces) of the granulator (denoted with subscript b) (see Figure 5.3). Forces are derived as in case 2 with a few minor simplifications. As a result of the wall being a flat plane, $d \rightarrow \frac{d}{2}$, $\tilde{m} \rightarrow m_a$, $\mathbf{r}_{ab} \rightarrow \mathbf{r}_a$. As a result of the wall being stationary ($u_b = 0$) and $m_b >> m_a$. the conservation of momentum equation can also be simplified such that final velocity of particle a can be calculated as $v_a = -e \times u_a$. Total external force is then defined as

$$F^{ext}(s_a, l_a, g_a) = F^{el}(s_a, l_a, g_a) + F^{fric}(s_a, l_a, g_a) \tag{5.18}$$

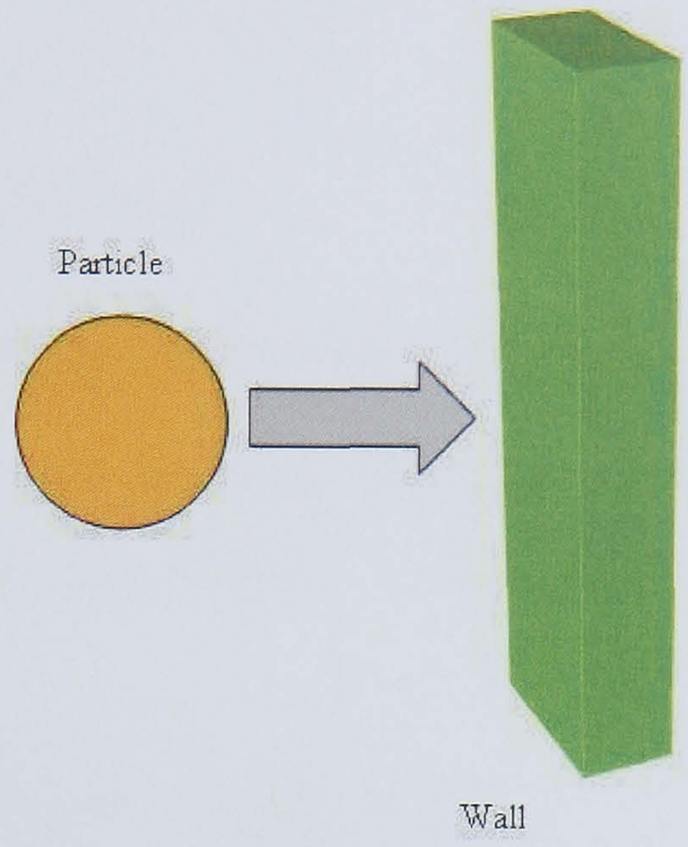

Figure 5.3: Schematic representation of 1-dimensional particle-wall collisions.

Case 4: Forces due to particle-impeller collisions

In the case of particle-wall collisions, a particle a collides with the impeller surfaces (denoted with subscript b). Forces are derived as in case 3 with a minor modification. Unlike particle-wall collisions, although $m_b >> m_a$, $u_b \neq 0$. As a result, the conservation of momentum equation can now be simplified such that $v_a = e \times 2u_b$. Total external force is then defined as

$$F^{ext}(s_a, l_a, g_a) = F^{el}(s_a, l_a, g_a) + F^{fric}(s_a, l_a, g_a) \tag{5.19}$$

For all cases of particle-particle/wall/impeller collisions, 1-dimensional head-on collisions are considered so as to effect the maximum force experienced by the particle(s). The kernel can also be adapted to take into account 2-dimensional collisions (i.e., particles colliding at an angle) and/or 1-dimensional collisions of a faster moving particle hitting a slower moving particle as they move in the same direction.

5.3.1.2 Contact Area

The contact area in which the different forces act upon are derived for the three cases:

Case 1: Contact area for forces due to fluid flow

The force acts on the entire particle surface. Therefore contact area (A_c) is defined in

Equation 5.20 as,

$$A_c\left(s_a, l_a, g_a\right) = 4\pi R_a^2\left(s_a, l_a, g_a\right) \tag{5.20}$$

Case 2: Contact area for forces due to particle-particle collisions

In the case of particle-particle collisions, the contact area upon impact is circular in shape (Stachowiak and Batchelor, 2005). A reduced Young's modulus ($E^{'}$) is first defined in Equation 5.21 as,

$$E^{'}\left(s_a, l_a, g_a\right) = \left(\frac{1}{2}\left[\frac{1-\sigma_a^2}{E_a} + \frac{1-\sigma_b^2}{E_b}\right]\right)^{-1} \tag{5.21}$$

where σ_a and σ_b are the Poisson ratios of particles a and b; and E_a and E_b are the Young's moduli for particles a and b. A reduced radius ($R^{'}$) is then defined in Equation 5.22

$$R^{'}\left(s_a, l_a, g_a\right) = \left[2\left(\frac{1}{R_A} + \frac{1}{R_B}\right)\right]^{-1} \tag{5.22}$$

where R_a and R_b are the radii of particles a and b respectively. Contact radius (r_c) and contact area (A_c) are then defined respectively in Equations 5.23 and 5.24 as,

$$r_c(s_a, l_a, g_a) = \frac{3F_{ext}(s_a, l_a, g_a)R^{'}}{E^{'}} \tag{5.23}$$

$$A_c(s_a, l_a, g_a) = \pi r_c^2(s_a, l_a, g_a) \tag{5.24}$$

Cases 3 and 4: Contact area for forces due to particle-wall/impeller collisions

In the case of particle-wall collisions and particle-impeller collisions, the contact area upon impact is elliptical in shape (Stachowiak and Batchelor, 2005). A reduced radius ($R^{'}$) is defined in Equation 5.25 as follows:

$$R^{'} = \left[\frac{1}{R_{Ax}} + \frac{1}{R_{Ay}}\right]^{-1} \tag{5.25}$$

where R_{Ax} and R_{Ay} are the radii of particle a in the x and y directions. R_{Bx} and $R_{By} = \propto$ since one plane (wall or impeller) has an infinite radius of curvature in both directions.

The reduced Young's modulus $E^{'}$ is defined as in case 2. Contact area A_c is then defined in Equation 5.26,

$$A_c(s_a, l_a, g_a) = \pi AB \tag{5.26}$$

where A and B are the radii of the eclipse in the x and y directions. A and B are defined in Equations 5.27 and 5.28,

$$A = \left[\frac{6\bar{k}^2\bar{\varepsilon}FR^{'}}{\pi E^{'}}\right]^{\frac{1}{3}} \tag{5.27}$$

$$B = \left[\frac{6\bar{\varepsilon}FR^{'}}{\pi\bar{k}E^{1}}\right]^{\frac{1}{3}} \tag{5.28}$$

where $\bar{\varepsilon} = 1.0003 + \frac{0.5968R_x}{R_y}$ and $\bar{k} = 1.0339\left(\frac{R_x}{R_y}\right)^{0.636}$. $\frac{R_x}{R_y} = 1$ for spherical particles. $\bar{\varepsilon}$ is a simplified integral and $\bar{k}$ is an ellipticity parameter.

5.3.2 Intrinsic Strength

The different types of bonds that may exist within the types of granules are classified as follows: 1) forces due to immobile films, 2) forces due to mobile liquid bridges, 3) forces due to solid bridges, 4) forces due to attractive effects between solid particles and 5) forces due to mechanical interlocking between solid particles. The relative importance of these bonding forces varies from case to case, depending on the type and size of the granule. In the case of wet granules, based on theoretical analysis, contributions by 1), 3), 4) and 5) are usually negligible and the strength of wet granules are primarily determined by liquid bridge forces (Reynolds et al., 2005). The liquid bridge is therefore responsible for holding two or more particles together (Simons, 2007; Willett et al., 2007; Simons et al., 1994; Iveson, 2002) (see Figure 5.4).

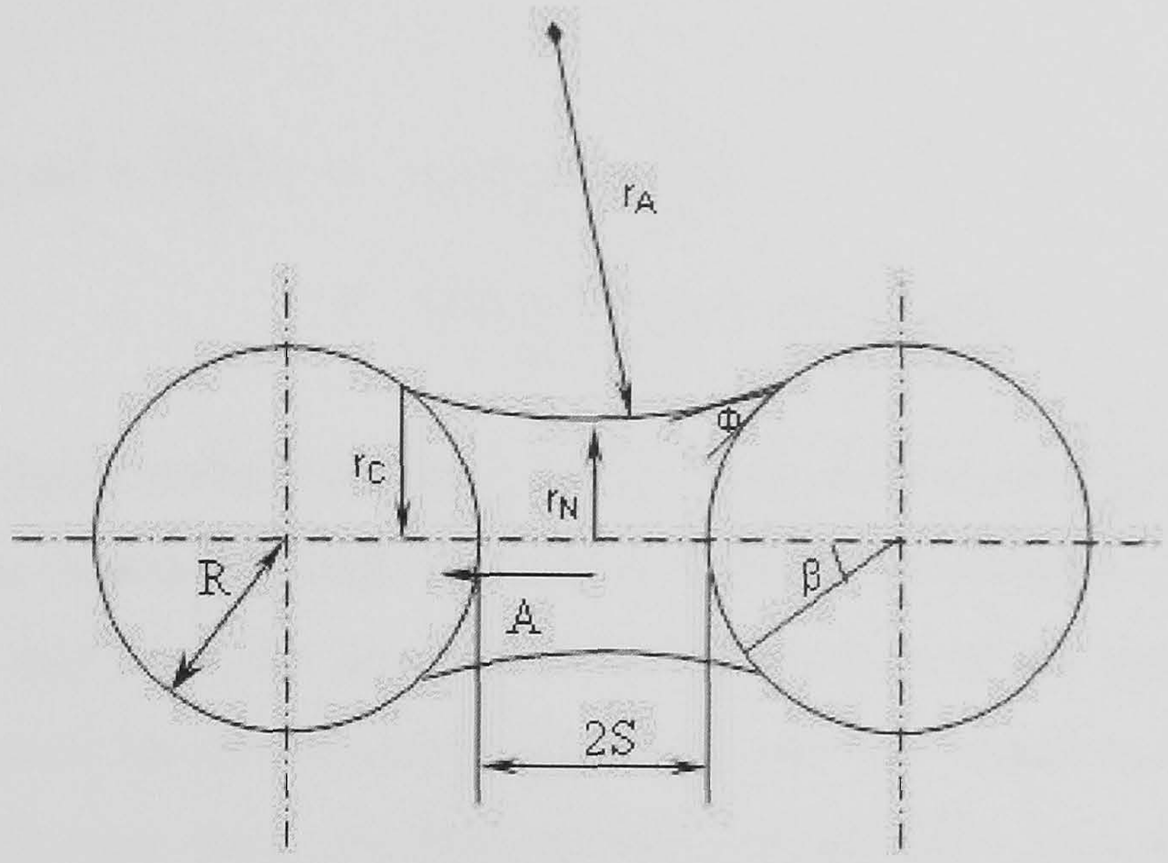

Figure 5.4: Schematic of a liquid bridge between two equi-sized particles.

In the current breakage model, any granule from a particular finite volume can break into m daughter particles of volume fraction θ_a such that $\sum_{a=1}^{m} \theta_a = 1$. As a first attempt to derive the breakage kernel, $m = 2$ and $\theta_1 = \theta_2 = 0.5$. Therefore, this means that any granule from any finite volume comprises of two smaller equi-sized particles held together by one liquid bridge. The following theoretical development of the kernel in this study is based on the above qualification. However, the theory can be extended to handle multiple fragments ($m > 2$) which would result in multiple liquid bridges and possibly unequal-sized fragments.

The liquid bridge forces (F_{int}) are in turn made up of capillary forces (F_{cap}), viscous forces (F_{vis}) and frictional forces (F_f). Viscous forces are an important factor to account for, as liquid bridges cannot be regarded as stationary and the inter-particle attractive force depends on the viscosity of the binder liquid. The effects of buoyancy forces are negligible (Princen, 1968) and as a result are not accounted for. Similarly the effects of gravity are negligible, and therefore neglected (Willett et al., 2007). F_{cap} consists of two components, the force due to surface tension (F_γ) and the force due to reduced hydrostatic pressure (F_p). The capillary suction pressure (ΔP_{cap}) across the liquid-vapour interface is given by the Laplace-Young equation (Simons, 2007; Willett et al., 2007) and is defined in Equation 5.29,

$$\Delta P_{cap}(s_a, l_a, g_a) = \frac{2\gamma_{LV}}{r} = \gamma_{LV}(\frac{1}{r_A} + \frac{1}{r_N}) = \gamma_{LV}(\frac{\ddot{y}}{[1+\dot{y}^2]^{\frac{3}{2}}} + \frac{1}{y(1+\dot{y}^2)^{\frac{1}{2}}}) \quad (5.29)$$

where γ_{LV} is the liquid surface tension, r is the curvature of the bridge surface which can be calculated from the two principal radii of curvature of the surface, r_A and r_N as shown in Figure 5.4. $\dot{y}$ and $\ddot{y}$ are the first and second derivatives of the liquid bridge profile. Equation 5.29 cannot be solved analytically and either the boundary or gorge methods have to be used to solve them numerically (Hotta et al., 1974; Lian et al., 1993). The latter method gave a better estimate of the total force (Lian et al., 1993) and therefore is used in this work. F_γ, F_p and F_{cap} are then defined in Equations 5.30-5.32.

$$F_\gamma(s_a, l_a, g_a) = 2\pi r_A \gamma_{LV} \quad (5.30)$$

$$F_p(s_a, l_a, g_a) = -\pi r_A^2 \Delta P_{cap} = -\pi r_1^2 \gamma_{LV}[\frac{1}{r_A} + \frac{1}{r_N}] \quad (5.31)$$

$$F_{cap}(s_a, l_a, g_a) = F_\gamma + F_p = 2\pi r_A \gamma_{LV} - \pi r_A^2 \gamma_{LV}[\frac{1}{r_A} + \frac{1}{r_N}] \quad (5.32)$$

r_A and r_N are defined in Equations 5.33 and 5.34,

$$r_A(s_a, l_a, g_a) - r_N(s_a, l_a, g_a) = \frac{A}{tan(\frac{\pi}{2} - \beta - \phi)} + Rsin\beta \quad (5.33)$$

$$r_N(s_a, l_a, g_a) = (-1)^n\{A^2 + [Rsin\beta - (r_A - r_N)]^2\}^{\frac{1}{2}} \quad (5.34)$$

where ϕ is the contact angle, β is the half-filled angle and R is the reduced radius defined in Equation 5.22. n and A are defined in Equation 5.35 and 5.36 respectively.

$$n = \left[0, \left(\beta + \phi\right) > \frac{\pi}{2}\right) \; or \; 1, (\beta + \phi) <= \frac{\pi}{2}\Big)\Big] \tag{5.35}$$

$$A(s_a, l_a, g_a) = S + R(1 - cos\beta) \tag{5.36}$$

where S is half of the separation distance (see Figure 5.4) and is defined in Equation 5.37 as,

$$S(s_a, l_a, g_a) = \left[1 + \frac{\pi}{2}\right] \times V_{br}^{\frac{1}{3}} \tag{5.37}$$

The liquid bridge volume (V_{br}) is known apriori and is determined by the amount of liquid on the surface (surfaces of the two smaller particles that comprise of the larger granule) that can be used to form the liquid bridge. If the volume of air (in both smaller particles) is greater than the volume of liquid (in both smaller particles) for a particular finite volume, no liquid is available to form liquid bridges. Available liquid is defined as the difference between volumes of liquid and air. V_{br} is then defined in Equation 5.38 as

$$V_{br}(s_a, l_a, g_a) = 2\pi\Bigg[A(r_A - r_N)^2 + r_A^3\left(\frac{A}{r_A} - \frac{A^3}{3r_A^3}\right) + r_A^2(r_A - r_A)sin^{-1}\left(\frac{A}{r_A}\right) + (-1)^n A(r_A - r_N)(r_A^2 - A^2)^{\frac{1}{2}} - R(A - S)^2 - \frac{(A - S)^3}{3}\Bigg] \tag{5.38}$$

Knowing V_{br}, and substituting Equations 5.36, 5.37, 5.34, 5.33 in Equation 5.38, β can be solved for iteratively for each bin. Thereafter, Equations 5.33 and 5.34 can be solved for r_A and r_N.

The contact radius r_c, is defined in Equation 5.39 as,

$$r_c(s_a, l_a, g_a) = Rsin\beta \tag{5.39}$$

The viscous force F_{vis}, is defined in Equation 5.40 as,

$$F_{vis}(s_a, l_a, g_a) = \frac{3}{2}\pi\mu R^2 \frac{1}{S}\frac{da}{dt} \tag{5.40}$$

where μ is the liquid viscosity and $\frac{da}{dt}$ is the half-gap velocity which without exact knowledge, is a potential tuning parameter. The frictional force, which is due to the work of

adhesion on liquid and the corresponding inter-particle contact area is defined in Equation 5.41 as,

$$F_f(s_a, l_a, g_a) = \gamma_{LV}(cos\theta + 1)\frac{\pi r_c^2 \times \frac{1}{circ}}{S} \tag{5.41}$$

where $circ$ is the circularity index of the particle. For a sphere, $circ = 1$ and $circ \rightarrow 0$ as the non-sphericity increases. The total force of the liquid bridge is then defined in Equation 5.42 as,

$$F_{int}(s_a, l_a, g_a) = F_{cap} + F_{vis} + F_f \tag{5.42}$$

The intrinsic strength due to the liquid bridge is then defined in Equation 5.43 as,

$$\sigma_{liq}(s_a, l_a, g_a) = \frac{F_{int}}{2\pi r_c^2} \tag{5.43}$$

When an external force is applied to the particles, there exist solid-solid attractions (known as cohesive strength) which need to be overcome. This is defined in Equation 5.44 as,

$$\sigma_c(s_a, l_a, g_a) = \frac{2\gamma_s 4\pi R^2}{V_{part}} \tag{5.44}$$

where γ_s is the surface energy of the solid and V_{part} is the volume of the particle. Therefore, the intrinsic strength is now defined in Equation 5.45 as,

$$\sigma_{int}(s_a, l_a, g_a) = \sigma_{liq} + \sigma_c \tag{5.45}$$

5.3.3 Overall Kernel Formulation

In the above section, σ_{ext} and σ_{int} were derived based on first principles allowing for the formulation of the overall breakage kernel. For cases 1, 3 and 4, K_{break} is defined in Equation 5.46.

$$K_{break}(s_a, l_a, g_a) = \frac{\sigma_{ext}(s_a, l_a, g_a)}{\sigma_{int}(s_a, l_a, g_a)} \tag{5.46}$$

For case 2, K_{break} is defined in Equation 5.47.

$$K_{break}(s_a, l_a, g_a, s_b, l_b, g_b) = \frac{\sigma_{ext}(s_a, l_a, g_a, s_b, l_b, g_b)}{\sigma_{int}(s_a, l_a, g_a)} \tag{5.47}$$

Although the external forces for each of the cases have been derived separately for the different cases, the actual external forces applied on the particle are based on the probability of a particle of characteristic (s_a, l_a, g_a) hitting either a particle of characteristic (s_b, l_b, g_b), a wall surface, or the impeller surface. Fluid forces act in addition to these particle-particle, particle-wall and particle-impeller forces. The system is assumed to be free in-space such that each particle is able to collide with another particle, a wall or the impeller. A probability (in terms of the surface area) is assigned for each type of collision that may occur. Therefore the three-dimensional kernels derived for cases 1, 3 and 4 and the six-dimensional kernel derived for case 2 are transformed into an effective 3-dimensional kernel (K^{eff}_{break}) as defined in Equation 5.48,

$$K^{eff}_{break}(s_a, l_a, g_a) = \Sigma^{s_{upper}}_{s_b=1} \Sigma^{l_{upper}}_{l_b=1} \Sigma^{g_{upper}}_{g_b=1} [\frac{\sigma^{particle}_{ext}(s_a, l_a, g_a, s_b, l_b, g_b)}{\sigma_{int}(s_a, l_a, g_a)} \times F(s_b, l_b, g_b) \times N_a \times \frac{SA(s_b, l_b, g_b)}{TSA + WA + IA}] + \left[\frac{\sigma^{wall}_{ext}(s_a, l_a, g_a)}{\sigma_{int}(s_a, l_a, g_a)} \times \frac{WA}{TSA + WA + IA}\right] + \left[\frac{\sigma^{impeller}_{ext}(s_a, l_a, g_a)}{\sigma_{int}(s_a, l_a, g_a)} \times \frac{IA}{TSA + WA + IA}\right] + \left[\frac{\sigma^{fluid}_{ext}(s_a, l_a, g_a)}{\sigma_{int}(s_a, l_a, g_a)}\right] \tag{5.48}$$

where F is the particle density, WA is the total wall surface area, TSA is the total surface area of all the particles, SA is the surface area of an individual particle, IA is the impeller surface area and N_a is Avagardo's constant, s_{upper}, l_{upper} and g_{upper} are the upper limits of the finite volumes in each of the three solid, liquid and gas dimensions. $K^{break}_{eff}(s_a, l_a, g_a)$ is updated at each time step as $F(s_a, l_a, g_a)$ changes at each time step. In the next section, simulation results of the breakage model are presented. The mechanistic kernel is qualitatively compared with an existing empirical and semi-empirical kernel from the literature. Thereafter, effects of material properties and process/design parameters on granule characteristics are examined.

5.4 Simulation Results of the Breakage Model

All model simulations were carried out on a 2GHz intel dual-core single processor desktop computer with 1GB RAM, using the intel fortran compiler. Simulation time was 1800 s. Table 5.1 presents the nominal values of all material properties and process/design parameters used in the simulations. The values correspond to a hypothetical case of limestone as the primary powder, water as the liquid binder, steel blades as the impeller, and glass walls as the interior surfaces. High-shear laboratory-scale dimensions are assumed for the granulator geometry. Any viscosities and surface tensions reported are obtained for conditions at room temperature and pressure (r.t.p).

Table 5.1: Nominal values of material properties and process/design parameters.

Property/Parameter	**Value**	(Unit)
γ_s	4.48×10^{-2}	(Nm^{-2})
γ_l	7.28×10^{-2}	(Nm^{-2})
μ_l	1.0×10^{-3}	(Pa.s)
ϕ	7.54×10^{-1}	(rad)
ρ_s	2.72×10^{3}	(Kgm^{-3})
ρ_l	1.0×10^{3}	(Kgm^{-3})
μ_a	1.85×10^{-5}	(Pa.s)
E_p	4.50×10^{10}	(Pa)
E_w	7.0×10^{10}	(Pa)
E_i	2.0×10^{11}	(Pa)
σ_p	0.22	(-)
σ_w	0.17	(-)
σ_i	0.30	(-)
e_p	0.60	(-)
e_w	0.50	(-)
e_i	0.80	(-)
$circ$	1.0	(-)
C_d	0.47	(-)
θ	0.50	(-)
TSA	2.02×10^{-1}	(m^2)
WA	6.13×10^{-1}	(m^2)
IA	3.06×10^{-1}	(m^2)
D_{lower}	246	(μm)
A	1.5×10^{-8}	(s^{-1})
$\frac{dA}{dt}$	5.0×10^{-2}	(ms^{-1})

[2]TSA refers to the total surface area of the initial seed particles. TSA will change as the particle density changes during the course of granulation.

5.4.1 Comparison of the Mechanistic Kernel with Empirical and Semi-Empirical Kernels

Figures 5.5a-c depict the simulated shape of the mechanistic breakage kernel (see Equation 5.48) with respect to two dimensions (i.e., solid-liquid, solid-gas or liquid-gas) keeping the third dimension constant (i.e., solid, liquid or gas). The shapes observed are in agreement with expected phenomenological behaviour. In Figure 5.5a, for a very small liquid content and constant gas volume, it can be observed that K_{break}^{eff} decreases marginally as solid volume increases. This is attributed to the fact that at very low liquid contents, the strength of the bond is mainly due to the cohesive strength between solid particles. Hence increase in solid volume increases the cohesive strength. For the case of a large liquid content, K_{break}^{eff} increases as solid volume increases. This is because, in the current case, the strength of the bond is mainly due to the liquid bridges and as solid volume increases, the liquid bridge strength decreases (due to a smaller liquid-to-solids ratio). The sharp peak seen in the figure as solid volume and liquid volume approach zero is due to negligible solid cohesive forces and liquid bridge forces that result in an exponential increase in K_{break}^{eff}. In Figure 5.5b, it can be seen that there is an increase in K_{break}^{eff} as both solid and gas volumes increase. This is due to the fact that at a constant liquid volume, increases in solid and gas volumes cause the liquid bridge strength to decrease significantly. In Figure 5.5c, it is observed that there is an increase in K_{break}^{eff} as liquid volume decreases and gas volume increases. This is because liquid directly affects the liquid bridge strength and gas volume adversely affects the liquid bridge strength.

The above mechanistic breakage kernel is then qualitatively compared with an existing empirical and semi-empirical breakage kernel from the literature. The empirical kernel is a power law expression based on experimental observations proposed by Pandya and Spielman (1983) and is defined in Equation 5.49.

$$K_{break}^{empirical}(s,l,g) = P_1 G(R(s,l,g))^{P_2} \tag{5.49}$$

where $K_{break}^{empirical}$ is the breakage kernel, P_1 and P_2 are adjustable constants, G is the shear

rate in the system and R is the particle radius. The semi-empirical kernel used in the works of Selomuya et al. (2003) and Soos et al. (2006) is defined in Equation 5.50 as.

$$K_{break}^{semi-empirical}(s,l,g) = (\frac{4}{15\pi})^{\frac{1}{2}} \times G \times (-\frac{B}{G^2 R(s,l,g)}) \tag{5.50}$$

where B is an adjustable parameter. Values used for all adjustable constants and shear rates are taken from Table 2 in Soos et al. (2006). Figures 5.49 a-c depict the simulated shapes of the empirical breakage kernel with respect to two dimensions, keeping the third constant. It can be seen that there is no distinction between the three graphs and that there is a monotonic increase of the kernel metric in all three dimensions. This is incongruous to expected phenomenological behaviour. Firstly, although the increase in liquid content increases the volume of the particle, it also increases the liquid bridge strength. Secondly, increase in the solid volume would reduce the overall change in momentum upon collision (assuming total kinetic energy is constant), thereby resulting in a lesser impact force. Both these reasons negate a straightforward monotonic increase in the solid and liquid dimensions. Similarly, the shapes in Figures 5.50, depict the shapes of the semi-empirical breakage kernel. It can be seen that the kernel metric is approximately constant in all three dimensions and spatial variations, effectively likening it to a constant kernel which is unable to account for the phenomenological behaviour of granule breakage. However, the above described empirical and semi-empirical kernels have been quantitatively validated (Soos et al., 2006) and in another study a constant breakage kernel was used to quantitatively describe breakage kinetics (Tan et al., 2004). This essentially shows that kernels that are fundamentally unsound, can still predict breakage kinetics, by tuning adjustable constant(s) that serve to compensate for any phenomenological mismatch. This approach is the spawn of a lack of a mechanistic understanding of the granule breakage mechanism. However, a mechanistic understanding/model of the breakage process is preferable due to advantages offered such as the predictive capabilities of the model. In the following sections/chapter the breakage kernel is further tested both qualitatively and quantitatively to ascertain its validity and use in the population balance framework.

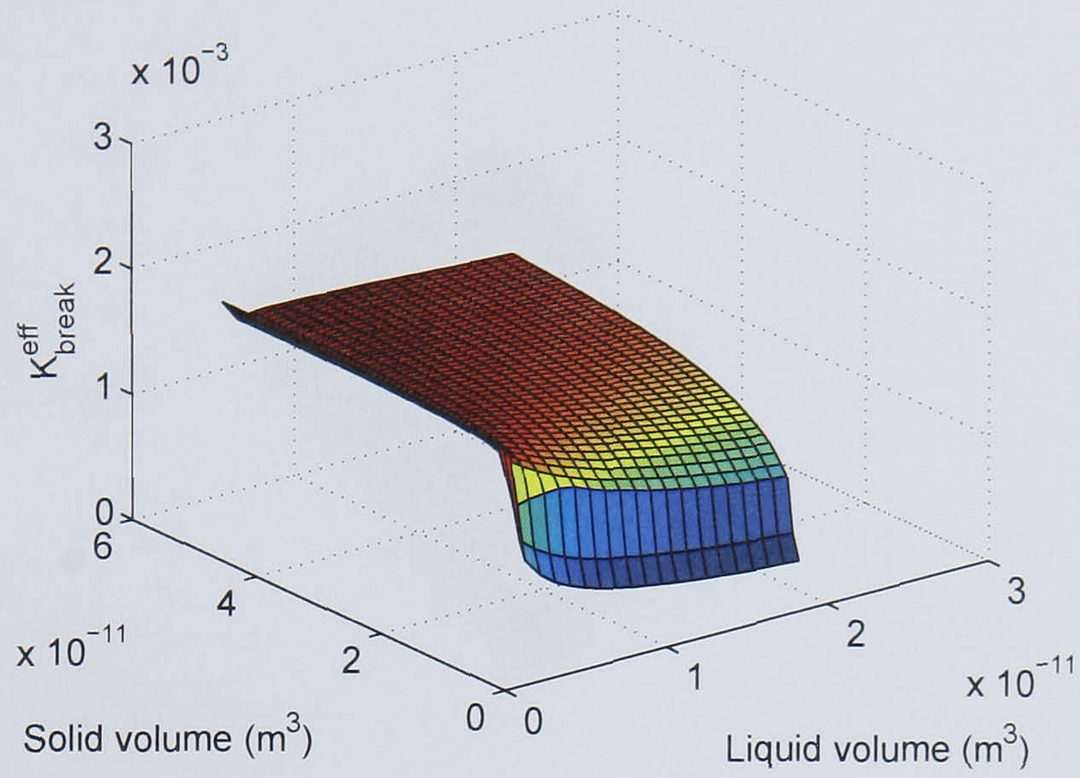

(a)

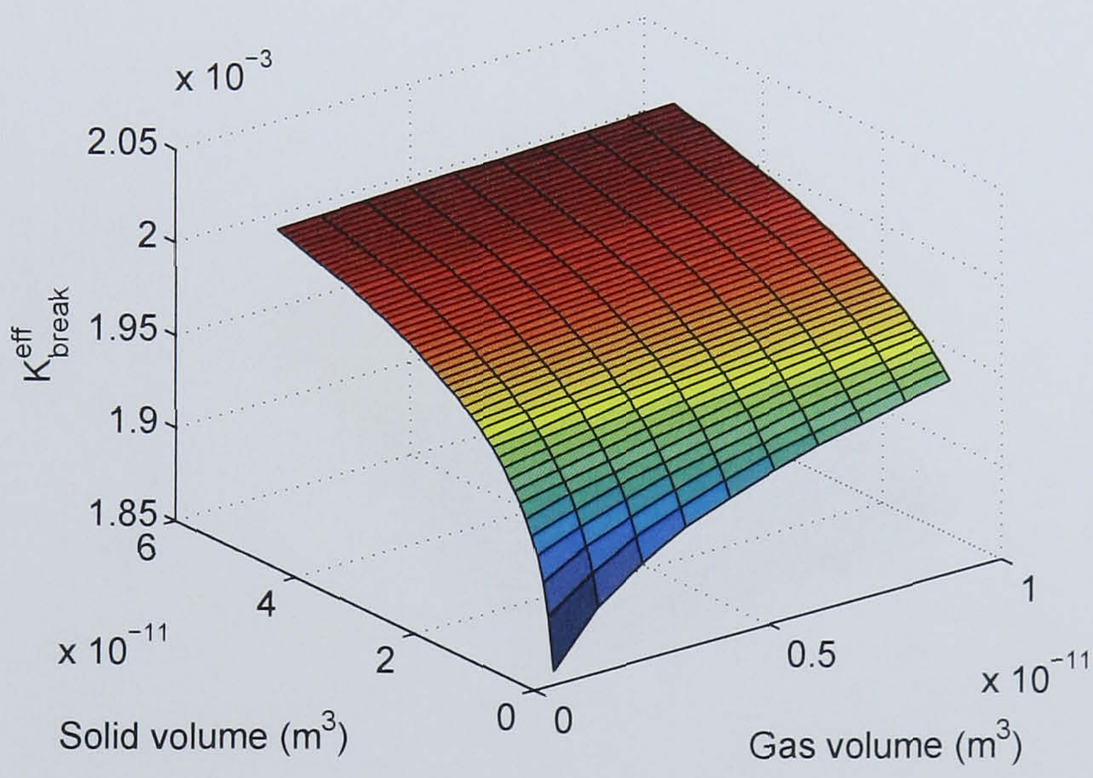

(b)

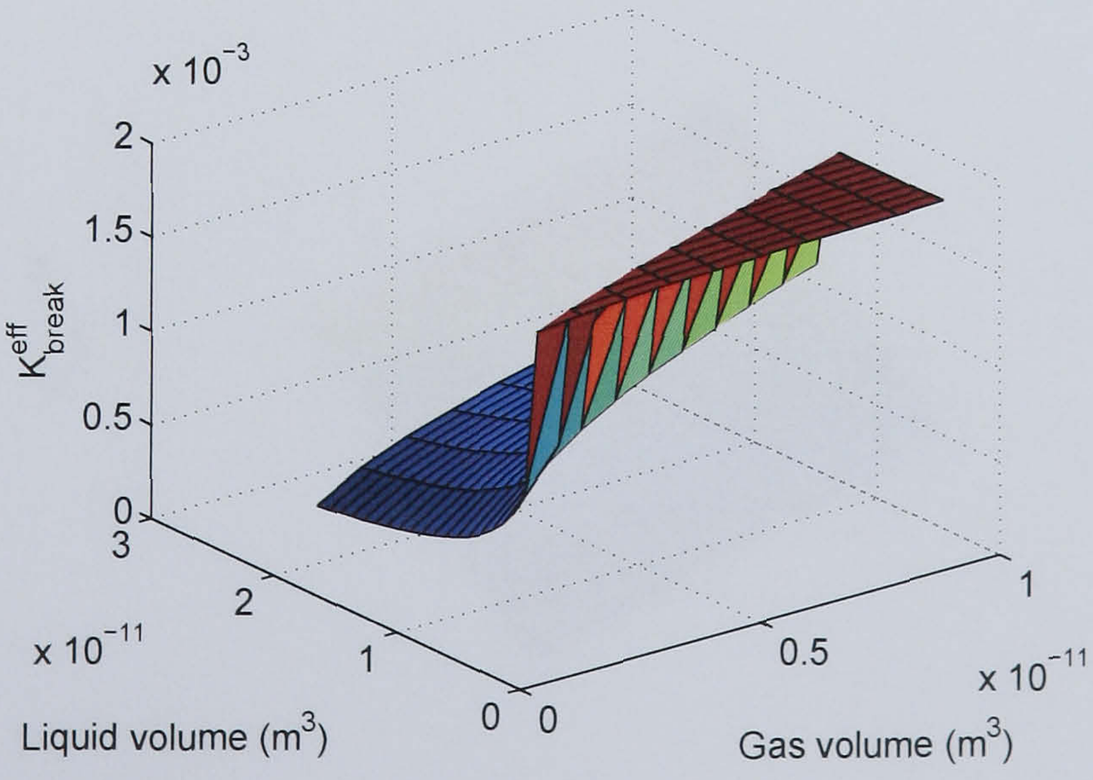

(c)

Figure 5.5: Shape of the mechanistic kernel (Equation 5.48) with respect to two dimensions keeping the third constant: (a) volume of gas constant, (b) volume of liquid constant and (c) volume of solid constant.

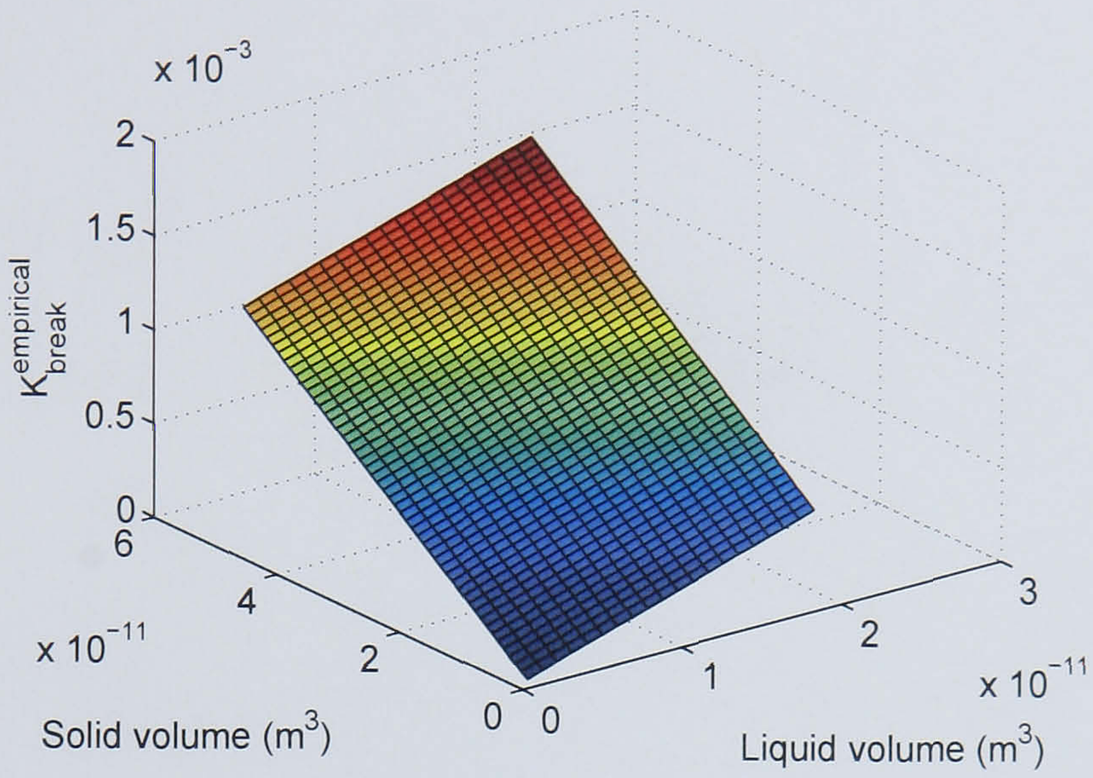

(a)

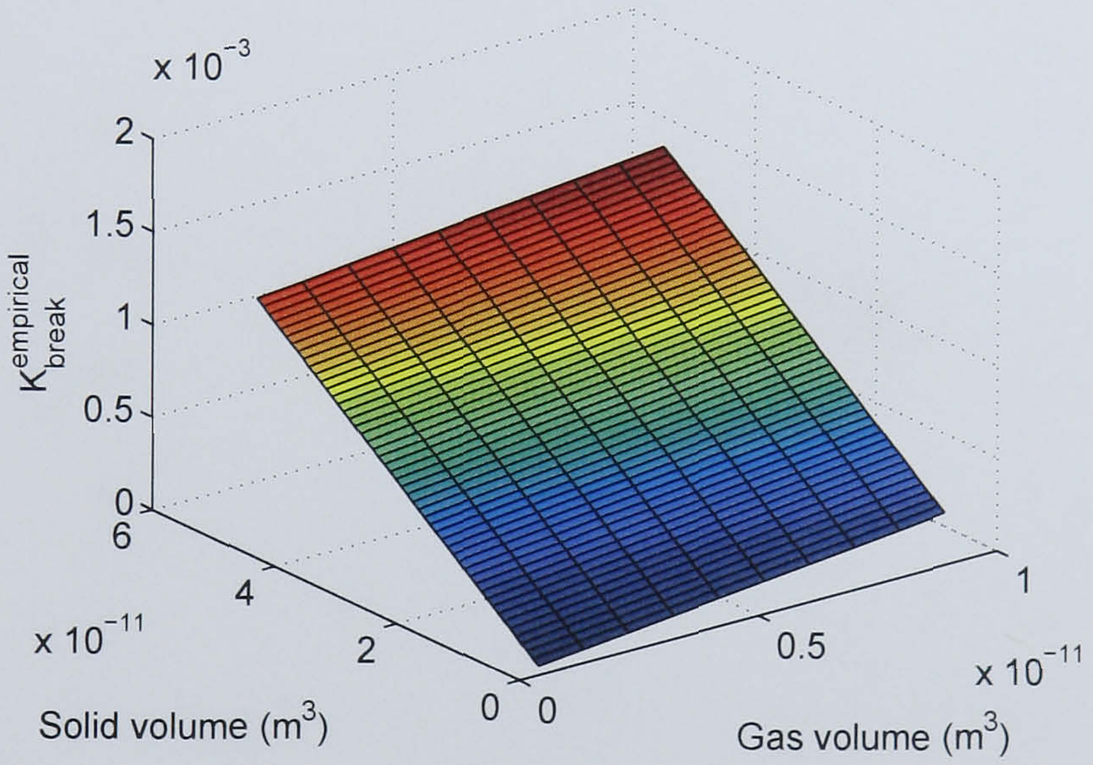

(b)

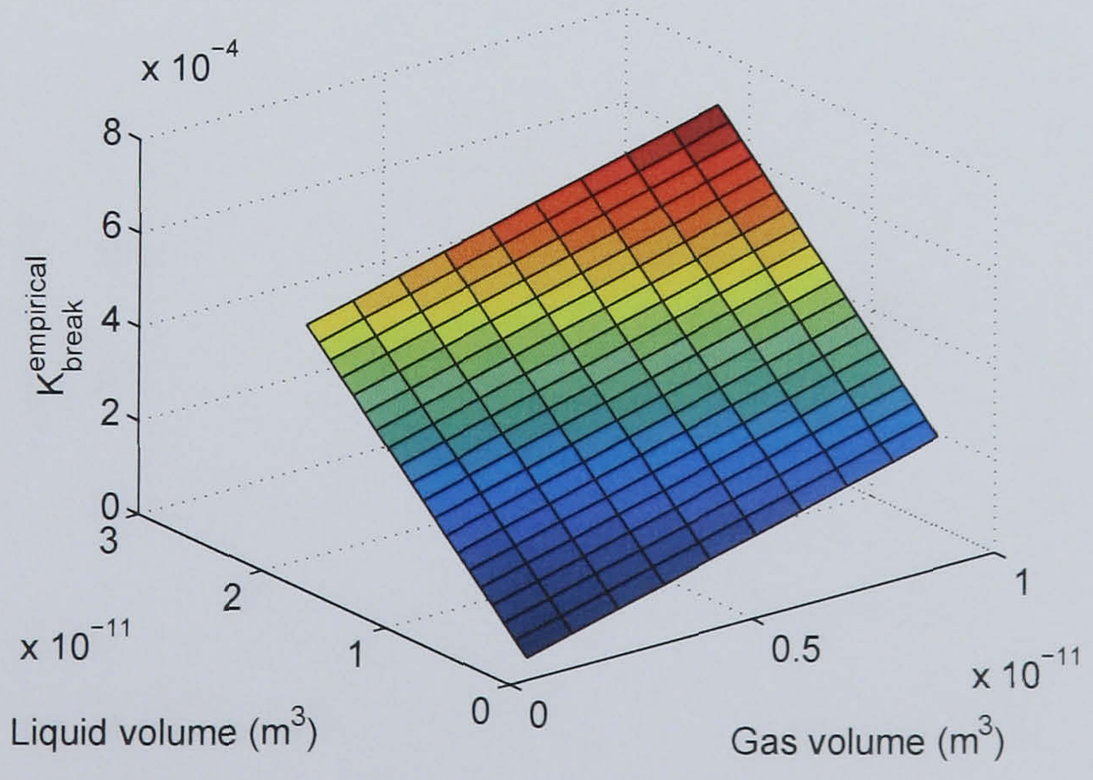

(c)

Figure 5.6: Shape of the empirical kernel (Equation 5.49) with respect to two dimensions keeping the third constant: (a) volume of gas constant, (b) volume of liquid constant and (c) volume of solid constant.

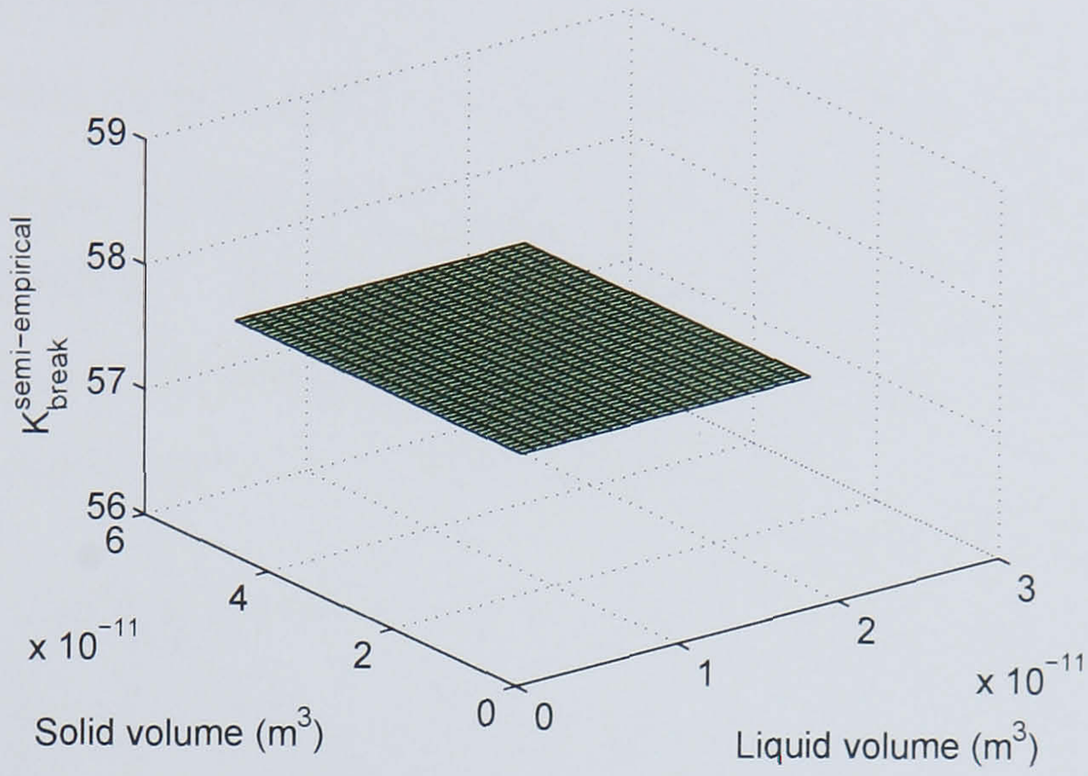

(a)

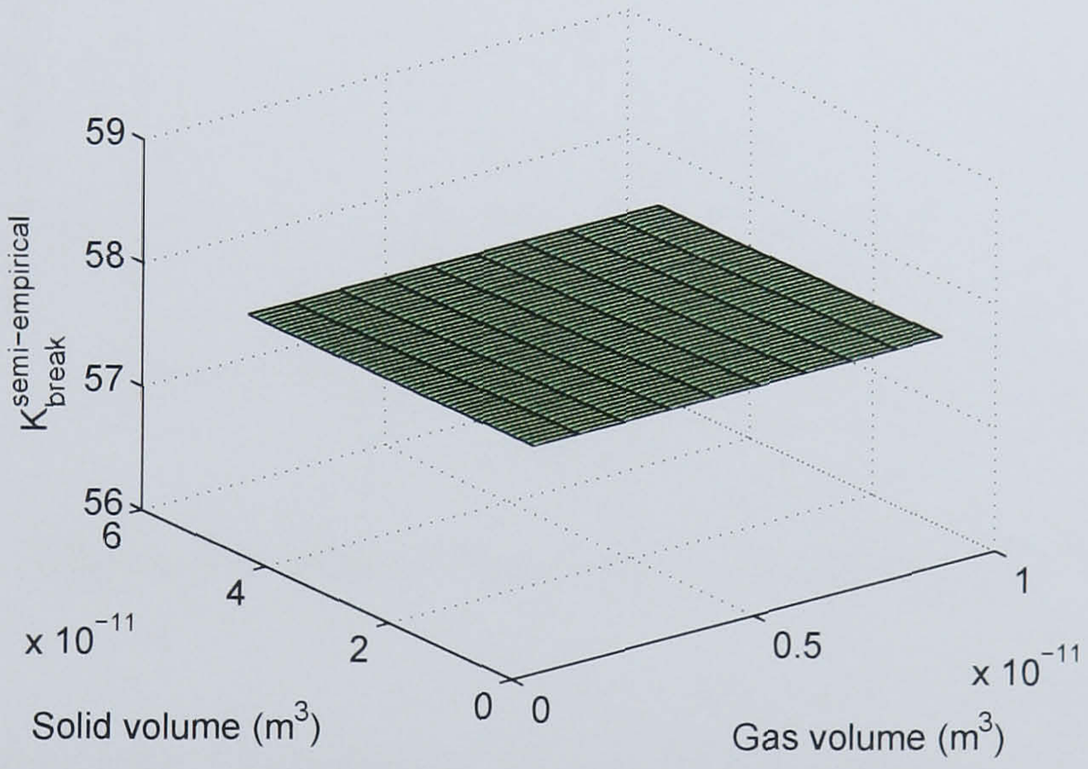

(b)

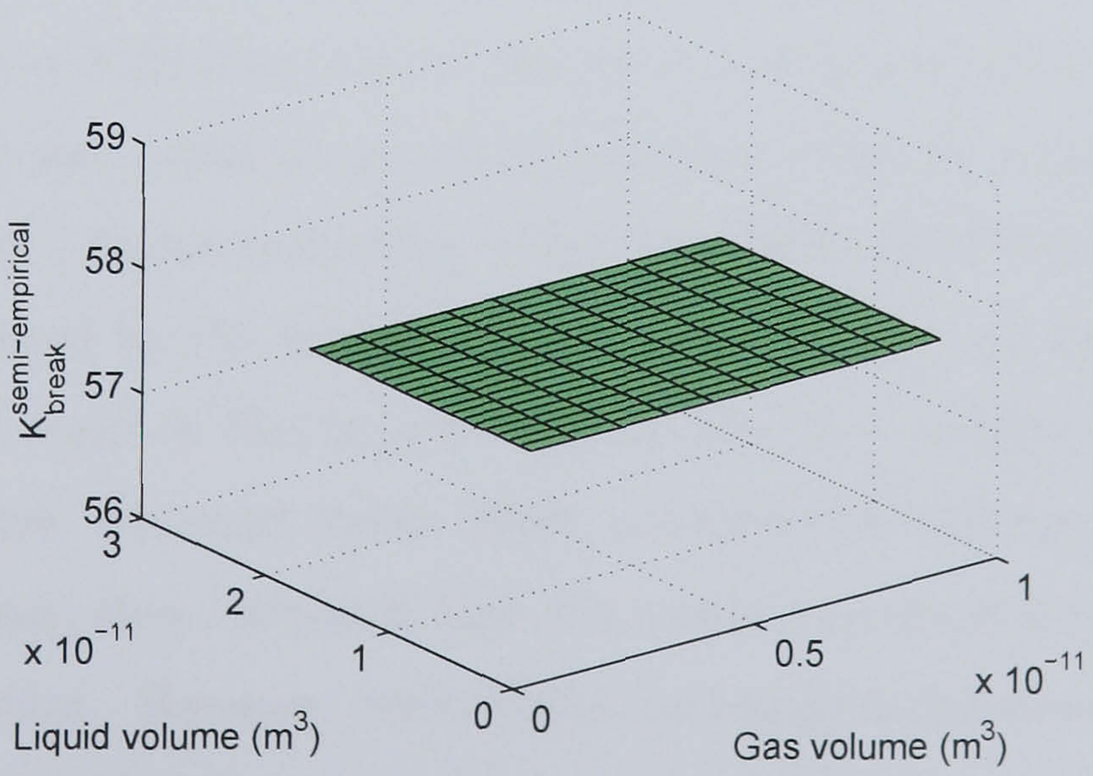

(c)

Figure 5.7: Shape of the semi-empirical kernel (Equation 5.50) with respect to two dimensions keeping the third constant: (a) volume of gas constant, (b) volume of liquid constant and (c) volume of solid constant.

5.4.2 Test of Breakage Kinetics

Figure 5.8 depicts the a semi-log plot of the fraction of particles remaining in the initial seed (i.e., $d_0 = 549\mu m$) as a function of time. First order breakage kinetics should yield a straight line with gradient $-K$. It is a good test of the form of the breakage model and is independent of the choice of breakage function. From Figure 5.8, it can be seen that a straight line is produced with $-K = 6.42 \times 10^{-4} s^{-1}$.

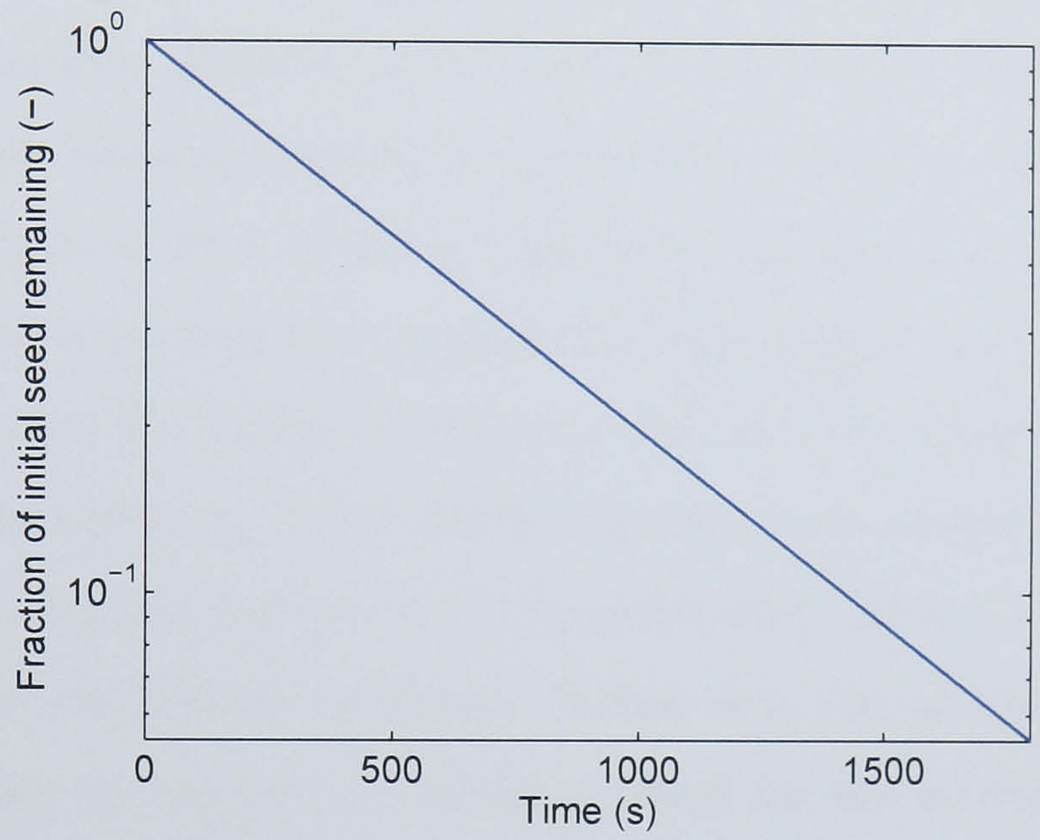

Figure 5.8: Plot of first order breakage kinetics.

5.4.3 Decoupling the Manner of Granule Breakage

In the experimental findings of Smith (2008), it was reported that the primary manner of granule breakage in high-shear mixers was due to particle-impeller collisions. This was followed by particle-wall collisions and particle-particle collisions. Possible reasons for this occurrence could be 1) higher probability of particles colliding with the impeller, 2) higher impact force generated by the impeller, followed by the walls, 3) larger Young's modulus of the impeller result in less deformation resulting in a smaller contact area, hence higher external stress. Although Smith (2008) reported their findings for limited number of granulation recipes, they intimated that this would be a general trend for the case of high-shear granulation. However, undertaking numerous experiments altering material properties and process/design parameters to confirm their postulation would be exceedingly laborious and time-consuming. The ability to model and predict the experimentally

observed trends *in-silico* would be very useful. Altering any parameters and properties in the model would also be convenient. Figures 5.9a and 5.9b depict the evolutions of total particles and average diameter of each individual manner of granule breakage as well as their combined effect for a typical granule recipe and granulator geometry (see Table 5.1). In the current simulation, based on the surface areas, $P_p = 0.18$, $P_w = 0.55$, and $P_i = 0.27$, where P_p is the probability of a particle hitting any other particle, P_w is the probability of a particle hitting a wall surface and P_i is the probability of a particle hitting the impeller surface. Results show that the main manner of particle breakage is due to particle-impeller collisions followed by particle-wall collisions and then particle-particle collisions. The effects of fluid forces are negligible compared to the above collisions. It must be noted that the probabilities assigned for each collision can be subject to change depending on more exact knowledge of collisions. For instance, based on theoretical analysis of their experimental findings, Smith (2008) reported that a large number of particles underwent collisions with the impeller in the impeller zone. Hence, a larger probability may be assigned to particle-impeller collisions. Either way, the breakage model is extremely useful in decoupling the manner of breakage based on the intrinsic material properties as well as user-defined process and design parameters. Model results are consistent with experimental findings and this lends credence to the validity of the model.

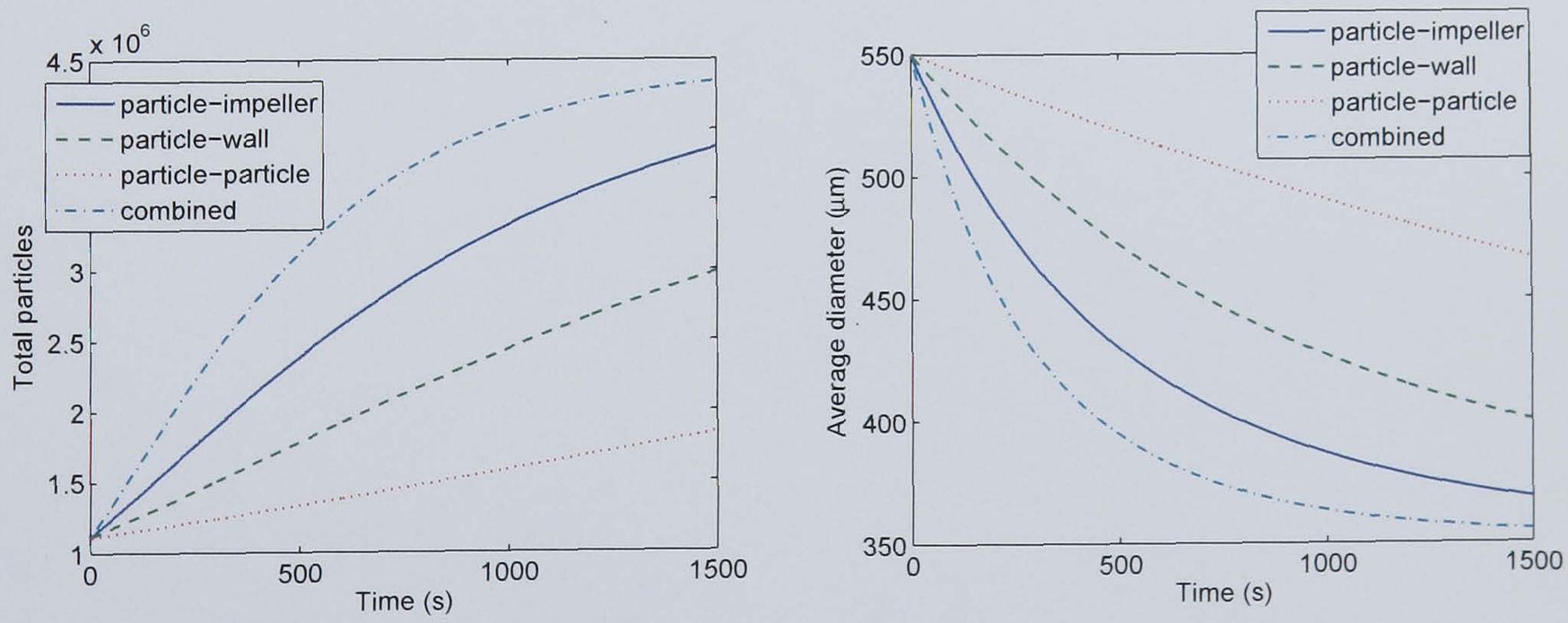

(a) (b)

Figure 5.9: Evolution of (a) total particles and (b) average diameter, for the various manner of granule breakage.

5.4.4 Evolutions and Distributions of Granule Properties under Nominal Conditions

Figure 5.10a depicts the simulated temporal evolution of the total particles in the system which increases due to particle breakage. It can be seen that the rate of breakage decreases with time and this is attributed to the fact that as the average size of the granule decreases, the rates of breakage decrease as well. Figure 5.10b shows the decrease in average particle diameter with time and this is consistent with granule breakage behaviour. Figures 5.10c and 5.10d depict the change in average porosity and binder content with time respectively. Average binder content reported remains constant throughout as no binder is added or removed to/from the system. A marginal increase is observed for average porosity and this attributed to the consolidation effect not strong enough as compared to particle breakage, to effect any decrease in particle porosity. Figures 5.11a-e depict the intermittent and end-point two-dimensional distribution of total particles with respect to particle diameter and fractional binder content. As seen in the plots, the particles in the initial seed undergo breakage to form a smaller mode of particles with a larger distribution width. This observation is consistent with experimental trends.

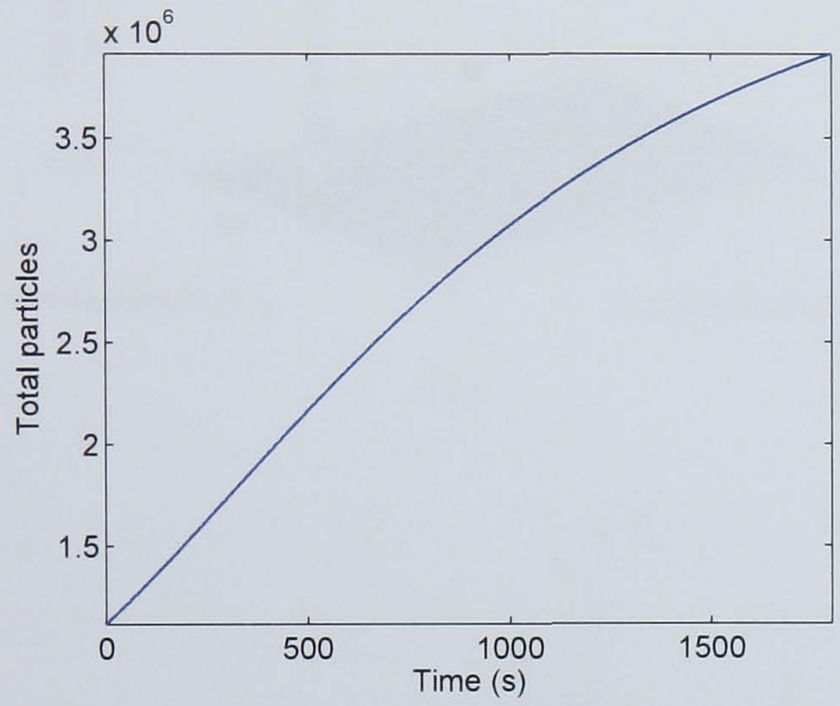

(a)

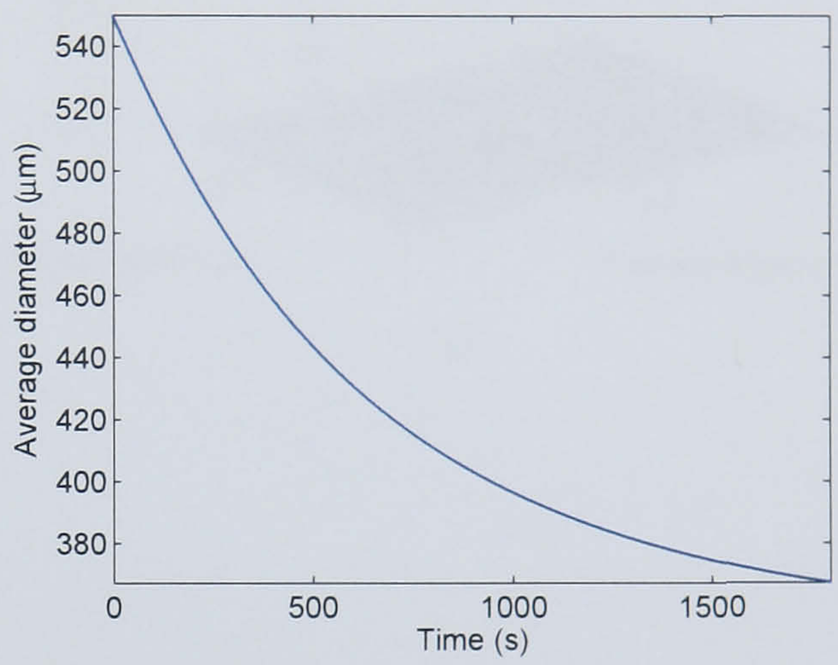

(b)

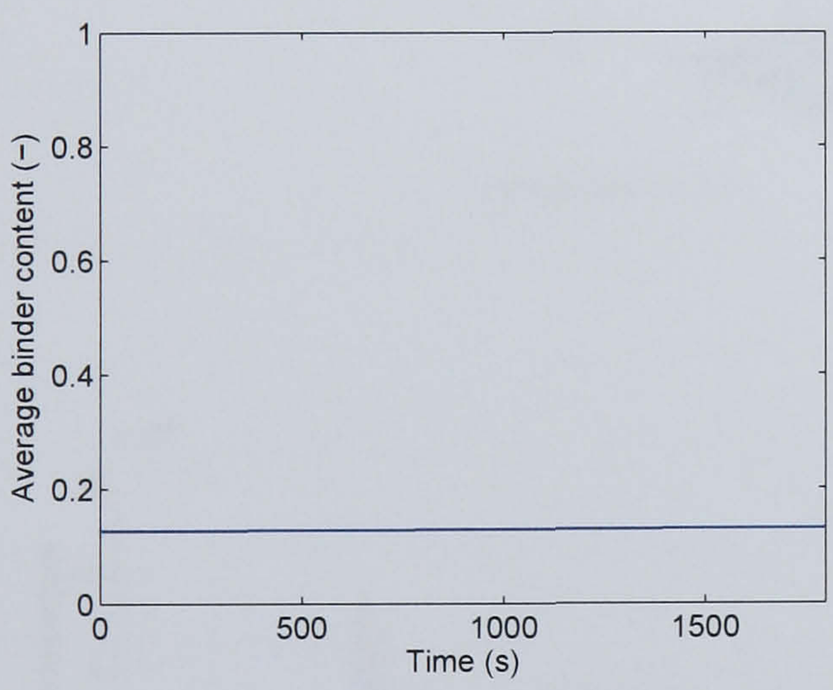

(c)

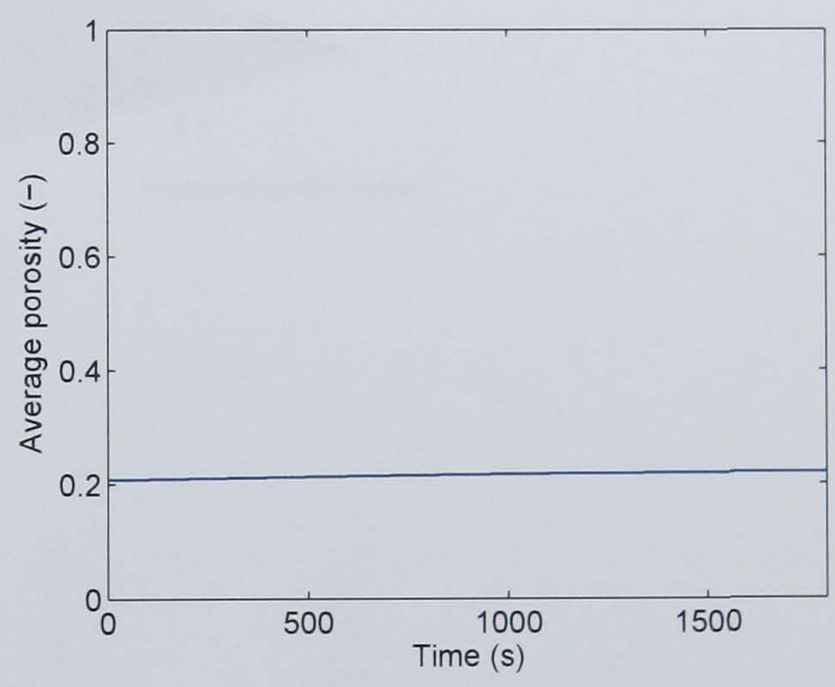

(d)

Figure 5.10: Evolution of (a) total particles, (b) average diameter, (c) average binder content and (d) average porosity.

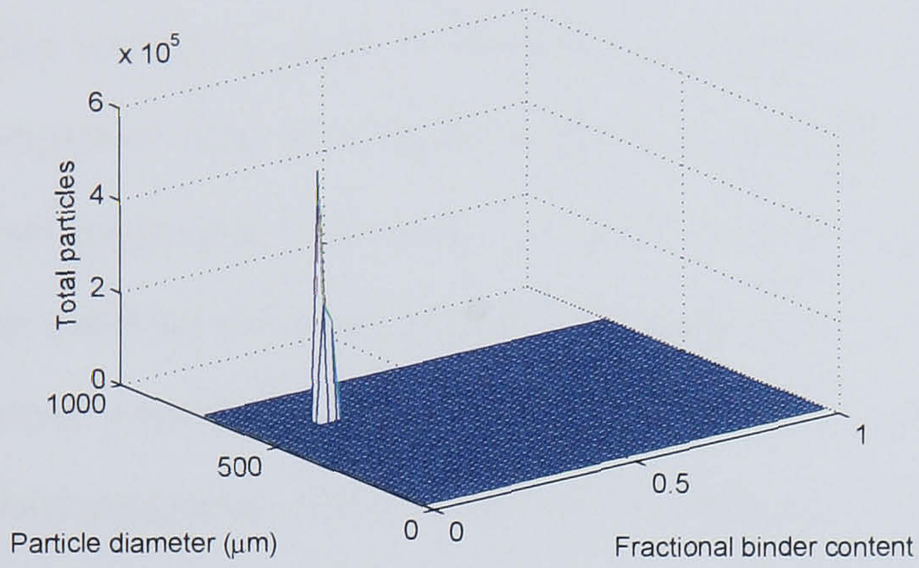

(a)

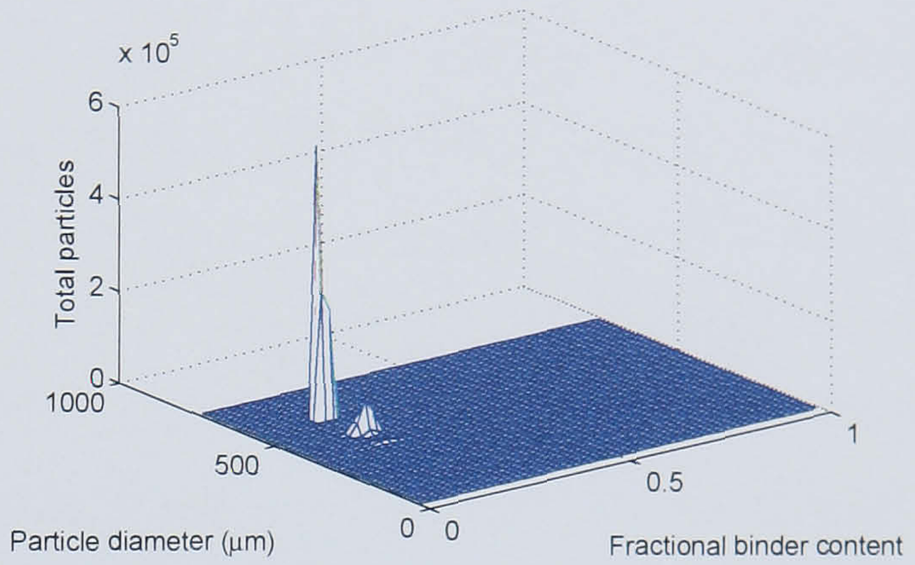

(b)

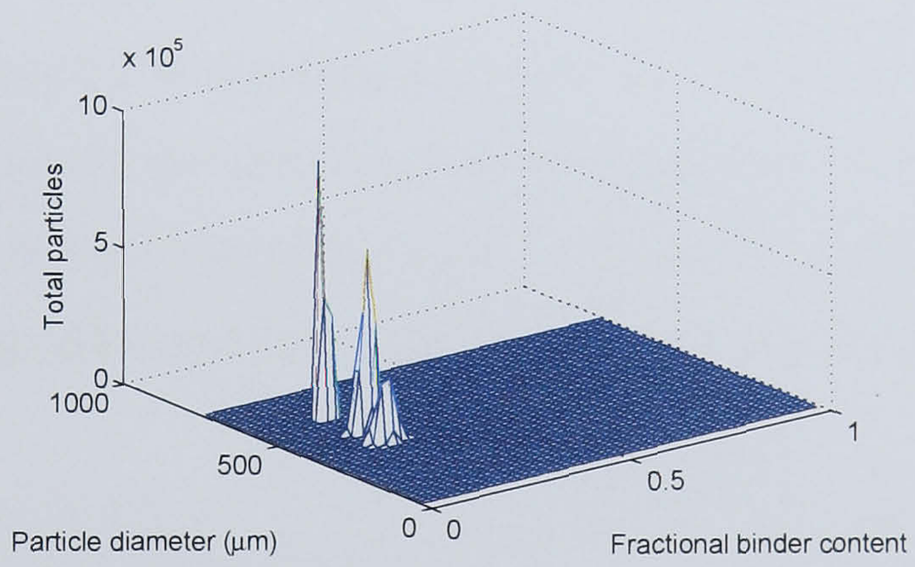

(c)

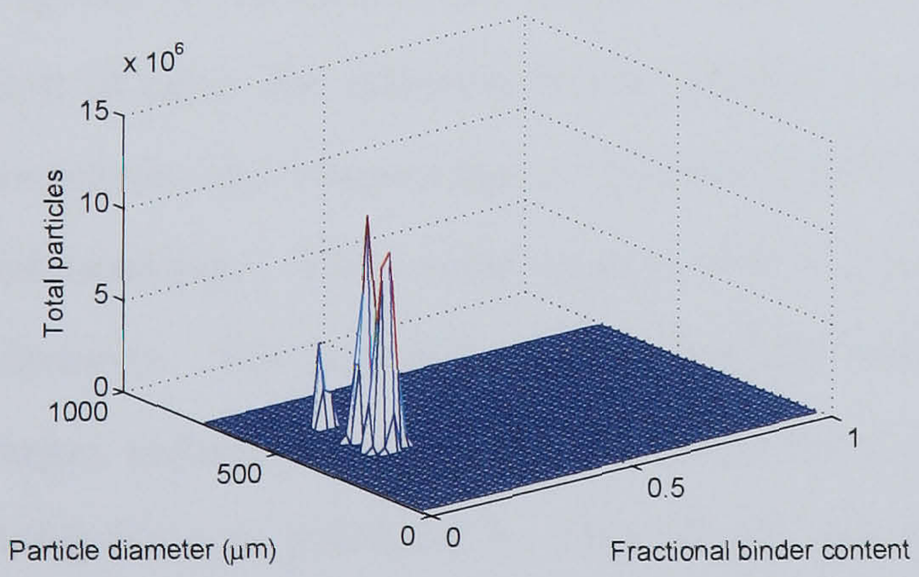

(d)

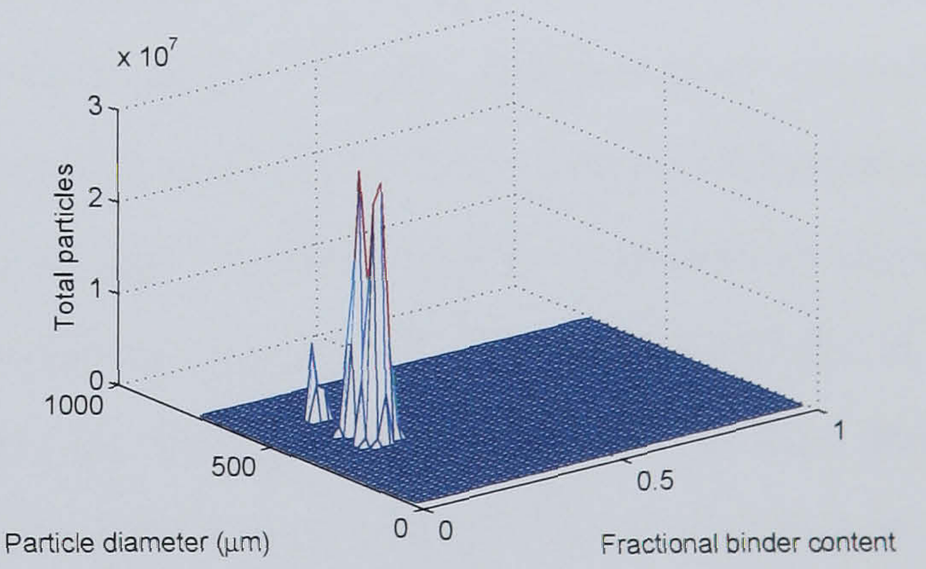

(e)

Figure 5.11: Evolution of the granule size distributions under breakage at various time instances– (a) $t = 0\,s$, (b) $t = 50\,s$ and (c) $t = 200\,s$, (d) $t = 500\,s$, (e) $t = 1790\,s$.

5.4.5 Effect of Material Properties and Process/Design Parameters on Granule Properties

An important feature of any grey-box model (such as the breakage model developed in this study) is that it should incorporate key material properties and process/design parameters that are based on first-principles. At the same time. it should incorporate one or two empirical constants (in the current model, A is the only empirical constant) that can be used to account for any uncertainties (which are inherent as physics and chemistry can never exactly depict real phenomena). However, one should be careful that the empirical constant does not subdue the influence of the mechanistic parameters and be the dominating parameter. If this is the case, the mechanistic model is essentially a pseudo-empirical model, thus negating its value. The effects of key mechanistic parameters that are known apriori to have a significant effect on granule properties, should be captured by the model. This would be a good test for the developed breakage model and to qualitatively ascertain its value and validity. In the current scenario, effects of key mechanistic parameters are examines by considering their typical deviations from the nominal conditions reported in Table 5.1.

5.4.5.1 Effect of Binder Viscosity

Figures 5.12a and 5.12b depict a plot of total particles and average diameter as a function of time, for different liquid binder viscosities. It can be seen that as binder viscosity increases, the viscous forces increase resulting in stronger liquid bridges and reduced granule breakage. The model is also able to capture the nonlinear effects of increased binder viscosity. For instance, increasing the viscosity by the same factor of five results in a larger reduction of granule breakage from the case of $0.005\,Pa.s$ to $0.025\,Pa.s$ than from $0.001\,Pa.s$ to $0.005\,Pa.s$. This clearly shows that at higher viscosities, the dominance of the viscous forces compared to the capillary forces is relatively higher. As a result, for the same change in binder viscosity, a greater change in granule properties is effected. This phenomenon was also corroborated by Iveson (2002) who observed that at a more viscous regime, the viscous forces dominated over capillary forces.

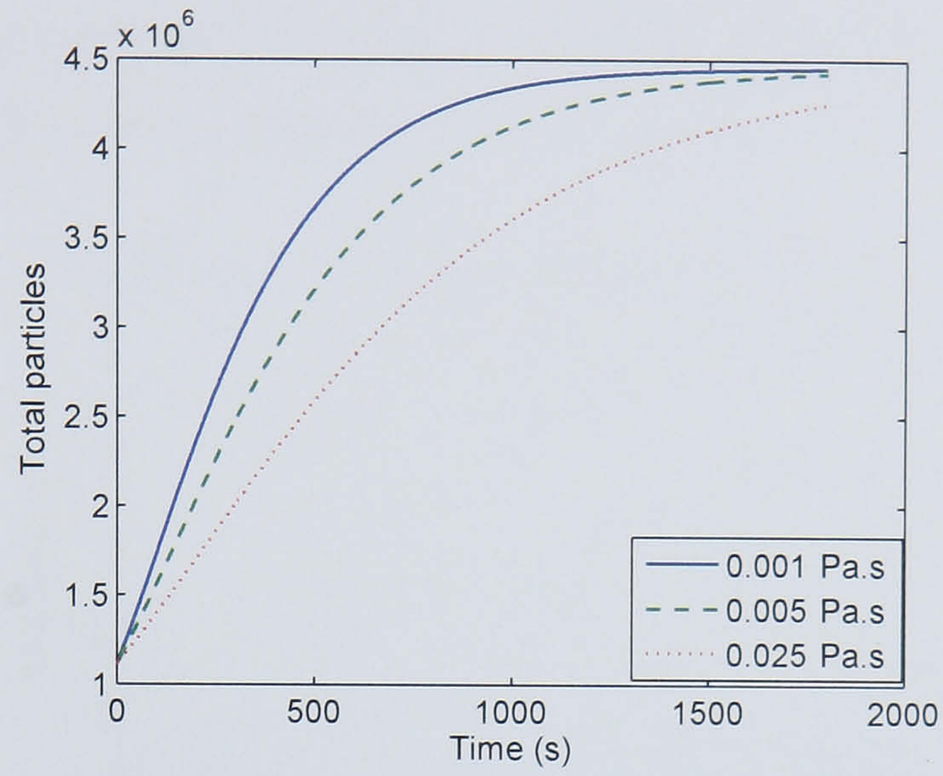

(a)

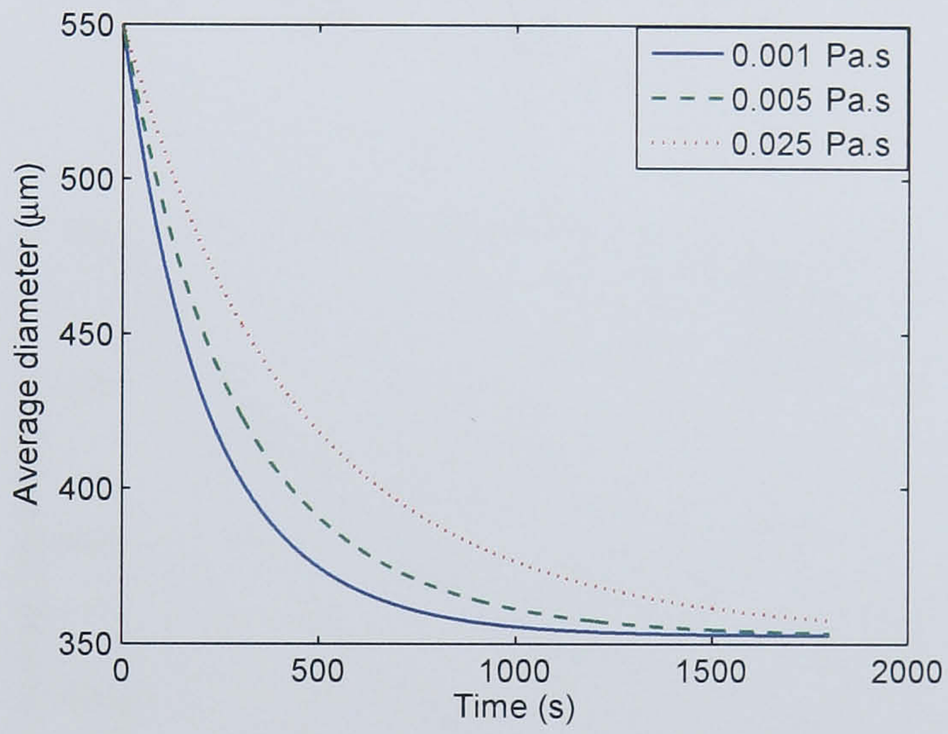

(b)

Figure 5.12: Evolution of (a) total particles, (b) average diameter, under varying binder viscosities.

5.4.5.2 Effect of Binder Surface Tension

Figures 5.12a and 5.12b depict a plot of total particles and average diameter as a function of time, for different liquid surface tensions. It can be seen that as binder surface tension decreases, the capillary forces decrease resulting in weaker liquid bridges and increased granule breakage. Similar to the case of binder viscosity, the model is able to capture the nonlinear effects of reducing surface tension. As the surface tension continues to be reduced by a factor of two, the rate of increase in granule breakage is reduced. This indicated that as surface tension reduces, the capillary forces are relatively weaker than

the viscous forces thus resulting in this lesser rate of increase in breakage. This observation has also been reflected by Iveson (2002).

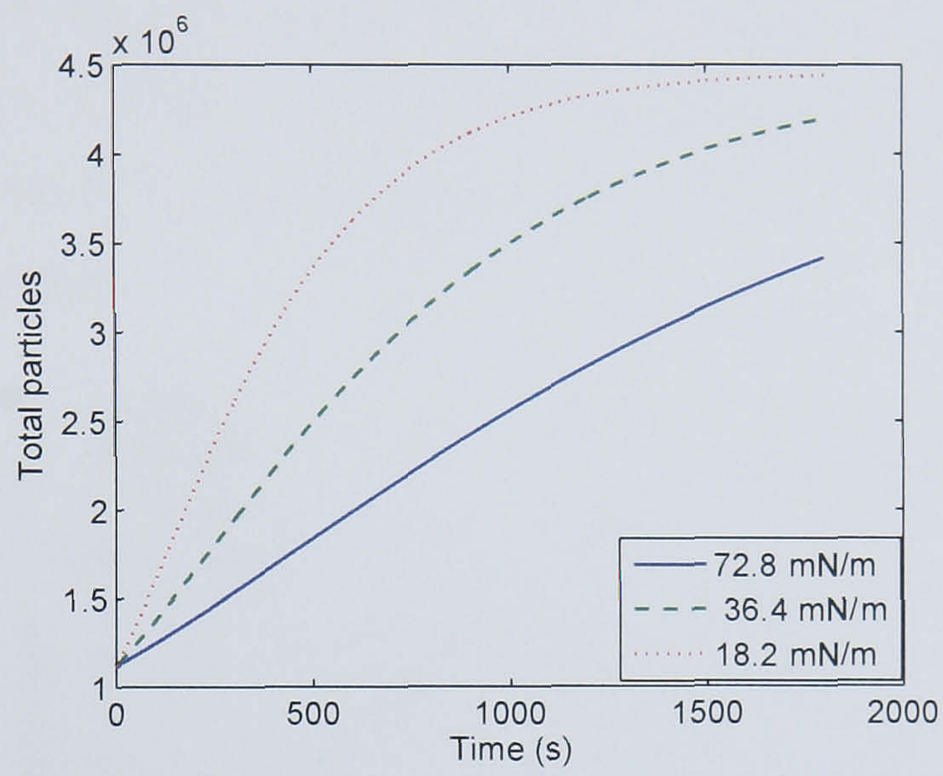

(a)

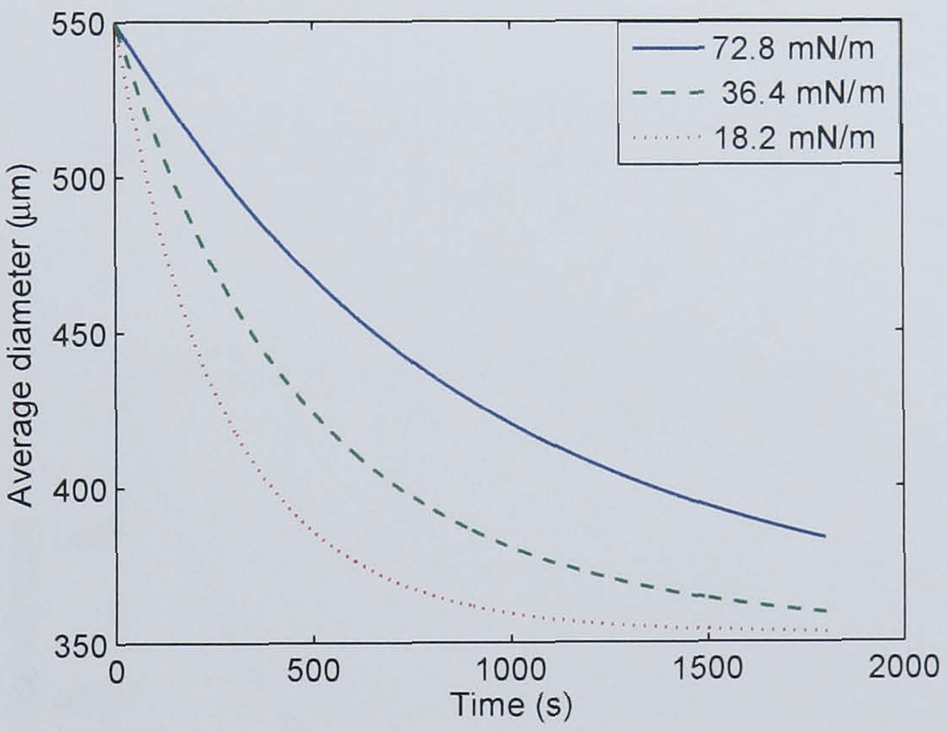

(b)

Figure 5.13: Evolution of (a) total particles, (b) average diameter, under varying binder surface tensions.

5.4.5.3 Effect of Contact Angle

Figures 5.14a and 5.14b depict a plot of total particles and average diameter as a function of time, for various contact angles. An angle of 0^o corresponds to a case of perfect wetting, 90^o corresponds to a case of hydrophobicity (i.e., high reluctance to wet the surface) and 45^o corresponds to an in-between case. It can be seen that as the contact angle increases, granule breakage increases. In particular, there is a tremendous increase in

granule breakage from 45^o to 90^o. As ϕ increases from 0^o to 45^o, the frictional forces decrease due to reduced work of adhesion and a smaller contact area (due to lesser wetting area). This reduced wetting also reduces the capillary forces of the liquid bridge. For the case of 45^o to 90^o, the wetting area is almost negligible and this results in $F_{cap} \approx 0$. Furthermore, due to the water liquid bridges, $F_{cap} >> F_f$. This explains the drastic increase in granule breakage.

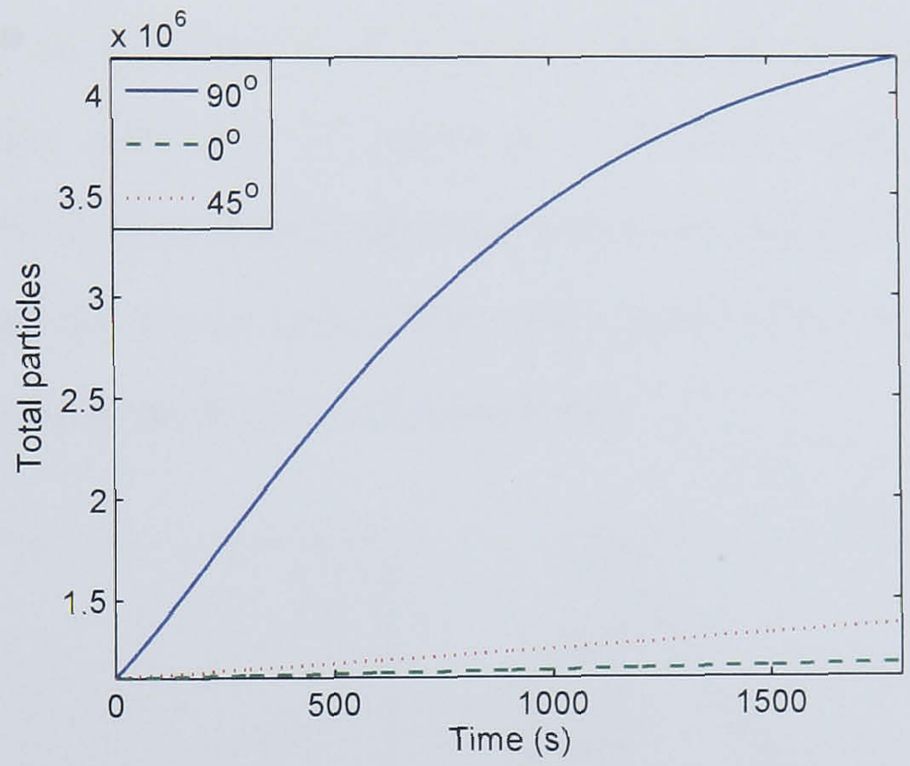

(a)

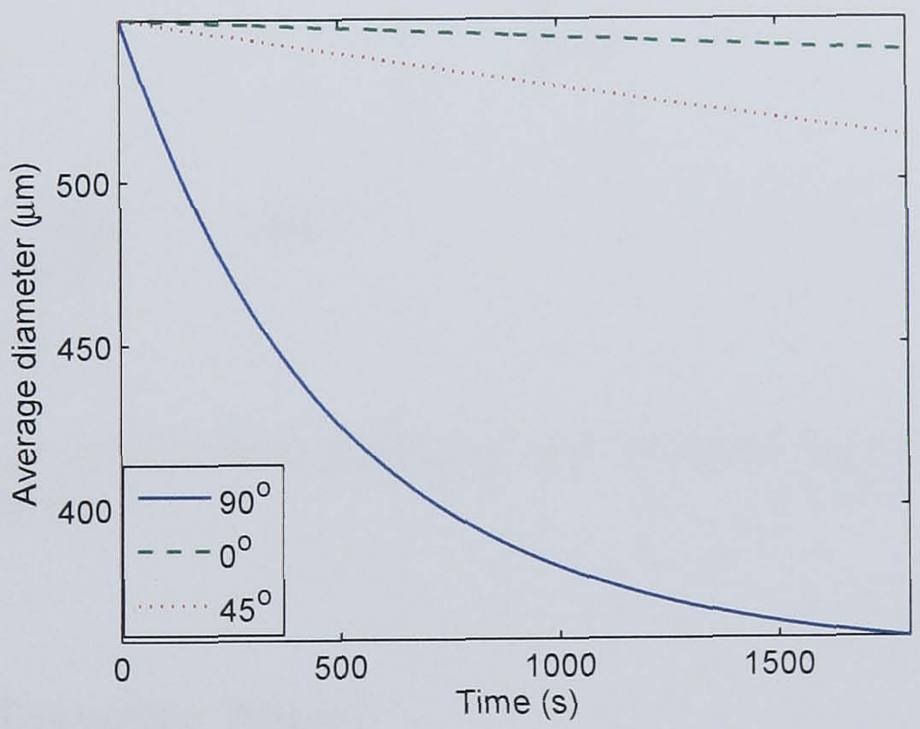

(b)

Figure 5.14: Evolution of (a) total particles, (b) average diameter, under varying contact angles.

5.4.5.4 Effect of Primary Particle Size Distribution

Figures 5.15a and 5.15b depict a plot of total particles and average diameter as a function of time, for different primary particle size distributions. FV corresponds to the number of finite volumes the initial seed particles are distributed within, whilst maintaining the initial average diameter. It can be observed that increasing the width of the initial PSD increases granule breakage. This can be attributed to the fact that deviating from the nominal case (FV=1), an increase in K_{break}^{eff} for the larger particles outweighs a decrease in K_{break}^{eff} for the smaller particles. A larger psd will have more finite volumes deviating from the nominal finite volume, resulting in a gradual overall increase of the average K_{break}^{eff}. As a result the average breakage rate for a wider sized distribution is higher explaining the increase breakage rates as initial psd increases.

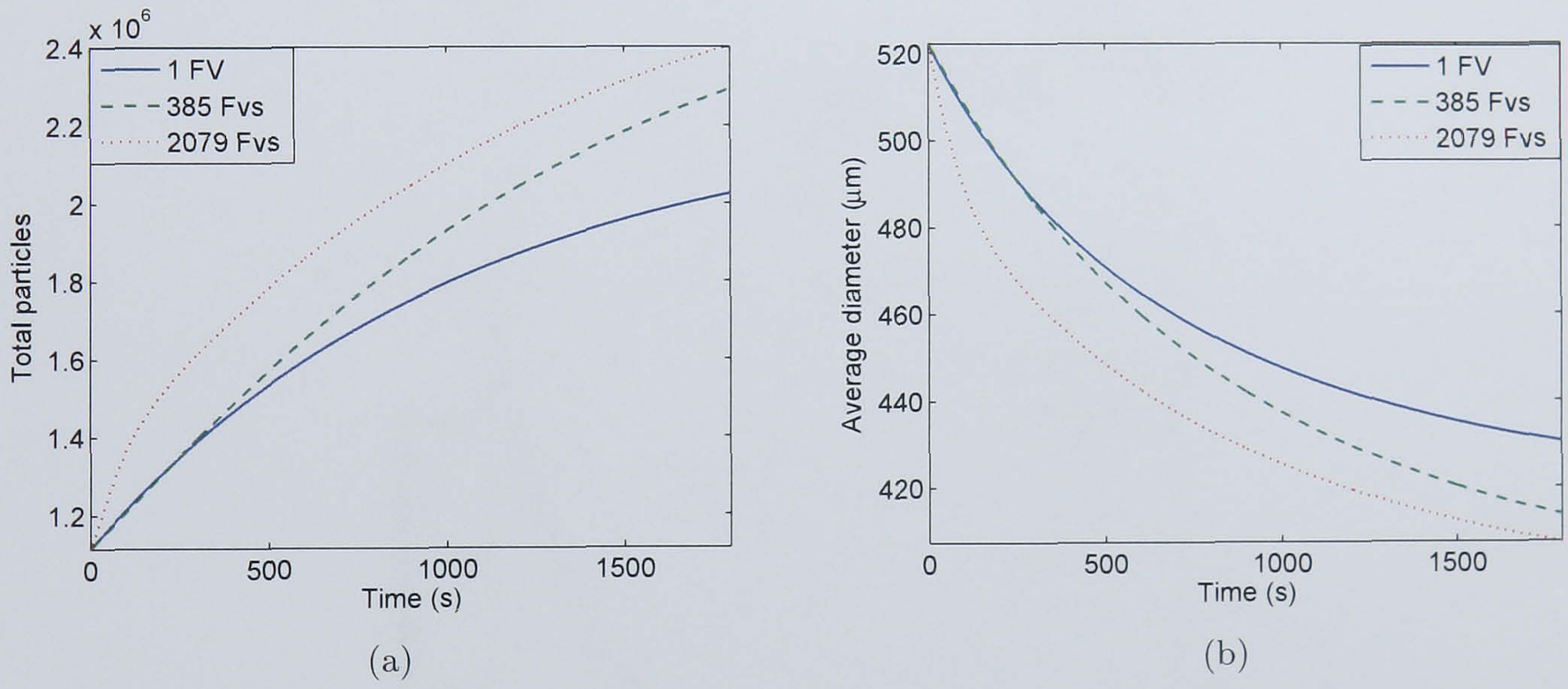

(a) (b)

Figure 5.15: Evolution of (a) total particles, (b) average diameter, for different primary particle size distributions.

5.4.5.5 Effect of Impeller Speed

Figures 5.16a and 5.16b depict a plot of total particles and average diameter as a function of time, for different impeller speeds. It can be seen that increasing the impeller speed results in increased granule breakage. This is attributed to the larger impact forces acting on the granule.

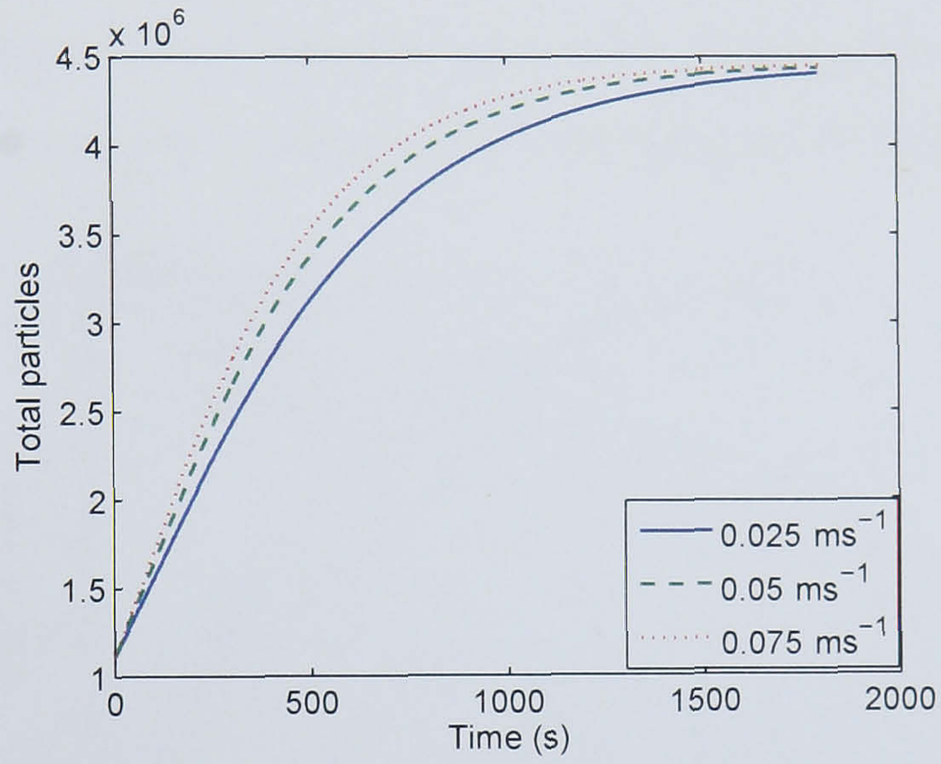

(a)

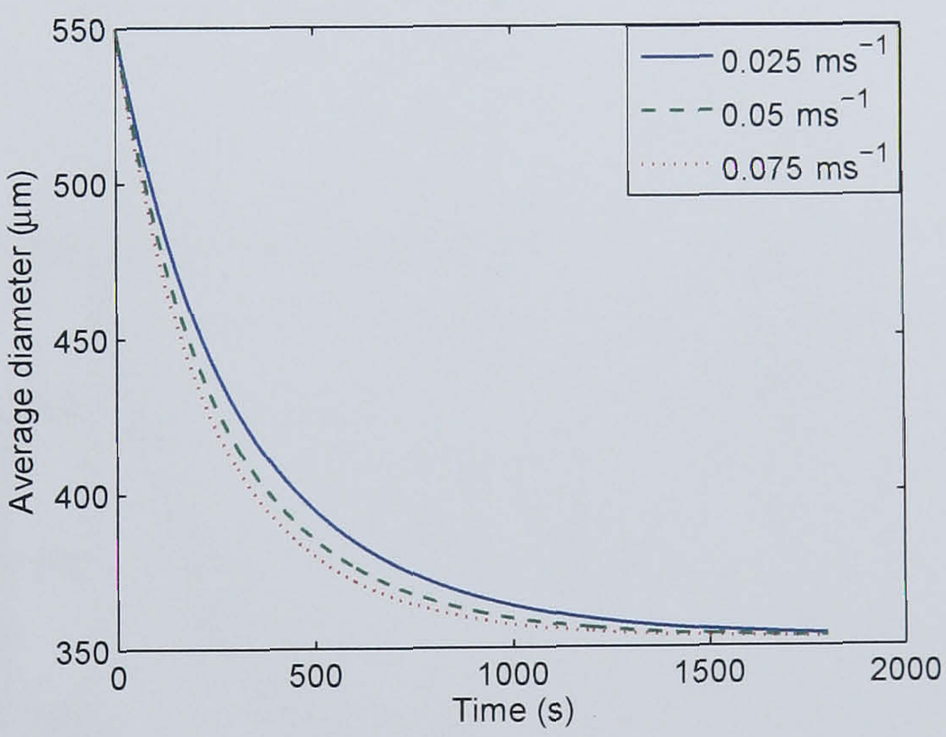

(b)

Figure 5.16: Evolution of (a) total particles, (b) average diameter, under varying impeller speeds.

5.4.5.6 Effect of Coefficient of Restitution

Figures 5.17a and 5.17b depict a plot of total particles and average diameter as a function of time, for different coefficient of restitutions. For the inelastic case, $e_p = e_w = e_i = 0.2$ and for the elastic case, $e_p = e_w = e_i = 0.8$. Results clearly show that granule breakage is sensitive to variations in coefficient of restitutions. For the elastic case, granule breakage rates are the highest due to larger impact forces. For the inelastic case, due to impact losses, the impact forces are lower, resulting in reduced granule breakage.

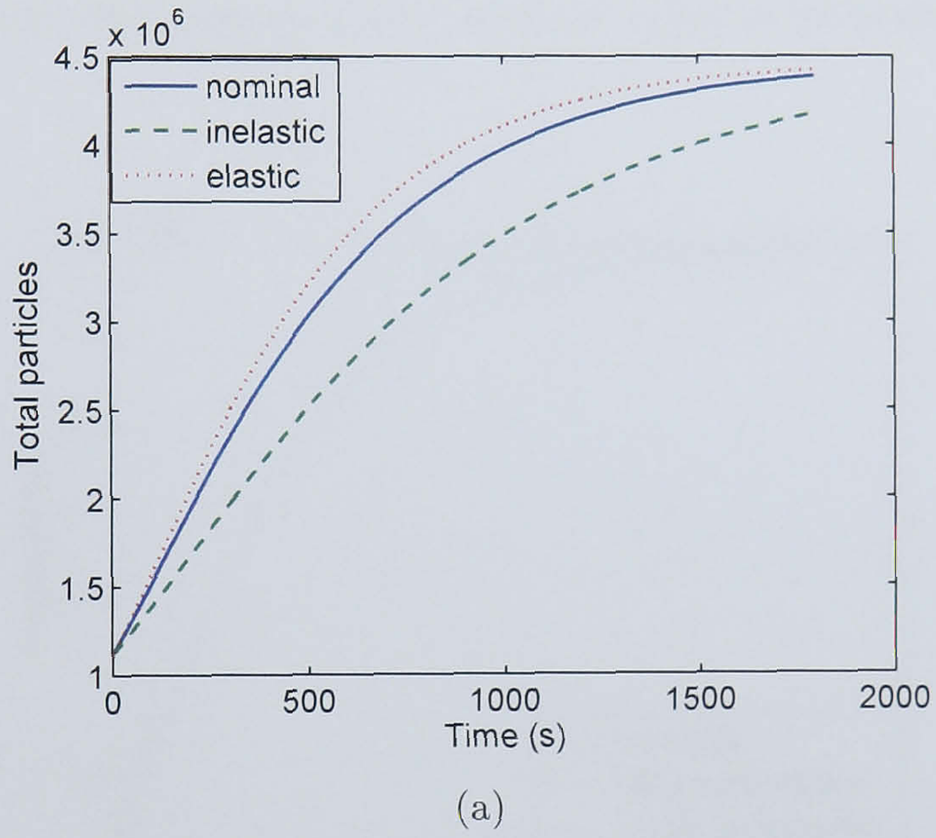

(a)

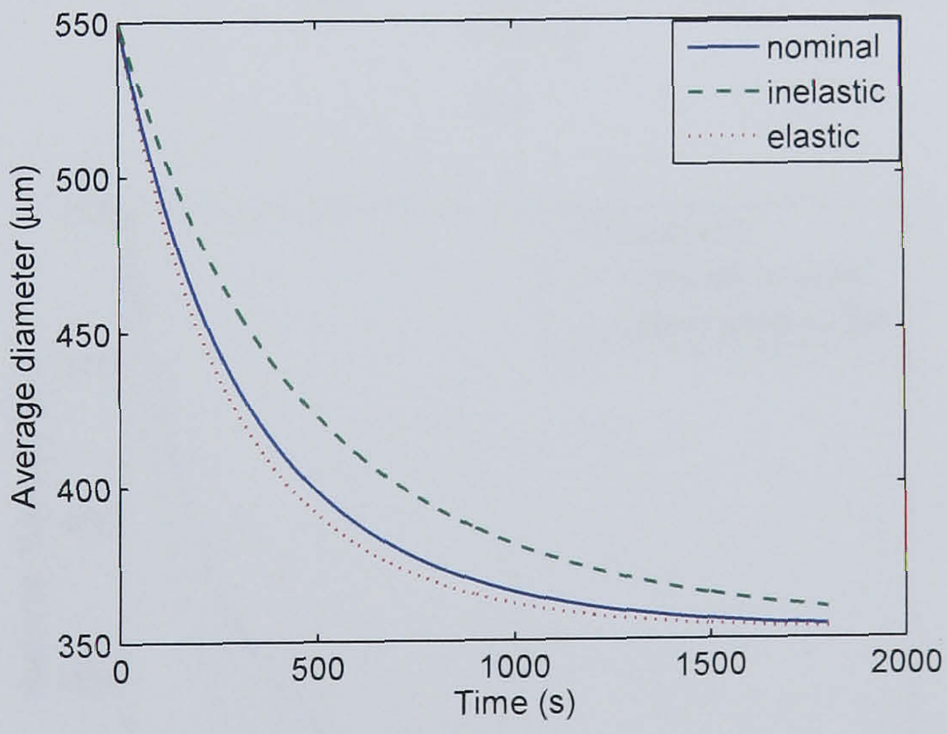

(b)

Figure 5.17: Evolution of (a) total particles, (b) average diameter, for different coefficients of restitutions.

5.4.5.7 Effect of Young's Modulus

Figures 5.18a and 5.18b depict a plot of total particles and average diameter as a function of time, for different Young's modulii. For the less deformable case, $E_p = 2E_p^{nominal}$, $E_w = 2E_w^{nominal}$ and $E_i = 2E_i^{nominal}$. For the more deformable case, $E_p = 0.5E_p^{nominal}$, $E_w = 0.5E_w^{nominal}$ and $E_i = 0.5E_i^{nominal}$. Results clearly show that granule breakage is sensitive to variations in material deformability. For the less deformable case, the contact area upon collisions is reduced resulting in higher external stresses and hence increased breakage. For the more deformable case, contact area is increased resulting in reduced granule breakage.

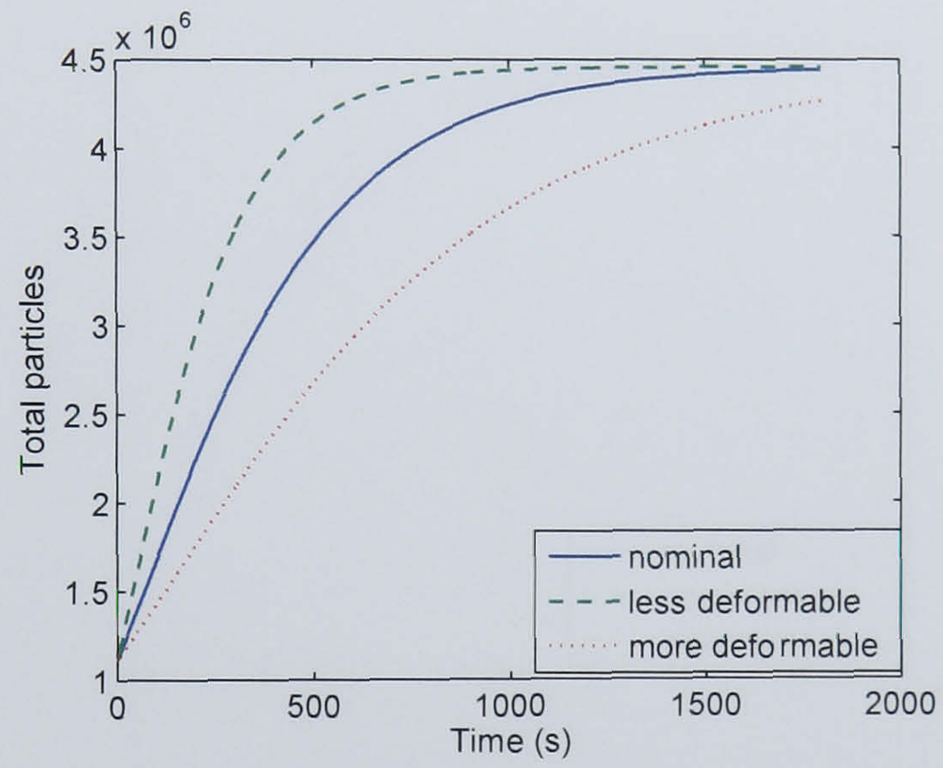

(a)

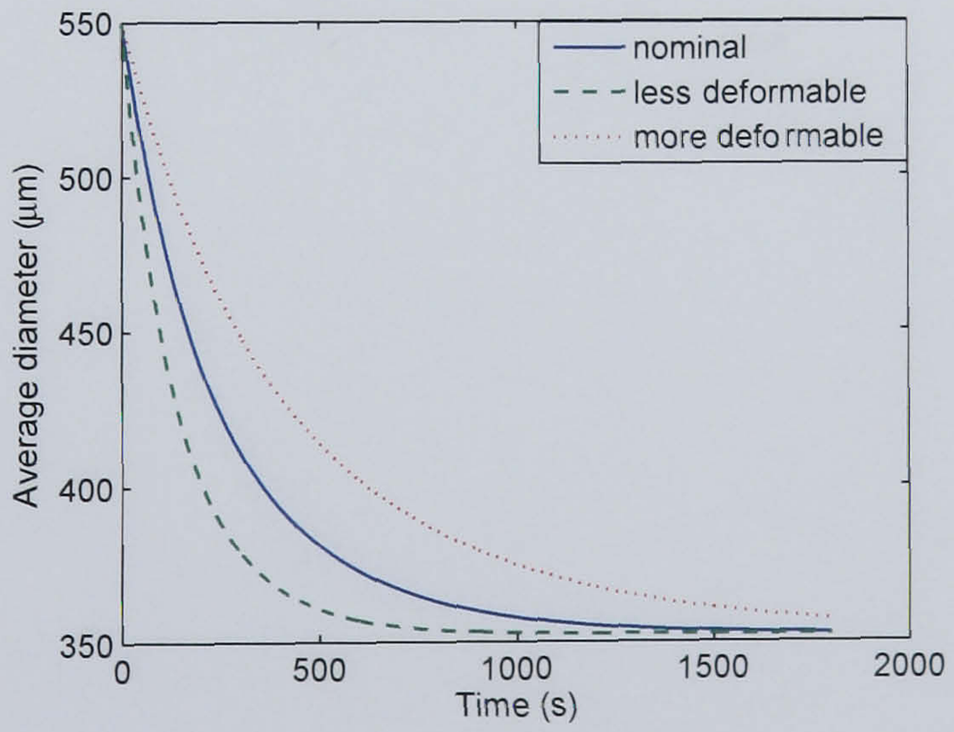

(b)

Figure 5.18: Evolution of (a) total particles, (b) average diameter, for different Young's moduli.

5.4.5.8 Effect of Poisson Ratio

Figures 5.19a and 5.19b depict a plot of total particles and average diameter as a function of time, for different Poisson ratios. For the incompressible case, $\sigma_p = \sigma_w = \sigma_i = 0.02$. For the compressible case, $\sigma_p = \sigma_w = \sigma_i = 0.50$. Results clearly show that granule breakage is sensitive to variations in material compressibility. For the compressible case, there is a reduction in the contact area in the axial direction resulting in higher external stresses and hence increased breakage. For the incompressible case, axial contact area is increased (compared with the nominal case), resulting in lower external stresses and hence reduced granule breakage.

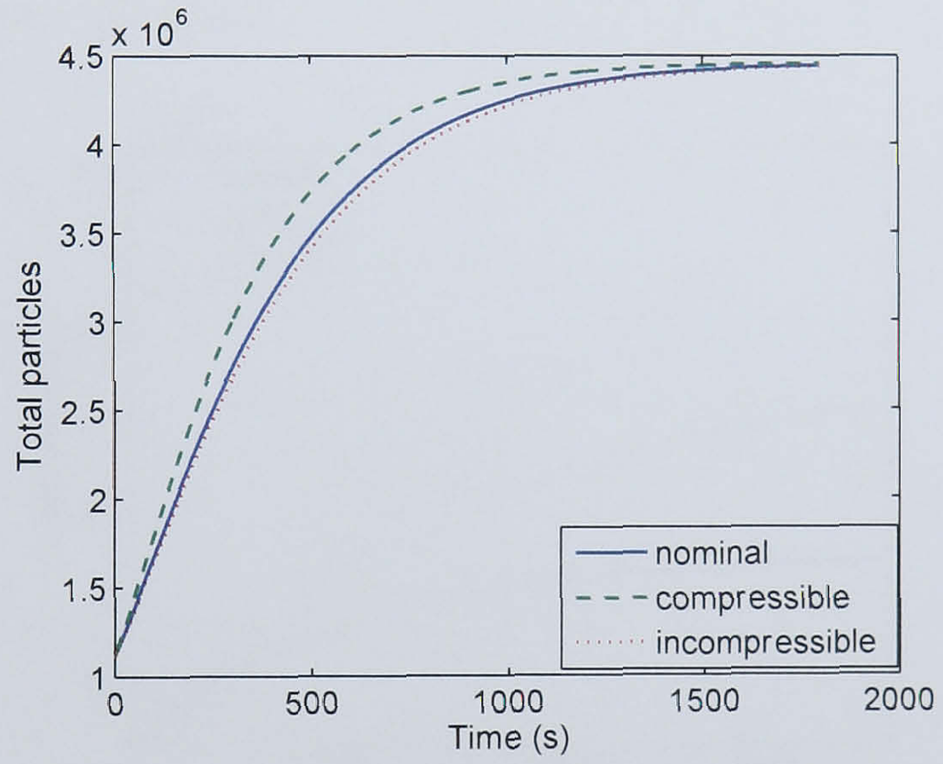

(a)

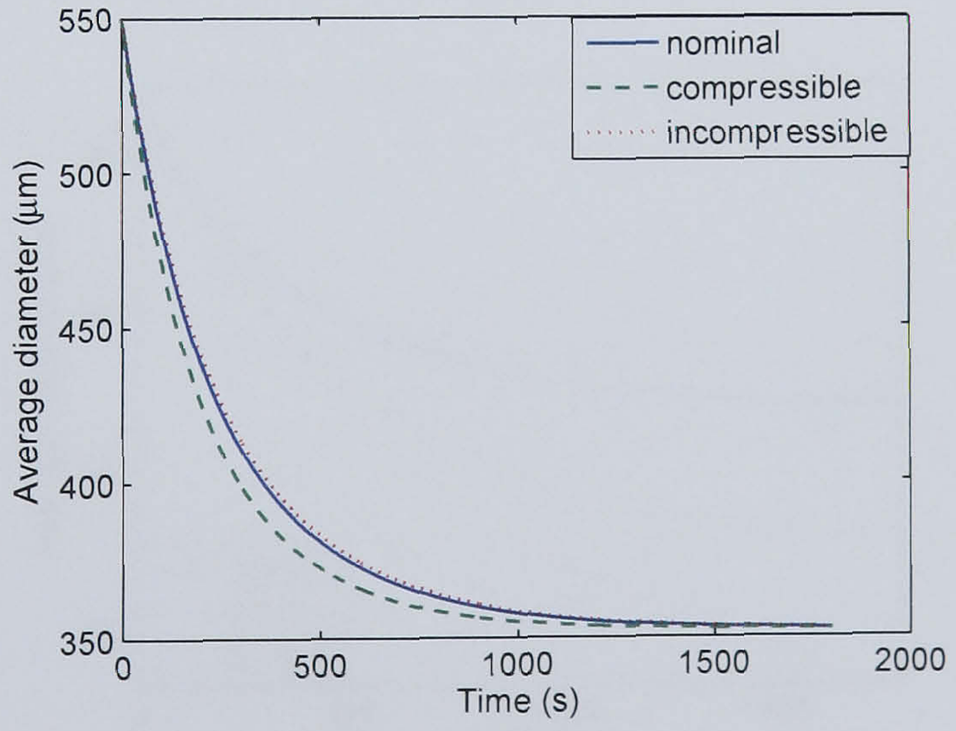

(b)

Figure 5.19: Evolution of (a) total particles, (b) average diameter, for different Poisson ratios.

5.4.5.9 Effect of Daughter Particle Volume Fraction

Figures 5.20a and 5.20b depict a plot of total particles and average diameter as a function of time, for different daughter particle volume fractions. Results show that as the difference in volume fractions of the 2 daughter particles increases, granule breakage increases. Let us assume that for the case of $\theta_1 = \theta_2 = 0.5$, a granule breaks into two equi-sized particles occupying an arbitrary bin j_3. Similarly, for the case of $\theta_1 = 0.9$ and $\theta_2 = 0.1$, a granule will break such that the larger fragment occupies bin j_5 and the smaller fragment occupies j_1, such that $V_{j5} > V_{j3} > V_{j1}$, where V denotes volume. Since $k^{eff}_{break}(j_5) + k^{eff}_{break}(j_1) > 2k^{eff}_{break}(j_3)$, based on this logic breakage increases as the difference in the volume fraction of the daughter particles increases.

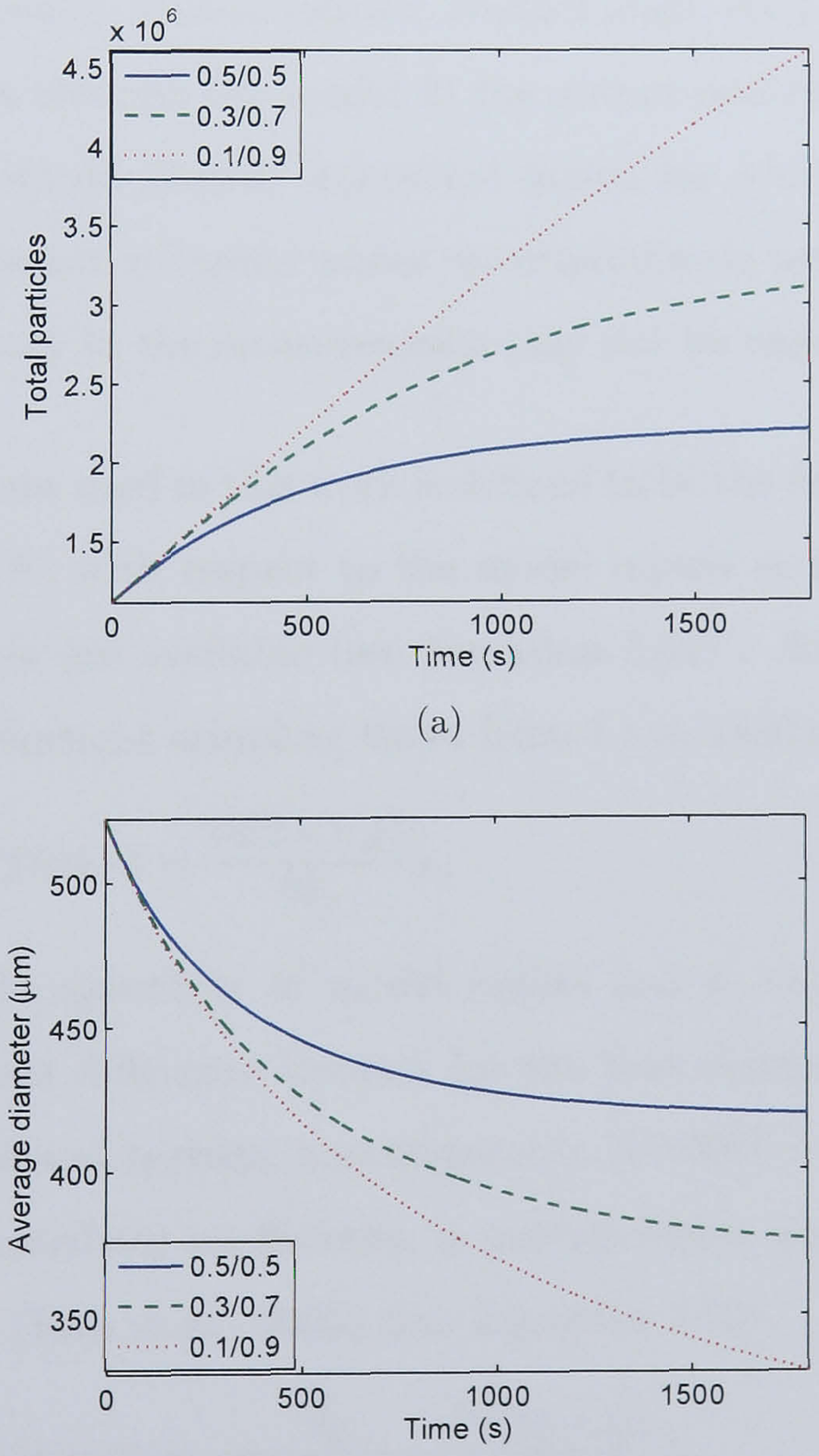

Figure 5.20: Evolution of (a) total particles, (b) average diameter, for different daughter particle volume fractions.

5.4.6 Dynamic Sensitivity Analysis of Model Inputs

In this section, a dynamic parameter-driven sensitivity analysis of the model output (particle density distribution, F) is performed. A detailed sensitivity analysis has two main purposes. Firstly, the importance of a model input is ascertained by quantifying its effect on the output. The model inputs can be ranked in order of importance. More effort and resources can be spent on sensitive inputs, and insensitive inputs can be kept constant during the model calculations. This has the potential of reducing the overall dimensional space of the problem. Alternatively, the process can be redesigned to increase the input sensitivities. This serves to potentially increase the overall controllability of the process. Secondly, there are always uncertainties involved in any of the experimentally measured model inputs (e.g. viscosity, surface tension, contact angle etc.). As a result, these uncertainties may propagate through the model to the output and can yield erroneous results. A sensitivity analysis would identify important inputs for which accurate measurements are required. For less sensitive inputs whose uncertainties do not affect the model output, a high degree of accuracy in the measurements may not be required.

The sensitivity coefficient used in this work is defined to be the first order partial derivative of the model output (F) with respect to the model inputs at the particular times when potential measurements are available (see Equation 5.51) . In the current scenario, 10 measurements at intermittent sampling times from $1\,s$ to $1800\,s$ are considered.

$$sensitivity\ coefficient = \frac{\partial F(s,l,g)}{\partial \theta_p}|_{t_n} \tag{5.51}$$

Here, θ_p represents the spectrum of model inputs and t_n depicts the sampling times. A second order centered difference formula for the first derivative is utilised. Since the model is nonlinear and and perhaps non-monotonic, a $\pm 50\%$ is applied to the inputs. To effectively compare sensitivity coefficients, a scaling factor was introduced to scale the sensitivity coefficients (Kou et al., 2005) (see Equation 5.52).

$$sensitivity\ coefficient = \frac{\hat{\theta}_p}{\hat{F}(s,l,g)\,|_{t_n}} \frac{\partial F(s,l,g)}{\partial \theta_p}\,|_{t_n} \tag{5.52}$$

Here, $\hat{\theta}_p$ is the current value of the model input prior to making a change and $\hat{F}(s,l,g)$ is the current value of the model output at time t_n, prior to making any change. Tables 5.2

and 5.3 depict the respective sensitivity coefficients of the particle density with respect to material properties and process/design parameters.

Results show that the most sensitive parameter is the volume fraction of the daughter particles $\theta_{v_{a,b}}$. This is expected because as $\theta_{v_{a,b}}$ varies, the daughter particles occupy different finite volumes (bins) which can have very different breakage kernel metrics (k_{break}^{eff}). As a result, the breakage rates are significantly different for even marginal changes in $\theta_{v_{a,b}}$. Results also show that changes in model inputs such as drag coefficient (C_d), circularity index (circ), viscosity of air (μ_a), solid surface tension (γ_s) and the proportionality constant (A) do not influence the model output. C_d and μ_a influence the fluid forces which are negligible compared to the more dominant particle-particle, particle-wall and particle-impeller forces and as a result have no effect on the output. Similarly, $circ$ and γ_s affect the frictional forces of the liquid bridges which are negligible compared to the more dominant capillary and viscous forces. The fact that a change in A does not influence the model output bodes well with the current mechanistic breakage model, as large changes in A would be required to effect any change in model output. This coupled with the sensitivity coefficients for other model inputs show that the model is primarily driven by fundamental material properties and process/design parameters rather than any empirical constant. It can also be observed that in terms of uncertainty propagation, more accurate measurements would be required for model inputs such as the Young's modulus of the impeller (E_i) and wall (E_w), binder surface tension (γ_l), binder viscosity (μ_l) and contact angle (ϕ).

Table 5.2: Parameter sensitivity with respect to material properties.

Time (s)	$\frac{\partial F}{\partial \gamma_s}$	$\frac{\partial F}{\partial \gamma_l}$	$\frac{\partial F}{\partial \mu_l}$	$\frac{\partial F}{\partial \phi}$	$\frac{\partial F}{\partial \rho_s}$	$\frac{\partial F}{\partial \rho_l}$	$\frac{\partial F}{\partial E_p}$	$\frac{\partial F}{\partial \sigma_p}$	$\frac{\partial F}{\partial e_p}$	$\frac{\partial F}{\partial circ}$	$\frac{\partial F}{\partial C_d}$	$\frac{\partial F}{\partial TSA}$
1	0	3.982	2.52	8.77	1.15	0.10	3.21	0.31	0.07	0	0	1.31
10	0	3.95	2.50	8.67	1.14	0.09	3.19	0.31	0.07	0	0	1.30
40	0	3.84	2.44	8.34	1.12	0.09	3.12	0.30	0.07	0	0	1.28
80	0	3.70	2.36	7.97	1.08	0.09	3.04	0.29	0.07	0	0	1.25
250	0	3.14	2.02	6.32	0.56	0.08	2.70	0.25	0.06	0	0	1.12
500	0	2.43	1.58	4.61	0.77	0.06	2.22	0.20	0.05	0	0	0.93
800	0	2.10	1.42	3.99	0.66	0.06	1.83	0.18	0.05	0	0	0.84
1000	0	2.27	1.57	4.17	0.74	0.06	2.08	0.20	0.07	0	0	0.95
1500	0	2.75	1.97	4.79	0.96	0.08	2.81	0.25	0.07	0	0	1.26
1800	0	3.06	2.22	5.27	1.11	0.09	3.30	0.28	0.09	0	0	1.45

Table 5.3: Parameter sensitivity with respect to process and design properties.

Time (s)	$\frac{\partial F}{\partial \mu_a}$	$\frac{\partial F}{\partial E_w}$	$\frac{\partial F}{\partial E_i}$	$\frac{\partial F}{\partial \sigma_w}$	$\frac{\partial F}{\partial \sigma_i}$	$\frac{\partial F}{\partial e_w}$	$\frac{\partial F}{\partial e_i}$	$\frac{\partial F}{\partial \theta_{v_a}}$	$\frac{\partial F}{\partial WA}$	$\frac{\partial F}{\partial IA}$	$\frac{\partial F}{\partial A}$	$\frac{\partial F}{\partial \frac{dA}{dt}}$
1	0	0.64	1.12	0.03	0.21	0.28	0.44	479.76	0.97	2.49	0	0
10	0	0.63	1.11	0.04	0.20	0.27	0.44	66.38	0.96	2.47	0	0
40	0	0.62	1.09	0.03	0.20	0.27	0.43	21.56	0.95	2.43	0	0
80	0	0.60	1.07	0.03	0.20	0.28	0.41	13.89	0.93	2.36	0	0
250	0	0.52	0.94	0.03	0.17	0.22	0.36	8.65	0.85	2.09	0	0
500	0	0.42	0.77	0.02	0.14	0.17	0.29	7.42	0.73	1.73	0	0
800	0	0.38	0.63	0.02	0.12	0.16	0.25	7.03	0.61	1.39	0	0
1000	0	0.42	0.71	0.02	0.13	0.18	0.28	7.18	0.71	1.57	0	0
1500	0	0.54	0.93	0.03	0.16	0.23	0.35	7.37	0.98	2.10	0	0
1800	0	0.62	1.08	0.03	0.19	0.26	0.39	7.43	1.16	2.44	0	0

[3]Only θ_{v_a} is listed as a model input as it is implicit that $\theta_{v_b} = 1 - \theta_{v_a}$

5.5 Model Validation Studies in High Shear Granulation

Model validation is an important step in the overall development and formulation of a model. A model that has been successfully validated can be used for further process analysis, to facilitate design, optimisation, control and scale-up of the process. In the case of granulation, validation of a first-principles based granule breakage model has not been reported in the literature. The only study by Dhanarajan and Bandyopadhyay (2007) (their energy-based breakage model was discussed in Chapter 2) showed some initial work towards model validation. However, their study was restricted to the one-dimensional validation of evolutions of granule weight fractions (for small, large and intermediate granules) and did not account for distributions in granule size and/or evolutions of binder content and porosity. Furthermore, their model was validated for only one experimental setting without examining its potential to predict granule output (e.g the weight fractions) at different experimental settings. It must be noted that the ability of the model to accurately predict specific output (e.g. evolutions and distributions) is a key component that distinguishes sound first-principles based models from empirical or semi-empirical models. The latter by virtue of their lack of a physical basis, are not viable for prediction purposes. Therefore, in this study, the developed breakage model is validated at a nominal set of experimental conditions and the tuned model is used to predict with greater accuracy multi-dimensional evolutions of distributions at other operating conditions and/or formulations.

5.5.1 Materials and Methods

For the high-shear granulation experiments, glass-ballotini (Potters, UK) was used as the primary powder. This material had a volume mean diameter (d_{30}) of $112\mu m$ and a size range of $75\mu m$ to $150\mu m$. The measured skeletal density of the material was $2.48\, kgm^{-3}$. Polyvinyl alcohol (Fisher Scientific, USA) in water (PVOH-H_2O) (2.5% and 5% concentration by mass) was used as the liquid binder.

The high-shear granulation experiments were performed using a laboratory scale food processor mixer (Kenwood). The high-shear mixer is a vertical axis granulator with a

diameter of $0.2\,m$ and a height of $0.15\,m$. All the experiments were conducted with an impeller angular speed of $500\,rpm$. For each experiment, approximately $500\,g$ of dry powder was granulated with PVOH-H_2O (2.5%) to form larger wet granules. These granules were then sieved and granules within the $500 - 600\,\mu m$ size range were then used as the starting material to perform the breakage-only granulation experiments. Due to only limited amount of residual binder and no additional input of binder, granule breakage is dominant over granule growth. Samples were taken at distinct intervals by scooping approximately $40\,g$ of material from different locations within the mixer. In order to test the reproducibility of the sampling method, one experiment was performed where the granulation process was ceased after 10 minutes and four samples were withdrawn from the mixer. By comparing the standard deviation across the samples, it was realised that there was minimal sampling error. The samples were subsequently dried overnight at ambient temperature. After drying, the granule size distribution (GSD) was determined via a particle size and shape analyser (Ankersmidt). An average binder content at different sampling times was measured prior to the overnight drying, by means of thermo-gravimetry. In a similar fashion, the average porosity was determined by means of pycnometry, after the overnight drying. All experiments and measurements were performed thrice to ensure reproducibility.

5.5.2 Model Validation Results and Discussion

The proposed experimental design serves to emphasize granule breakage such that aggregation rates can be neglected. Nucleation does not apply as it is restricted to nuclei formed from primary particles and in the current predominantly breakage-only case, the initial feed are larger granules. Therefore, the population balance model accounting for only breakage and consolidation is validated by comparing the simulated output with experimental measured data. Granule samples were taken out from the drum granulator at time instances of $60\,s$, $120\,s$, $240\,s$ and $600\,s$. In the model, the primary particles are mono-dispersed with an average diameter of $550\mu m$. Other model inputs such as the initial number of seed particles and those listed in Table 5.1 (with the exception of ϕ) were set as per experimental conditions (e.g. $D_{lower} = 150\mu m$ as this corresponds to the lower limit of the primary particle diameter and once the particles reach this diameter, they can-

not break into smaller constituent particles). A and ϕ (for which accurate measurements were not available) and the consolidation constant (c) were used as tuning parameters for matching the predicted model outputs with experimental measurements of the granule attributes. The first set of data (case 1) was used to tune the model i.e.. estimate the three parameters in the model. Subsequently, the tuned model was used to predict the GSD and evolution of average diameter at different operating conditions/formulations (cases 2 and 3). Case 1 corresponds to a binder viscosity of $0.0052\,Pa.s$ (2.5% PVOH-H_2O) and binder-to-solids ratio of 0.125 (i.e., $\frac{L}{S} = 0.125$) . Case 2 corresponds to a binder viscosity of $0.022\,Pa.s$ (5.0%PVOH-H_2O) with $\frac{L}{S} = 0.125$. Case 3 corresponds to a binder viscosity of $0.0052\,Pa.s$ with $\frac{L}{S} = 0.15$. All other material properties and process/design parameters were the same for the three cases. The model was tuned by increasing or decreasing one of the selected parameters while holding the others constant and using the first set of data, the parameters, $c = 5 \times 10^{-5}$, $A = 1.5 \times 10^{-9}$ and $\phi = 0.694$ were obtained. These values for the parameters were used thereafter for the second and third set of data.

Figure 5.21a depicts the simulated temporal evolution of the total particles in the system which increases due to particle breakage, for cases 1, 2 and 3. Due to the higher binder viscosity in case 2, the liquid bridge strength is higher which in turn slows down the rate of breakage compared to case 1. Similarly, due to a higher binder content in case 3 as compared to case 1, the liquid bridge strength is higher resulting in reduced breakage. Figure 5.21b shows the change in average particle diameter with time. The model is able to capture the particle level phenomena and sensitivities of the process resulting in a close match between the simulated profile and experimentally measured data for all cases. Due to the higher liquid bridge strength, average particle diameter for cases 2 and 3 is higher than that of case 1. Figures 5.21c and 5.21d depict the change in average binder content and porosity with time respectively, for case 1. It can be seen that within acceptable measurement error, the model is able to capture of the range of these average properties. Average binder content reported remains constant throughout as no binder is added or removed to/from the system. A marginal increase is observed for average porosity and as mentioned earlier, this is attributed to the consolidation effect not strong enough as compared to particle breakage, to effect any decrease in particle porosity. Similar

observations were obtained for cases 2 and 3.

Figures 5.22 a-d, 5.23 a-d and 5.24 a-d show the model and experimental GSDs at each time instance corresponding to the intermittent sampling times (i.e.. 60s, 120s, 240s and 600s) during the experiment for cases 1, 2 and 3 respectively. The GSDs are represented as the normalised volume frequency (V_f) of granules with respect to granule diameter (D) as defined in Equation 5.53

$$V_f(D,t) = \frac{F(D,t)}{\int F(D,t)dD} \times \frac{V(D)}{\int V(D)dD} \tag{5.53}$$

where V is the particle volume. A clear progression is observed during the course of granulation whereby particles undergo breakage forming smaller sized particles, which is depicted by a gradual reduction in the peak corresponding to $550\mu m$. It can be seen that the tuned model is able to accurately capture the experimental GSD for case 1 and thereafter able to accurately match/predict accurately the GSD for cases 2 and 3.

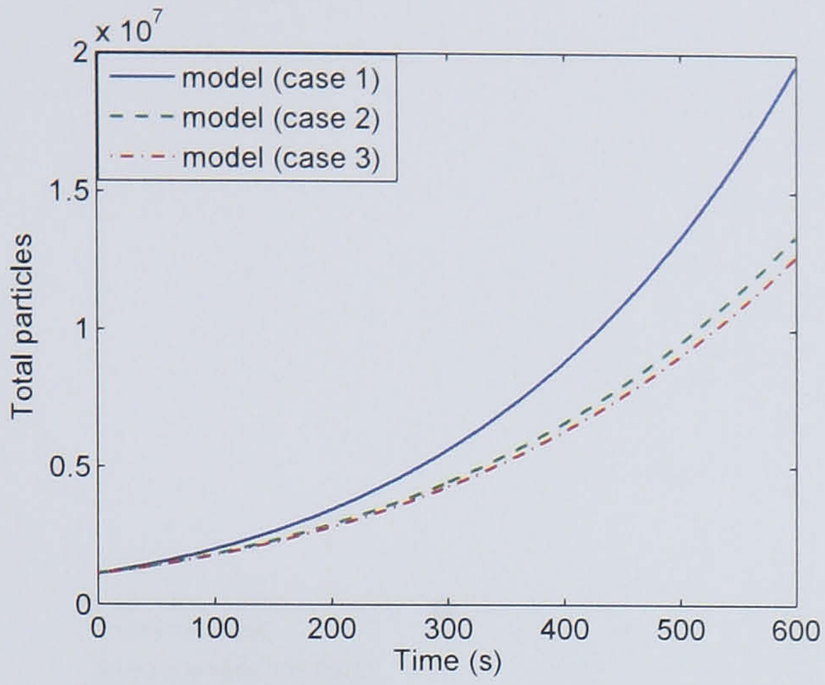

(a)

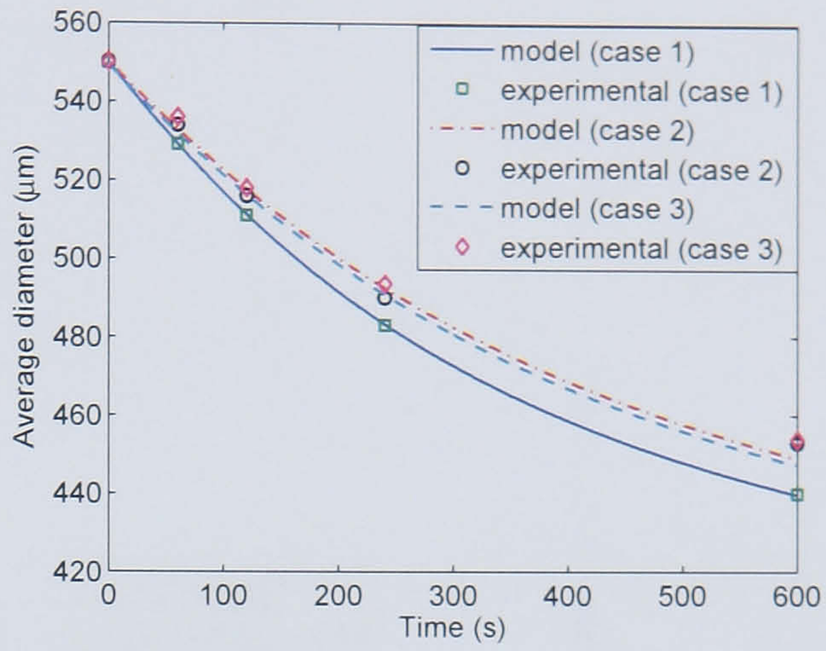

(b)

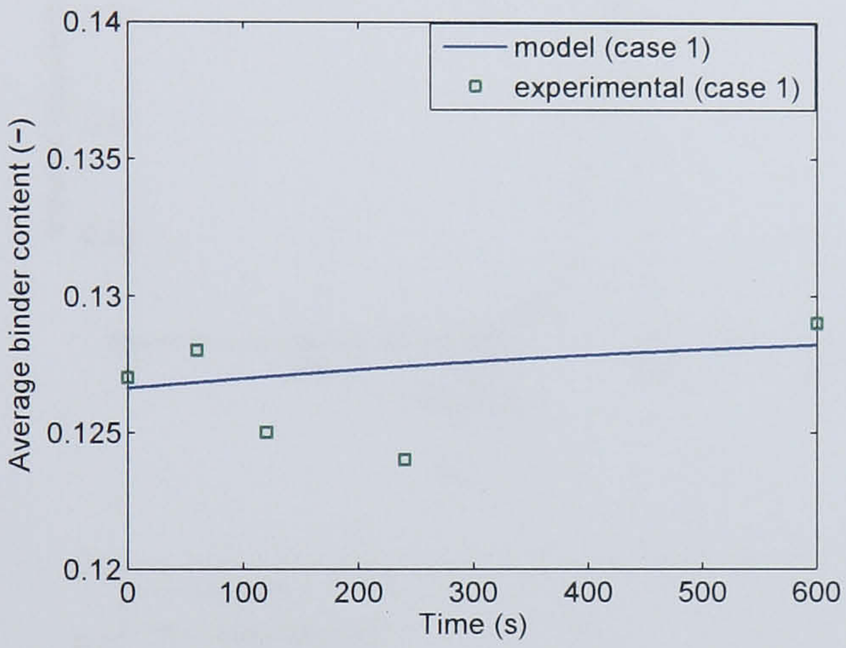

(c)

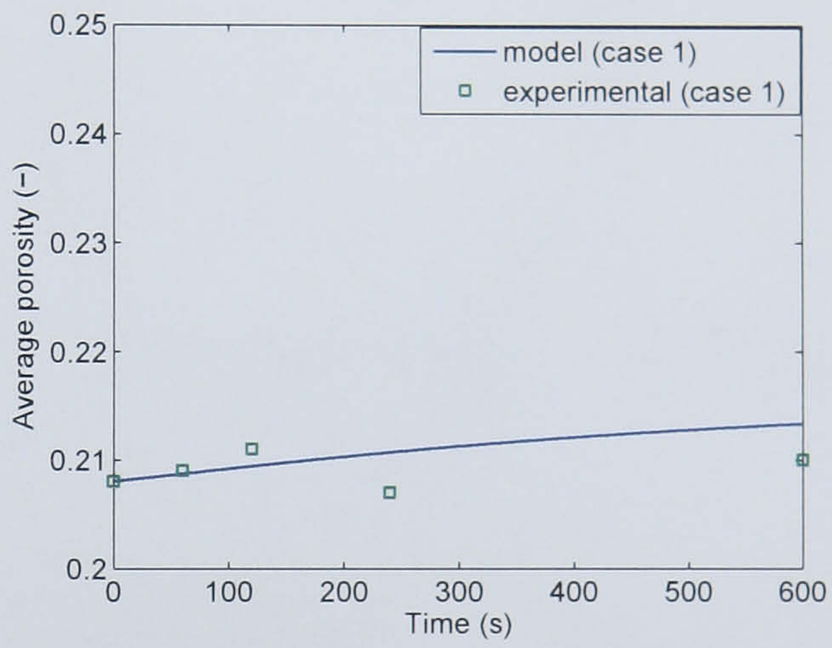

(d)

Figure 5.21: Comparisons between temporal evolutions of experimentally measured and model predictions of (a) total particles, (b) average diameter, (c) average binder content and (d) average porosity.

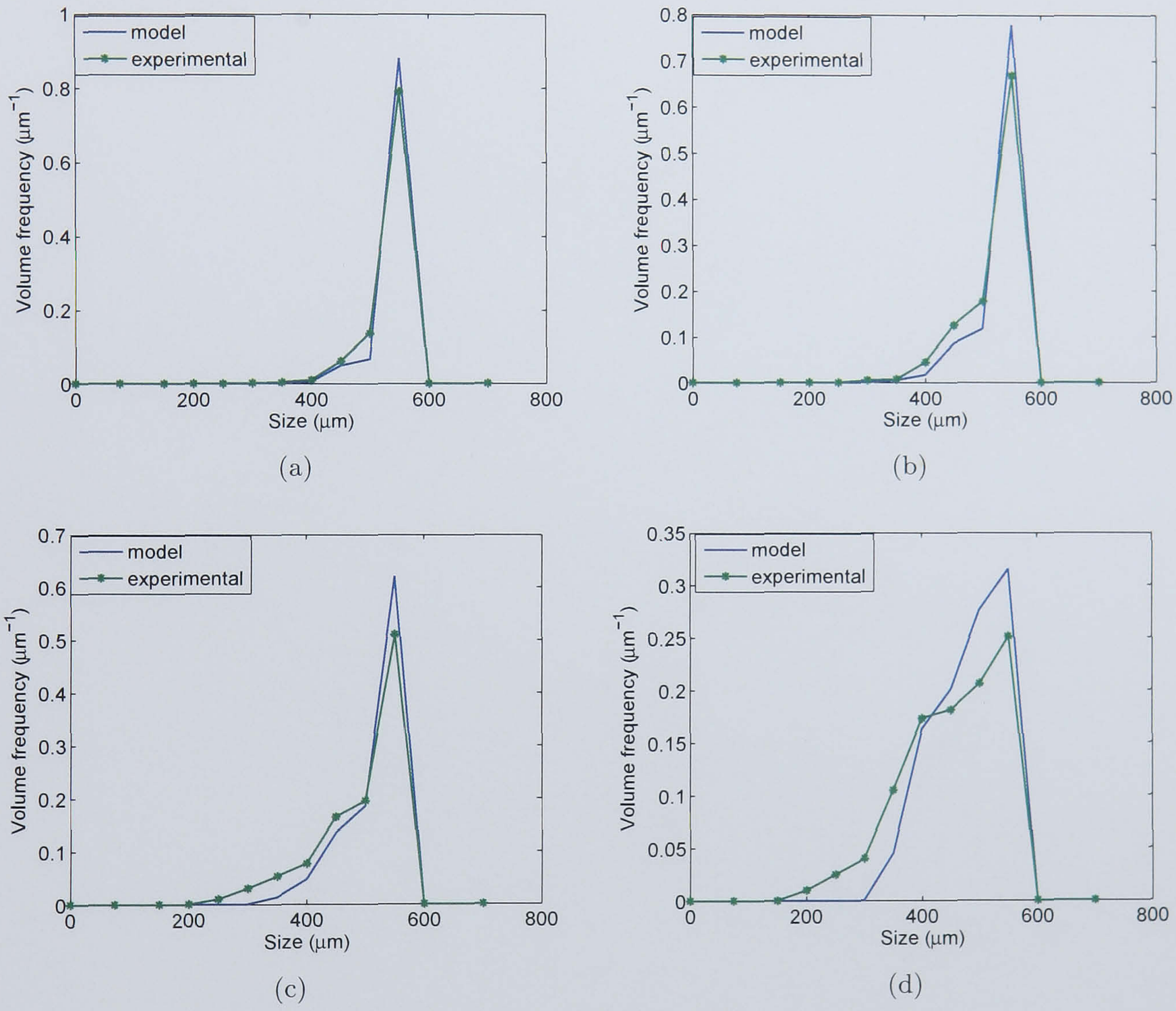

Figure 5.22: Comparisons between simulated and experimental GSDs for case 1 for (a) t=1 min, (b) t=2 min, (c) t=4 min and (d) t=10 min.

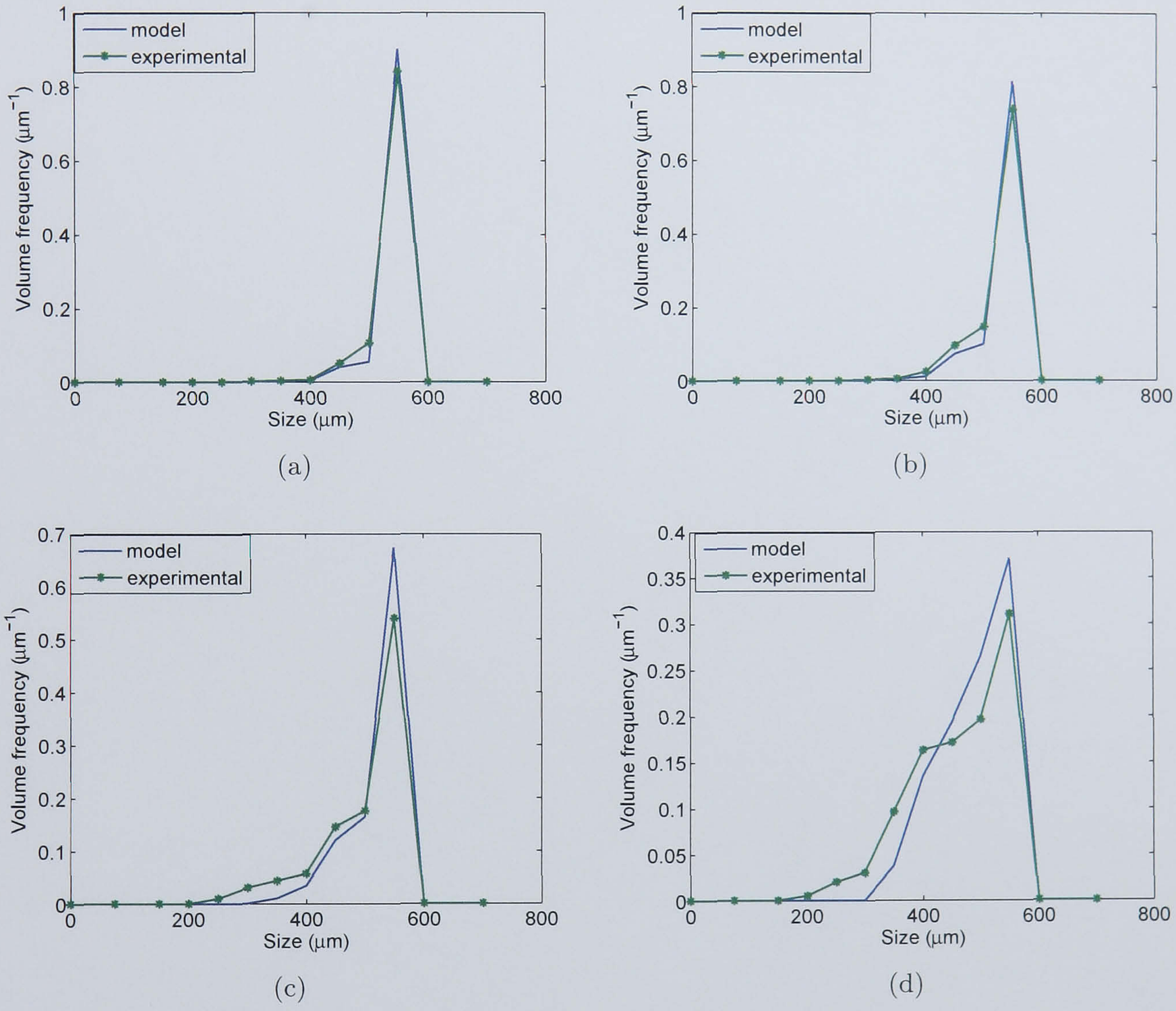

Figure 5.23: Comparisons between simulated and experimental GSDs for case 2 for (a) t=1 min, (b) t=2 min, (c) t=4 min and (d) t=10 min.

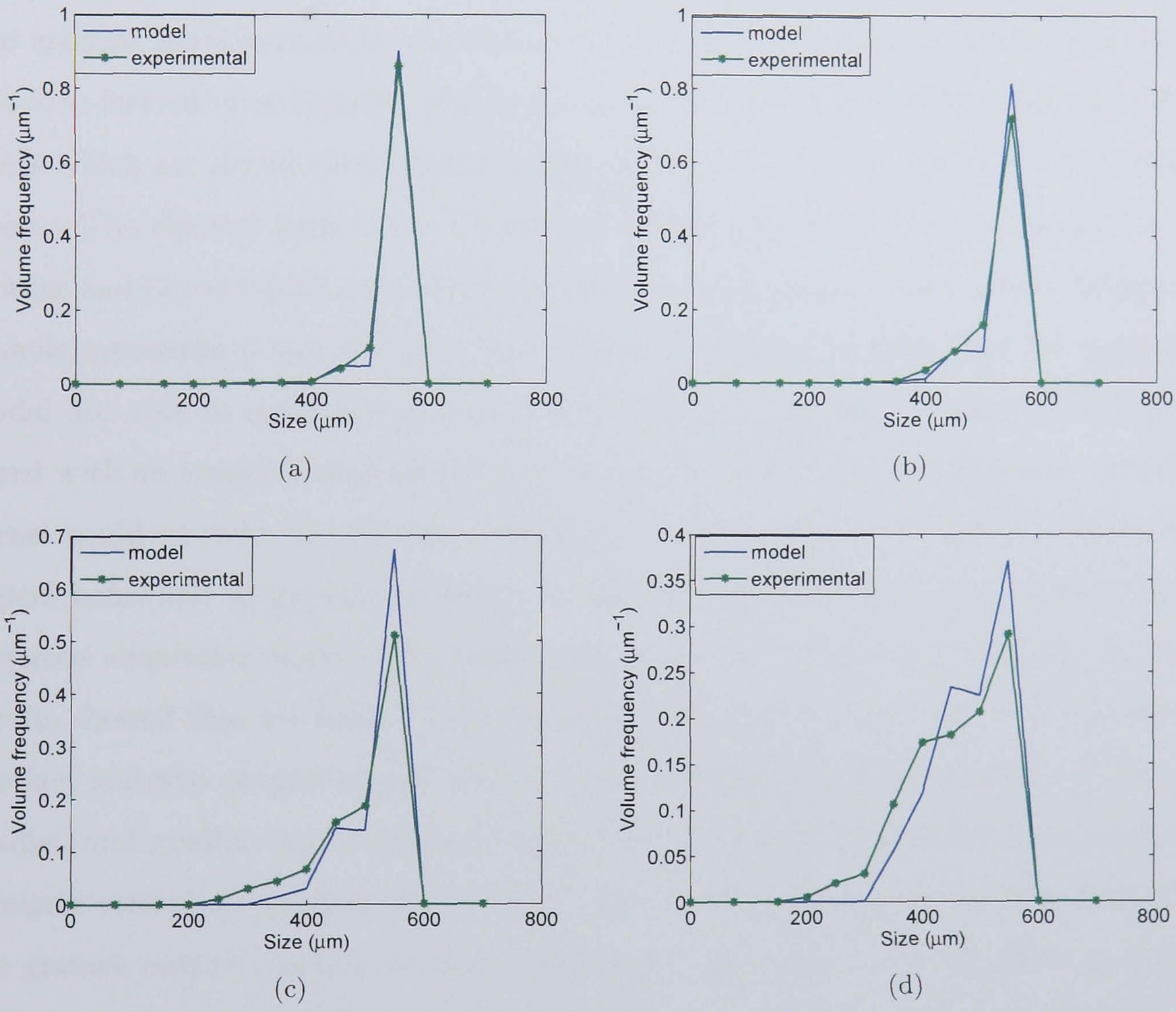

Figure 5.24: Comparisons between simulated and experimental GSDs for case 3 for (a) t=1 min, (b) t=2 min, (c) t=4 min and (d) t=10 min.

5.6 Summary

In this chapter, the theoretical development of a novel breakage kernel was presented. The kernel was based on the underlying physics and chemistry of the granule breakage phenomenon. The kernel was formulated as a quotient of external stress applied over the intrinsic strength of a granule, which is analogous to the Stokes' deformation criteria and is a realistic characterisation of granule breakage. The external stress is modelled taking into account particle-particle, particle-wall and particle-impeller collisions; and the contact area formed upon impact. The intrinsic strength is characterised by the liquid bridge forces which are determined mainly by the capillary forces, viscous forces and frictional forces. The derived kernel is a function of several important material properties (i.e., powder and liquid binder properties) and process/design parameters, which influence the granule intermittent and end-point properties. The kernel shapes from the mechanistic model are able to qualitatively predict the expected breakage behaviour. When compared with an empirical and semi-empirical kernel, it could be seen that the mechanistic kernel could account for the rate differences in accordance with expected phenomenological behaviour of granule breakage, unlike the empirical and semi-empirical kernels. Rigorous simulation studies were undertaken to test the form of the breakage model and results showed that the model accurately described the breakage kinetics. The effects of the key material properties and process/design parameters on the granule output were studied and qualitatively confirmed that the kernel/model predictions were accurate. A dynamic sensitivity analysis of the model inputs was performed and results showed that the granule output (particle density distribution) was sensitive to variations in expected properties/parameters such as contact angle, viscosity, surface tension and volume fraction of daughter particles formed. This along with the fact that the influence of the empirical constant in the kernel does not dominate the mechanistic parameters, corroborates the overall effectiveness of the kernel development. Successful high-shear experiments were also performed to mimic predominantly breakage only behaviour whereby the rate of breakage was greater than that of growth enhancing mechanisms such as nucleation and aggregation. Quantitative validation of the GSDs between the model predictions and those obtained from experiments for the various cases showed very good agreement. The

model predictions for the average properties (i.e., size, binder content and porosity) were in close agreement to the experimentally measured data. Overall, these results are promising toward a comprehensive first-principles predictive model for the granulation process. that can help reduce the number of labour and capital intensive experiments required for a more in-depth understanding of the granulation process.

Chapter 6

Model Validation Studies under Low Shear Conditions

In this chapter, a combined dynamic population balance model is presented for the granulation process, employing a three-dimensional population balance framework. The nucleation, aggregation and breakage kernels used in the population balance model are derived using mechanistic representations of the underlying particle physics and chemistry. Thus, the fundamental properties of the powder and the liquid were used as parameters in the model to predict the granulator dynamics and granule properties. The population balance model is validated against experimental data from a Ballotini-HPC recipe obtained using a lab-scale fluid bed granulator (i.e., under low shear conditions) for granule size, fractional binder content and porosity. A reasonably good agreement between experimental and simulation results were obtained for the granule size distribution under different experimental conditions. In addition, accurate model predictions were made for the evolution of the average properties (i.e., size, fractional binder content and porosity) for various operating conditions, embodying the advantage of first-principles based mechanistic kernels.

[1]Part of this chapter is based on, R. Ramachandran, C.D. Immanuel, F. Stepanek, J.D. Litster and F.J. Doyle III, "A Combined Mechanistic Model for Nucleation, Aggregation and Breakage in a Population Balance Model of Granulation", To be presented at the AIChE Annual Meeting, Philadelphia, USA. 2008.

6.1 Introduction and Objectives

Fluid bed granulation is a process by which granules are produced in a single piece of equipment. It involves suspending the particles in an air stream and spraying a liquid binder from the top down onto the fluidized bed. Particles in the path of the spray are wetted and adhere to other wet particles to form a granule. Advantages of fluid bed granulation over other granulation methods are usually indicated to be higher product density and lower solvent and energy consumption (Boerefijn and Hounslow, 2005). The granulation process in a fluid bed requires a binary nozzle, a solution delivery system and compressed air to atomise the liquid binder. When the binder liquid is sprayed on to a fluidised bed, relatively loose and porous granules are formed. During spraying, a portion of the liquid is immediately lost to evaporation and thus the system has little tendency to pass beyond the liquid bridge phase. In chapter 4, the mechanistic nucleation and aggregation models were validated for a drum granulation system. In chapter 5, the mechanistic breakage model was validated for a high-shear granulation system. The impetus behind the work in this chapter is to validate and predict granule time evolutions of distributions for the combined cases of nucleation, aggregation and breakage, for a fluid-bed granulation system.

6.2 Experimental

6.2.1 Materials

The powder used in the experiments is glass ballotini supplied by Potters Europe. The size distribution of these primary particles ranges from $75 - 150\mu m$. The density of the glass ballotini is approximately 2500 kgm^{-3}. Hydroxypropylcellulose (HPC) supplied by Fisher Scientific, with a molecular weight of 100000 was used as the liquid binder.

6.2.2 Experimental Setup

The experiments reported here are conducted in a laboratory scale fluid bed granulator (4M8-Fluidbed, Pro-Cept). The equipment is a $2\,kg$ product capacity fluid bed granulator and dryer. The schematic diagram for the experimental setup can be seen in Figure 6.1.

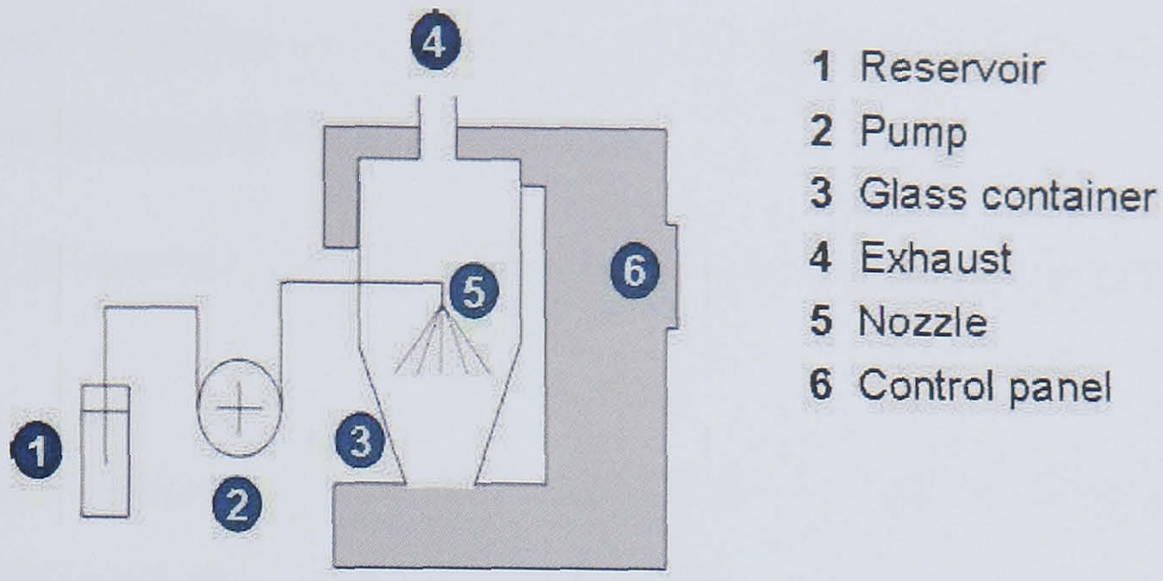

Figure 6.1: Experimental setup: 1. Reservoir (binder), 2. Pump, 3. Exhaust, 4. Control panel, 5. Nozzle, 6. Glass container.

The experiments are conducted in the glass container with the lower portion being conical in shape and a cylindrical upper portion. The whole container is $0.48\,m$ in height while the upper cylindrical portion has an inner diameter of $0.25\,m$ and height of $0.15\,m$. The fluidising air flows from the bottom of the container through a distribution grid which ensures a uniform distribution of fluidising air. For all experiments, the binder spray nozzle used is a movable, two-fluid (binder and air) spray nozzle. Spray from the nozzle is in a downward direction, counter current to the fluidising air flow.

6.2.3 Experimental Protocol

Prior to conducting any experiments, it is important to establish an experimental protocol that is to be observed during the course of the actual experiments (Tan et al., 2006). Therefore, the granules are manufactured according to the following experimental procedure:

1. The liquid binder (at a specified viscosity) is prepared a day before to allow for complete dissolution of solute (HPC) in solvent (water)

2. The glass ballotini (200g) is loaded into the fluidising chamber.

3. The bed is fluidised for a short period of time (2min) at a low fluidising flow rate

until the bed temperature (indicated by the outlet temperature) is approximately the same as the required temperature.

4. The nozzle is inserted into the chamber and the binder is pumped through for spraying.

5. The timing commences once the spraying starts and the fluidising air flow rate is immediately increased to the designated flow rate.

6. The experiment is run for approximately 10 min to simulate a typical batch experiment.

7. At the end of the experiment, samples of the product are obtained and subsequently analysed for various attributes.

6.2.4 Effect of Variables

Fluid bed granulation is inherently a more complex process than the other methods of granulation. This is mainly due to the large number of variables available at the operator's disposal in obtaining a suitable recipe for achieving good granulation. Different systems (ballotini-HPC in this case) require a different set of variables. Important factors that affect the fluid bed granulation process can be divided into two distinct groups which are equipment related variables and process related variables. The former includes 1)pressure drop and 2) filter shaking. The latter includes 1) inlet air temperature, 2) nozzle atomization pressure, 3) fluidisation air velocity and 4)nozzle position. Equipment related variables are generally fixed and cannot be altered prior to or during the course of granulation. Process related variables on the other hand can be altered and do have significant impact on the end point granule attributes such as size and porosity. Tan et al. (2006) showed by conducting experiments in a small-scale fluid bed granulator, it was observed that different operating conditions influence the granule growth behavior, size distribution and in some cases, the morphology of the granules produced. The results reported by Tan et al. (2006) are important because this conclusively shows that various granule attributes such as granule size, binder content and granule porosity would vary in both time and space dimensions under different operating conditions. This would enable

us to validate the mechanistic kernels for the different operating conditions. A positive outcome would reveal that the kernel is valid over a wide range of operating conditions.

6.2.5 Data Characterisation Methods

Size analysis was performed by means of the particle size and shape analyser (Ankersmid). Binder content was measured by means of thermogravimetry and porosity was measured using pycnometry. These methods have previously been discussed in chapters 3-5.

6.2.6 Experimental Design

An experimental design is essentially a systematic investigation carried out on a process. A series of structured tests is designed in which planned changes are made to the input variables of the process. The effects of these changes on a pre-defined output are then assessed. The first step in the experimental design is to identify the input(s) and define the process output(s) to be measured. The inputs are grouped into three categories, 1) physical parameters, 2) empirical constants and 3) design parameters (see Chapters 4 and 5 for more details).

Different operating conditions result in different batches of granules with different internal attributes (such as size, binder content, porosity) (Hemati et al., 2003). However, it is possible that given a set of operating conditions, little or even no granules may be produced. Furthermore, a set of operating conditions that produce a good batch of granules in one particular system, may not be applicable to another system. The purpose of obtaining a good batch of granules is to facilitate data analysis from which useful information may be extracted. Hitherto, there exists no published literature on suitable operating conditions to achieve good granulation for a ballotini-HPC system using fluid bed granulation. Hence, the first step prior to commencing the design of experiments is to ascertain a set of operating conditions (termed as the nominal case, as it may not be optimal) that is able to produce a sufficient percentage of granules that can be analysed subsequently. This is carried out by selecting a set of operating conditions of a system while not exactly matching the ballotini-HPC system but is similar (in terms of powder density and liquid binder viscosity). This set of conditions is termed as the base case from which a careful paramet-

ric study (varying one parameter at a time, keeping the others constant) is carried out until a nominal set of operating conditions is identified. The nominal set identified (See Table 6.1) represent the starting point from which the variables/parameters are increased or decreased to obtain another new set of experimental data.

It was shown by several authors such as Madec et al. (2003); Blandin et al. (2003) that aggregation is only possible within a certain binder to solids ratio (BSR). Below the minimum value aggregation is either nil or minimal and resulting granules are extremely weak. Above the maximum value, the granules are wet, prone to form chunks and are heterogenous in size and shape (Subero-Couroyer et al., 2006). The operational BSR is system specific and may be found empirically. For the ballotini-HPC system, the BSR is found to be in the range of 0.20-0.25. It is observed that within this range, a small change in the BSR value could have a big effect on the final granule size and porosity. Aside from the BSR, Hemati et al. (2003) have shown that binder viscosity also has an impact on granule size and porosity. In this system, a range of 5% to 10% concentration of HPC as binder is tested. It is observed that at a viscosity corresponding to less than 5% concentration of HPC, granules are weak and very little growth is observed and at the viscosity corresponding to more than 10% concentration of HPC, solution delivery of the binder is severely affected. It must be noted that to fully capture the richness of the mechanistic model, experimental conditions should be as varied as possible but ensuring that experiments are conducted within a suitable operating range as mentioned above. Taking this into consideration, the BSR and binder viscosity are altered within specified bounds keeping all other experimental conditions constant. The nominal experiment at a fixed time is repeated thrice to ensure reproducibility of experimental data.

Table 6.1: Nominal experimental conditions for ballotini-HPC system.

Condition	**Value**
Air speed (cm^3/min)	80
Temperature (^OC)	40
Nozzle air pressure (bar)	1
Binder flow rate (ml/min)	15
Binder volume (ml)	45
HPC concentration $(wt\%)$	8

6.3 Results and Discussion

In this chapter, the results from three granulation experiments are reported. For case 1 the target binder-to-solids ratio was 0.225 with a binder concentration of 8%. For case 2, the experimental conditions remain identical to case 1 with the exception of changing the target binder-to-solids ratio to 0.25. Finally, for case 3 the experimental conditions remain the same as for case 1 with the exception of varying the binder concentration to 10%. Thus, case 1 and case 2 allow for a comparison between different liquid binder-to-solids content whilst case 1 and case 3 will enable comparisons to be made between the effects of binder concentrations and hence binder viscosities. Samples were collected at different times and subjected to a measurement of the size distribution, fractional binder content and porosity.

The model simulations were carried out on a 2GHz Intel Dual Core single processor desktop computer with 2GB RAM using the intel FORTRAN compiler. The total discretised domain for the simulation comprised of 40, 20 and 12 bins along the solid, liquid and gas internal coordinate axes, respectively. The width of the bin along the solid volume is $\Delta R_s = 1.0 \times 10^{-5}\, m$, the width of the bin along the liquid volume ranges between $\Delta R_l = 2.50 \times 10^{-7}\, m$ to $\Delta R_l = 3.50 \times 10^{-5}\, m$ and the width of the bin along the gas volume is $\Delta R_g = 1.5 \times 10^{-6}\, m$. The computation time required for the simulation of the population balance model accounting for nucleation, aggregation and consolidation was approximately $1.5\, hrs$ for all cases.

The population balance model was validated by comparing the simulated variables with experimental measurements. Granule samples were taken out from the drum granulator at the time instances of $180\,s$, $300\,s$, $420\,s$, $600\,s$ and $900\,s$. The primary particles were mono-dispersed with a median diameter of $123\,\mu m$. Other model inputs such as the initial number/mass of seed particles, volume of the binder droplet, duration of binder addition, and binder flow rate were set as per actual experimental conditions.

Table 6.2: Values of the adjustable constants used for model validation.

No.	Property	Value
1	c	5.0×10^{-4} (-)
2	c_1	2.0×10^{7} (-)
3	A_0	$4.0 \times 10^{-20}\ mol/m^3$
4	A	$3.0 \times 10^{-18}\ mol/m^3$
5	D_{upper}	$680\ \mu m$

6.3.1 Case 1

Case 1 corresponds to a binder-to-solids ratio of 0.225 and a binder concentration of 8%. The total particles in the system reduces over time and this can be attributed to the effects of nucleation and aggregation outweighing that of breakage (Figure not shown). This trend is expected as the initial binder spray results in the increasing growth and upon ceasing the binder spray, the residual binder in the system results in an overall continued positive growth. Figures 6.2a-c depict the changes in average particle diameter, fractional binder content and porosity. The plots show a good agreement between the simulated profiles and experimentally measured data.

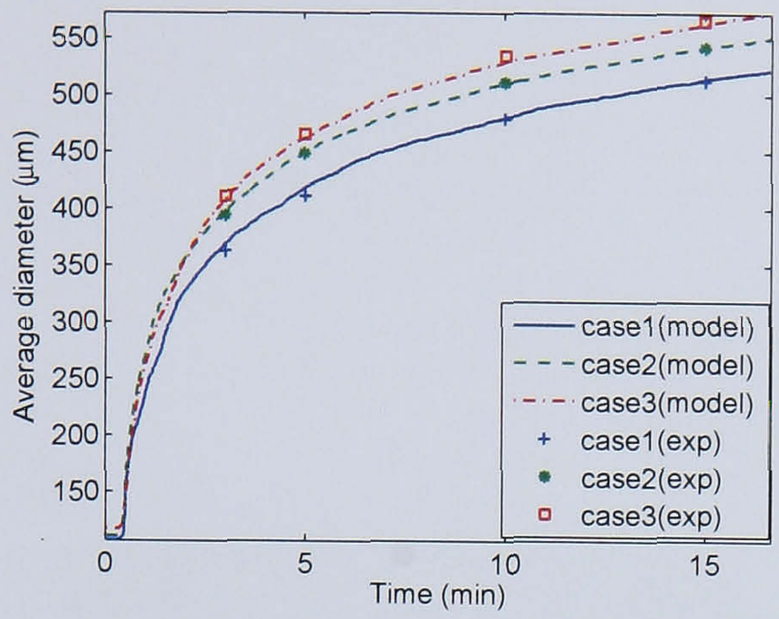

(a) Comparison between model predictions and experimental data for the evolution of average granule diameter for cases 1, 2 and 3

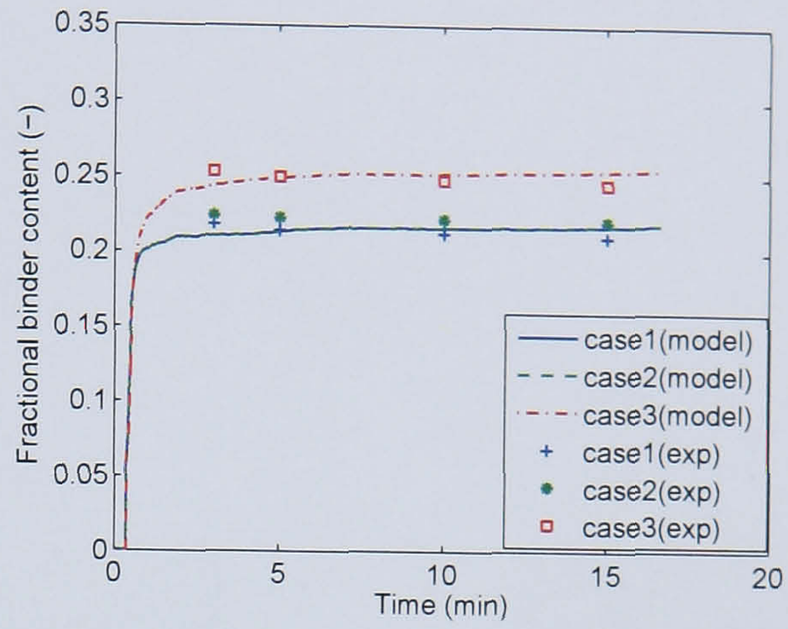

(b) Comparison between model predictions and experimental data, for the evolution of fractional binder content for binder-to-solids ratio for cases 1, 2 and 3

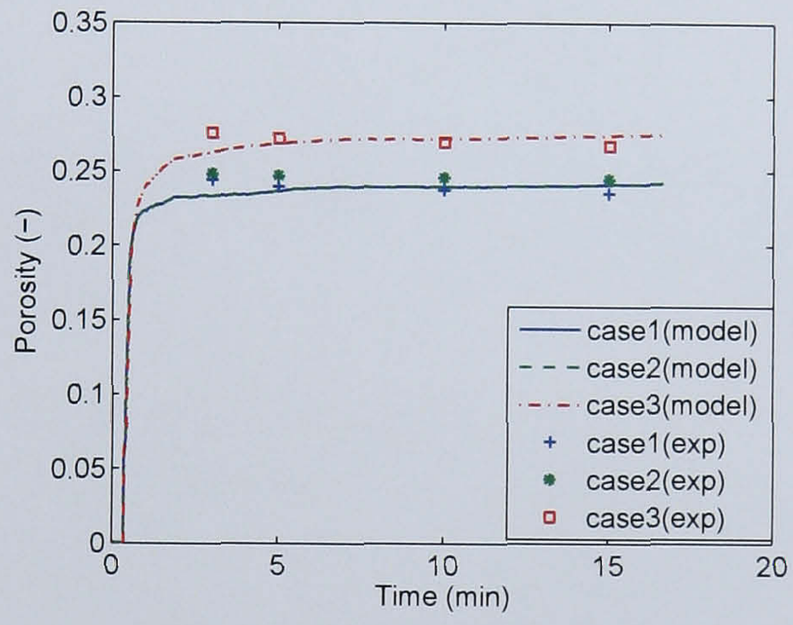

(c) Comparison between model predictions and experimental data, for the evolution of average porosity distribution for cases 1, 2 and 3

Figure 6.2: Time profiles for the average granule diameter, fractional binder content and average porosity for cases 1, 2 and 3 with comparisons made between model simulated predictions and experimental measurements.

The GSD profiles at the intermittent sampling times during the experiment (i.e. $180\,s$, $300\,s$, $420\,s$, $600\,s$ and $900\,s$) are compared with those obtained experimentally as seen in Figure 6.3. The GSDs are represented as the normalised number frequency of granules with respect to granule size. A clear progression is observed during the course of granulation whereby particles agglomerate together forming larger sized granules, which is depicted by the gradual reduction in the peak spanning $0 - 200\,\mu m$ and a corresponding growth in the peak spanning $600 - 750\,\mu m$ (note the change in the range of the y-axis).

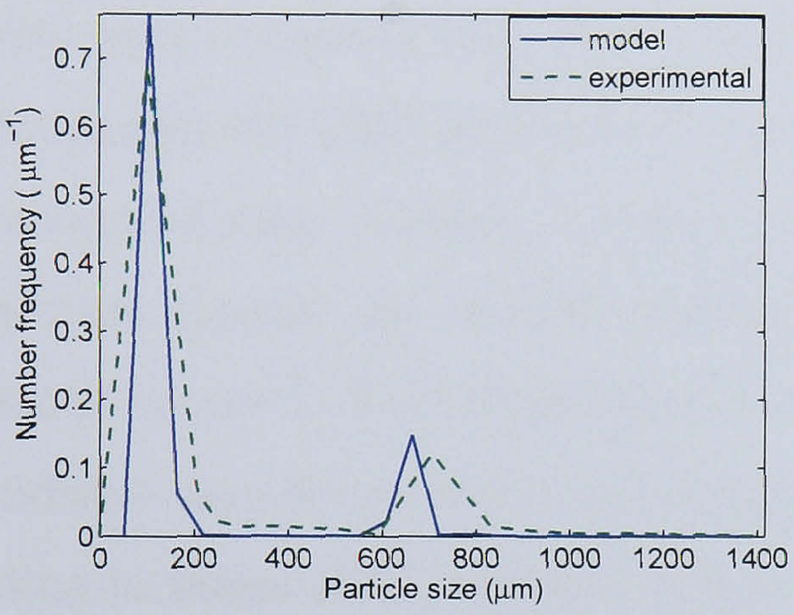

(a) time $= 3\,min$

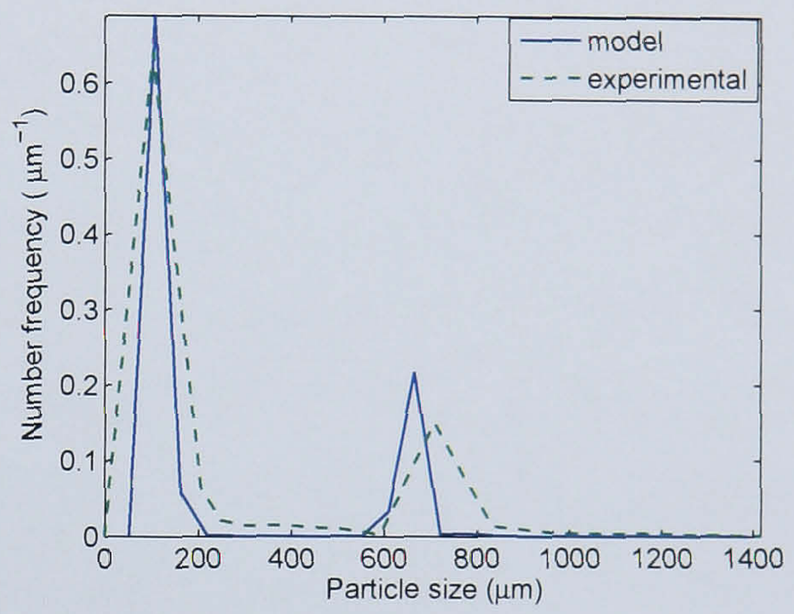

(b) time $= 7\,min$

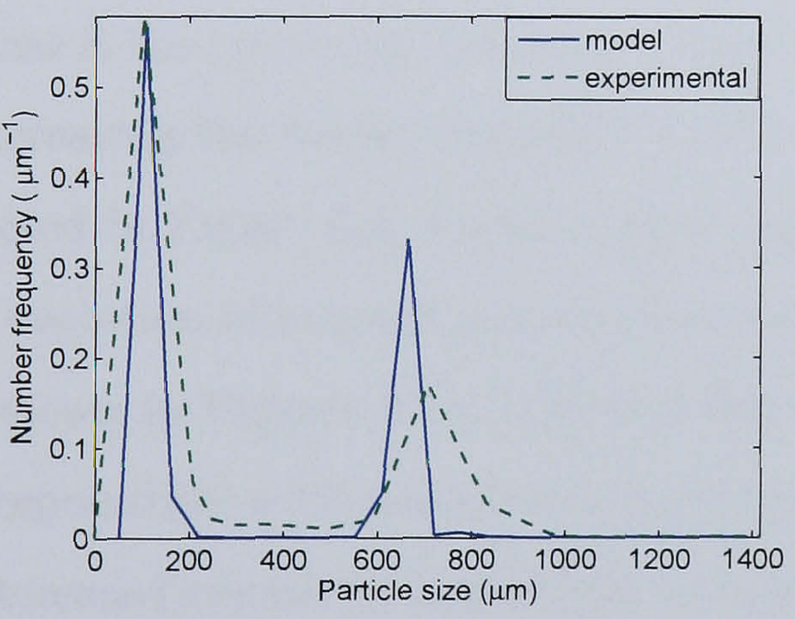

(c) time $= 10\,min$

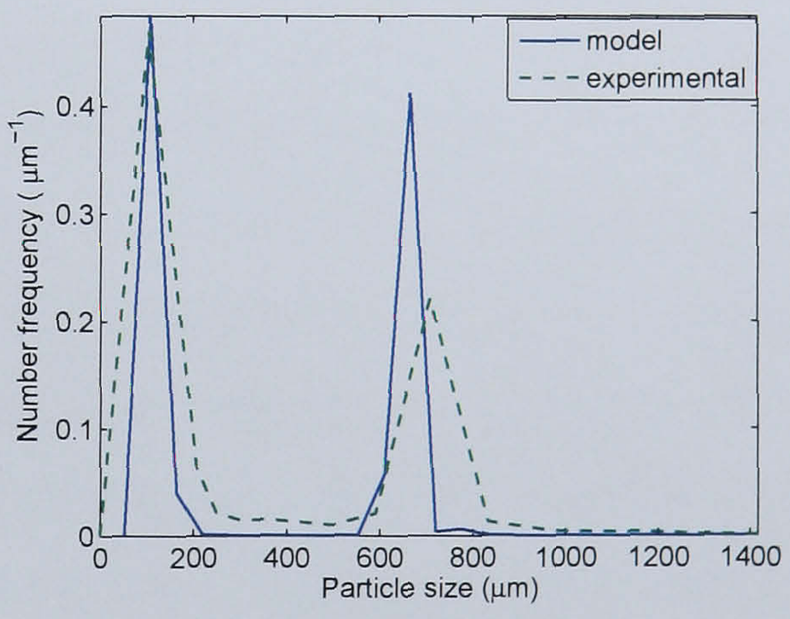

(d) time $= 15\,min$

Figure 6.3: Comparison of simulated and experimentally-measured granule size distribution at various time instances for binder-to-solids ratio = 0.225 and binder concentration = 8% (case 1).

6.3.2 Cases 2 and 3

Case 2 pertains to a binder-to-solids ratio of 0.25. while the other operating conditions remain unchanged as case 1. The various adjustable parameters are maintained at the values arrived at in case 1. Intuitively, the mean granule diameter and the fractional binder content should increase compared to the nominal conditions in case 1 which was operating at a lower binder-to-solids ratio. The simulated GSDs, fractional binder content and average porosity were compared with their experimental counterparts. In Figure 6.4. the model predictions for the GSD with the experimental data show a close correspondence between the two sets of data. Further, it is confirmed in Figures 6.2(a) and 6.2(b) respectively that the average granule size and the average fractional binder content are higher for case 2 compared to case 1. This is consistent with the theory that a higher binder-to-solids ratio (provided it does not exceed a certain upper bound) promotes nucleation and aggregation resulting in larger sized particles. Figure 6.2(c) shows a good match also of the average porosity predictions with the experiments.

In Case 3, the operating conditions were identical to those used in case 1 with the exception of increasing the binder viscosity to 10%. The ability of the model to predict the GSD is reflected in Figure 6.5, where a good alignment is achieved with the experimental data. The evolution of average granule diameter, fractional binder content and average porosity are shown in Figures 6.2a, 6.2b and 6.2c respectively. Model predictions provide a good correspondence with measurements of these averaged properties. The experiments indicate an increased sensitivity in the GSD to change in the binder viscosity from 8% to 10%, which is captured by the model prediction as well. In addition, the model adequately captures the trend seen in the experimental results for the average fractional binder content and average porosity among cases 1-3. Similar to the model validation for the drum granulation case, he fractional binder content and the porosity were treated as secondary variables and perfect match of these variables was not essential, and therefore not pursued during the parameter adjustment. The goal of parameter adjustment was to ensure a good match of the GSD and the average granule size. However, to ensure the predictive capability of the model under other operating conditions, it is important for these secondary variables to capture the non-linear trends shown by the experiments and in doing so, the model clearly

exhibits this ability.

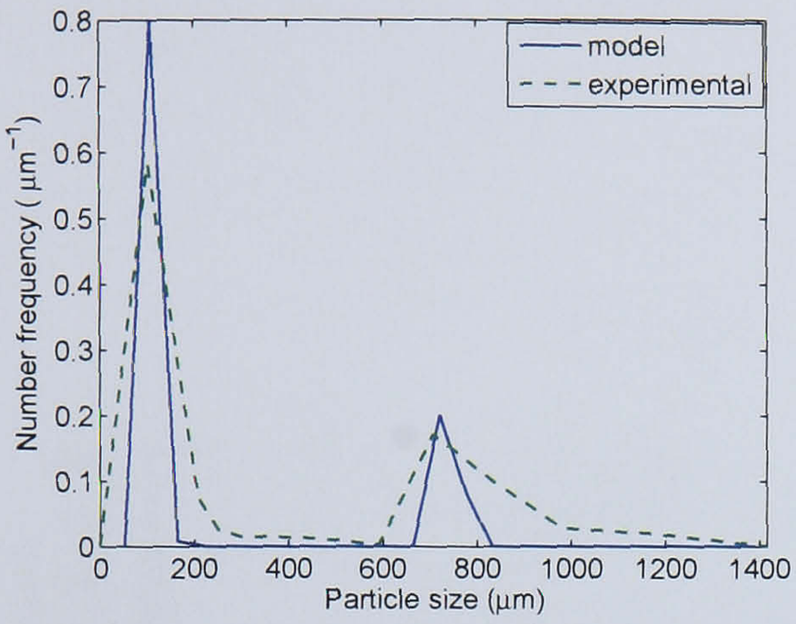

(a) time $= 3\,min$

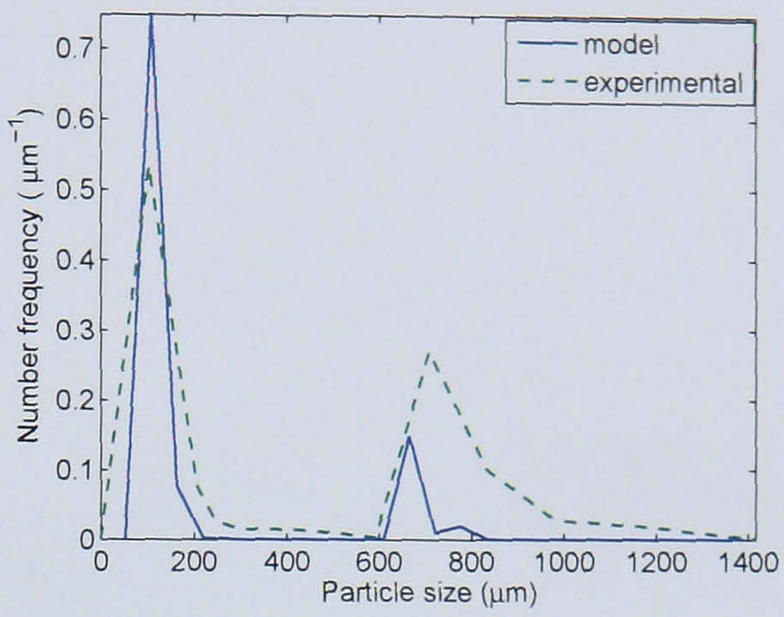

(b) time $= 5\,min$

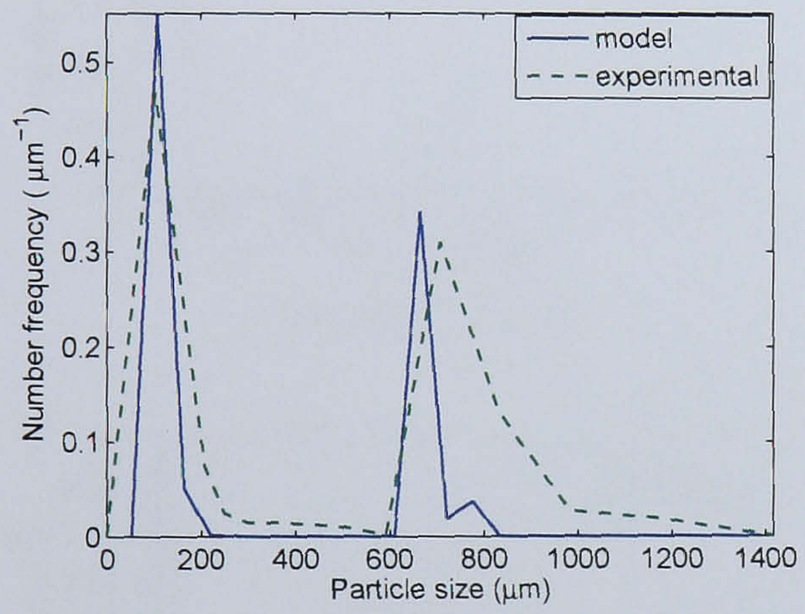

(c) time $= 10\,min$

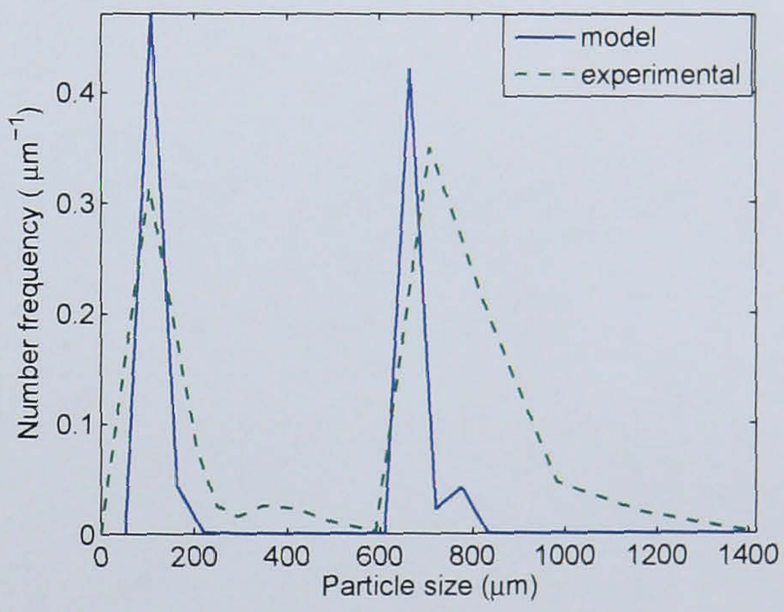

(d) time $= 15\,min$

Figure 6.4: Comparison of simulated and experimentally-measured granule size distribution at various time instances for binder-to-solids ratio = 0.25 and binder concentration = 8.0% (case 2).

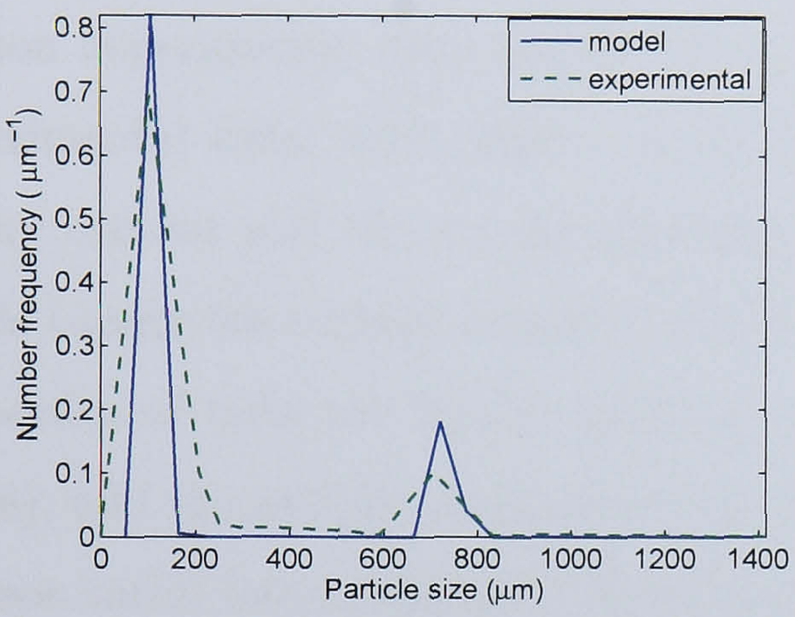

(a) time $= 3\,min$

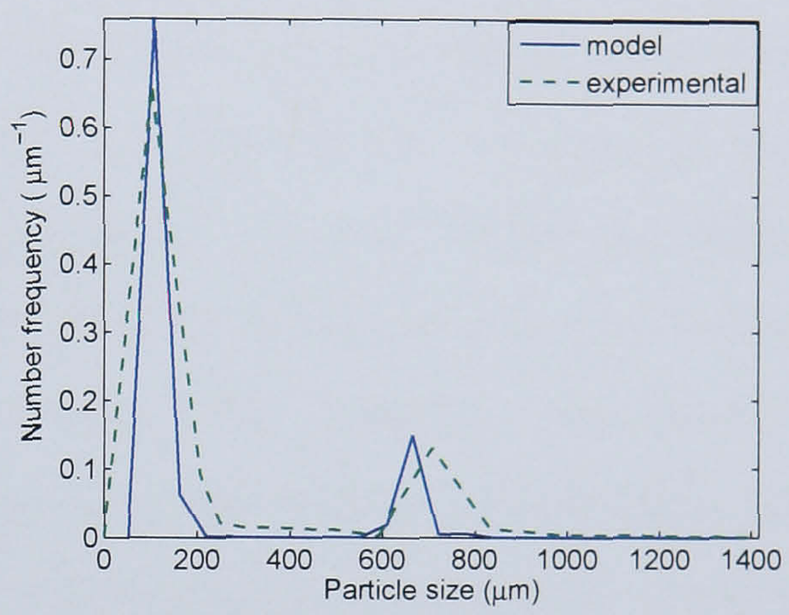

(b) time $= 5\,min$

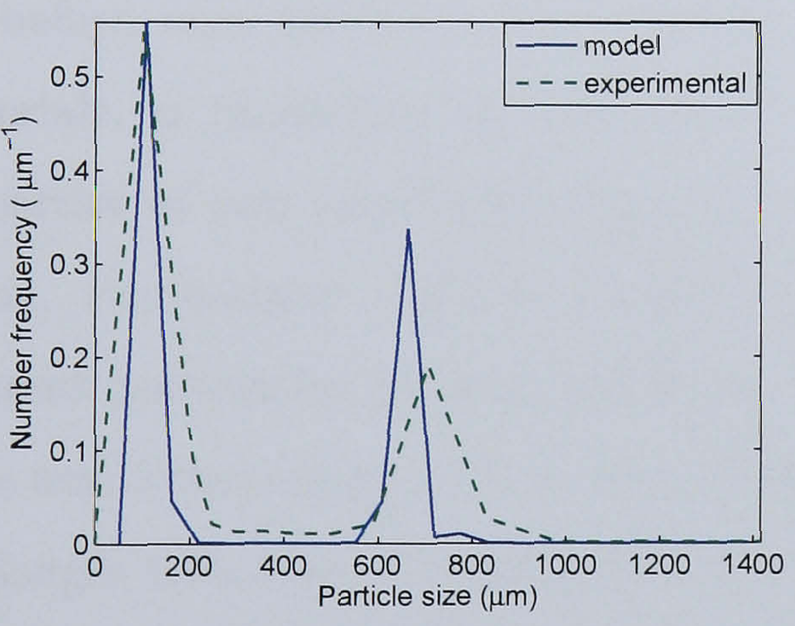

(c) time $= 10\,min$

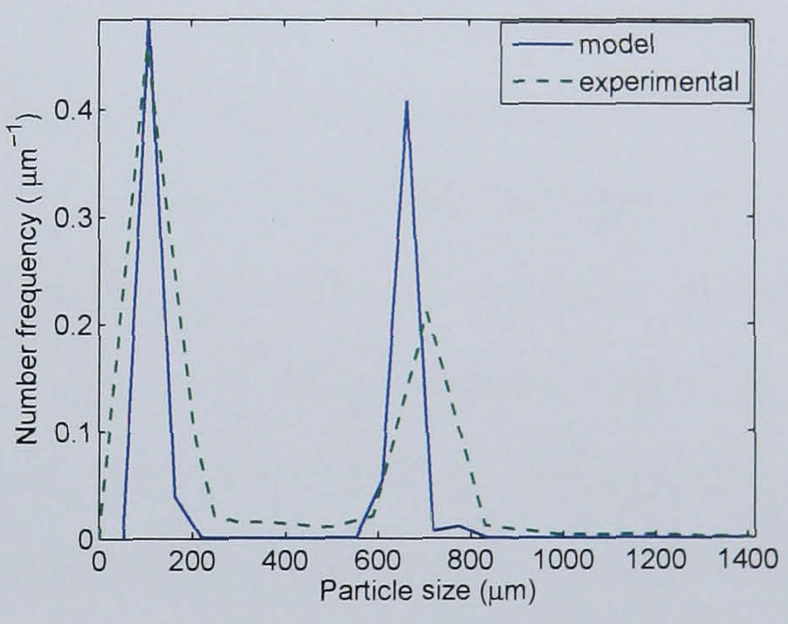

(d) time $= 15\,min$

Figure 6.5: Comparison of simulated and experimentally-measured granule size distribution at various time instances for binder-to-solids ratio = 0.225 and binder concentration = 8.0% (case 3).

6.4 Conclusions

In this chapter, a combined three-dimensional population balance model of a granulation process employing mechanistic representations for the nucleation, aggregation and breakage phenomena was validated for a Ballotini-HPC recipe under low shear conditions. Laboratory scale experiments were performed to obtain data on granule size distribution, fractional binder content and porosity. The comparison of the model with the batch granulation experimental data showed close correspondence between model simulations and experimental data, with respect to the granule size distribution, the average fractional binder content and the average porosity. These studies further confirm and support the thesis (under the current experimental conditions) that the incorporation of fundamental properties of both the binder liquid (e.g. viscosity, surface tension, solid-liquid contact angle), and the powder properties (e.g., density, size, size distribution, Young's modulus, Poisson ratio) into mechanistic kernels for the underlying granulation phenomena will enable an improved tracking of the dynamic behaviour of the granulation process. As pointed out before, once validated, such a model will be particularly valuable for scale-up of new materials, in predicting the granulator operation and dynamics given the fundamental properties of new materials with only a small number of carefully-designed experimentation. Furthermore, the fact that the mechanistic model was successfully validated for different granulation systems (albeit not exhaustively for many varying operating conditions and formulation) such as drum, high-shear and now fluid-bed, is promising toward the longer term step of developing a first-principles based generalised model which is capable of predicting/tracking granule properties for different systems and conditions.

Chapter 7

Controllability Analysis and Identification of Optimal Control-Loop Pairings in a MIMO Granulation Process

This chapter details a methodology for the controllability analysis and identification of optimal control-loop pairings for a multiple-input multiple-output granulation process. The work is based on a mechanistic three-dimensional population balance model (3D-PBM), which was validated at the batch-scale for various operating conditions and formulations (see Chapters 4-6). The main objective was to operate the granulation process under optimal conditions, by establishing the effect of manipulated variables on controlled outputs and identifying suitable control-loop pairings. Models directly identified from simulated step test data were the basis of the control-loop pairings. Novelty of the work lies in the investigation of **multiple optimal control loop pairings**, facilitating the possibility of increased efficiency in the control and operation of the granulation process.

7.1 Introduction and Objectives

As described earlier, granulation is a complex process whereby fine particles agglomerate to form larger granules, due to adhesive forces brought about by the liquid binder. In a continuous granulation process, feed material is continuously introduced into the granulator as granule growth occurs. The granulator is fitted with several spray nozzles through which the liquid binder is introduced into the granule bed. The granules formed are then dried and classified based on product specification(s). Granules that do not conform to product specification(s) and recycled and reprocessed. Prior to the actual design of the controller for the granulation process, it is important to know how well the process can be controlled and what factors may hinder the control loop performance that may be achieved in reality. It is also imperative that appropriate plant inputs and outputs are selected for control purposes and furthermore they are paired correctly as incorrect pairings may limit and hinder control loop performance. Therefore, a plant is said to be controllable if there exists a controller that can in principle, be able to achieve a certain output state via certain admissible input changes (Eek and Bosgra, 2000). Controllability is an intrinsic plant property and is determined by the plant design such as sensor locations, recycle loops, internal couplings and sizing of equipment. Controllability conditions for granulation processes are also made more challenging given the presence of internal variables (Semino and Ray, 1995a). The aim of the present work is to systematically ascertain the controllability of the granulation process by examining the effect of control handles such as binder and feed flowrates on controlled variables such as average size, distribution width, bulk density and moisture content. Thereafter, suitable control loop pairings are identified facilitating a better understanding of the design and operation of the granulation process. Furthermore, the studies are based on validated mechanistic models of the granulation process, lending credence to the insights obtained from the results.

7.2 Formulation of the Continuous Population Balance Model

The population balance equation must be re-written for the continuous case (see Equation 7.1). This is to account for inflow and outflow terms which would facilitate long term

running of the process from which suitable transfer functions (based on step response data) can be identified. Therefore,

$$\frac{\partial F(s,l,g,t)}{\partial t} + \frac{\partial}{\partial g}(F(s,l,g,t)\frac{dg}{dt}) = \Re_{nuc} + \Re_{agg} + \Re_{break} + R_f X_0(s,l,g,t) - R_f X(s,l,g,t) \quad (7.1)$$

whereby R_f is the input flowrate (number density per second)) of particles. X is the concentration of particles and is defined as $X(s,l,g,t) = \frac{F(s,l,g,t)}{\int F(s,l,g,t)dsdldg}$. X_0 is the input concentration of the particles.

7.2.1 Compartmentalisation of the Model

The compartmentalised model used in this study is based on a pilot-plant drum granulation facility located at the University of Queensland, Australia (Glaser et al., 2008). The schematic of the horizontal drum granulator can be seen in Figure 7.1 and consists of three sections (labelled 1, 2 and 3) wherein each compartment consists of a binder spray nozzle (labelled u_1, u_2 and u_3). The solid feed inflow is denoted by Rf_{in} and the corresponding outflow as Rf_{out}. In the compartmentalised granulator (3 compartments) the population balance equation is effectively solved thrice at each iteration. Assuming that u_1 is turned on and u_2 and u_3 are turned off, this means that as particles enter the first compartment, binder addition takes place leading to granule growth (defined to be the resultant effects of nucleation, aggregation, breakage and consolidation) and as the particles proceed to the second and third compartments, binder addition has ceased. However, growth still takes place due to the presence of the residual binder among the particles. Compartmentalising the granulator in such a manner will also allow us to realistically examine the effect of spray nozzle position which is an important design parameter in the granulation process.

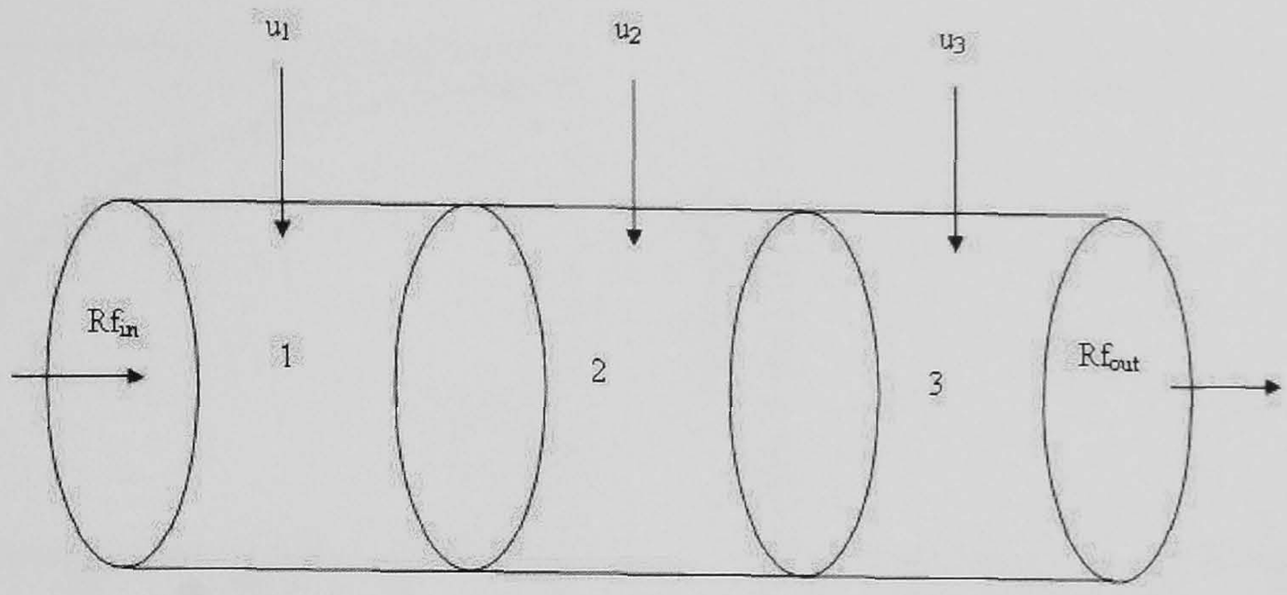

Figure 7.1: Compartmentalised model of the granulator.

7.2.2 Simulation Results

Figures 7.2a-d depict the effect of the position of the spray nozzle on key granule properties. The properties considered in this work are 1) volume-mean diameter of the granule (d_{30}), 2) width of the granule distribution ($d_{84/16}$), which is defined as $\sqrt{\frac{d_{84}}{d_{16}}}$, 3) bulk density ($\rho_b$) of the granules, which is defined as $\frac{M_s}{V_t}$, where M_s is the total solid mass and V_t is the total particle volume, and 4) moisture content (m_c) of the granules. It can be seen that d_{30}, m_c and ρ_b are dependent on the spray nozzle position. The nonlinearity of the granulation phenomena is also illustrated as seen by the larger changes in granule attributes from compartment 2 and 3, then from compartment 1 and 2. $d_{84/16}$ on the other hand is independent of the spray nozzle position.

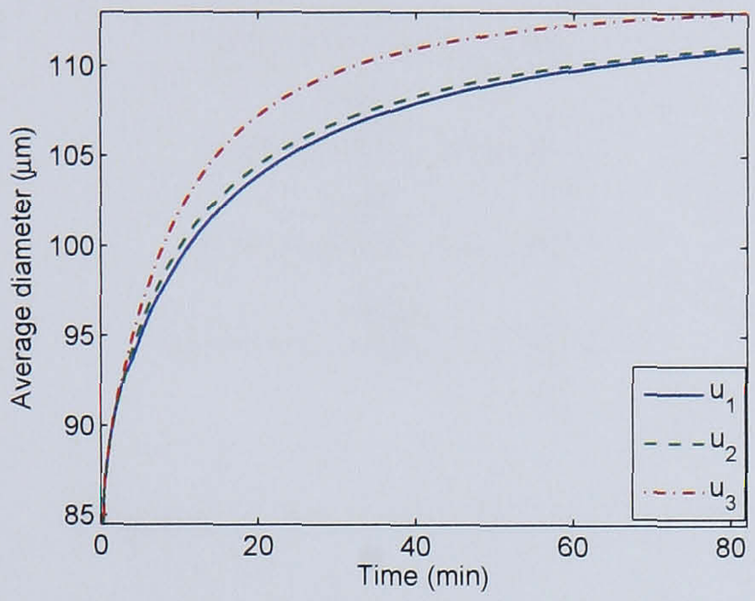

(a) Simulated output for total particles for different spray zones in the granulator

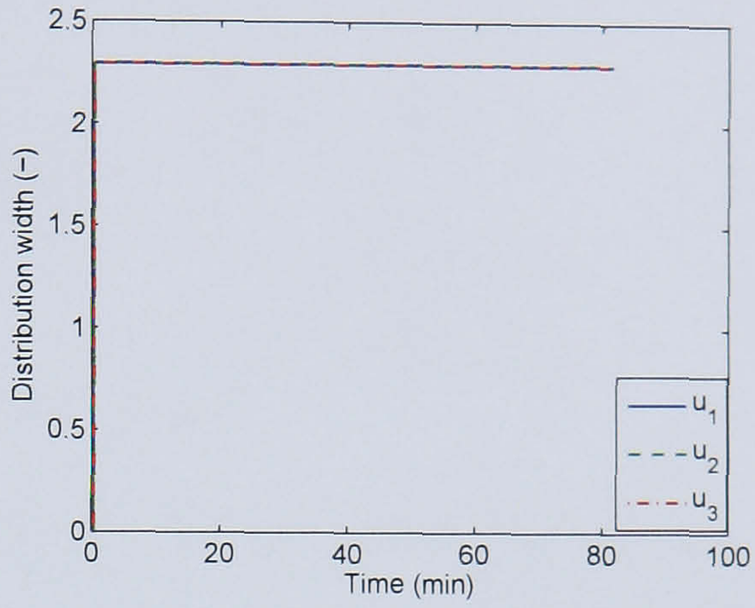

(b) Simulated output of average particle diameter for different spray zones in the granulator

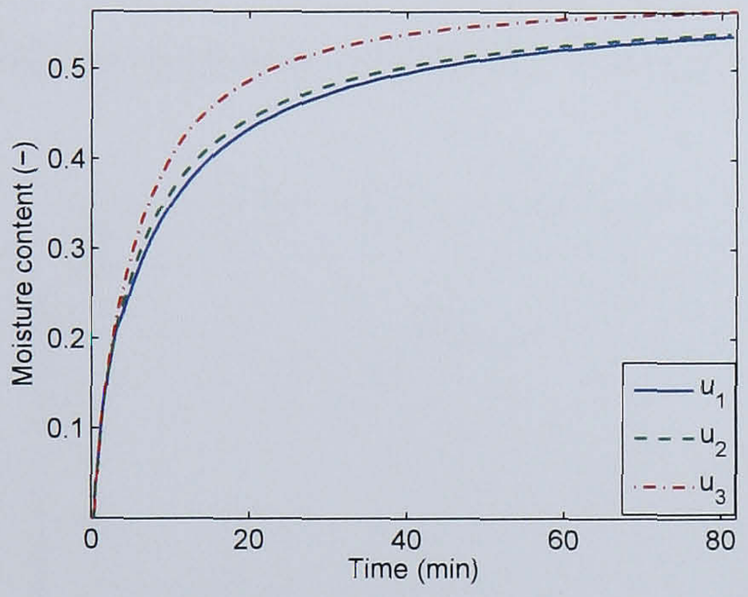

(c) Simulated output of moisture content for different spray zones in the granulator

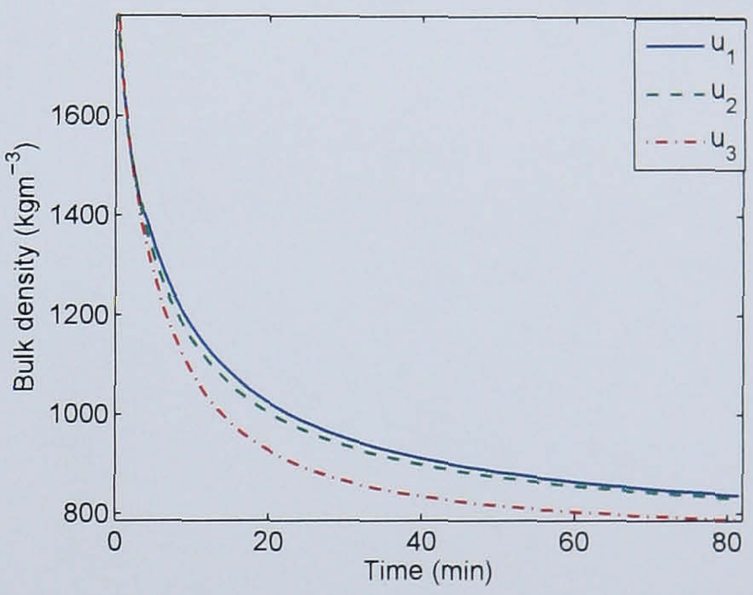

(d) Simulated output of bulk density for different spray zones in the granulator

Figure 7.2: Time profiles for total particles, average diameter, average moisture content and average porosity for different spray nozzle positions under start-up conditions.

7.3 Controllability Studies

A simulation-based controllability analysis on the mechanistic population balance model was performed. The model depicts a multiple-input multiple-output granulation process shown in Figure 7.3.

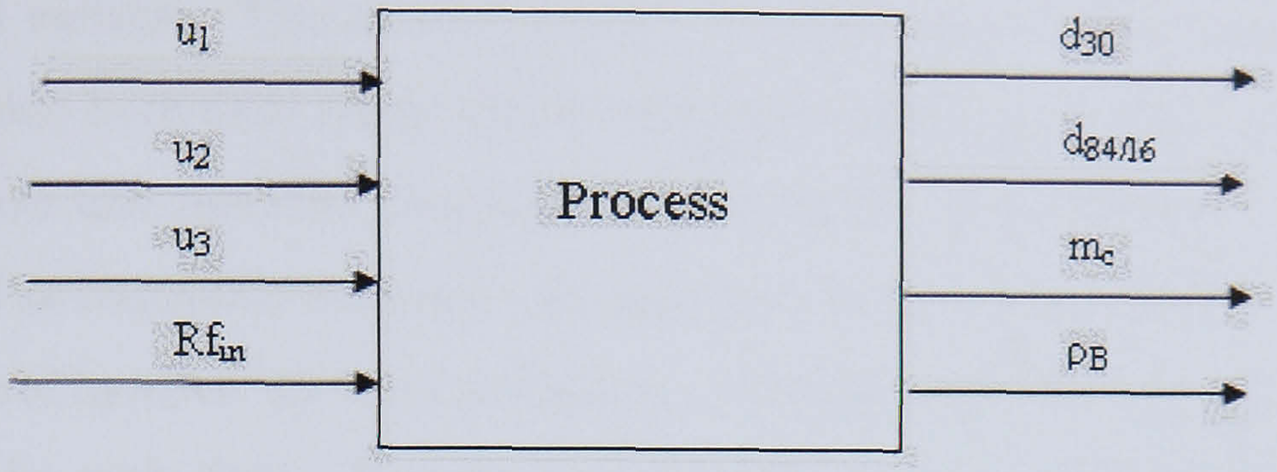

Figure 7.3: A block diagram of the process and its control objectives.

Open-loop step tests were performed on the model to ascertain the controllability of the process outputs. A step change was made to the nozzles and solid feed flowrates at $t = 2500$, as depicted in Figures 7.4a and b.

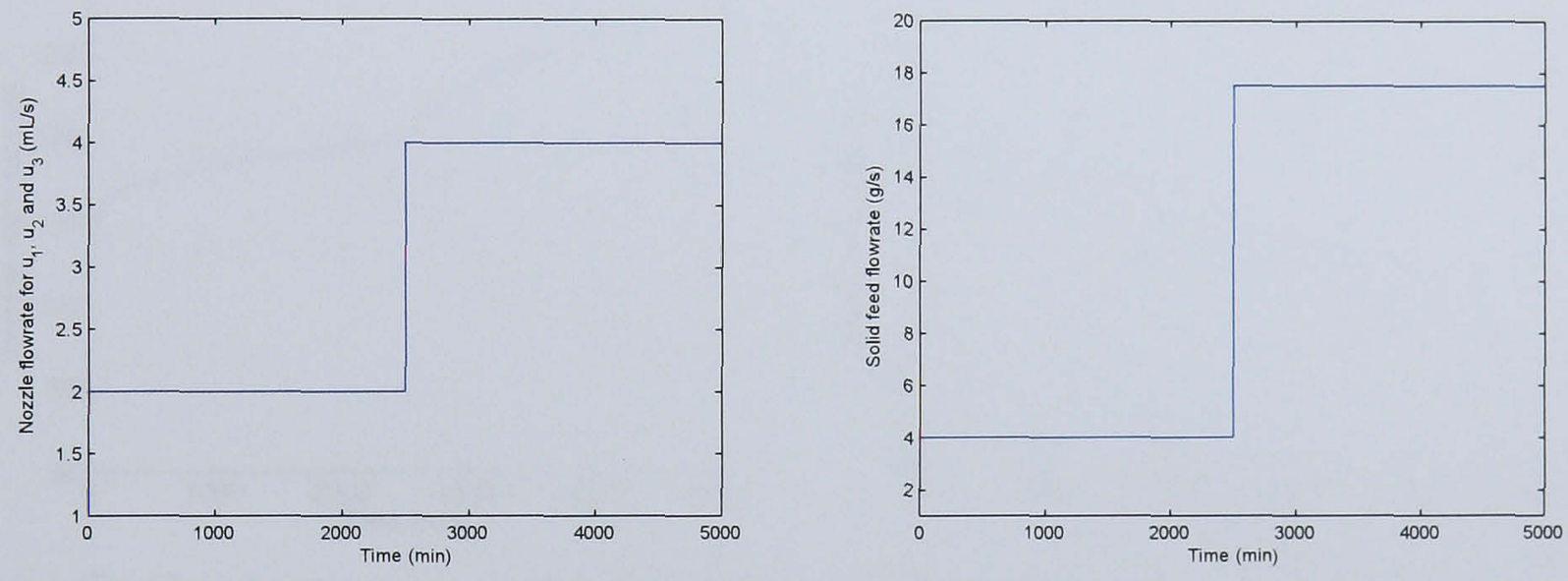

(a) Step change made to the nozzle flowrates (b) Step change made to solid feed flow rate

Figure 7.4: Profiles of step changes made to the manipulated variables.

Results from Figures 7.5a-d, 7.6a-d, 7.7a-d and 7.8a-d show that the average diameter, moisture content and bulk density are controllable through the manipulations of u_1, u_2, u_3 and Rf_{in}. As seen from Figures 7.5a-d, 7.6a-d, 7.7a-d and 7.8a-d, a positive step change in the nozzle flowrates result in a corresponding increase both the average granule diameter and moisture content and a decrease in the bulk density. In contrast, a positive step change in the solid feed flowrate, results in a decrease in the average granule diameter due to a higher proportion of smaller fine particles and a decrease in the moisture content due to a higher proportion of dry particles. Bulk density on the other hand shows an increase. Results also show that step changes in the manipulations have no effect on the size distribution width. This implies that $d_{84/16}$ is not controllable and cannot be selected

as a controlled variable. This observation has also been reported in Glaser et al. (2008) who observed that both their experimental and simulated $d_{84/16}$ were not influenced by any admissible inputs and therefore deemed not controllable. As a result only d_{30}, ρ_b and m_c can be selected as controlled variables with any three of u_1, u_2, u_3 and Rf_{in} as the possible choices of control handles. In many scenarios, distribution width is an important variable that needs to be controlled. This is because, differing size distributions (albeit having the same mean size) may spuriously affect downstream operations such as tabletting. In such instances other manipulated inputs may have to be selected (as demonstrated in the conceptual control framework in section 3.4) or the process has to be redesigned to facilitate enhanced controllability.

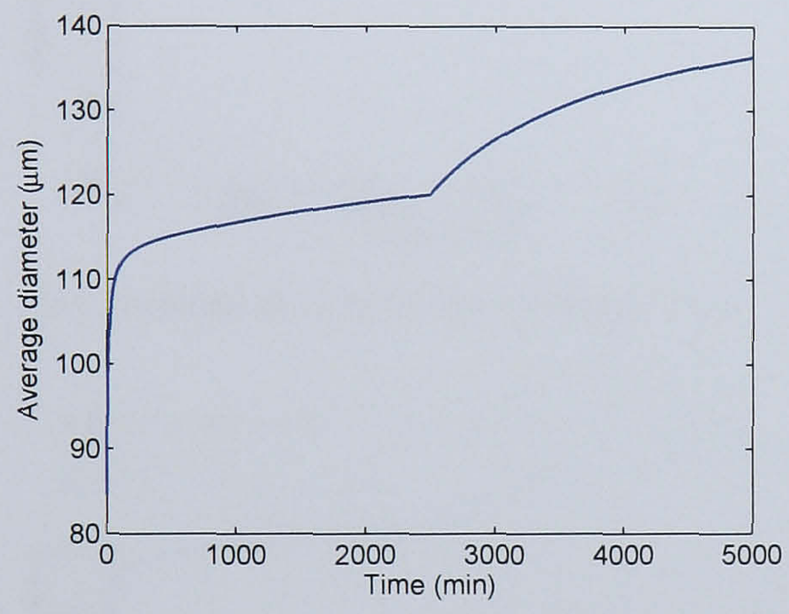

(a) Simulated output for average diameter

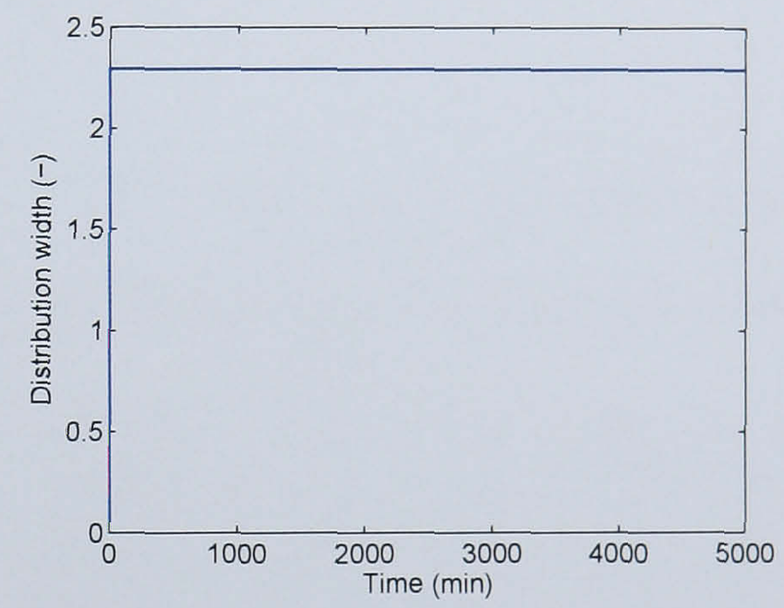

(b) Simulated output for distribution width

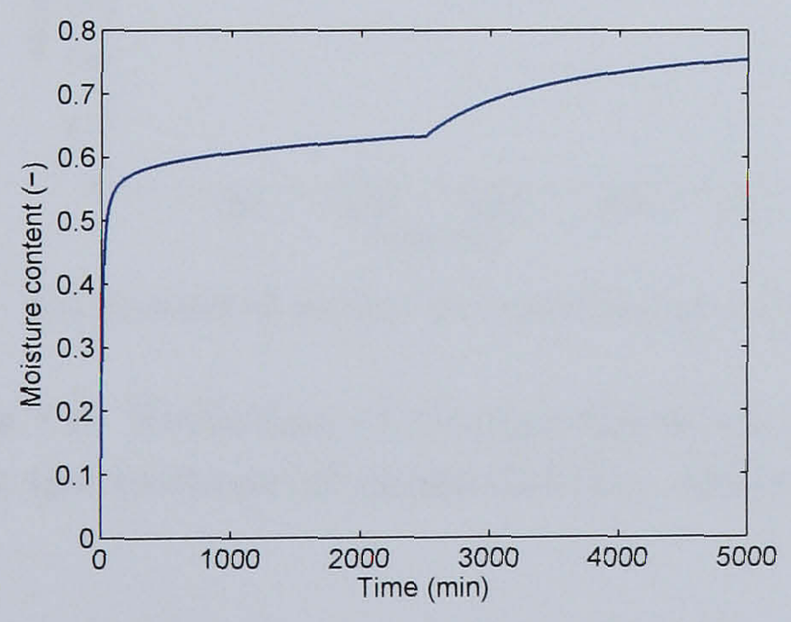

(c) Simulated output for moisture content

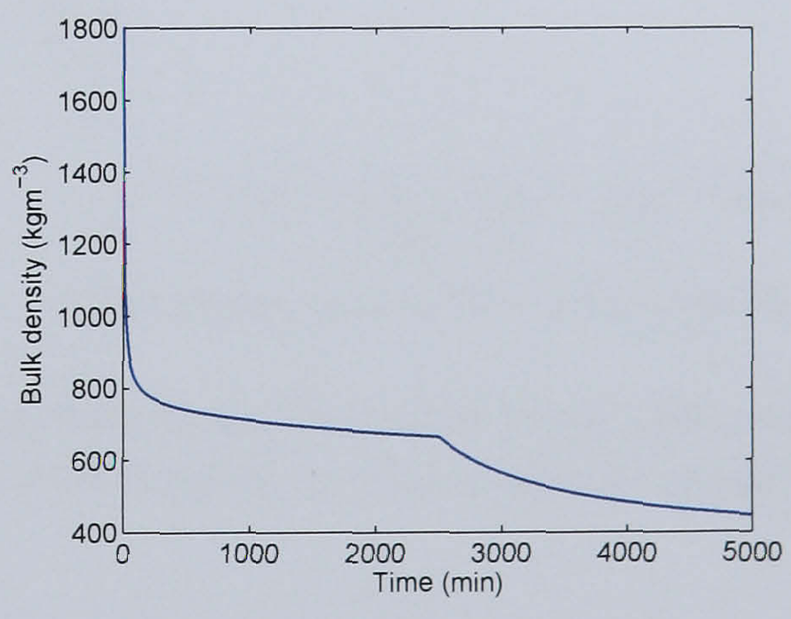

(d) Simulated output for average porosity

Figure 7.5: Evolution of average diameter, distribution width, moisture content and porosity for the purpose of controllability analysis with regards to a step change made to u_1.

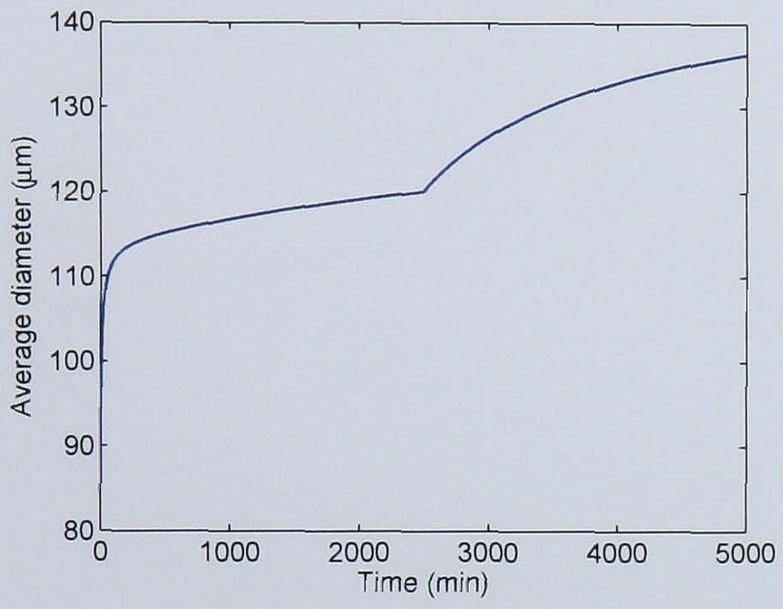

(a) Simulated output for average diameter

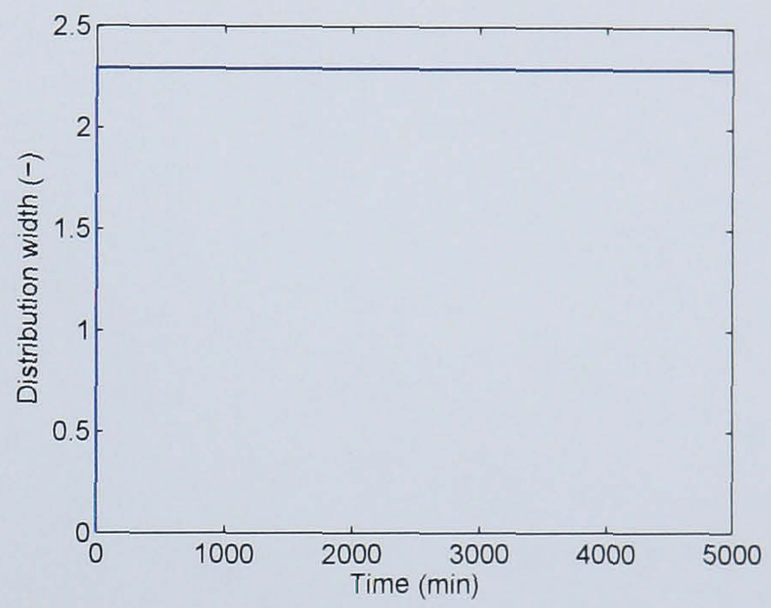

(b) Simulated output for distribution width

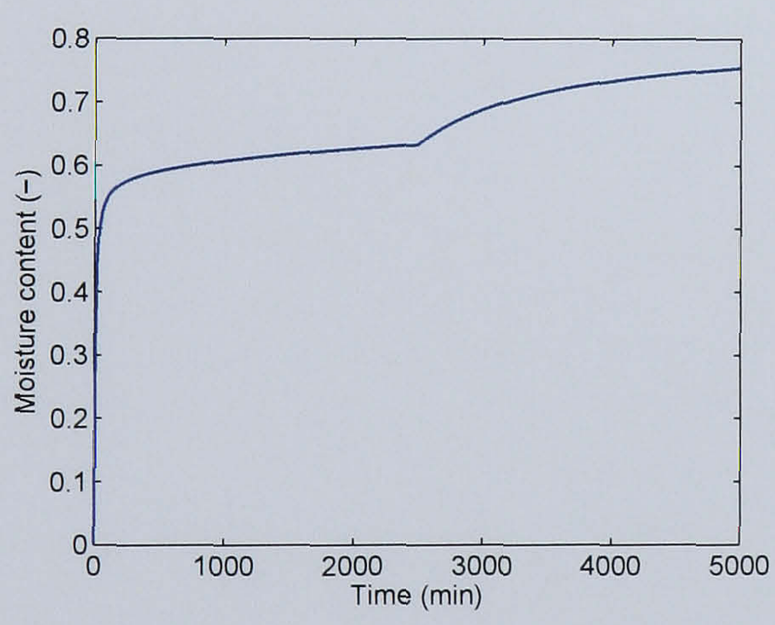

(c) Simulated output for moisture content

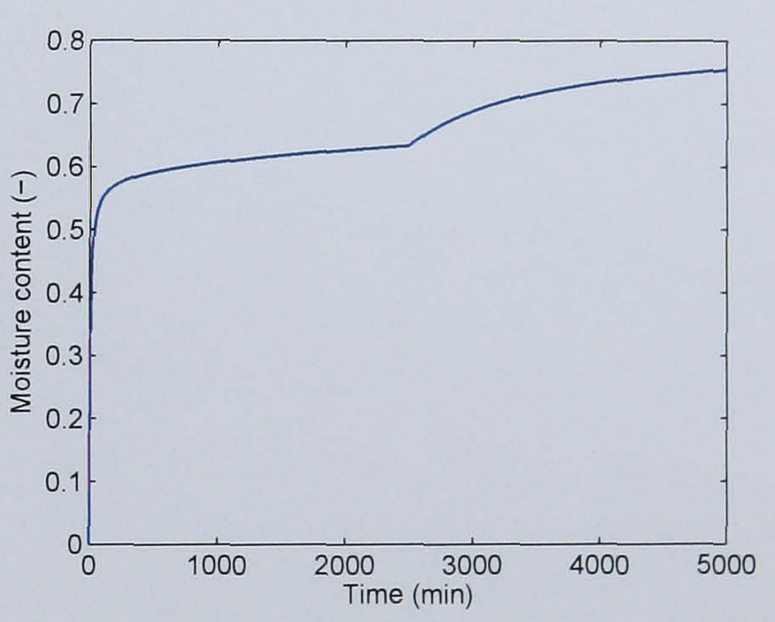

(d) Simulated output for average porosity

Figure 7.6: Evolution of average diameter, distribution width, moisture content and porosity for the purpose of controllability analysis with regards to a step change made to u_2.

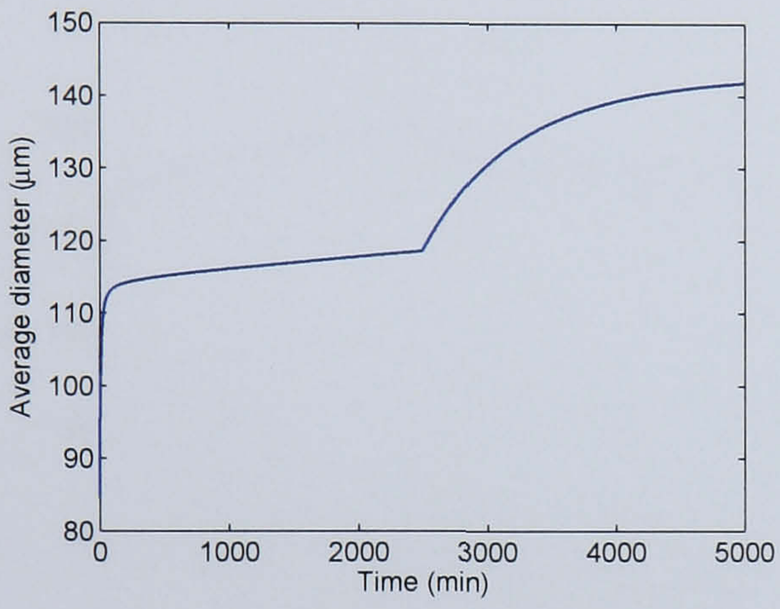

(a) Simulated output for average diameter

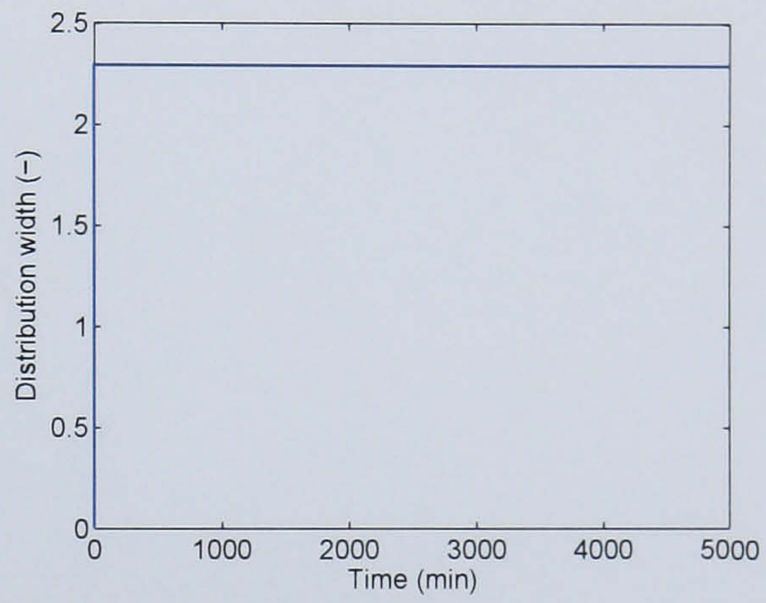

(b) Simulated output for distribution width

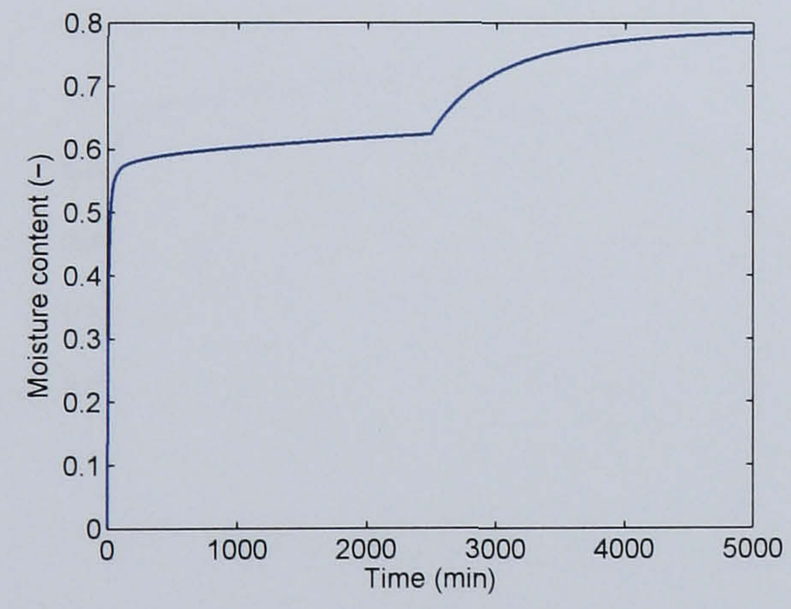

(c) Simulated output for moisture content

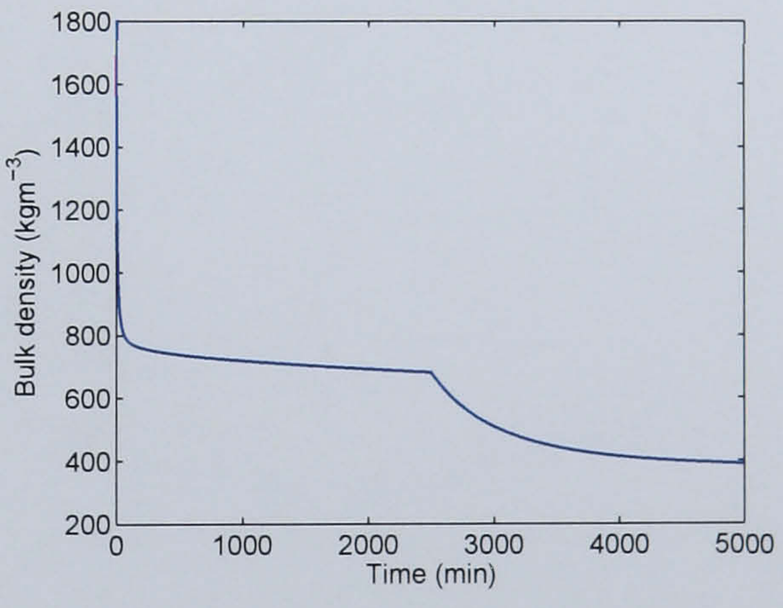

(d) Simulated output for average porosity

Figure 7.7: Evolution of average diameter, distribution width, moisture content and porosity for the purpose of controllability analysis with regards to a step change made to u_3.

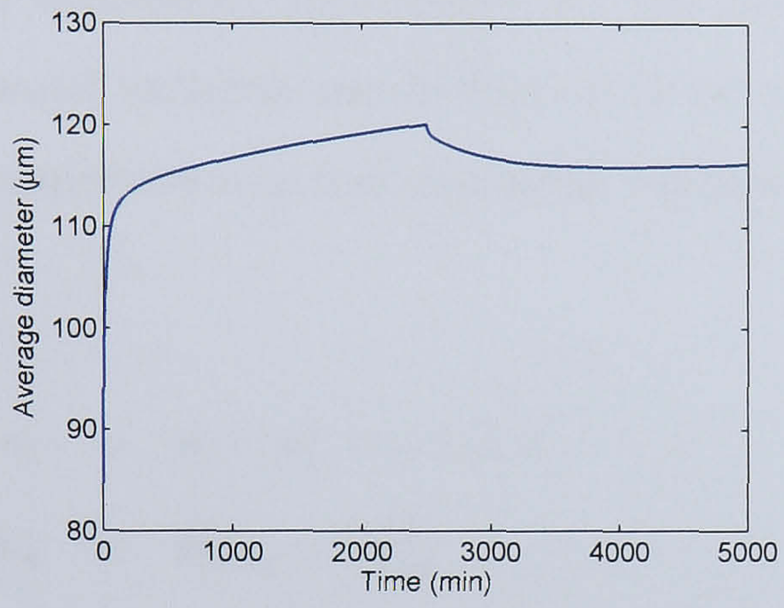

(a) Simulated output for average diameter

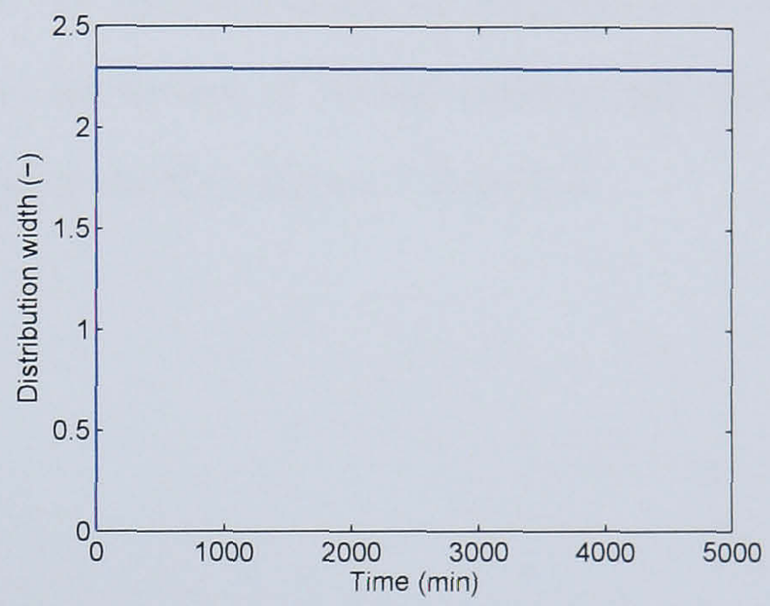

(b) Simulated output for distribution width

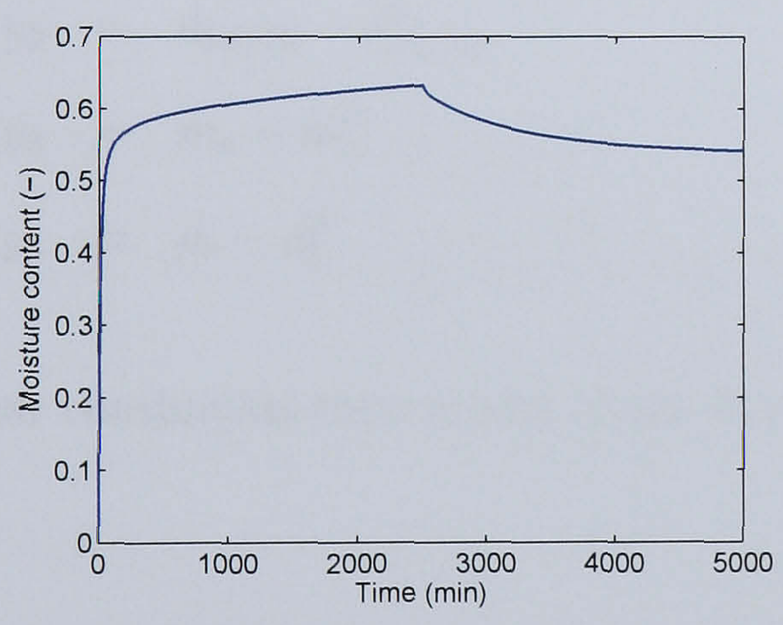

(c) Simulated output for moisture content

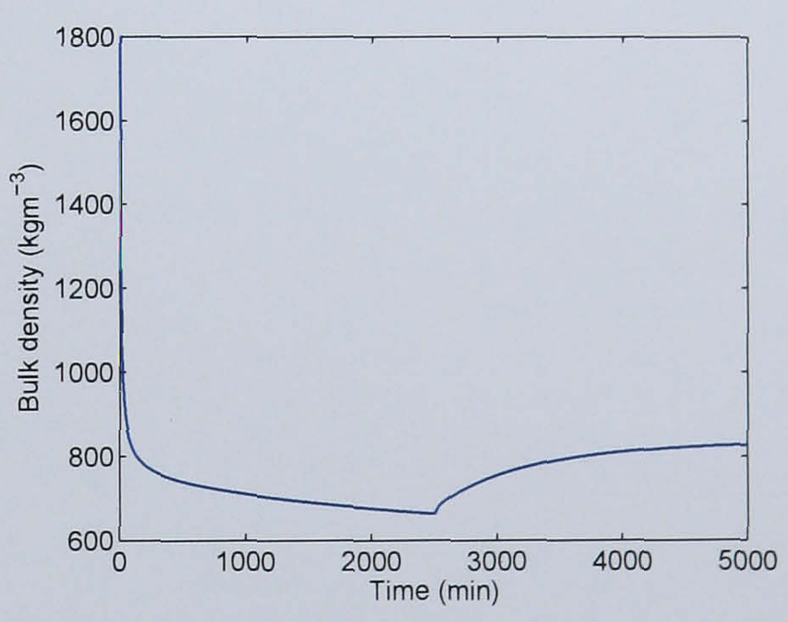

(d) Simulated output for average porosity

Figure 7.8: Evolution of average diameter, distribution width, moisture content and porosity for the purpose of controllability analysis with regards to a step change made to Rf_{in}.

7.4 Identification of Optimal Control-Loop Pairings

In the previous section, the controllability of the granulation process incorporating its key mechanisms was examined. In this section, given the possible choices for controlled and manipulated variables, an optimal combination of control-loop pairings were selected to facilitate efficient control of the process. Although the granulation process is nonlinear, an approximate linear model which relates the four outputs to the four manipulated inputs can be considered appropriate for the purpose of identification of control-loop pairings. The model variables are defined in terms of the deviation of actual process variables from their respective nominal operating regions as seen in Equations 7.2 to 7.7.

$$n_i = u_i - u_i^0, i = 1, 2, 3 \tag{7.2}$$

$$n_4 = Rf_{in} - Rf_{in}^0 \tag{7.3}$$

$$y_1 = d_{30} - d_{30}^0 \tag{7.4}$$

$$y_2 = d_{84/16} - d_{84/16}^0 \tag{7.5}$$

$$y_3 = m_c - m_c^0 \tag{7.6}$$

$$y_4 = \rho_b - \rho_b^0 \tag{7.7}$$

A linear continuous-time model of the form,

$$\mathbf{y}(s) = \mathbf{G}_{ij}\mathbf{n}(s) \tag{7.8}$$

is obtained from the process data. The individual step response data indicate that a first-order plus time delay transfer function of the form

$$\mathbf{G}_{ij} = \frac{k_{ij}e^{-\theta_{ij}s}}{\tau_{ij}s + 1} \tag{7.9}$$

where k is the process gain, τ is the process time constant and θ is the process time

delay, is adequate to represent the behaviour observed in each of the responses. From the open-loop step test data, the corresponding transfer functions were determined as.

$$\mathbf{y}(s) = \begin{bmatrix} \frac{8.95}{1195s+1} & \frac{9.01}{1190s+1} & \frac{9.10}{1186s+1} & \frac{-0.27}{240s-1} \\ 0 & 0 & 0 & 0 \\ \frac{0.05}{915s+1} & \frac{0.06}{911s+1} & \frac{0.07}{908s+1} & \frac{-0.005}{377s-1} \\ \frac{-106}{920s+1} & \frac{-110}{915s+1} & \frac{-113}{910s+1} & \frac{9}{377s+1} \end{bmatrix} \mathbf{n}(s) \tag{7.10}$$

It must be noted that various other step changes (within the vicinity of the nominal operating conditions) were made to the manipulated variables. It was hypothesised that due to the nonlinearity of the process, the process dynamics could be different resulting in different transfer functions which could then go on to result in different control-loop pairings. However, results confirmed that the transfer functions obtained were almost identical. Therefore, the process was deemed linear over the vicinity of the current operating conditions.

7.4.1 Relative Gain Array

In a multiple-input multiple-output system, where there are more manipulations available than outputs, the manipulations to use for pairing with the corresponding outputs need to be decided. Pairings must be made such that the interaction within the control loops are minimised. As there are three controlled variables and four manipulated variables, one of the manipulated variables must be discarded whist the other variables are paired optimally. This is done by means of the relative gain array (Λ). The relative gain array can be useful for establishing the best input-output pairings for use in the control of a multi-variable system. The array (Λ) is defined as the element-by-element product (the Hadamard or Schur product) of the transfer-function matrix G(s) and the transpose of the inverse of this matrix as seen in Equation 7.11.

$$\mathbf{\Lambda} = \mathbf{G} \times (\mathbf{G}^{-1})^T \tag{7.11}$$

Typically, the relative gain array is evaluated at zero frequency (i.e.. at steady state). Relative gains in the range 0 to 1 indicate moderate interaction, with values of 0.5 being

the worst. To minimize interaction, variables with relative gains closest to 1 should be paired as this implies that the gains are largely unaffected by the closing of other loops. Variables with negative gains should not be paired for control as i) the overall closed-loop system may be rendered unstable, (ii) the loop with the negative relative gain is unstable by itself or (iii) the closed-loop system is unstable if the loop with the relative negative gain is opened. Relative gains of greater than 5 usually imply severe loop interaction. A matrix of the steady state gains of the current 3×4 system is shown in Equation 7.12 and the matrix of the relative gain array (Λ) is shown in Equation 7.13. More details on the RGA can be found in Ogunnaike and Ray (1994).

$$\mathbf{G}(s=0) = \begin{bmatrix} 8.95 & 9.01 & 9.10 & -0.27 \\ 0.05 & 0.06 & 0.07 & -0.005 \\ -106 & -110 & -113 & 9 \end{bmatrix} \tag{7.12}$$

$$\mathbf{\Lambda} = \begin{bmatrix} \lambda_{11} & \lambda_{12} & \lambda_{13} & \lambda_{14} \\ \lambda_{31} & \lambda_{32} & \lambda_{33} & \lambda_{34} \\ \lambda_{41} & \lambda_{42} & \lambda_{43} & \lambda_{44} \end{bmatrix} \tag{7.13}$$

7.4.1.1 Discarding n_1

Assuming that n_1 is discarded and not considered as one of the manipulations, the 3×4 system reduces to a 3×3 as shown in Equation 7.14.

$$\mathbf{G}(s=0) = \begin{bmatrix} 9.01 & 9.10 & -0.27 \\ 0.06 & 0.07 & -0.005 \\ -110 & -113 & 9 \end{bmatrix} \tag{7.14}$$

The calculated Λ for the 3×3 system is computed as

$$\mathbf{\Lambda} = \begin{bmatrix} 1.36 & 0.21 & -0.58 \\ -7.20 & 8.40 & -0.20 \\ 6.83 & -7.61 & 1.78 \end{bmatrix} \tag{7.15}$$

For a 3×3 system, there would be six possible theoretical pairings. From Equation 7.15, it can be seen that there is only one possible pairing with all relative gain array elements positive (i.e., $n_2 \longleftrightarrow y_1$, $n_3 \longleftrightarrow y_3$, $n_4 \longleftrightarrow y_4$).

7.4.1.2 Discarding n_2

Assuming that n_2 is discarded and not considered as one of the manipulations, 3×4 system reduces to a 3×3 as shown in Equation 7.16.

$$\mathbf{G}(s=0) = \begin{bmatrix} 8.95 & 9.10 & -0.27 \\ 0.05 & 0.07 & -0.005 \\ -106 & -113 & 9 \end{bmatrix} \tag{7.16}$$

The calculated Λ for the 3×3 system is computed as

$$\mathbf{\Lambda} = \begin{bmatrix} 0.70 & 0.87 & -0.57 \\ -3.08 & 4.36 & -0.28 \\ 3.38 & -4.24 & 1.86 \end{bmatrix} \tag{7.17}$$

From Equation 7.17, it can be seen that there is only one possible pairing with all relative gain array elements positive (i.e., $n_1 \longleftrightarrow y_1$, $n_3 \longleftrightarrow y_3$, $n_4 \longleftrightarrow y_4$).

7.4.1.3 Discarding n_3

Assuming that n_3 is discarded and not considered as one of the manipulations, 3×4 system reduces to a 3×3 as shown in Equation 7.18.

$$\mathbf{G}(s=0) = \begin{bmatrix} 8.95 & 9.01 & -0.27 \\ 0.05 & 0.06 & -0.005 \\ -106 & -110 & 9 \end{bmatrix} \tag{7.18}$$

The calculated Λ for the 3×3 system is computed as

$$\mathbf{\Lambda} = \begin{bmatrix} -0.22 & 1.81 & -0.58 \\ -6.43 & 7.80 & -0.36 \\ 7.66 & -8.61 & 1.96 \end{bmatrix} \tag{7.19}$$

From Equation 7.19, it can be seen that there is no pairing with all relative gain array elements positive. This implies that the nozzle spray rate (n_3) has to be one of the chosen manipulations and cannot be discarded.

7.4.1.4 Discarding n_4

Assuming that n_4 is discarded and not considered as one of the manipulations, 3×4 system reduces to a 3×3 as shown in Equation 7.20.

$$\mathbf{G}(s=0) = \begin{bmatrix} 8.95 & 9.01 & 9.10 \\ 0.05 & 0.06 & 0.07 \\ -106 & -110 & -113 \end{bmatrix} \tag{7.20}$$

The calculated Λ for the 3×3 system is computed as

$$\mathbf{\Lambda} = \begin{bmatrix} 73.72 & -142.00 & 69.68 \\ -7.62 & -24.97 & 18.35 \\ -79.94 & 167.98 & -87.03 \end{bmatrix} \tag{7.21}$$

From Equation 7.21, it can be seen that there is only one possible pairing with all relative

gain array elements positive (i.e., $n_1 \longleftrightarrow y_1$. $n_3 \longleftrightarrow y_3$, $n_2 \longleftrightarrow y_4$).

7.4.2 Concluding Discussion

Based on section 7.4.1.1 to 7.4.1.4, it was seen that n_3 (third nozzle) could not be discarded as a manipulation. Altogether, given that we are dealing with a non-square 3×4 system, there exist in total three possible options for control-loop pairings. With the first option (i.e, section 7.4.1.1), it can be seen that λ_{12} and λ_{44} are close to unity implying that these pairings ($n_2 \longleftrightarrow y_1$) and $n_3 \longleftrightarrow y_3$) result in relatively less indirect interaction when other loops are closed. λ_{33} has a very high relative gain, implying that when this loop is closed, it results in large interactions with the other loops, causing potential difficulties in overall control. With the second option (i.e, section 7.4.1.2), it can be seen that λ_{11} and λ_{44} are close to unity, and similar to the case in section 7.4.1.1 these pairings ($n_1 \longleftrightarrow y_1$) and ($n_3 \longleftrightarrow y_3$) result in relatively less indirect interaction, when other loops are closed. In contrast, λ_{33} does not have a very high relative gain compared to section 7.4.1.1, implying that when this loop is closed, it will not result in large interactions within the other loops. With the third option (i.e, section 7.4.1.4), it can be seen that λ_{11}, λ_{42} and λ_{42} have very high relative gains, implying that when each loop is closed, it results in severe interactions with the other loops. This would be very undesirable for control purposes. Intuitively, this can be explained as follows. Selecting the three nozzle spray rates as the manipulations is undesirable as their effect on the controlled variables are very similar (small differences in the gains and time constants). Hence, a manipulation in one of the inputs (in a closed-loop configuration) would have an almost equal impact on the all the three controlled variables. As a result, the ensuing interactions would make control and regulation of the variables very difficult. Furthermore, the dynamics of the feed flow rate are greater than that of the nozzle spray rates. This shows that a change in the feedflow rate would have a faster effect on any of the controlled variables. Therefore, the feedflow rate (n_4) should be one of the manipulations considered. Overall, the results show that the optimal control-loop pairing is that of $n_1 \longleftrightarrow y_1$, $n_3 \longleftrightarrow y_3$ and $n_4 \longleftrightarrow y_4$ (i.e, first compartment nozzle with average diameter, third compartment nozzle with moisture content and feed flowrate with bulk density). These pairings are valid over the vicinity of the current operating regime and therefore provide valuable insight pertaining to this localised operating regime. Deviating

from this operating regime could potentially result in different control-loop pairings. This will be discussed more in detail in Chapter 8 under Future research.

7.5 Summary

In this chapter, a continuous and compartmentalised population balance model of a granulation process was presented, which depicted a realistic model of a pilot-plant granulation process. The model considered was based on granulation mechanisms that have been previously derived from first principles and validated at the batch-scale for different granulation systems. Model simulations elegantly captured the effect of nozzle positions on the granule output. As a direct consequence of the compartmentalisation, the controllability of the granulation process could be examined taking into account all the important granule inputs and outputs, providing valuable insight into the control and operation of the granulation process. Results show that the average diameter, moisture content and bulk density are realistic choices of controlled variables, with the three nozzle spray rates and the solid feed rate as possible choices of manipulated variables. The size distribution width was not sensitive to any of the manipulated variables and therefore deemed uncontrollable, thus corroborating the work of Glaser et al. (2008). This is also an important finding as size distribution may be an important variable that needs to be tightly regulated. As a result this paves the way for alternative manipulated variables that have shown to influence the GSD (see section 3.4) By means of step tests and a relative gain array analysis, several possible control-loop pairings were identified and within them, an optimal control-loop pairing was selected. Such a study on a MIMO granulation process lends valuable insight and knowledge which can then be applied to an actual granulation process.

Chapter 8

Distribution and Accessibility of Binder in Wet Granules

The effect of primary particle morphology on the spatial distribution of binder in wet granules was investigated by numerical simulations. The shape factors of four commonly used pharmaceutical excipients – mannitol, lactose, microcrystalline cellulose, and calcium phosphate – were evaluated by digital image analysis and used for three-dimensional computer reconstruction of virtual particle populations. The formation of wet agglomerates was simulated by close random packing of primary particles and then finding the equilibrium distribution of a liquid binder in the pore space within the close packed structures, using the Volume of Fluid (VOF) method. The spatial distribution of binder in the computer-generated wet agglomerates was then analysed and the dependence of the fractional surface coverage by liquid on the overall binder/solids ratio was systematically obtained for different values of primary particle surface roughness. The obtained dependence was used to explain experimentally observed differences in the granulation kinetics of the four pharmaceutical excipients under otherwise identical conditions.

[1]Part of this chapter is based on, F. Stepanek, P. Rajniak, C. Mancinelli, R.T. Chern and R. Ramachandran, "Distribution and accessibility of binder in wet granules", Powder Technology, 2008, *In Press*

8.1 Introduction

The ability to relate the kinetics of granule growth in a wet granulation process to the material properties of primary particles and binder is a key pre-requisite of any attempt to construct physically based (as opposed to empirical) predictive models of granulation. The rate of agglomeration can be expressed similarly to reactions kinetics by a "mass action law": the rate of coalescence of particles from two classes, i and j, is proportional to the frequency of collision between the particles and the probability that a single collision event will be successful – i.e. give rise to agglomeration rather than rebound (Cameron et al., 2005; Gantt and Gatzke, 2006). In the context of multi-dimensional population balance modelling of wet granulation, a class is specified not only by its size, but also by composition (binder/solids ratio, mass fraction of different solids, porosity).

Criteria for the successful collision of liquid-coated particles have been derived in the form of the critical Stokes' number (Ennis et al., 1991; Tardos et al., 1997; Liu et al., 2000), which expresses the ability of a viscous binder layer covering a particle to dissipate the kinetic energy of a particle-particle collision. If the kinetic energy is higher than a certain critical value (depending on the thickness and viscosity of the binder layer), the particles will rebound upon collision, otherwise they will coalesce. In wet granules composed of primary particles with non-spherical shape, the surface coverage by a binder can be rather non-uniform both in terms of localisation and thickness. Moreover, where binder is present, it may not always be accessible to an incoming particle during collision due to steric hindrance.

The objective of the present work, therefore, was to investigate in detail the spatial distribution of wet binder in granules composed of primary particles with a range of shapes and surface roughness values, and to derive – by means of computer simulations – functional relationships between the volumetric composition of a granule (binder/solids ratio) and the fraction of binder accessible on its surface, as well as the average thickness of the binder layer. Such relationship can then be combined with the Stokes' number analysis in order to derive coalescence kernels for multi-dimensional population balance modelling that reflect the heterogeneity of complex granule structures.

The chapter is structured as follows: first we describe the computational methods for the representation of primary particles and their wet agglomerates. as well as the methods for analysing the surface composition. A parametric study of the effect of primary particle surface roughness and granule size on the accessible binder fraction is presented next. Finally, experimental data demonstrating the effect of primary particle surface roughness on granulation kinetics are discussed and shown to be consistent with the results of previous theoretical analysis.

8.2 Materials and Methods

8.2.1 Representation of Primary Particle Morphology

The morphology of primary particles was modelled as the so-called Gaussian blobs (Stepanek and Rajniak, 2006), (i.e., spheres whose radius is modulated by a Gaussian-correlated random surface). A class of such objects is fully specified by a set of three numerical descriptors: the mean radius of gyration, r_g, the surface roughness amplitude, a, and the surface roughness correlation length, L. A single Gaussian particle is generated in the following way. Let $X(\mathbf{u})$, $\mathbf{u} \in [0; 2\pi] \times [-\pi/2; +\pi/2]$ be a field of independent normally distributed random variables. A field of Gaussian-correlated random variables is obtained from X by applying a linear filter (Adler and Thovert, 1998)

$$Y(\mathbf{u}) = \sum_{\mathbf{v} \in [0;L]^2} \exp(v^2/L^2) X(\mathbf{u}+\mathbf{v}) \tag{8.1}$$

and renormalisation, where $v = \|\mathbf{v}\|$ is a distance calculated using the geodesic metric. A single Gaussian particle is formed by modulating the surface of a sphere with radius r_g by the correlated random field $Y(\mathbf{u})$ scaled by amplitude a. A population of distinct Gaussian particles with mean parameters $[r_g, a, L]$ is generated by repeating the procedure for different random initialisations of the un-correlated field X. The process of forming a single particle is shown schematically in Figure 8.1.

The parameters $[r_g, a, L]$ can be conveniently measured on real particle samples using digital image analysis. A series of optical microscopy images of a statistically significant number of particles from a sample are first obtained, then converted to a binary form using

a thresholding algorithm, and finally the contours of individual particles from each image are extracted. An example of one such contour is plotted in Figure 8.2a. The radius of gyration function, i.e. the distance $r = \|\mathbf{r} - \mathbf{r_c}\|$ from each point on the particle surface, $\mathbf{r}$, to the particle's center of mass, $\mathbf{r_c}$, as function of the rotation angle of a vector connecting the two points, $\theta = \tan^{-1}[(r^y - r_c^y)/(r^x - r_c^x)]$, is then constructed (see Figure 8.2b). The mean of this function is the mean radius of gyration, i.e..

$$r_g = \frac{1}{2\pi}\int_0^{2\pi} r(\theta)d\theta \tag{8.2}$$

and the difference between the maximum and the minimum of the function, scaled by r_g, is the dimensionless surface roughness amplitude

$$a = \frac{\max\big(r(\theta)\big) - \min\big(r(\theta)\big)}{r_g} \tag{8.3}$$

The third parameter – the surface roughness correlation length – is a measure of the average spacing between the maxima on the particle surface. The surface roughness correlation function is defined by

$$K(\theta) = \frac{\int_0^{2\pi}(r(\omega+\theta) - r_g)\cdot(r(\omega) - r_g)d\omega}{\int_0^{2\pi}(r(\omega) - r_g)^2 d\omega} \tag{8.4}$$

An example of the correlation function is plotted in Figure 8.2c. The correlation length, L, is the zero-order moment of the correlation function, i.e.,

$$L = \int_0^{2\pi} K(\theta)d\theta \tag{8.5}$$

Note that L is a dimensionless quantity; the scaling factor is r_g.

In this work the shape parameters of four common pharmaceutical excipients – lactose, mannitol (Pearlitol SD200, Roquette Pharma, Lestrem, France), microcrystalline cellulose (Avicel Ph102, FMC Biopolymer, Pennsylvania, PA, USA), and calcium phosphate (A-Tab, Innophos, Cranbury, NJ, USA) – have been evaluated and used for the reconstruction of virtual particle populations. Optical microscopy images of these four materials and the reconstructed particle populations are shown in Figure 8.3. Further details of the particle shape analysis and 3D reconstruction will be discussed in section 8.3.1.

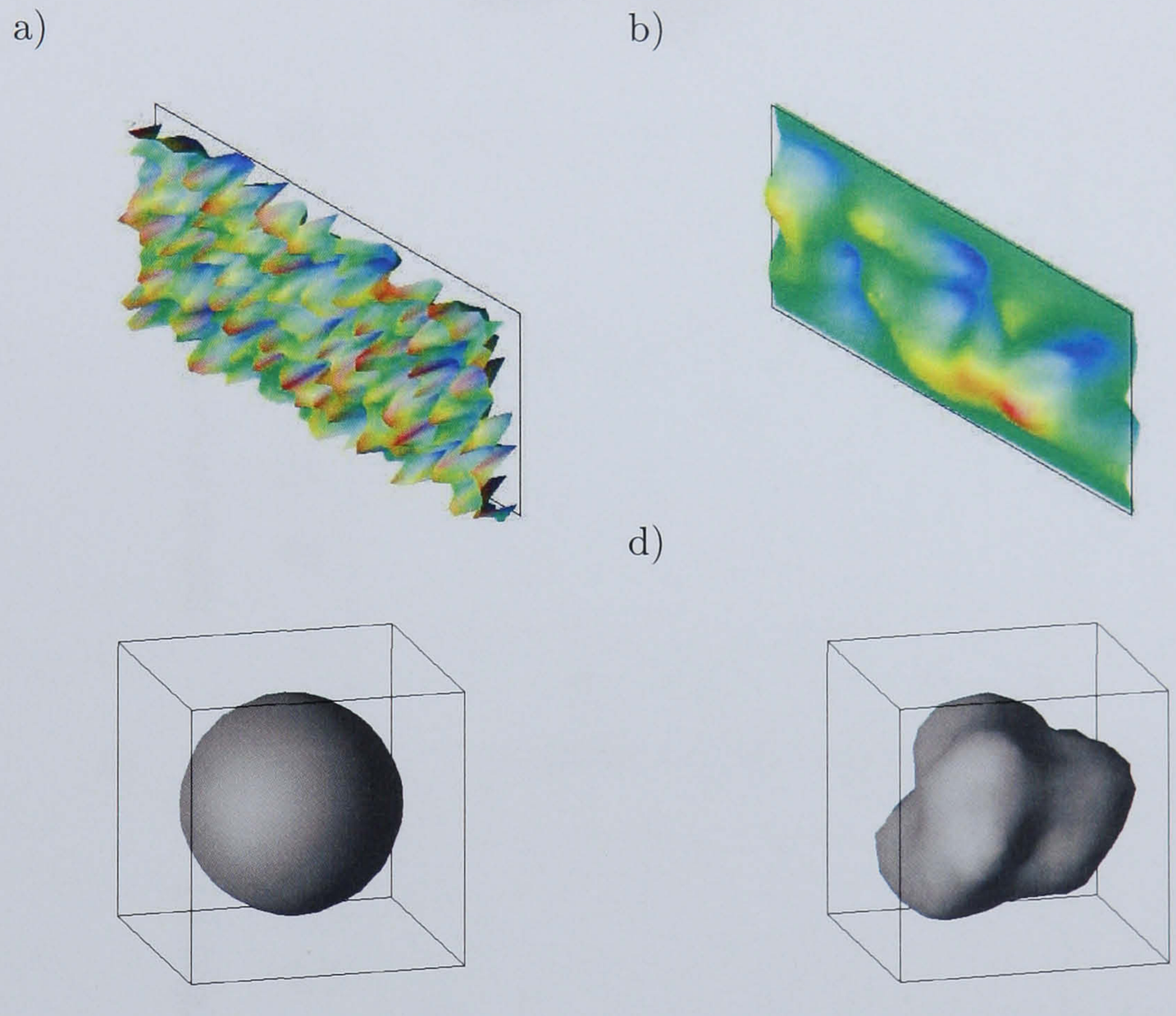

Figure 8.1: Reconstruction of a single primary particle: a) field of independent random variables; b) Gaussian-correlated random field; c) underlying spherical particle with radius r_g; d) particle surface modulated by the correlated random field.

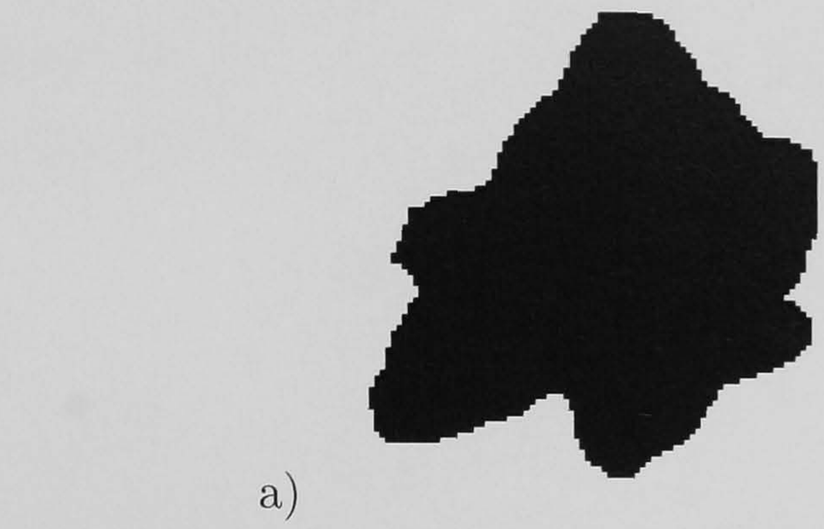

a)

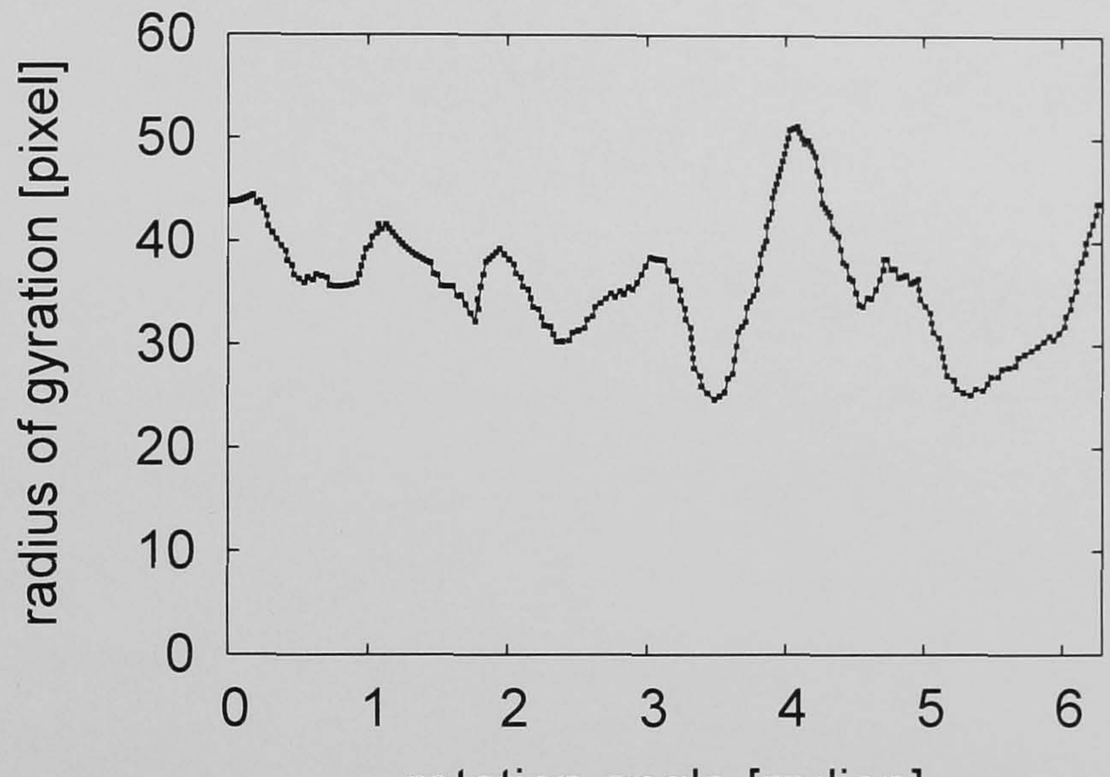

b)

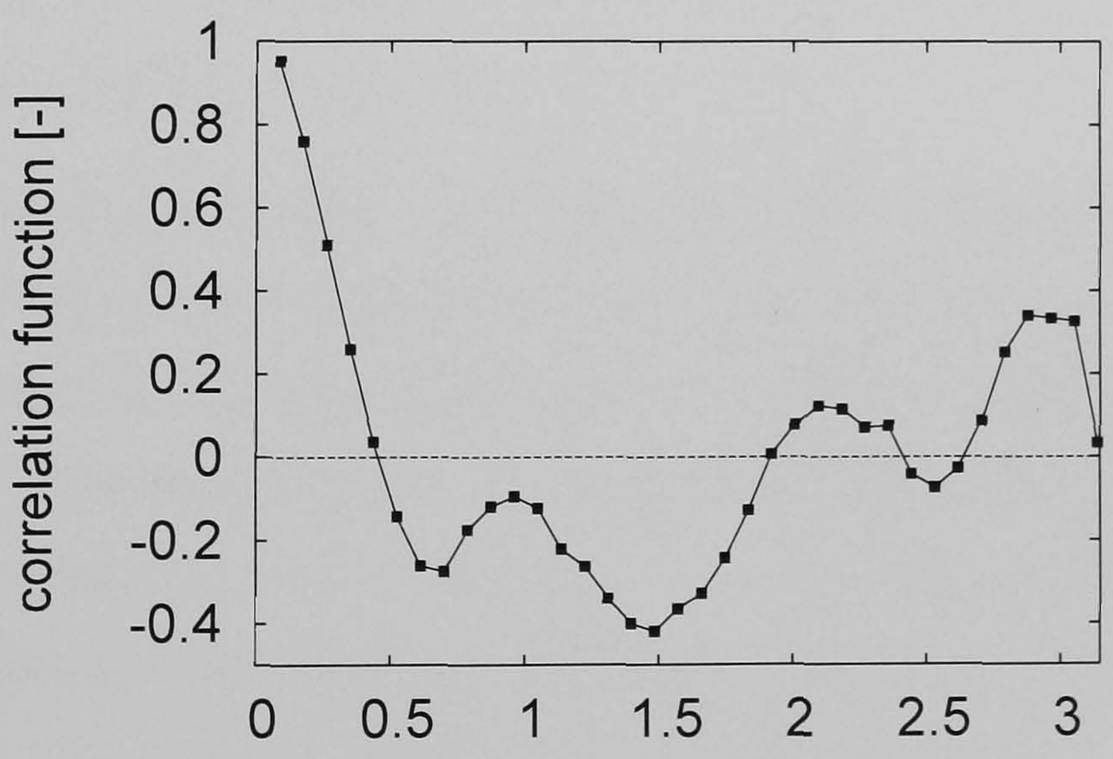

c)

Figure 8.2: Analysis of primary particle shape: a) binary contour of a single particle; b) radius of gyration function; c) surface roughness correlation function.

8.2.2 Computer Simulation of Wet Granule Structure

The structure of each wet granule (i.e., the spatial distribution of the solid phase and the liquid binder within the granule) were encoded by the phase functions (Adler and Thovert. 1998; Rider and Kothe, 1998; Kosek et al.. 2005), defined as

$$f_i(\mathbf{x}) = \begin{cases} 1 & \text{if } \mathbf{x} \in \text{phase } i \\ 0 & \text{if } \mathbf{x} \notin \text{phase } i \\ 0 < f_i < 1 & \text{if } \mathbf{x} \in \text{interface} \end{cases} \tag{8.6}$$

The value of $f_i(\mathbf{x})$ is the volume fraction of discretisation volume element with coordinates $\mathbf{x} = [x, y, z]$ on a cubic grid of N^3 points with spatial discretisation step h. filled by phase i.

Granule structures were formed according to a simplified procedure described in Stepanek and Ansari (2005). The close random packing of primary particles of the required shape was first created using the ballistic deposition algorithm (Coelho et al., 1997). Then the equilibrium distribution of a liquid binder within the close packed structure was found for systematically increasing binder volumes; in equilibrium, all three-phase contact lines must satisfy a prescribed equilibrium contact angle (kept constant at 5° throughout this work) and all two-phase liquid-gas interfaces belonging to the same percolation cluster must have the same mean curvature.

For a given random particle packing, encoded by the phase function f_S defined by Equation 8.6, the equilibrium liquid phase distribution was determined by means of the virtual capillary condensation method (Štěpánek et al., 2007) as follows. A thin layer of liquid ($f_L \approx 10^{-4}$) was first added to all solid-vapour interfaces (i.e., points $\mathbf{x}$ where $0 < f_S(\mathbf{x}) < 1$). A required total liquid volume was then chosen and the values of the liquid phase function f_L at all liquid-vapour interface points were iteratively updated according to

$$f_L^{j+1}(\mathbf{x}) = f_L^j(\mathbf{x}) + \alpha\left(\kappa^j(\mathbf{x}) - \bar{\kappa}^j\right) \quad \forall \mathbf{x} : 0 < f_L^j(\mathbf{x}) < 1 \tag{8.7}$$

where α is a numerical parameter controlling the speed and stability of convergence, $\bar{\kappa}$ is the average curvature of all gas-liquid interfacial points belonging to the same liquid-phase percolation cluster, and $\kappa^j(\mathbf{x})$ is the local curvature at point $\mathbf{x}$ in the j-th iteration.

The local curvature is evaluated numerically from the liquid phase function f_L in every iteration. First, the unit normal vectors, oriented from the liquid toward the vapour phase. are constructed at all liquid-vapour interface points (Rider and Kothe. 1998):

$$\mathbf{n}_L(\mathbf{x}) = -\frac{\nabla \hat{f}_L(\mathbf{x})}{\|\nabla \hat{f}_L(\mathbf{x})\|} \quad \forall \mathbf{x} : 0 < f_L(\mathbf{x}) < 1 \tag{8.8}$$

In the equation above, $\nabla = [\frac{\partial}{\partial x}, \frac{\partial}{\partial y}, \frac{\partial}{\partial z}]$ is the gradient operator and $\hat{f}_L$ is the "mollified" phase function, obtained from f_L by the application of the 1-6-1 smoothing kernel. Once the interface normal vectors are known, the curvature at point $\mathbf{x}$ can be calculated from:

$$\kappa(\mathbf{x}) = -\nabla \cdot \mathbf{n}_L(\mathbf{x}) \quad \forall \mathbf{x} : 0 < f_L(\mathbf{x}) < 1 \tag{8.9}$$

The second-order, symmetric finite difference approximations of the partial derivatives in ∇ have been used in Eqs. 8.8 and 8.9, i.e., $\partial f_L/\partial x|_i \approx (f_L^{i+1} - f_L^{i-1})/2h$, etc.

The liquid phase will spontaneously redistribute itself towards points of large curvature (convex liquid-vapour interfaces) and away from points with low. or negative (concave liquid-vapour interfaces if present), curvature. The iteration of Equation 8.7 stops when the total liquid volume, V_L, reaches the required value and $\max_{\mathbf{x}} |\bar{\kappa}^j - \kappa^j(\mathbf{x})| \leq \delta$ where δ is a prescribed error tolerance. The liquid and solid phase volumes, V_L and V_S, respectively, can be evaluated directly from the phase functions as $V_i = \sum_{\mathbf{x}} f_i(\mathbf{x}) h^3$. Examples of model granules with varying binder/solids ratio, generated by the algorithm described above, are shown in Figure 8.4.

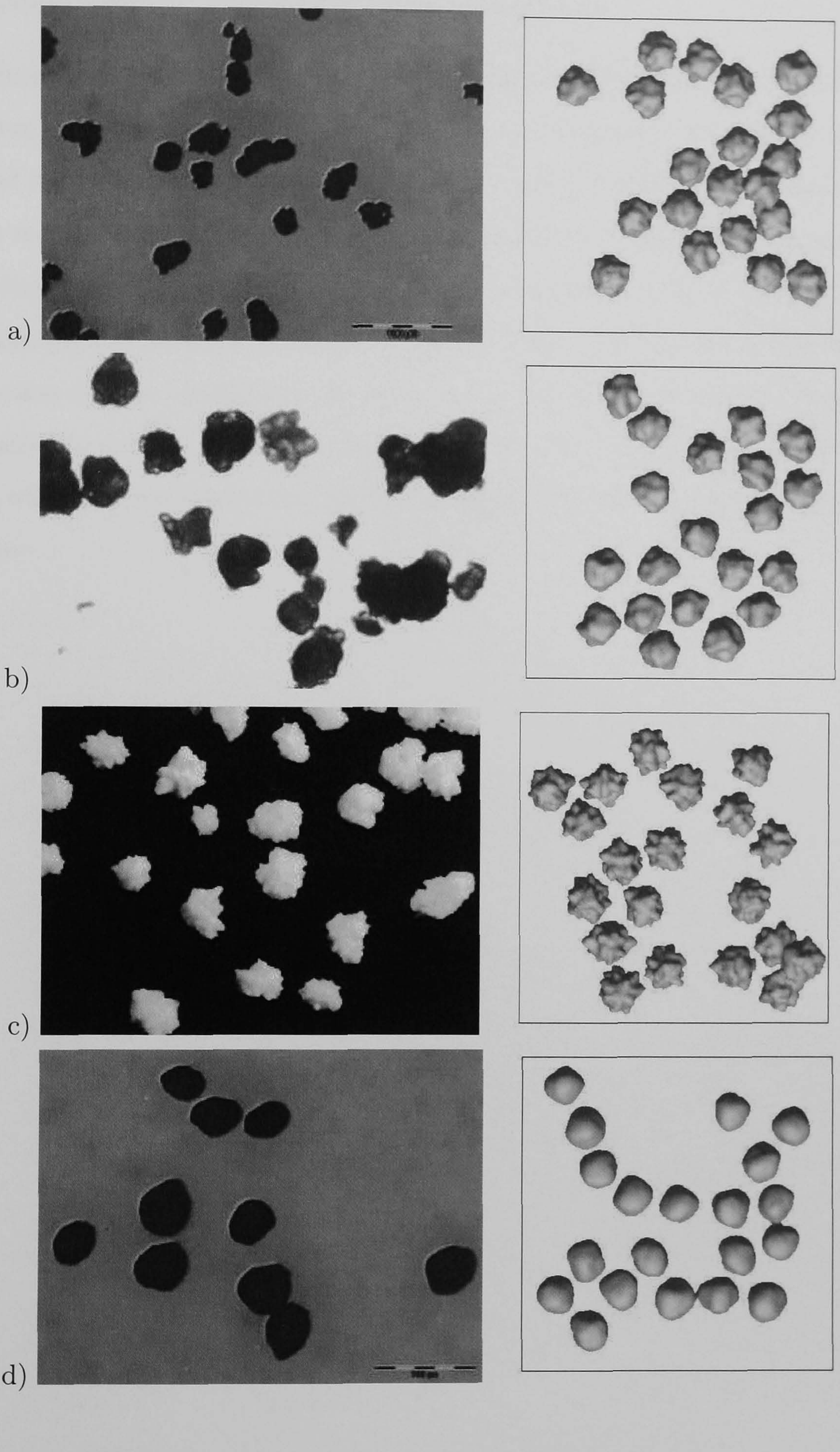

Figure 8.3: Optical microscopy images and three-dimensional computer reconstructed populations of primary particles used in this work: a) lactose; b) mannitol; c) A-Tab; d) Avicel. The scale bar in the optical images is 1000 μm. Different illumination modes were used in order to maximise contrast in each case.

8.2.3 Evaluation of Accessible Binder Fraction

A three-dimensional granule model encoded by the phase functions (Equation 8.6) bears full information about the spatial distribution of the primary particles and the liquid binder, and it can be used for visualisation (see Figure 8.4). However, further geometrical analysis is required in order to evaluate relevant parameters quantifying the structure. In our case, these are: (i) the binder/solid ratio, as a measure of the granule volume-based composition; (ii) the fractional surface coverage by binder, defined as the proportion of the granule's outer surface occupied by the binder; (iii) the accessible binder fraction, defined as the relative frequency at which primary particles arriving at the granule from random directions will land on a binder-wet region; and finally (iv) the average thickness of surface binder layer.

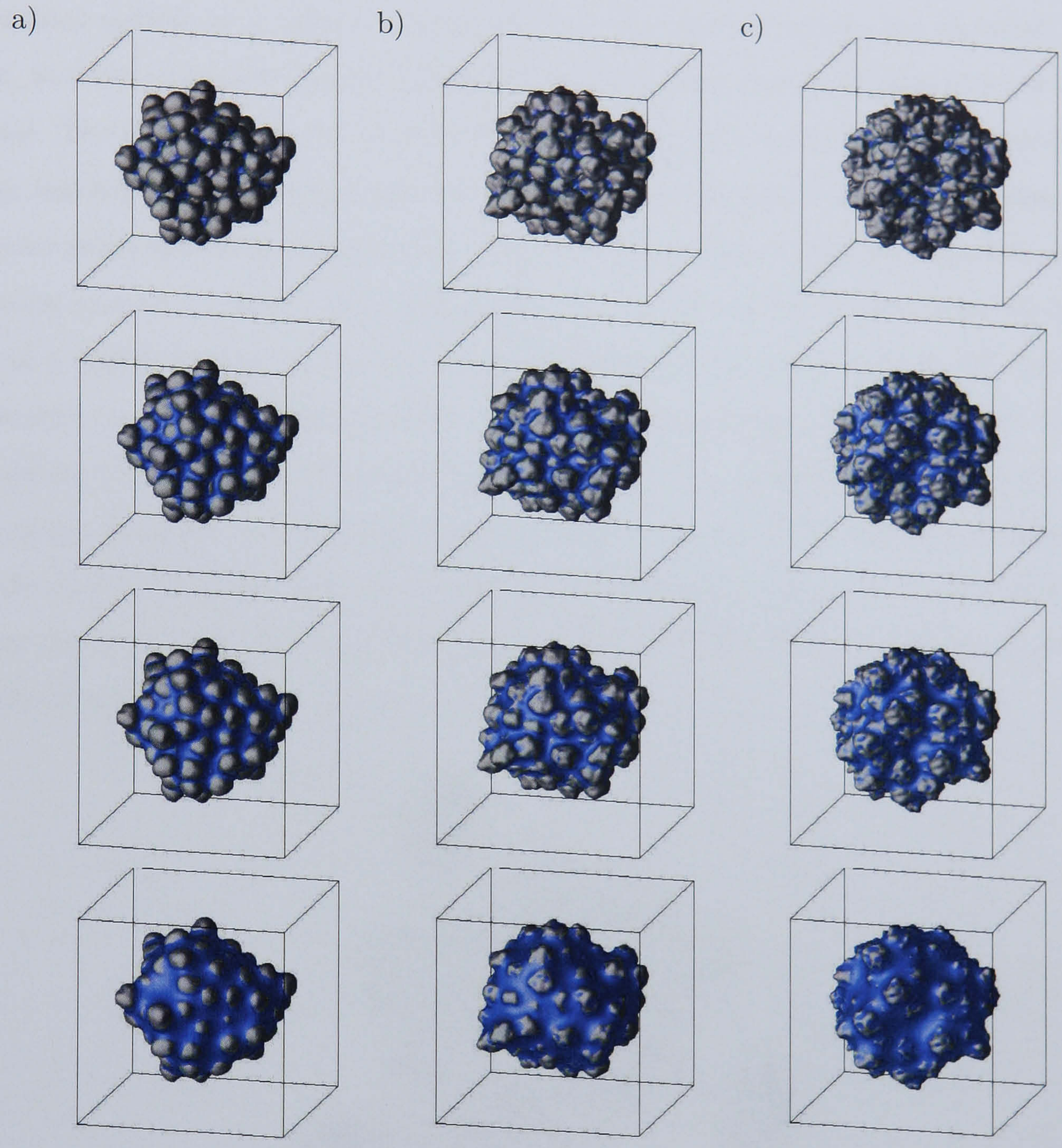

Figure 8.4: Computer-generated "virtual granules" consisting of a) Avicel; b) Mannitol; c) A-Tab primary particles (each granule contains 120 primary particles). The fractional surface coverage is approximately 0.01, 0.05, 0.10, and 0.50, from top to bottom. The volumetric binder/solids ratio varies according to the primary particle shape, as shown in Figure 8.6.

Criteria (i) and (ii) can be evaluated directly from the phase functions. The solid and liquid volumes are $V_i = \sum_{\mathbf{x}} f_i(\mathbf{x})h^3$, $i = S, L$, and the surface areas are $A_i = \sum_{\mathbf{x}} h^2$ $\forall \mathbf{x} : 0 < f_i(\mathbf{x}) < 1$, $i = S, L$. In the case of the surface area calculation, only points contained outside of a sphere covering 80 % of the granule volume are included in the sum, in order to exclude the granule internal surfaces that may be present at lower binder ratios. The accessible binder fraction was evaluated by the so-called *shooting method*. A large number ($N_{shot} \approx 200$) of primary particles were sequentially introduced towards the granule using the ballistic deposition algorithm, but instead of being integrated into the existing granule structure, only the number, N_{wet}, of incoming particles that would end up in a binder-covered region was counted. It should be noted that on the surface of a smooth, spherical particle partially coated by a binder, the accessible binder fraction would be equal to the fractional surface coverage – i.e., criteria (ii) and (iii) would be the same. However, as will be discussed in detail in section 8.3.2, in a real granule some binder may be shielded from the incoming particle by existing primary particles (this is especially the case at low binder fractions when pendular capillary bridges predominate), as shown schematically in Figure 8.5.

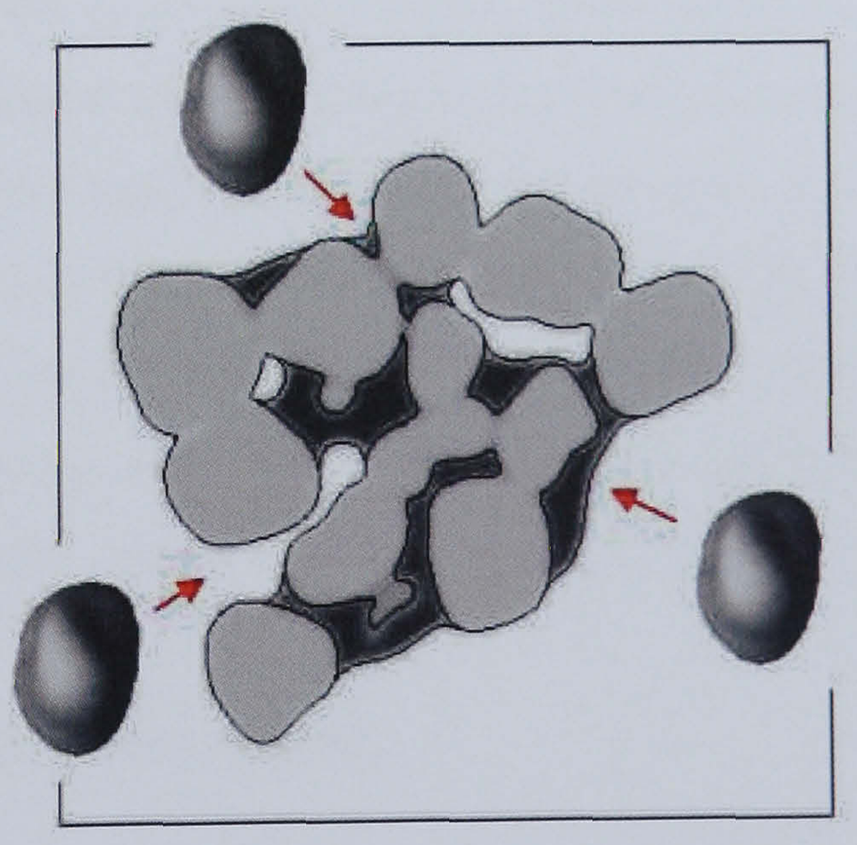

Figure 8.5: Schematic illustration of the principle of the shooting method for determining the accessible binder fraction. (The underlying granule is shown in cross-section, binder is in dark grey, primary particle in light grey.)

The final quantity of interest is the thickness of the binder layer that is present on the

granule surface and can contribute to kinetic energy dissipation during collisions. This quantity was also evaluated by the shooting method, but instead of merely counting the impacted particles, the total volume of binder displaced during each collision by the incoming particles was also noted. The ratio of the total displaced binder volume, V_{wet}, over the total volume of the incoming particles, V_{shot}, was used as a measure of the average binder quantity present on the granule surface. Details of a computational parametric study relating the quantities V_L/V_S, A_L/A_S, N_{wet}/N_{shot}, and V_{wet}/V_{shot}, will be discussed in section 8.3.2 below.

8.2.4 Experimental Methods

Granulation experiments were carried out in a bottom-spray Wurster-type fluidised bed granulator (Glatt GPCG3, Glatt GmbH, Binzen, Germany), with 920 g batches of a narrow sieve fraction of each material ($D_{50} = 120$ μm for lactose and mannitol, and $D_{50} = 152$ μm for A-Tab and Avicel). The binder used was a 15 wt.% aqueous solution of hydroxy propyl cellulose (HPC-SL, Nisso Soda Co. Ltd., Tokyo, Japan): 80 g (dry basis) of the binder was added in each case. The binder solution was sprayed at a rate of approximately 11-13 g/min, and granule samples were taken at regular intervals for size distribution analysis by the Sympatec laser diffraction system (Sympatec GmbH, Clausthal-Zellerfeld, Germany). The granule growth profiles were reported as the mass-mean granule diameter as function of the dimensionless granulation time, which was defined as the time at which sample was taken over the total binder spraying time. All other granulation conditions (air flow rate, humidity, temperature) were kept constant for all four materials. Full details of the experimental procedure are reported in Rajniak et al. (2007).

8.3 Results and Discussion

8.3.1 Primary Particle Morphology

The four typical pharmaceutical excipients chosen for this study represent a spectrum of particle morphology – from very smooth (Avicel), through intermediate (lactose and mannitol) to rather rough (A-Tab). Optical microscopy images of a few typical particles from each material are shown in the left column of Figure 8.3. After evaluating the par-

ticle shape descriptors according to the procedure described in Sec. 8.2.1. the following values of dimensionless surface roughness amplitude and correlation length were obtained: Avicel ($a = 0.21$, $L = 0.62$), mannitol ($a = 0.35$, $L = 0.37$), lactose ($a = 0.35$, $L = 0.30$), A-Tab ($a = 0.55$, $L = 0.22$). Examples of three-dimensional reconstructed particle populations possessing the same morphological characteristics are shown in the right column of Figure 8.3, next to the corresponding optical image of real particles. The mean gyration radius used for all four particle shapes was the same, $r_g = 60$ μm, as the purpose of the present work was to investigate the net effect of particle shape, rather than particle size distribution.

8.3.2 Effect of Primary Particle Morphology on Binder Distribution

Three-dimensional virtual granules were constructed according to the algorithm described in section. 8.2.2 from a population of randomly realised particles of each of the four types. Each granule consisted of 120 different primary particles. For each primary particle type, granules with 20 different binder/solids ratios were realised, covering a range of V_L/V_S from 0.01 to approximately 0.30. Several examples of granules with varying binder content and different primary particle morphology are shown in Figure 8.4. The four characteristics introduced in section. 8.2.3 were evaluated for each granule, and they are summarised in Figures 8.6–8.8.

As shown in Figure 8.6, the fractional surface coverage by binder is an increasing function of the volumetric binder/solids ratio in the granule, and the functional relationship goes through two distinct phases. At lower V_L/V_S ratios, the fractional coverage is essentially independent of the particle shape – this segment corresponds to the pendular state of the granule, where the liquid binder is present in the form of binary bridges at primary particle contacts. At higher V_L/V_S ratio, a transition to the capillary state occurs. The transition is already particle shape dependent, because of the different pore volume existing in the random packing of each particle type. For smooth particles (Avicel), the transition occurs at a much lower binder/solids ratio than for rough ones (A-Tab).

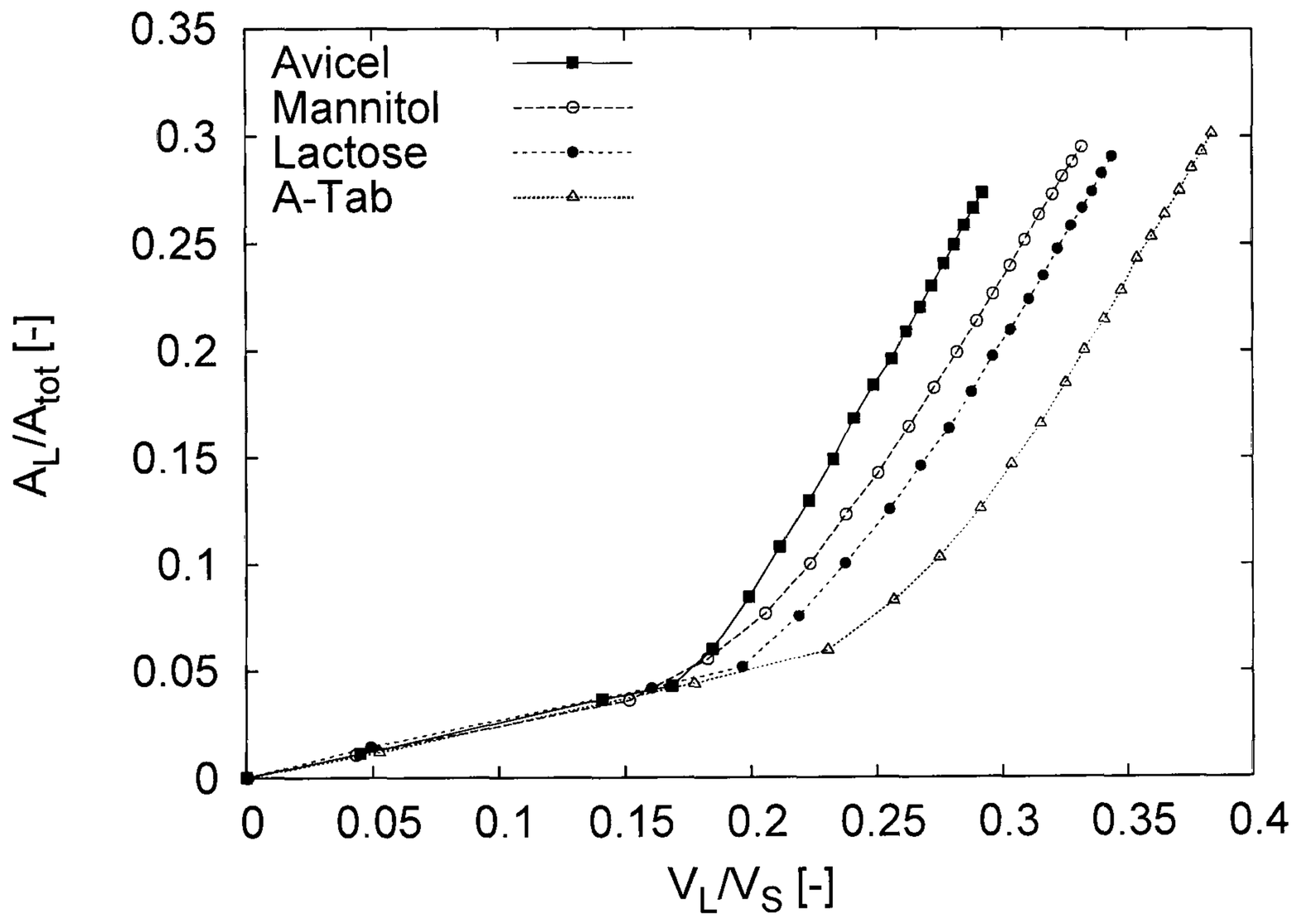

Figure 8.6: Effect of primary particle shape on the relative fractional coverage by binder as function of granule composition, for granules consisting of 120 primary particles.

The accessible binder fraction, shown in Figure 8.7, follows a qualitatively different functional dependence on the granule composition (binder/solids ratio) than the surface coverage. The effect of the primary particle shape is equally strong, though, in the order of smooth (Avicel), medium (mannitol and lactose), to rough (A-Tab). The simulation data points were fitted by a sigmoidal function of the form

$$y = \frac{1}{1 + e^{-b(x-c)}}. \tag{8.10}$$

The values of fitting parameters b and c are listed in Tab. 8.1. The explanation for the sigmoidal dependence is as follow: at relatively low binder fractions, most of the binder is present as binary capillary bridges between primary particles, and is therefore sterically hindered from any new incoming primary particles. Hence the number of particles that contact a binder during collision, N_{wet}, is zero despite non-zero binder volume. Once a certain critical (particle shape dependent) value of the binder content is exceeded, each incremental binder volume becomes exposed to incoming primary particles, giving rise to a relatively rapid increase in N_{wet}/N_{shot} as function of V_L/V_S. By comparing Figure 8.6 and 8.7, it is obvious that the accessible binder fraction approaches 100 % well before the fractional surface coverage. This trend can be understood by analysing a single collision event: even if an incoming primary particle initially hits a dry patch on the granule surface, it may still roll down and deposit on a wet binder region (see Figure 8.5).

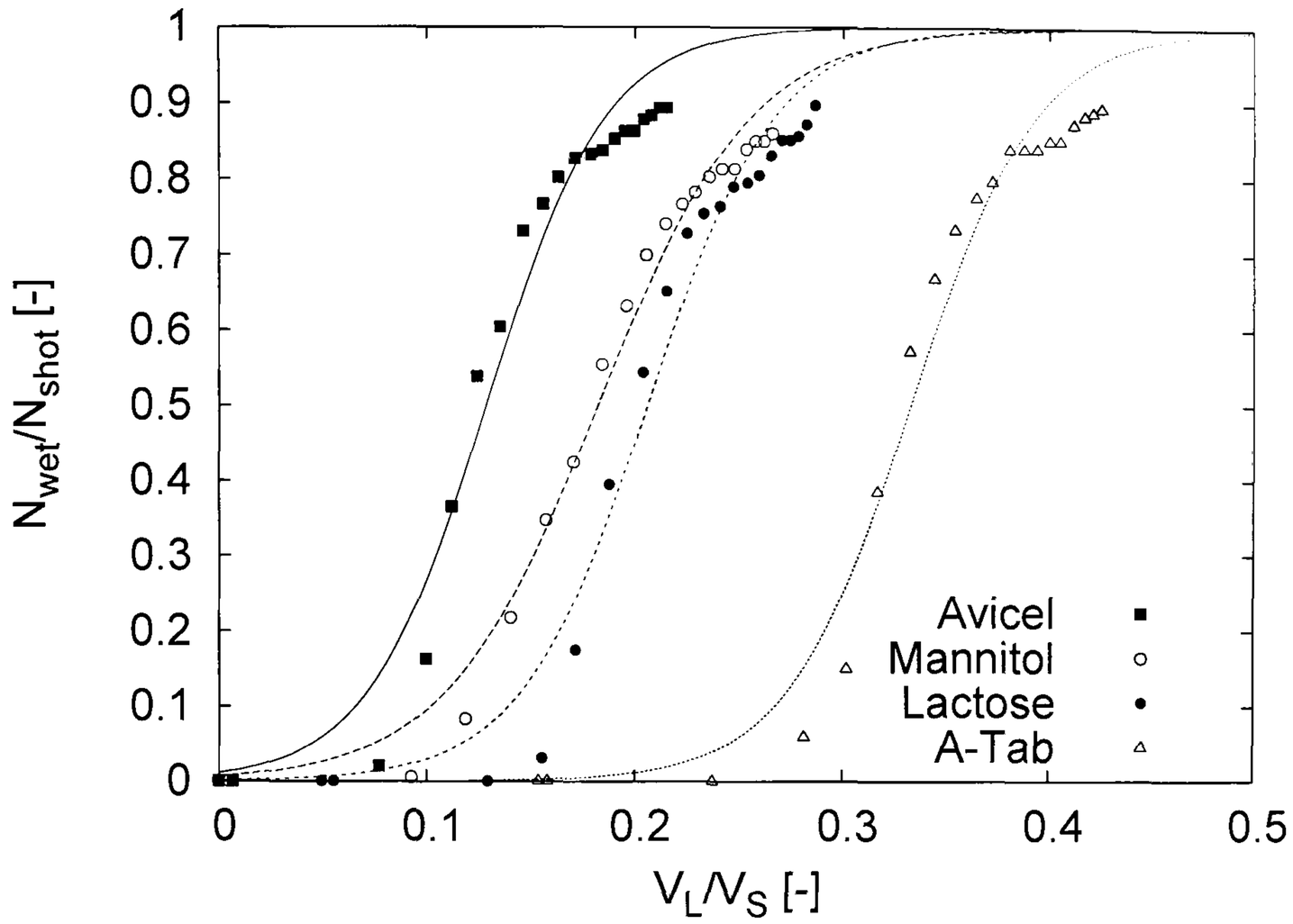

Figure 8.7: Effect of primary particle shape on the accessible binder fraction as function of granule composition, for granules containing 120 primary particles. Points are simulation data points, lines are fits by a sigmoidal function.

The dependence of the third characteristic – the binder volume on the granule surface – on the volumetric binder/solids ratio in the granule is plotted in Figure 8.8. As was the case for the accessible binder fraction, the volume of displaced binder is effectively zero below a certain critical binder content due to the shielding effect, but once this critical value is exceeded, the displaced binder volume rises sharply. The order at which the onset of the sharp increase occurs is again clearly correlated with the primary particle morphology.

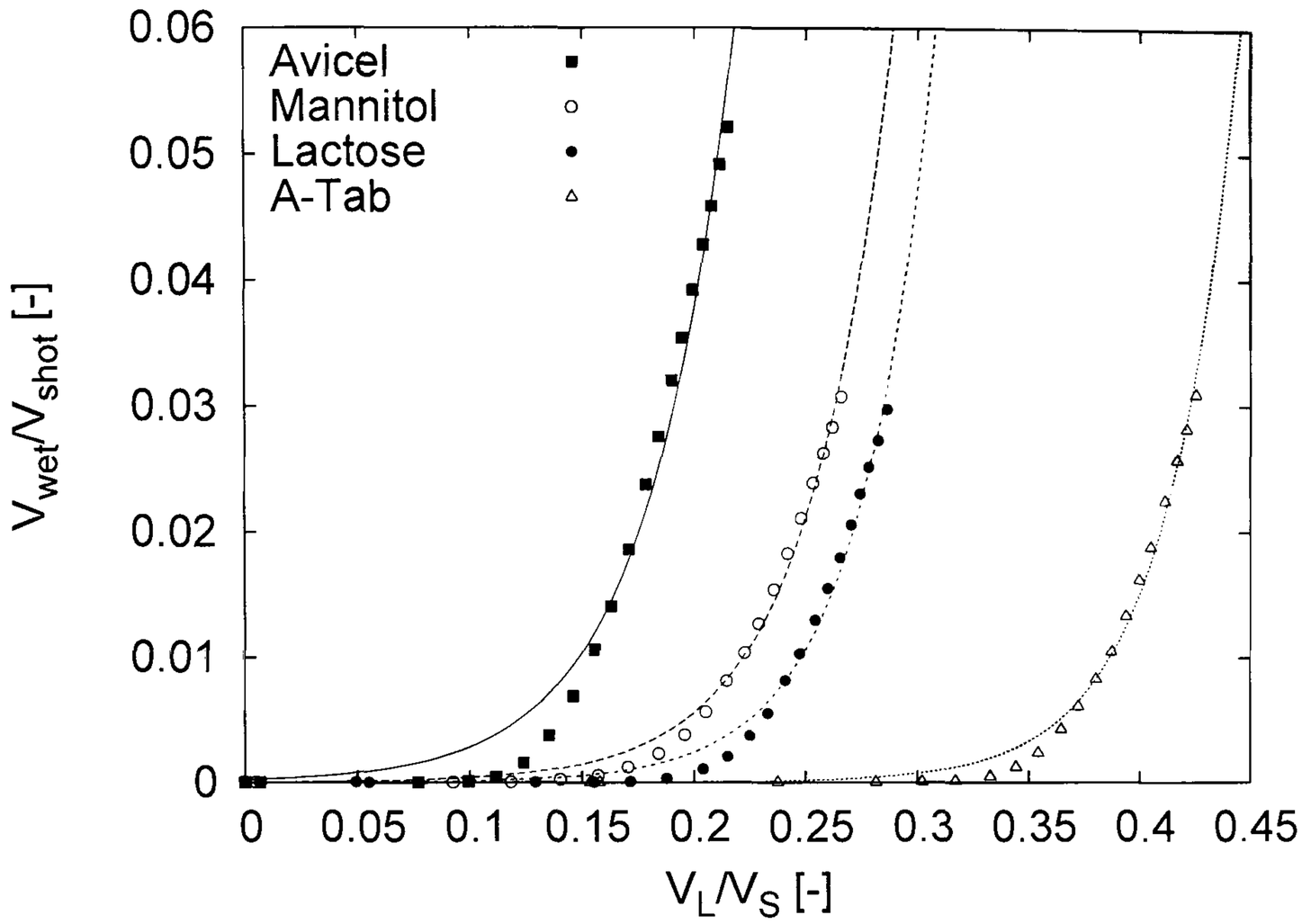

Figure 8.8: Effect of primary particle shape on the relative displaced binder volume as function of granule composition, for granules containing 120 primary particles. Points are simulation data points, lines are fits by an exponential function.

Table 8.1: Parameters b and c of the sigmoidal fitting function, Equation 8.10, based on data from Figure 8.7.

Excipient	b	c
Avicel	35.1	0.129
Mannitol	27.4	0.182
Lactose	33.0	0.206
A-Tab	33.5	0.333

8.3.3 Effect of Granule Size on Binder Distribution

For primary particles of a given packing density, the available intra-granular pore volume increases with the third power of the granule diameter, whereas the granule surface area scales with the square of diameter. Therefore, it can be expected that the accessible binder fraction and possibly also the binder thickness will be size depended. In order to determine their size dependence, granules containing a varying number of mannitol primary particles (from 20 to 120) were realised and analysed.

The results of the effect of granule size on the relationship between the granule composition (V_L/V_S) and each of the three surface characteristics. are summarised in Figure 8.9–8.11. It is apparent that all three characteristics – the fractional coverage A_L/A_S, the accessible binder fraction N_{wet}/N_{shot}, and the displaced binder volume V_{wet}/V_{shot} – depend on the granule size in a systematic way, albeit the effect is less strong than that of primary particle shape.

The graph plotted in Figure 8.10 is practically very useful because it allows a direct estimation of the amount of binder that needs to be sprayed to a given batch of primary particles in order to cause granulation[1] (minimum binder requirement), and/or, an estimation of the maximum theoretically attainable granule size for a given binder/solids ratio. The data points in Figure 8.10 were again fitted by a sigmoidal function, Equation 8.10, and the values of fitting parameters b and c for a different number of primary particles in the granule are listed in Table /reftab:sigmasize. In combination with a graph showing the dependence of binder layer thickness (Figure 8.11) on granule size and composition, it provides necessary information for the construction of a size- and composition-dependent granulation kernel for primary particles of given morphology, which is required in multi-dimensional population balance modelling of granulation.

Let C_{ij} be the number of collisions between particles from classes i and j per unit volume per unit of time. The number of *successful* collisions, C_{ij}^{suc}, can be expressed as

$$C_{ij}^{suc} = \psi_{ij}^{geom} \psi_{ij}^{phys} C_{ij} \tag{8.11}$$

where ψ^{geom} and ψ^{phys} are the geometrical and the physical collision success factors.

[1] This value is sometimes called the "liquid-carrying capacity" of the powder.

respectively. The geometrical success factor, which represents the necessary (but not sufficient) condition for agglomeration, can be expressed as

$$\psi_{ij}^{geom} = 1 - (1 - \eta_i)(1 - \eta_j) \tag{8.12}$$

where $\eta \equiv N_{wet}/N_{shot}$ is the accessible binder fraction, discussed above. The dependence of η on the binder/solids ratio in a granule is given by Equation 8.10, whereby the parameters b and c are granule size-dependent and can be calculated for the required size by interpolation from values given in Tab. 8.2.

The physical success factor, ψ_{ij}^{phys}, can be expressed based on the Stokes' number analysis (Ennis et al., 1991; Tardos et al., 1997; Liu et al., 2000). In the simple case of considering granule coalescence due to energy dissipation in the viscous binder layer (and not due to plastic deformation of the underlying granules), we will have

$$\begin{aligned} St_v \leq St_v^* : &\qquad \psi^{phys} = 1 \\ St_v > St_v^* : &\qquad \psi^{phys} = 0 \end{aligned} \tag{8.13}$$

where the critical viscous Stokes' number, $St_v^* = 2\ln\left(\frac{\lambda}{h_a}\right)$, contains two parameters that depend on the three-dimensional granule morphology and binder distribution: the surface asperity, h_a, and the binder layer thickness, λ. The surface asperity of the primary particles is given from the morphological analysis, i.e. $h_a = (a/2)r_g$ where a and r_g are the dimensionless surface roughness amplitude and the mean radius of gyration, respectively. The binder layer thickness, λ, can be estimated from the displaced binder volume, $\phi \equiv V_{wet}/V_{shot}$, as $\lambda = 2r_g\phi^{1/3}$. For two colliding granules, the binder layer thickness is additive, i.e. $\lambda_{ij} = \lambda_i + \lambda_j$. The above set of equations thus makes it possible to link microstructure-related parameters of wet granules (primary particle morphology, binder content and binder distribution) with a macroscopic description of granulation by a population balance model via the agglomeration kernel. A population balance model of granulation which uses the kernel proposed above is the subject of a parallel publication (Rajniak et al., 2008).

Table 8.2: Parameters b and c of the sigmoidal fitting function. Equation 8.10, based on data from Figure 8.10.

no. of primary particles	b	c
40	30.5	0.117
60	24.5	0.143
80	27.8	0.159
120	27.4	0.182

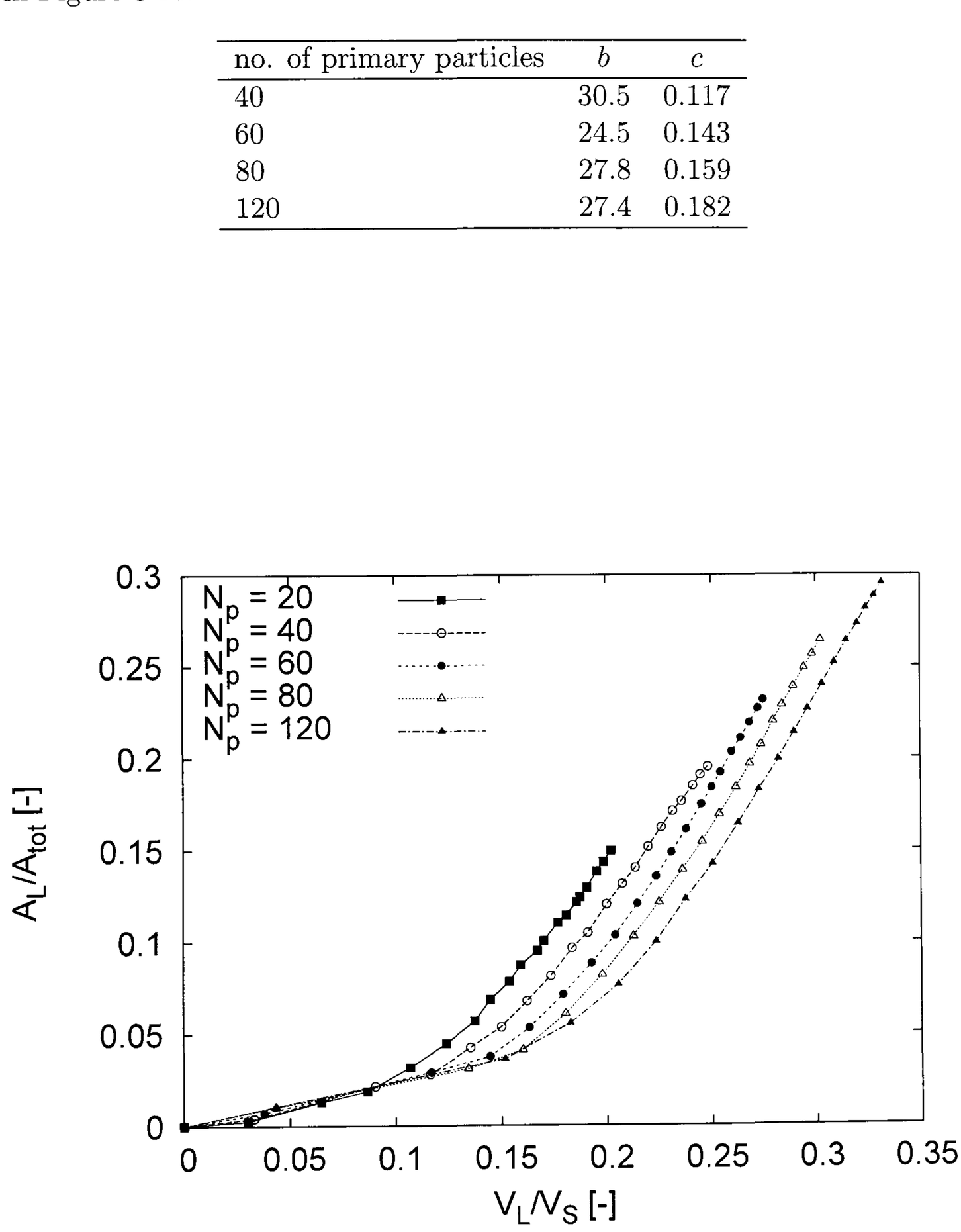

Figure 8.9: Effect of granule size (number of primary particles in granule. N_p) on the fractional surface coverage by binder as function of granule composition, for mannitol primary particles.

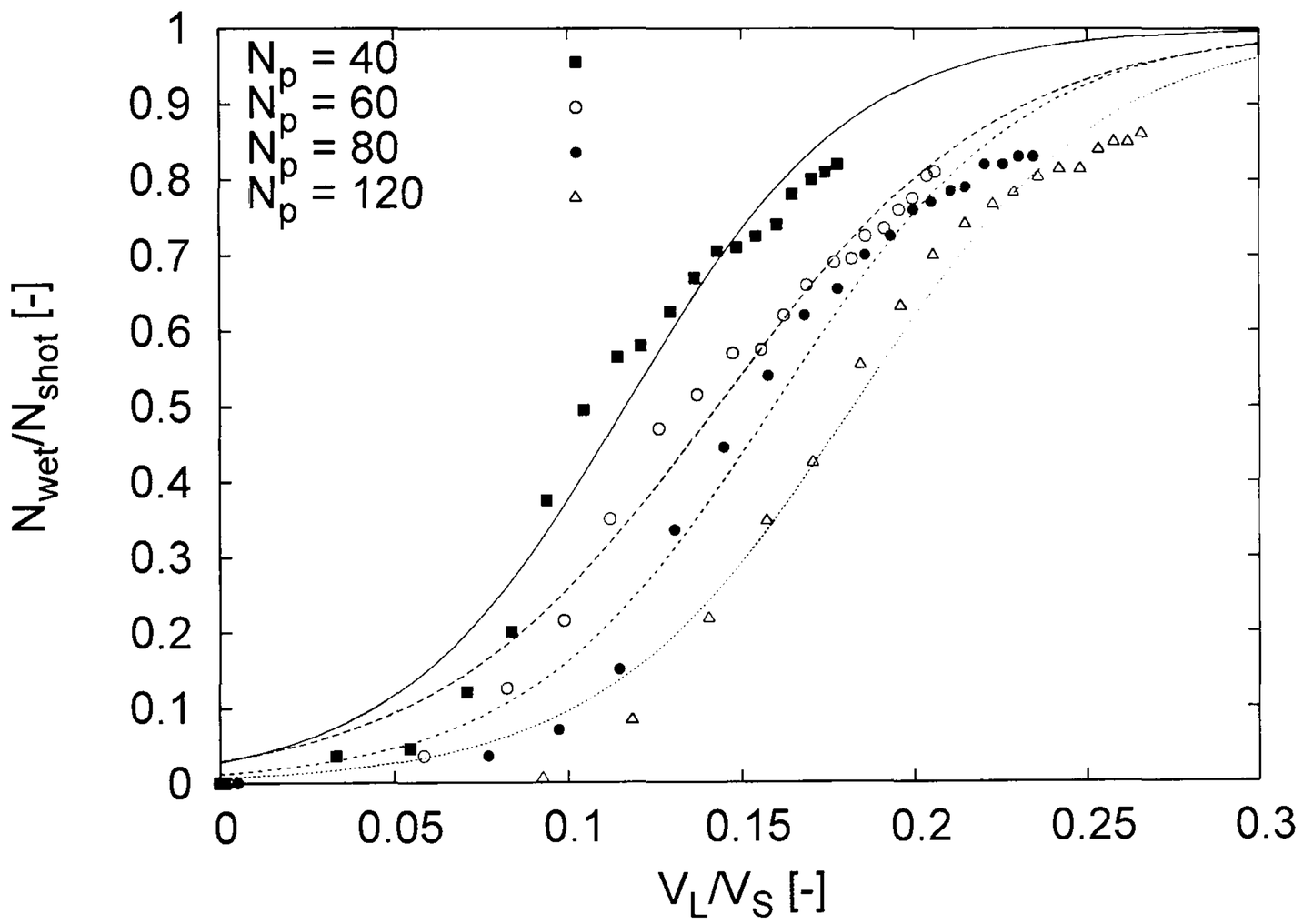

Figure 8.10: Effect of granule size (number of primary particles in granule, N_p) on the accessible binder fraction as function of granule composition, for mannitol primary particles. Points are simulation data points, lines are fits by a sigmoidal function.

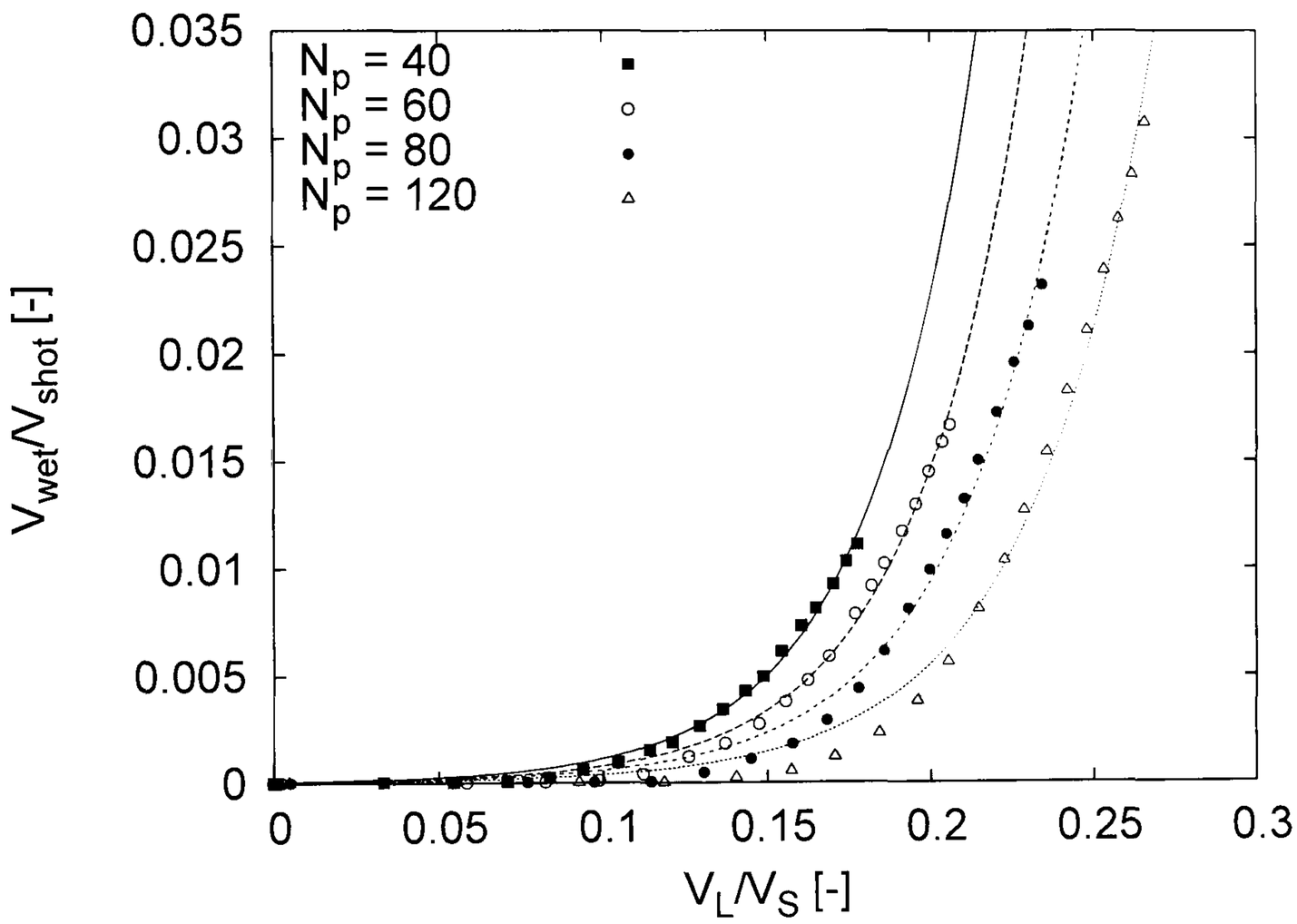

Figure 8.11: Effect of granule size (number of primary particles in granule, N_p) on the relative displaced binder volume as function of granule composition, for mannitol primary particles. Points are simulation data points, lines are fits by an exponential function.

8.3.4 Experimental Growth Kinetics

The effect of primary particle morphology on the rate of granulation was also investigated experimentally by fluidised bed granulation of the four above-mentioned powders using aqueous solution of HPC as a binder. The measured granule growth curves are reported in Figure 8.12. The growth kinetics reveals a strong dependence on the primary particle morphology – the smooth Avicel particles undergo rapid granulation as soon as the binder is sprayed, and also reach the largest final granule size ($D_{50} \approx 650$ μm). Both lactose and mannitol, which have similar surface roughness, show intermediate behaviour: the granule growth rate is slower than that of Avicel, but the granule size is still proportional to the binder amount from the on-set of spraying. This contrasts with the growth kinetics of A-Tab (rough primary particles), where a considerable initial lag with no granulation is clearly present. The final granule size, however, is comparable with that of lactose and mannitol, i.e. $D_{50} \approx 400 - 450$ μm. The observed trends are consistent with the results of binder distribution analysis presented in earlier sections. In the case of A-Tab, a sufficient binder volume has to accumulate on the particles before granulation can even begin, whereas the smooth Avicel particles show immediate granule growth. Further discussion of the experimental data and their comparison with simulation results obtained by means of a population balance model can be found in Rajniak et al. (2008).

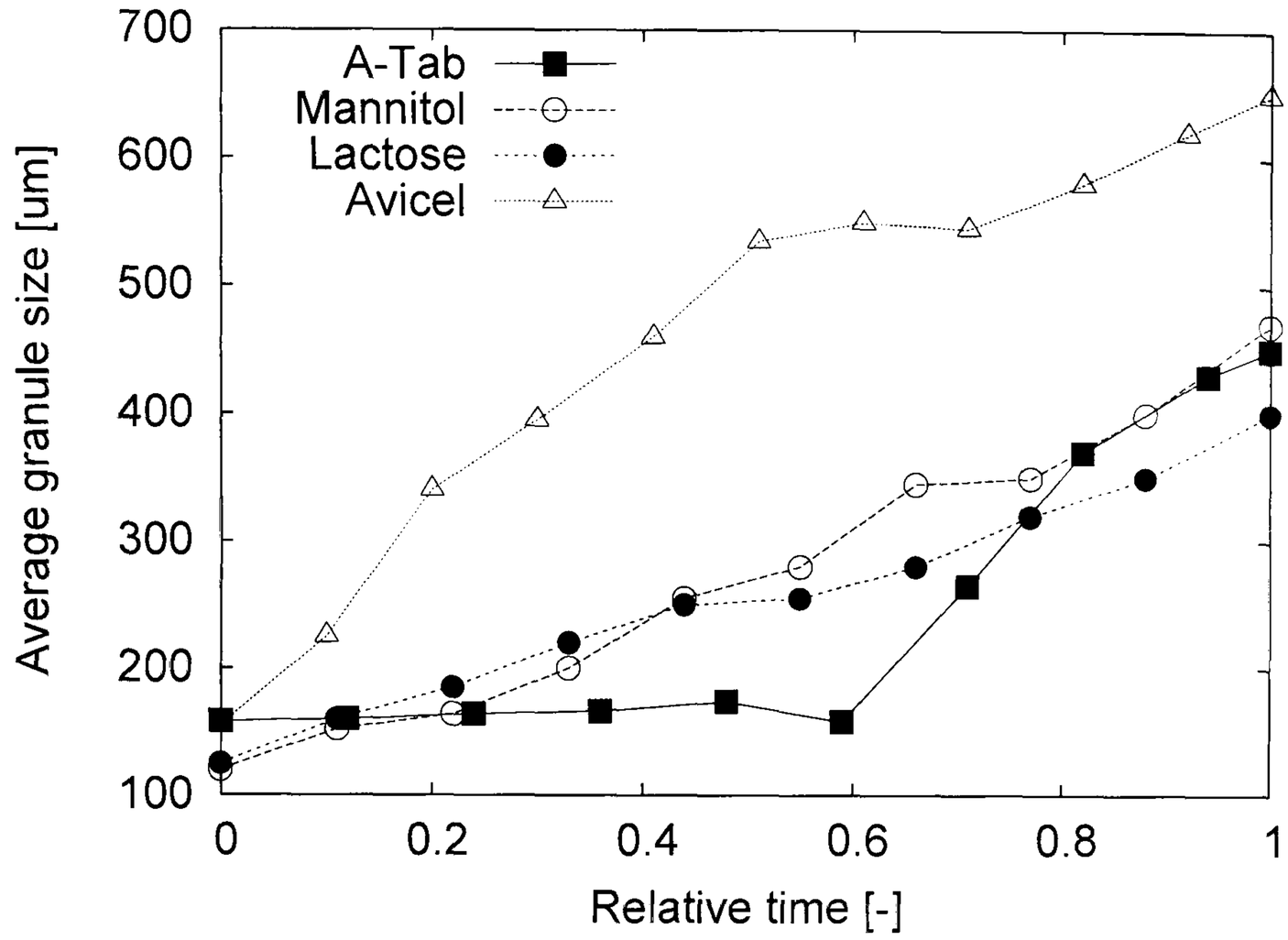

Figure 8.12: Experimental granulation kinetics of Avicel, mannitol, lactose, and A-Tab obtained by fluid-bed granulation with 15% aqueous solution of hydroxy-propyl cellulose binder. The relative time indicates the proportion of the total binder amount added.

8.4 Conclusions

The relationship between the volumetric composition of wet granules and the amount of binder available on their surface was investigated by means of numerical simulation. It has been shown that the fractional surface coverage of wet granules follows a bi-linear dependence on the binder/solids ratio, corresponding to the pendular and the capillary state of the granules. However, the fraction of binder that is *accessible*, and can therefore contribute to particle coalescence during collisions, follows a non-linear (sigmoidal) dependence on the binder/solids ratio. Both the accessible binder fraction and the average binder layer thickness depend very strongly on the primary particle morphology, and can be used to explain experimentally observed difference in granule growth kinetics of various pharmaceutical excipients under otherwise identical conditions. It was also shown that the accessible binder fraction and the binder layer thickness depend on the granule size. The

composition- and size-dependence of granule surface properties should be considered when constructing kernels for multi-dimensional population balance models of granulation.

The model presented in this work is of course still a considerable simplification of reality. First of all, the liquid distribution in the granules was assumed to be in the asymptotic state (equilibrium contact angles and constant mean curvature were satisfied). whereas in an actual granulation process, the mean time between particle collisions may be shorter than the time required for binder droplets to reach this asymptotic state (Stepanek and Ansari, 2005). Second, our analysis assumed the primary particles within the granule were in the close random packing limit, and remained static during collision. In reality, particle rearrangement and squeeze flow of binder would occur to some degree even during collisions with primary particles. Finally, we have analysed granules containing only binder in the liquid state, whereas in many granulation processes, binder solidification (by drying, cooling, or chemical reaction) occurs over the same time-scale as binder spreading and particle-particle collision. This would introduce an additional heterogeneity into the granule structure – namely that of the binder local "age", which could manifest itself e.g. by different viscosity in different parts of the granule surface, and hence should also be considered in a physically based granulation kernel.

Nevertheless, the analysis carried out in this work has provided information that helped us understand the effect of primary particle morphology on granulation kinetics, which together with the effect of primary particle surface properties (Thielmann et al., 2008) and binder properties (Rajniak et al., 2007) makes it possible to establish relationships between material properties and granulation process behaviour.

Chapter 9

Conclusions and Future Research

As mentioned in the thesis objectives, this research is concerned with a more systems-centric approach to the granulation problem, which could potentially enhance the design, control and scale-up of the granulation process. This chapter is organised as follows. The chapter begins with the conclusions of this thesis in section 9.1. The primary contributions of this thesis are then summarised in section 9.2. Finally, suggestions for future work are provided in section 9.3.

9.1 Conclusions

Granulation is a particle agglomeration process, in which small particles are agglomerated together by means of a viscous binder. However, despite its wide applications in industry and many years of research, granulation at the industrial scale has remained more of an art than a science. Many industrial plants often operate well below their design capacity and have large recycle ratios which causes the plant to shut down. There is also no formal methodology for the operation and control of granulation processes. Engineers and operators cannot predict the granulation behaviour from its fundamental properties (i.e., solid and liquid properties). Expensive and extensive laboratory and pilot-plant scale tests are still required. Progress on the understanding of granulation is however being made and the current research addresses some of the existing gaps and challenges in granulation research and contributes to the overall progress of understanding the granulation problem.

Dynamic model development and solution:

The population balance model has proven to be a suitable framework to model the temporal evolutions and distributions of key granule attributes. Many of the population balance models in the literature are either one- or two-dimensional in nature and do not account for all/most of the key important granule properties. In this work, a three-dimensional population balance model is presented which can account for granule size, binder content and porosity, providing a realistic characterisation of the granule process. As a result of this detailed dynamic model, granule properties such as the ones mentioned above can be simulated providing useful insight into the intricate workings of the granulation mechanisms. The population balance equation is a hyperbolic nonlinear integro-partial differential equation whose solution involves complex finite difference/element techniques due to the hyperbolic nature of the equation. The additional computational load for such an equation limits its utility for engineering problems where real time analysis is required for process control constraints. A fast and efficient solution technique (known as the hierarchical two-tier technique), was developed for one dimensional population balance models and extended to this three dimensional case. The main feature of the technique is that the off-line analytical solution proposed for the aggregation quadratures leads to a substantial reduction in computational load. To further expedite solving the population balance model based on this technique, a parallel programming framework was implemented to the code. Results showed that parallel computing is effective in further reducing execution time, enabling the complex population balance model to be potentially relevant for process control purposes.

Mechanistic kernels:

A major challenge in developing population balance models is the identification of suitable kernels for the granule mechanisms. Due to limited knowledge of the granulation mechanisms (especially for nucleation and breakage) many of the proposed kernels in the literature are empirical or semi-empirical in nature. This results in two main disadvantages. Firstly, empirical models are limited in their usage and are valid over a narrow operating region. Secondly, these models cannot be used for predictive purposes as they are not a function of material properties and design parameters. As a result they cannot

be used to gain insight into the sensitivities, controllability and scale-up of the granulation process. In this research, the granulation mechanisms presented are derived from first-principles and are formulated based on the kinetics and thermodynamics of the process, solid properties of the primary powder, liquid properties of the binder, and process/design parameters. These mechanistic models allow for further studies to be made in the areas of sensitivity studies, controllability analysis and scale-up.

Experimental studies and Model validation:

Experimental studies were performed for a drum granulation system. Based on the results, the sensitivity in the granulation process and the non-homogeneity of key particle attributes (size, binder content, and porosity) was evident. The important process manipulations for feedback control and potential disturbances were identified, formulating a comprehensive control configuration for batch granulation. The experimental studies also provided the relevant knowledge for a pilot-plant operation using the same granulation recipe. Furthermore, the importance of multi-scale process models that link fundamental material properties with the granulation mechanisms and end-granule properties was also evident from the experiments. A three-dimensional population balance equation structure in terms of the particle size, binder content and porosity was confirmed to be an ideal framework for the process model. Further experiments were also performed for a fluid-bed and high-shear granulation system. Together with the drum granulation data, they were used for model validation purposes. Results showed that the mechanistic models were able to predict the evolutions/distributions for multiple granule properties. This is promising toward the long term goal of formulating a predictive dynamic population balance model, that is applicable for different granulation systems.

Sensitivity studies and Controllability analysis:

Subsequent to the implementation of the dynamic population balance model, a sensitivity study and a controllability analysis were performed. The sensitivity study highlighted the importance and uncertainties of certain parameters suggesting that accurate estimations would be required for these parameters. Prior to the controllability analysis, the model was compartmentalised for the purpose of a realistic controllability analysis taking into account

multiple controlled variables and manipulated inputs. Results elegantly depicted the issues associated with the controllability of the process, indicating that the size distribution width could not be controlled. Further open-loop step tests were performed and by means of an RGA analysis, various potential pairings were discarded and an optimal control-loop was identified. This has the potential to improve subsequent control of the granulation process.

Discrete element modelling:

There are different ways to arrive at mechanistic kernels. As an alternative to deriving mechanistic kernels based on fundamental properties, the effect of primary particle morphology on the spatial distribution of binder in wet granules was investigated by numerical simulations. Results have helped understand the effect of primary particle morphology on granule kinetics, which together with the effect of primary particle surface properties and binder properties makes it possible to establish linkages between material and process/design properties with granulation process behaviour.

9.2 Summary of Contributions

The primary contributions of the thesis are summarised below.

1. Theoretical development and formulation of a first-principles based mechanistic breakage kernel. Detailed simulations and tests were undertaken to qualify the validity of the derived kernel. Sensitivity studies were also performed to ascertain the important and influence of the various parameters.

2. Experimental studies in high-shear granulation. Multi-dimensional data were gathered for the purpose of quantitative validation of the breakage model.

3. Experimental studies in drum granulation. These studies were performed to investigate the growth kinetics of Calcite, liquid binder mal-distribution as well as to identify process sensitivities and suitable control configurations. Also to provide knowledge for scale-up purposes. Data obtained from characterisation of granule size distribution, binder content and porosity were used for model validation purposes.

4. Experimental studies in fluid-bed granulation. Data obtained were used to quantitatively validate a combined mechanistic model incorporating nucleation, aggregation, breakage and consolidation.

5. Implementation of the LAM/MPI framework on the dynamic population balance model to alleivate computational time.

6. Development of a continuous combined mechanistic population balance model for the purpose of a detailed controllability analysis taking into account multiple inputs and multiple-outputs.

7. Identification of an optimal control-loop pairing for the MIMO granulation process, in an attempt to rectify and improve the current state of granulation process control.

8. Implementation of an alternative methodology (ie., via discrete element modelling) to establish the effects of material and process/design properties on granulation behaviour.

9.3 Future Research

In the course of this research, several important recommendations are made, to be considered for future research. They are discussed below.

1. In the present work, experiments were carried out to validate the population balance model under different shear conditions (i.e., fluid-bed, drum and high-shear). Properties such as binder viscosity, binder content and drum load were varied to ascertain if the model could predict the new dynamics exhibited by the process. Future research directions could include performing more experiments to vary other properties such as surface tensions, impeller properties etc. and to use these results for model validation purposes.

2. The present population balance model incorporates mechanistic descriptions for nucleation, aggregation and breakage which are the key mechanisms of the granulation process. An empirical relation is used for the consolidation mechanism. Layering

and drying not considered. However, in the event of ambient temperature fluctuations, the drying phenomenon may assume importance and should be accounted for. Similarly, in a regime where the capillary forces are more dominant then the viscous forces, layering assumes importance and should be accounted for. In keeping with the mechanistic descriptions of nucleation, aggregation and breakage, mechanistic models could be derived for the cases of consolidation, layering and drying. This would then provide a holistic model based completely on the physics and chemistry of the granulation process. For instance, in deriving the layering model, the work of cohesion between solids should be one of the important parameters to be accounted for. For consolidation, liquid saturation is an important property and for drying. temperature gradients should be computed.

3. Another feature of the population model implemented in this research is that while it accounts for important granule properties such as size, binder content and porosity. it does not account for another important property such as composition. Composition is an important property that assumes importance for instance in the pharmaceutical industry where compounds generally consist of two or more solid components. This is a motivating factor to consider even higher-order PBE models for granulation problems. In the pharmaceutical industry, one also needs to know how a drug distributes in the granules. One of the common scale-up and operational issues in that industry is segregation: polydisperse granulations size-segregate during transfer to a tablet press. If the drug concentration is non-uniformly distributed across size fractions (quite typical), size segregation can lead to non-uniformity in the drug content of the tablets. This can and does lead to batch failure. Thus, the drug concentration distribution needs to be controlled along with particle size distribution. Using the population balance framework, a first approach would be to rewrite the density function as $F(s_1, s_2, l, g)$, where s_1 and s_2 indicate the different solid components in the mixture.

4. The present model assumes no variations in macroscopic variables (e.g. temperatures, stresses, velocity etc.) This is a valid assumption for small-scale granulators such as the ones studied in this research. In scaling up to the pilot-plant or industrial

scale it is important to formulate a formal link to the macro-scale phenomena in the granulator due to the dependence of the meso-scale processes on the macroscopic variables. There are multiple ways to connect the particle balance to macro-scale energy and momentum balances. One approach is to augment the current particle property list with additional terms for temperature and velocity, yielding an even higher order population balance equation. This may become computationally very difficult to solve. A compromise would be to have a compartmentalised model of a granulator with lumped parameters for stress, velocities, temperatures within each compartment and an exchange of particles between each compartment. Another option would be to incorporate the population balance model within a CFD environment.

5. Based on the results in chapter 7, future work could entail performing a controllability analysis and identification of optimal control-loop pairings at differing operating conditions. This would confirm if the obtained control-loop pairings are universal (i.e., independent of operating conditions). In the event that the pairings are not universal (i.e., they are different for different operating conditions), this would mean that different control schemes would be required at different operating conditions. Such knowledge would be useful to the engineer/operator when making any engineering decisions. Further to the identification of the control-loop pairings, a regulatory controller (e.g. PI) could be tuned based on the transfer function models. Thereafter the controller can be implemented on the first-principle model as a surrogate process. Effectiveness for set-point tracking and disturbance rejection can be shown. Positive results may indicate that advanced control (e.g. MPC) need not be implemented for the present lumped objectives.

List of Publications and Presentations

Refereed journal publications:

R. Ramachandran, C.D. Immanuel, F. Stepanek, James D. Litster and F.J. Doyle III., 2008,"Controllability Studies and Controller Design of Granulation Processes", Journal of Process Control. *In Preparation.*

R. Ramachandran, C.D. Immanuel, F. Stepanek, James D. Litster and F.J. Doyle III., 2008,"A Combined Mechanistic Population Balance Model in Fluid-Bed Granulation", AIChE Journal. *In Preparation.*

R. Ramachandran, C.D. Immanuel, F. Stepanek, James D. Litster and F.J. Doyle III., 2008,"A Mechanistic Model for Granule Breakage in Population Balances of Granulation: theoretical kernel development and experimental validation", Chemical Engineering Research and Design. *Accepted.*

T. Glaser, C.F.W. Sanders, F.Y. Wang, I.T. Cameron, J.D. Litster, J. Poon, R. Ramachandran, C.D. Immanuel, F.J. Doyle III., 2008, "Model Predictive Control of Continuous Drum Granulation", Journal of Process Control. *Accepted.*

J. Poon, R. Ramachandran, C. Sanders, T. Glaser. C.D. Immanuel, F.J. Doyle III. J.D. Litster, F. Stepanek, F.Y. Wang and I.T. Cameron., 2008. "Experimental Validation Studies on a Multi-Dimensional and Multi-Scale Population Balance Model of Batch Granulation", Chemical Engineering Science. *In Press.*

R. Ramachandran, J. Poon, C.F.W. Sanders, T. Glaser, C.D. Immanuel, F.J. Doyle III, J.D. Litster, F. Stepanek, F.Y. Wang and I.T. Cameron., 2008, "Experimental Studies on Distributions of Granule Size, Binder Content and Porosity in Batch Drum Granulation: Inferences on process modelling requirements and process sensitivities", Powder Technology, 188 (2), 89-101, 2008.

F. Stepanek, P. Rajniak, R. Chern, C. Mancinelli and R. Ramachandran.. 2008, "Distribution and accessibility of binder in wet granules", Powder Technology. *In press.*

Refereed conference proceedings:

R. Ramachandran, C. D. Immanuel, F. Stepanek, J. D. Litster and F. J. Doyle III., 2009. Experimental validation of a multi-dimensional population balance model incorporating breakage, in high-shear mixer granulation. Oral presentation, 13^{th} European Conference on Mixing, London, UK.

R. Ramachandran, J. Poon, F.J. Doyle III, J.D. Litster, F. Stepanek and C.D. Immanuel., 2007. A Mechanistic Model for the Nucleation and Aggregation Phenomena in Population Balances of Granulation. Oral presentation. International Conference on Modelling and Simulation (CITICOMS), Coimbatore, India.

R. Ramachandran, J. Poon, C.F.W. Sanders, T. Glaser, F.J. Doyle III, J.D. Litster. F. Stepanek, F.Y. Wang, I.T. Cameron and C.D. Immanuel., 2007. A Three-dimensional Population Balance Model of Granulation employing Mechanistic Kernels. Oral Presentation. 6th European Congress of Chemical Engineering, Copenhagen, Denmark.

Conference presentations:

R. Ramachandran, C D. Immanuel, J. D. Litster, F. J. Doyle III and F. Stepanek., 2008. A Combined Mechanistic Model for Nucleation, Aggregation and Breakage in a Population Balance Model of Granulation. Oral presentation. AIChE Annual Meeting. Philadelphia, USA.

T. Glaser, C.F.W. Sanders, F.Y. Wang, I.T. Cameron, J.D. Litster. J. Poon, R. Ramachandran, C.D. Immanuel and F.J. Doyle III,, 2007. Model Predictive Control of Continuous Drum Granulation of Limestone. Oral presentation. AIChE Annual Meeting, Salt Lake City, USA.

R. Ramachandran, J. Poon, C.F.W. Sanders, T. Glaser, F.J. Doyle III, J.D. Litster, F. Stepanek, F.Y. Wang, I.T. Cameron and C.D. Immanuel., 2007. A Mechanistic model for Nucleation and Aggregation in Population Balances of Granulation: Batch Characterisation Studies and Experimental Validation. Oral presentation. AIChE Annual Meeting, Salt Lake City, USA.

R. Ramachandran, J. Poon, C.F.W. Sanders, T. Glaser, F.J. Doyle III, J.D. Litster, F. Stepanek, F.Y. Wang, I.T. Cameron and C.D. Immanuel., 2007. A Three-dimensional Population Balance Model of Granulation with Mechanistic and Phenomenological Kernels. Oral Presentation. 3^{rd} International Conference on the Population Balance Modelling, Qubec city, Canada.

R. Ramachandran, J. Poon, F.J. Doyle III, J.D. Litster, F. Stepanek and C.D. Immanuel., 2007. Batch Characterisation Studies on Drum Granulation: Formulation Properties and Growth Kinetics. Poster presentation. Third International Granulation Workshop. University of Sheffield, Sheffield, UK.

R. Ramachandran, J. Poon, F. Stepanek, C.D. Immanuel, F.J. Doyle III, J.D. Litster and I.T. Cameron., 2006. A Mechanistic Kernel for Aggregation and Nucleation Phenomena in Population Balance Models of Granulation. Oral presentation. AIChE Annual Meeting, San Francisco, USA.

R. Ramachandran, J. Poon, F. Stepanek, C.D. Immanuel, F.J. Doyle III.. 2006. A Mechanistic Description of the Aggregation Phenomenon in Population Balance Models of Granulation. Oral presentation. Engineering Conferences International Control of Particulate Processes VII, Harrison Hot Springs, British Columbia, Canada.

R. Ramachandran, J. Poon, F. Stepanek, C.D. Immanuel, F.J. Doyle III, J.D. Litster and I.T. Cameron., 2006. A Mechanistic Kernel for Aggregation and Nucleation Phenomena in Population Balance Models of Granulation. Poster presentation. 12^{th} UK Particle Technology Forum, London, UK.

F. Stepanek, P. Rajniak, R. Chern, C. Mancinelli and R. Ramachandran., 2006. Modeling of multi-component granule formation in a wet granulation process. Oral presentation. Fifth World Congress on Particle Technology, Lake Buena Vista, Florida, USA.

Bibliography

Abberger, T., 2001. The effect of powder type, free moisture and deformation behaviour of granules on the kinetics of fluid-bed granulation. European Journal of Pharmaceutics and Biopharmaceutics 52, 327–336.

Adetayo, A. A., Ennis, B. J., 1997. A unifying approach to modeling coalescence mechanisms. AIChE Journal 43, 927–934.

Adetayo, A. A., Ennis, B. J., 2000. A new approach to modeling granulation processes for simulation and control purposes. Powder Technology 108, 202–209.

Adetayo, A. A., Litster, J. D., Cameron, I. T., 1995. Steady state modelling and simulation of a fertilizer granulation circuit. Computers and Chemical Engineering 19, 383–393.

Adetayo, A. A., Litster, J. D., Desai, M., 1993. The effect of process parameters on drum granulation of fertilizers with broad size distributions. Chemical Engineering Science 48, 3951–3961.

Adler, P. M., Thovert, J. F., 1998. Real porous media: Local geometry and macroscopic properties. Appl. Mech. Rev 51, 537–585.

Alhamad, B., Romagnoli, J. A., Gomes, V. G., 2005. On-line multi-variable predictive control of molar mass and particle size distributions in free-radical emulsion copolymerization. Chemical Engineering Science 60, 6596–6606.

Allen, T., 1997. Particle size measurement volume 1: Powder sampling and particle size measurement. Chapman & Hall.

Andreani, P. A., Benezet, J. C., Garcia-Diaz, E., Siwak, J. M., Benhassaine, A., 2003. Granular self-organization and reactivity - adsorbates and agglomerates particle size influence. Powder Technology 130, 84–90.

Annapragada, A., Neilly, J., 1996. On the modelling of granulation processes: a short note. Powder Technology 89, 83–84.

Bardin, M., Knight, P. C., Seville, J. P. K., 2004. On control of particle size distribution in granulation using high shear mixers. Powder Technology 140, 169–175.

Barrett, P., Smith, B., Worlitschek, J., Bracken, V., O'Sullivan, B., O'Grady, D., 2005. A review of the use of process analytical technology for the understanding and optimization of production batch crystallization processes. Organic Process Research and Development 9, 348–355.

Bhattacharya, A., Ray, P., 2004. Studies on surface tension of poly (vinyl alcohol): Effect of concentration, temperature and addition of chaotropic agents. Journal of Applied Polymer Science 93, 122–130.

Biggs, C. A., Sanders, C., Scott, A. C., Willemse, A. W., Hoffman, A. C., Instone, T., Salman, A. D., Hounslow, M. J., 2003. Coupling granule properties and granulation rates in high shear granulation. Powder Technology 130, 162–168.

Blandin, A. F., Mangin, D., Rivoire, A., Klein, J. P., Bossoutrot, J. M., 2003. Agglomeration in suspension of salicyclic acid particles: influence of some process parameters on kinetics and agglomerate final size. Powder Technology 130, 316–323.

Boerefijn, R., Hounslow, M. J., 2005. Studies of fluid-bed granulation in an industrial r and d context. Chemical Engineering Science 60, 3879–3890.

Cameron, I. T., Wang, F. Y., Immanuel, C. D., Stepanek, F., 2005. Process systems modelling and applications in granulation: A review. Chemical Engineering Science 60, 3723–3750.

Capes, C. E., Danckwents, P. V., 1967. Granule formation by the agglomeration of damp particles: Part 1. the mechanism of granule growth. Transactiona of the Institute of Chemical Engineering 43, 116–124.

Chakravarthi, S., Ray, W. H., 1999. Boundary identification and control of distributed parameter systems using singular functions. Chemical Engineering Science 54, 1181 1204.

Christofides, P. D., 2001. Control of nonlinear distributed process systems: Recent development and challenges. AIChE Journal 47, 514–518.

Christofides, P. D., 2002. Control of nonlinear distributed parameter systems: An overview and new research directions. AIChE Journal 54, 341–346.

Coelho, D., Thovert, J. F., Adler, P. M., 1997. Geometrical and transport properties of random packings of spheres and aspherical particles. Phys. Rev. E 55, 1959–1977.

D. M. Newitt, J. M. C.-J., 1958. A contribution to the theory and practice of granulation. Trans. I. Chem. Eng 36, 422–441.

Darelius, A., Rasmuson, A., Bjorn, I. N., Folestad, S., 2005. High shear wet granulation modelling - a mechanistic approach using population balances. Powder Technology 160, 209–218.

Denesuk, M., Smith, G. L., Zelinski, B. J. J., Kreidl, N. J., Uhlman, D. R., 1993. Capillary penetration of liquid droplets into porous materials. Journal of Colloid Interface Science 158, 114–120.

Denn, M. M., 1986. Process Modelling. Longman Scientifc and Technical.

Dhanarajan, A. P., Bandyopadhyay, R., 2007. An energy-based population-balance approach to model granule growth in high-shear wet granulation processes. AIChE Journal 43, 927–934.

Dokucu, M. T., Park, M. J., Doyle III, F. J., 2008a. Multi-rate model predictive control of particle size distribution in a semibatch emulsion copolymerization reactor. Journal of Process Control 18, 105–120.

Dokucu, M. T., Park, M. J., Doyle III, F. J., 2008b. Reduced-order methodologies for feedback control of particle size distribution in semi-batch emulsion copolymerization. Chemical Engineering Science 63, 1230–1245.

Eek, R. A., Bosgra, O. H., 2000. Controllability of particulate processes in relation to sensor characteristics. Powder Technology 108, 137–146.

Eliasen, H., Schaefer, T., Kristensen, H., 1998. Effects of binder rheology on melt agglomeration in a high shear mixer. International Journal of Pharmaceutics 176, 73–83.

Ennis, B. J., Litster, J. D., 1997. Particle size enlargement. In: Perry's Chemical Engineering Handbook.

Ennis, B. J., Tardos, G., Pfeffer, R., 1991. A microlevel-based characterization of granulation phenomena. AIChE Journal 46, 529–539.

Faure, A., Grimsey, I. M., Rowe, R. C., York, P., Cliff, M. J., 1999. Applicability of a scale-up methodology for wet granulation processes in collette gral high shear mixer-granulators. European Journal of Pharmaceutical Sciences 8, 85–93.

Faure, A., York, P., Rowe, R. C., 2001. Process control and scale-up of pharmaceutical wet granulation processes: a review. European Journal of Pharmaceutics and Biopharmaceutics 52, 269–277.

Fevotte, F., Doyle III, F. J., 2005. Sensitivity analysis of multi-regime population balance model for control of multiple particulate properties in granulation. In: American Control Conference.

Gantt, J. A., Gatzke, E. P., 2006. A stochastic technique for multidimensional granulation modelling. AIChE Journal 52, 3067–3077.

Gatzke, E. P., 2001. Model predictive control of a granulation system using soft output constraints and prioritized control objectives. Powder Technology 121, 149–158.

Gay, D. H., Ray, W. H., 1995. Identification and control of distributed parameter systems by means of singular value decomposition. Chemical Engineering Science 50, 1519–1539.

Glaser, T., Sanders, C. F. W., Wang, F. Y., Cameron, I. T., Ramachandran, R., Litster, J. D., Poon, J. M. H., Immanuel, C. D., Doyle III, F. J., 2008. Model predictive control of drum granulation. Accepted in Journal of Process Control.

Gradinarsky, L., Brage, H., Lagerholm, B., Niklasson, I. N., Folestad, S., 2006. *In situ* monitoring and control of moisture content in pharmaceutical powder processes using an open-ended coaxial probe. Measurement Science and Technology 17, 1847–1853.

Hangos, K., Cameron, I. T., 2001. Process Modelling and Model Analysis. Academic Press.

Hapgood, K. P., 2000. Nucleation and binder distribution in wet granulation. Ph.D. thesis. The University of Queensland.

Hapgood, K. P., Litster, J. D., Biggs, S., Howes, T., 2002. Drop penetration into porous powder beds. Journal of Colloids and Interfacial Science 253, 353–366.

Heinrich, S., Peglow, M., Ihlow, M., Morl, L., 2003. Particle population modeling in fluidized bed-spray granulation - analysis of the steady state and unsteady behaviour. Powder Technology 130, 154–161.

Hemati, M., Cherif, R., Saleh, K., Pont, V., 2003. Fludized bed coating and granulation: influence of process-related variables and physiochemical properties on the growth kinetics. Powder Technology 130, 18–34.

Hogekamp, S., Pohl, M., 2003. Porosity measurements of fragile agglomerates. Powder Technology 130, 385–392.

Hoornaert, F., Wauters, P. A. L., Meesters, G. M. H., Pratsinis, S. E., Scarlett, B., 1998. Agglomeration behaviour of powders in a lodige mixer granulator. Powder Technology 96, 116–128.

Hotta, K., Takeda, K., Iinoya, K., 1974. The capillary binding force of a liquid bridge. Powder Technology 10, 231–242.

Hounslow, M. J., 1998. The population balance as a tool for understanding particle rate processes. KONA 16, 179–193.

Immanuel, C. D., Doyle III, F. J., 2003a. Computationally efficient solution of population balance models incorporating nucleation, growth and coagulation: application to emulsion polymerization. Chemical Engineering Science 52, 3681–3698.

Immanuel, C. D., Doyle III, F. J., 2003b. Heirarchical multiobjectitve strategy for particle-size distribution control. AIChE Journal 49, 2383–2399.

Immanuel, C. D., Doyle III, F. J., 2005. Solution technique for a multi-dimensional population balance model describing granulation processes. Powder Technology 156, 213–225.

Ingram, G. D., Cameron, I. T., Hangos, K. M., 2004. Classification and analysis of integrating frameworks in multiscale modelling. Chemical Engineering Science 59, 2171–2187.

Iveson, S. M., 2002. Limitations of one-dimensional population balance models of wet granulation processes. Powder Technology 124, 219–229.

Iveson, S. M., Holt, S., Biggs, S. R., 2000. Contact angle measurement of iron ore powders. Colloids and surfaces A: Physiochemical and engineering aspects 166, 203–214.

Iveson, S. M., Litster, J. D., 1998a. Growth regime map for liquid-bound granules. AIChE Journal 113, 1510–1518.

Iveson, S. M., Litster, J. D., 1998b. Liquid-bound granule impact deformation and coefficient of restitution. Powder Technology 99, 234–242.

Iveson, S. M., Litster, J. D., Ennis, B. J., 1996. Fundamental studies of granule consolidation part 1: Effects of binder contents and binder viscosities. Powder Technology 88, 15–20.

Iveson, S. M., Litster, J. D., Ennis, B. J., 1998. Fundamental studies of granule consolidation. part 2. quantifying the effects of particle and binder properties. Powder Technology 99, 243–250.

Iveson, S. M., Litster, J. D., Hapgood, K. P., Ennis, B. J., 2001. Nucleation, growth and breakage phenomena in agitated wet granulation processes: a review. Powder Technology 117, 3–39.

Iveson, S. M., Page, N. W., 2005. Dynamic strength of liquid-bound granular materials: The effect of particle size and shape. Powder Technology 152, 79–89.

Iveson, S. M., Page, N. W., Litster, J. D., 2003. The importance of wet-powder dynamics mechanical properties in understanding granulation. Powder Technology 130, 97–101.

Johansen, A., Schaefer, T., 2001. Effects of interactions between powder particle size and binder viscosity on agglomerate growth mechanisms in a high shear mixer. European Journal of Pharmaceutical Sciences 12, 297–305.

Kalani, A., Christofides, P. D., 2002. Simulation, estimation and control of size distribution in aerosol processes with simultaneous reaction, nucleation, condensation and coagulation. Chemical Engineering Science 26, 1153–1169.

Kenningley, S. T., Knight, P. C., Marson, A. D., 1997. An investigation into the effects of binder viscosity on agglomeration behaviour. Powder Technology 91, 95–103.

Knight, P., 2004. Challenges in granulation technology. Powder Technology 140, 156–162.

Knight, P. C., 1993. An investigation into the kinetics of granulation using a high shear mixer. Powder Technology 77, 159–169.

Knight, P. C., 2001. Structuring agglomerated products for improved performance. Powder Technology 119, 14–25.

Knight, P. C., Instone, T., Pearson, J. M. K., Hounslow, M. J., 1998. An investigation into the kinetics of liquid distribution and growth in high shear mixer agglomeration. Powder Technology 97, 246–257.

Knight, P. C., Johansen, A., Kristensen, H. G., Schaefer, T., Seville, J. P. K., 2000. An investigation of the effects of agglomeration of changing the speed of a mechanical mixer. Powder Technology 110, 204–209.

Kosek, J., Stepanek, F., Marek, M., 2005. Modelling of transport and transformation processes in porous and multi-phase bodies. Adv. Chem. Eng 30, 137–203.

Kostoglou, M., Kostandopoulos, A. G., Friedlander, S. K., 2006. Bivariate population dynamics simulation of fractal aerosol aggregate coagulation and restructuring. Journal of Aerosol Science 37, 1102–1115.

Kou, B., McAuley, K. B., Hsu, C. C., Bacon, D. W., Yao, K. Z., 2005. Mathematical model and parameter estimation for gas-phase ethylene homopolymerization with supported metallocene catalyst. Industrial Engineering Chemistry Research 44, 2428–2442.

Kristensen, H. G., 1996. Particle agglomeration in high shear mixers. Powder Technology 88, 197–202.

Kristensen, H. G., Holm, P., Schaefer, T., 1985. Mechanical properties of moist agglomeration in relation to granulation mechanisms part 2: effects of particle size distribution. Powder Technology 44, 239–247.

Leuenberger, H., Betz, G., 2007. Granulation process control - production of pharmaceutical granules: The classical batch concept and the problem of scale-up. Granulation.

Lian, G., Thornton, C., Adams, M. J., 1993. A theoretical study of the liquid bridge forces between two rigid spherical bodies. Journal of Colloid Interface Science 161, 138–147.

Litster, J. D., 2003. Scaleup of wet granulation processes: science not art. Powder Technology 130, 35–40.

Litster, J. D., Ennis, B. J., 2004. The Science and Engineering of Granulation Processes. Kluvwer Academic Publishers.

Litster, J. D., Hapgood, K. P., Michaels, J. N., Sims, A., Roberts, M., Kameneni, S. K., Hsu, T., 2001. Liquid distribution in wet granulation: dimensionless spray flux. Powder Technology 114, 32–39.

Liu, L. X., Litster, J. D., 2002. Population balance modelling of granulation with a physically based coalescence kernel. Chemical Engineering Science 57, 2183–2191.

Liu, L. X., Litster, J. D., Iveson, S. M., Ennis, B. J., 2000. Coalescence of deformable granules in wet granulation processes. AIChE Journal 46, 529–539.

Liu, L. X., Smith, R., Litster, J. D., 2008. Wet granule breakage in a breakage only high-shear mixer: Effect of formulation properties on breakage behaviour. Powder Technology, In press.

Liu, Y., Cameron, I. T., 2003. A new wavelet-based adaptive method for solving population balance equations. Powder Technology 130, 181–188.

Luding, S., Clement, E., Blumen, A., Rajchenbach, J., Duran. J.. 1994. Anomalous energy dissipation in molecular-dynamics simulations of grains: The "detachment" effect. Physical Review E 50, 4113–4124.

Ma, D. L., Tafti, D. K., Braatz, R. D., 2002. High resolution simulation of multidimensional crystallization. Industrial Engineering Chemistry 41, 6217–6223.

Madec, L., Falk, L., Plasari, E., 2003. Modelling of the agglomeration in suspension process with multidimensional kernels. Powder Technology 130, 147–153.

Mantzaris, N. V., Daoutidis, P., Srienc, F., 2001. Numerical solution of multi variable cell population balance models: 3. finite difference methods. Computers and Chemical Engineering 25, 1463–1481.

Micheals, J. N., 2003. Toward rational design of powder processes. Powder Technology 138, 1–6.

Mort, P. R., 2005. Scaleup of binder agglomeration processes. Powder Technology 150. 86–103.

Mort, P. R., Capeci, S. W., Holder, J. W., 2001. Control of agglomerate attributes in a continuous binder-aggolomeration process. Powder Technology 117. 173–176.

Mort, P. R., Tardos, G., 1999. Scale-up of agglomeration processes using transformations. Kona 17, 64–75.

Moura, M. J., Ferreira, P. J., Figueiredo, M. M., 2005. Mercury intrusion porosimetry in pulp and paper technology. Powder Technology 160, 61–66.

Ogawa, S., Kamijima, T., Miyamoto, Y., Miyajima, M., Sato, H., Takayama, K., Nagai. T., 1994. A new attempt to solve the scale-up problem for granulation using response surface methodology. Journal of Pharmaceutical Science 83, 439–443.

Ogunnaike, B. A., Ray, W. H., 1994. Process Dynamics, Modeling and Control. Oxford University Press.

Pandya, J. D., Spielman, L. A., 1983. Floc breakage in agitated suspensions: effect of agitation rate. Chemical Engineering Science 38, 1983–1992.

Pearson, J. M. K., Hounslow, M. J., Instone, T., Knight, P. C., 1998. Granulation kinetcis: the confounding of particle size and age. In: World Congress on Particle Technology.

Pinto, M. A., 2008. Modelling and control of biological systems. Ph.D. thesis, Imperial College London.

Pinto, M. A., Immanuel, C. D., Doyle III, F. J., 2007. A feasible solution technique for higher-dimensional population balance models. Computers and Chemical Engineering 31, 1242–1256.

Pinto, M. A., Immanuel, C. D., Doyle III, F. J., 2008. A two-level discretisation algorithm for the efficient solution of higher-dimensional population balance models. Chemical Engineering Science 63, 1304–1314.

Poon, J. M. H., 2008. A three-dimensional population balance model of granulation processes employing mechanistic kernels. Ph.D. thesis, Imperial College London.

Poon, J. M. H., Immanuel, C. D., Doyle III, F. J., Litster, J. D., 2008. A three-dimensional population balance model of granulation with a mechanistic representation of the nucleation and aggregation phenomena. Chemical Engineering Science 63, 1315–1329.

Portoghese, F., Berruti, F., Briends, C., 2008. Continuous on-line measurement of solid moisture content during fluidized bed drying using triboelectric probes. Powder Technology 181, 169–177.

Pottman, M., Ogunnaike, B. A., Adetayo, A. A., Ennis, B. J., 2000. Model-based control of a granulation system. Powder Technology 165, 1–10.

Princen, H. M., 1968. The effects of capillary liquid on the force of adhesion between spherical particles. Journal of Colloid Interface Science 26, 247–253.

Rajniak, P., Fox, R. O., Dhanasekharan, K., Stepanek, F., Chern, R., 2006. Solution of population balance equations for wet granulation. In: Fifth World Congress on Particle Technology.

Rajniak, P., Mancinell, C., Chern, R., Štěpánek, F., Farber. L.. Hill. B.. 2007. Experimental study of wet granulation in fluidized bed: Impact of the binder properties on the granule morphology. Int. J. Pharm 334, 92–102.

Rajniak, P., Štěpánek, F., Dhanasekharan, K., Fan, R., Mancinelli, C.. Chern, R., 2008. A combined experimental and computational study of wet granulation in a wurster fluid-bed granulator. Powder Technology In Press.

Ramaker, J. S., Jelgersma, M. A., Vonk, P., Kossen, N. W. F.. 1998. Scale-down of a high shear pelletisation process: flow profile and growth kinetics. Int J. Pharm 166. 89–97.

Rambali, B., Baert, L., Massart, D. L., 2003. Scaling up of the fluidized bed granulation process. International Journal of Pharmaceutics 252, 197–206.

Ramkrishna, D., 2000. Population Balances. Academic Press, San Diego.

Reynolds, G. K., Biggs, C. A., Salman, A. D., Hounslow, M. J., 2004. Non-uniformity of binder distribution in high-shear granulation. Powder Technology 140, 203–208.

Reynolds, G. K., Fu, J. S., Cheong, Y. S., Hounslow, M. J., Salman, A. D., 2005. Breakage in granulation: A review. Chemical Engineering Science 60, 3969–3992.

Reynolds, G. K., Le, P. K., Nilpawar, A. M., 2007. High shear granulation. Handbook of powder technology 11, 3–19.

Rider, W. J., Kothe, D. B., 1998. Reconstructing volume tracking. J. Comput. Phys 141, 112–152.

Saleh, K., Steinmetz, D., Hemati, M., 2003. Experimental study and modeling of fluidized bed coating and agglomeration. Powder Technology 130, 116–123.

Salman, A. D., Fu, J., Gorham, D. A., Hounslow, M. J., 2003. Impact breakage of fertiliser granules. Powder Technology 130, 359–366.

Sanders, C. F. W., Willemse, A. W., Salman, A. D., Hounslow, M. J., 2003. Development of a predictive high-shear granulation model. Powder Technology 138, 2003.

Sastry, K. V. S., 1975. Similarity size distribution of agglomerates during their growth by coalescence in granulation or green pelletization. International Journal of Mineral Processing 2, 187–203.

Sastry, K. V. S., Fuerstenau, D. W., 1973. Mechanisms of agglomerate growth in green pelletization. Powder Technology 7, 97–105.

Schaefer, T., 2001. Growth mechanisms in melt agglomeration in high shear mixers. Powder Technology 117, 68–82.

Schaefer, T., Holm, P., Kristensen, H. G., 1990. Wet granulation in a laboratory scale high shear mixer. Pharm Ind 52, 1147–1153.

Schaefer, T., Mathiesen, C., 1996. Melt pelletization in a high shear mixer: Effects of binder particle size. Int. J. Pharm 139, 139–148.

Scott, A. C., Hounslow, M. J., Instone, T., 2000. Direct evidence of heterogeneity during high-shear granulation. Powder Technology 113, 205–213.

Selomuya, C., Bushell, G., Amal, R., Waite, T. D., 2003. Understanding the role of restructuring in flocculation: the application of a population balance model. Chemical Engineering Science 58, 327–338.

Semino, D., Ray, W. H., 1995a. Control of systems described by population balance equations - i. controllability analysis. Chemical Engineering Science 50, 1805–1824.

Semino, D., Ray, W. H., 1995b. Control of systems described by population balance equations - ii. emulsion polymerization with constrained control action. Chemical Engineering Science 50, 1805–1824.

Shi, D., Mhaskar, P., El-Farra, N. H., Christofides, P. D., 2005. Predictive control of crystal size distribution in protein crystallisation. Nanotechnology 16, 562–574.

Simons, S. J. R., 2007. Granulation Handbook of Powder Technology, eleventh Edition. Elsevier, pp. 1256–1351.

Simons, S. J. R., Seville, J. P. K., Adams, M. J., 1994. An analysis of the rupture energy of pendular liquid bridges. Chemical Engineering Science 49, 2331–2339.

Smit, D. J., Hounslow, M. J., Newman, R., Paterson, W. R., 1995. Aggregation and gelation. 3. numerical classification of kernels and case studies of aggregation and growth. Chemical Engineering Science 50, 1025–1035.

Smith, M., Matsoukas, T., 1998. Constant-number monte carlo simulation of population balances. Chemical Engineering Science 53, 1777–1786.

Smith, R., 2008. Wet granule breakage in high shear mixer granulators. Ph.D. thesis, University of Queensland.

Soos, M., Sefcik, J., Morbidelli, M., 2006. Investigation of aggregation, breakage and restructuring kinetics of colloidal dispersions in turbulent flows by population balance modeling and light scattering. Chemical Engineering Science 61, 2349–2363.

Stachowiak, G. W., Batchelor, A. W., 2005. Engineering Tribology. Cambridge University Press.

Stepanek, F., Ansari, M. A., 2005. Computer simulation of microstructure formation. Chemical Engineering Science 60, 4019–4029.

Stepanek, F., Rajniak, P., 2006. Droplet morphologies on particles with macroscopic surface roughness. Langmuir 22, 917–923.

Stepanek, F., Rajniak, P., Chern, R., Mancinelli, C., Ramachandran, R., 2006. Modeling of multi-component granule formation in a wet granulation process. In: Fifth World Congress on Particle Technology.

Stepanek, F., Rajniak, P., Mancinelli, C., Chern, R. T., Ramachandran, R., 2008. Distribution and accessibility of binder in wet granules. Powder Technology. In press.

Subero-Couroyer, C., Mangin, D., Rivoire, A., Blandin, A. F., Klein, J. P., 2006. Agglomeration in suspension of salicylic acid fine particles: Analysis of the wetting period and effect of binder injection mode on the final aggolomeration size. Powder Technology 161, 98–109.

Tan, H. S., Salman, A. D., Hounslow, M. J., 2004. Kinetics of fluidised bed melt granulation iv: Selecting the breakage model. Powder Technology 143-144, 65–83.

Tan, H. S., Salman, A. D., Hounslow, M. J., 2005. Kinetics of fluidised bed granulation v: Simultaneous modelling of aggregation and breakage. Chemical Engineering Science 60, 3847–3866.

Tan, H. S., Salman, A. D., Hounslow, M. J., 2006. Kinetics of fluidized bed granulation - i: The effect of process variables. Chemical Engineering Science 61, 1585–1601.

Tardos, G. I., Irfan-Khan, M., Mort, P. R., 1997. Critical parameters and limiting conditions in binder granulation of fine powders. Powder Technology 98, 245–258.

Thielmann, F., Naderi, M., Ansari, M., Štěpánek, F., 2008. The effect of primary particle surface energy on agglomeration rate in fluidised-bed wet granulation. Powder Technology In Press.

Tzou, H. S., Bergman, L. A., 1998. Dynamics and control of distributed systems. Cambridge University Press.

Van den Dries, K., de Vegt, O. M., Girard, V., Vromans, H., 2003. Granule breakage phenomena in a high shear mixer; influence of process and formulation variables and consequences on granule homogeneity. Powder Technology 133, 228–236.

Verkoeijen, D., Pouw, G. A., Meesters, G. M. H., Scarlett, B., 2002. Population balances for particulate processes - a volume approach. Chemical Engineering Science 57, 2287–2303.

Vonk, P., Guillaume, C. P. F., Ramaker, J. S., Vromans, H., Kossen, N. W. F., 1997. Growth mechanism for high-shear pelletization. Int. J. Pharm 157, 93–102.

Štěpánek, F., Šoóš, M., Rajniak, P., 2007. Characterization of porous media by the virtual capillary condensation method. Coll. Surf. A Physicochem. Eng. Asp 300, 11–20.

Walker, G. M., Andrews, G., Jones, D., 2006. Effect of process parameters on the melt granulation of pharmaceutical powders. Powder Technology 165, 161–166.

Wang, F. Y., 2007. A multi-form modelling approach to the dynamics and control of drum granulation processes. Powder Technology 179, 2–11.

Wang, F. Y., Cameron, I. T., 2002. Review and future directions in the modelling and control of continuous drum granulation. Powder Technology 124. 238–253.

Wang, W., 2006. Image analysis of particles by modified ferret method - best fit rectangle. Powder Technology 165, 1–10.

Watano, S., 2001. Direct control of wet granulation processes by image processing system. Powder Technology 117, 163–172.

Watano, S., Miyanami, K., 1995. Image processing for on-line monitoring of granule size distribution and shape in fluidized bed granulation. Powder Technology 83, 55-60.

Watano, S., Numa, T., Koizumi, I., Osako, Y., 2001. Feedback control in high shear granulation of pharmaceutical powders. European Journal of Pharmaceutics and Biopharamceutics 52, 337–345.

Wauters, P. A. L., 2000. Modelling and mechanisms of granulation. Ph.D. thesis. Delft University of Technology.

Wehrle, P., Nobelis, P., Cuine, A., Stamm, A., 1993. Scaling-up of wet granulation. a statistical methodology. Drug Development and Industrial Pharmacy 19, 1983–1997.

Wilderboer, W. J., 2002. Design and operation of regime seperated granulators. Ph.D. thesis, The University of Queensland.

Willett, C. D., Johnson, S. A., Adams, M. J., Seville, J. P. K., 2007. Granulation Handbook of Powder Technology, eleventh Edition. Elsevier, pp. 1316–1351.

Yu, A. B., Feng, C. L., Zou, R. P., Yang, R. Y., 2003. On the relationship between porosity and interparticle forces. Powder Technology 130, 70–76.

Yu, Z. Q., Chew, J. W., Chow, P. S., Tan, R. B. H., 2007. Recent advances in crystallization control. Chemical Engineering Research and Design 85, 893–905.

Zhang, J., Litster, J. D., Wang, F. Y., Cameron, I. T., 2000. Evaluation of control strategies for fertiliser granulation circuits using dynamic simulation. Powder Technology 108. 122–129.

Zheng, D., Hoo, K. A., 2004. System identification and model-based control for distributed processes. Computers and Chemical Engineering 28, 1361–1375.

Zou, R. P., Xu, J. Q., Feng, C. L., Yu, A. B., Johnston, S., Standish, N., 2003. Packing of multi-sized mixtures of wet coarse spheres. Powder Technology 130, 77–83.

Appendix A

Batch Drum Granulation Data

Batch granulation experiments were carried out on a laboratory scale batch drum rotary granulator. The granulation recipe consisted of limestone powder (Aglime. Landmark, Australia) with a binder solution of 2% polyvinyl alcohol (PVOH) (Elvanol T66. Du Pont, USA). Granulation experiments pertaining to each of the binder-to-solids ratio and the amount of powder loaded into the drum granulator were performed on a single basis. For each of the experiments, steps were taken to ensure that for cases where the same amount of powder was to be granulated (*i.e.* varying only the binder-to-solids ratio whilst keeping the amount of powder used for granulation fixed). A calibrated balance was used to weigh 1.5 kg and 1.75 kg of powder for each experiment. The delivery of the liquid binder was via a pressure pot arrangement attached to a flat-fan spray nozzle. Consistency with respect to maintaining the pressure was determined by the laboratory supply taps. The choice in using a binder solution with concentration of 2.5% w/w provided a good balance in terms of providing continuous spray without incurring nozzle blockages and granulation.

A scoop sampling procedure was used in the experiments. The method involves plunging a scoop into the tumbling powder bed and extracting the sample. A particular feature of this method that was not conducive to accurate sampling was, to ensure an equal likelihood of all particles in the tumbling powder being sampled. It was observed via visual inspection that, larger granules tended to move towards the periphery of the drum interior whilst smaller granules remained near the center of the powder bed. To account for for this, six sub-samples were taken from different locations on the powder bed These six sub-samples

were pooled together to form representative sample of the powder bed for a particular time instant. Processing conditions pertaining to the granule samples after extraction from the drum granulator, such as the drying time in the oven and the duration on the sieve shaker were maintained for all granulation experiments. The consistency in the procedures used for the granulation experiments pertaining to the sampling method, binder flow rate, drum filling and the post analysis of the samples helped to ensure minimising errors. In retrospect, a minimum of three experiments would need to be carried out for each granulation condition for demonstration of reproducibility.

Table A.1: Normalised GSD for binder-to-solids ratio of 0.11 and 1.5 kg of powder–Set 1.

No.	Sieve fraction (μm)	t = 3 min	t = 5 min	t = 10 min	t = 15 min
1	< 250	0.746	0.713	0.598	0.518
2	$250 - 300$	0.081	0.078	0.095	0.091
3	$300 - 355$	0.021	0.021	0.025	0.021
4	$355 - 420$	0.017	0.008	0.015	0.015
5	$420 - 500$	0.015	0.015	0.014	0.015
6	$500 - 600$	0.013	0.013	0.013	0.013
7	$600 - 710$	0.010	0.010	0.010	0.010
8	$710 - 850$	0.002	0.002	0.021	0.020
9	$850 - 1000$	0.080	0.120	0.172	0.170
10	$1000 - 1180$	0.004	0.013	0.035	0.122
11	$1180 - 1400$	0.006	0.004	0.001	0.003
12	$1400 - 1700$	0.005	0.003	0.001	0.002

Table A.2: Normalised GSD for binder-to-solids ratio of 0.11 and 1.5 kg of powder–Set 2.

No.	Sieve fraction (μm)	t = 3 min	t = 5 min	t = 10 min	t = 15 min
1	< 250	0.778	0.717	0.603	0.503
2	$250 - 300$	0.073	0.084	0.097	.0101
3	$300 - 355$	0.019	0.019	0.029	0.018
4	$355 - 420$	0.010	0.011	0.012	0.017
5	$420 - 500$	0.012	0.012	0.018	0.013
6	$500 - 600$	0.012	0.010	0.016	0.011
7	$600 - 710$	0.008	0.012	0.011	0.012
8	$710 - 850$	0.001	0.004	0.028	0.023
9	$850 - 1000$	0.077	0.112	0.157	0.166
10	$1000 - 1180$	0.002	0.013	0.027	0.129
11	$1180 - 1400$	0.005	0.002	0.001	0.004
12	$1400 - 1700$	0.003	0.004	0.001	0.003

Table A.3: Normalised GSD for binder-to-solids ratio of 0.11 and 1.5 kg of powder–Set 3.

No.	Sieve fraction (μm)	t = 3 min	t = 5 min	t = 10 min	t = 15 min
1	< 250	0.764	0.699	0.589	0.509
2	$250 - 300$	0.080	0.085	0.088	0.093
3	$300 - 355$	0.021	0.021	0.022	0.020
4	$355 - 420$	0.015	0.015	0.017	0.015
5	$420 - 500$	0.015	0.014	0.015	0.016
6	$500 - 600$	0.013	0.011	0.013	0.013
7	$600 - 710$	0.010	0.014	0.014	0.012
8	$710 - 850$	0.002	0.002	0.031	0.020
9	$850 - 1000$	0.067	0.104	0.170	0.169
10	$1000 - 1180$	0.002	0.028	0.039	0.125
11	$1180 - 1400$	0.006	0.005	0.001	0.005
12	$1400 - 1700$	0.006	0.002	0.001	0.003

Table A.4: Granule porosity for binder-to-solids ratio of 0.11 and 1.5 kg of powder–Set 1.

No.	Sieve fraction (μm)	t = 3 min	t = 5 min	t = 10 min	t = 15 min
1	< 250	0.149	0.146	0.139	0.139
2	$300 - 355$	0.148	0.145	0.139	0.139
3	$420 - 500$	0.147	0.144	0.136	0.135
4	$500 - 600$	0.146	0.141	0.134	0.129
5	$850 - 1000$	0.141	0.136	0.131	0.125
6	$1180 - 1400$	0.138	0.134	0.128	0.122

Table A.5: Granule porosity for binder-to-solids ratio of 0.11 and 1.5 kg of powder–Set 2.

No.	Sieve fraction (μm)	t = 3 min	t = 5 min	t = 10 min	t = 15 min
1	< 250	0.149	0.145	0.139	0.139
2	$300 - 355$	0.148	0.145	0.138	0.139
3	$420 - 500$	0.146	0.144	0.135	0.135
4	$500 - 600$	0.145	0.140	0.134	0.130
5	$850 - 1000$	0.140	0.136	0.130	0.125
6	$1180 - 1400$	0.137	0.135	0.127	0.121

Table A.6: Granule porosity for binder-to-solids ratio of 0.11 and 1.5 kg of powder–Set 3.

No.	Sieve fraction (μm)	t = 3 min	t = 5 min	t = 10 min	t = 15 min
1	< 250	0.149	0.145	0.140	0.139
2	$300 - 355$	0.148	0.144	0.138	0.139
3	$420 - 500$	0.147	0.144	0.136	0.135
4	$500 - 600$	0.145	0.140	0.133	0.129
5	$850 - 1000$	0.140	0.136	0.131	0.125
6	$1180 - 1400$	0.137	0.135	0.127	0.122

Table A.7: Fractional binder content of granules for target binder-to-solids ratio of 0.11 with 1.5 kg of powder–Set 1.

No.	Sieve fraction (μm)	t = 3 min	t = 5 min	t = 10 min	t = 15 min
1	< 250	5.6	8.3	6.1	5.9
2	$250 - 300$	6.4	9.3	7.7	6.7
3	$300 - 355$	7.5	-	8.1	-
4	$355 - 420$	7.7	10.6	8.3	7.4
5	$420 - 500$	-	10.7	8.4	7.9
6	$500 - 600$	6.8	10.4	7.9	7.8
7	$600 - 710$	7.9	11.1	8.4	9.3
8	$710 - 850$	8.1	11.2	8.9	8.9
9	$850 - 1000$	7.3	11.5	-	8.2
10	$1000 - 1180$	7.8	12.2	-	9.1
11	$1180 - 1400$	8.3	11.1	9.4	8.8
12	$1400 - 1700$	8.2	11.6	9.4	8.9

Table A.8: Fractional binder content of granules for target binder-to-solids ratio of 0.11 with 1.5 kg of powder–Set 2.

No.	Sieve fraction (μm)	t = 3 min	t = 5 min	t = 10 min	t = 15 min
1	< 250	6.2	8.0	6.4	6.2
2	$250 - 300$	6.4	9.6	7.5	6.4
3	$300 - 355$	7.0	-	8.3	-
4	$355 - 420$	7.8	10.0	8.6	7.2
5	$420 - 500$	7.0	10.5	7.9	7.5
6	$500 - 600$	7.2	10.2	8.1	8.0
7	$600 - 710$	8.3	10.9	9.0	8.7
8	$710 - 850$	8.0	11.2	8.4	8.8
9	$850 - 1000$	8.1	11.3	8.6	8.7
10	$1000 - 1180$	7.9	11.8	-	9.1
11	$1180 - 1400$	8.0	12.0	8.7	9.0
12	$1400 - 1700$	8.4	11.8	9.3	9.2

Table A.9: Fractional binder content of granules for target binder-to-solids ratio of 0.11 with 1.5 kg of powder–Set 3.

No.	Sieve fraction (μm)	t = 3 min	t = 5 min	t = 10 min	t = 15 min
1	< 250	5.8	7.9	6.7	6.0
2	$250 - 300$	6.3	8.8	7.7	6.5
3	$300 - 355$	6.9	9.0	8.3	7.0
4	$355 - 420$	7.2	10.4	8.5	7.2
5	$420 - 500$	-	10.7	8.0	7.8
6	$500 - 600$	7.6	11.0	8.0	7.7
7	$600 - 710$	7.4	11.3	8.6	9.2
8	$710 - 850$	8.1	10.9	8.7	9.0
9	$850 - 1000$	8.0	11.1	9.1	8.7
10	$1000 - 1180$	7.5	11.8	-	8.8
11	$1180 - 1400$	8.2	11.5	9.0	9.2
12	$1400 - 1700$	8.4	11.7	9.1	9.2

Table A.10: Normalised GSD for binder-to-solids ratio of 0.12 and 1.5 kg of powder.

No.	Sieve fraction (μm)	t = 3 min	t = 5 min	t = 10 min	t = 15 min
1	< 250	0.530	0.432	0.363	0.212
2	$250 - 300$	0.074	0.073	0.073	0.073
3	$300 - 355$	0.025	0.024	0.024	0.025
4	$355 - 420$	0.015	0.015	0.014	0.015
5	$420 - 500$	0.015	0.015	0.015	0.025
6	$500 - 600$	0.013	0.013	0.013	0.023
7	$600 - 710$	0.010	0.010	0.010	0.010
8	$710 - 850$	0.002	0.002	0.002	0.002
9	$850 - 1000$	0.100	0.100	0.130	0.200
10	$1000 - 1180$	0.170	0.270	0.310	0.350
11	$1180 - 1400$	0.027	0.027	0.027	0.046
12	$1400 - 1700$	0.019	0.019	0.019	0.019

Table A.11: Granule porosity for binder-to-solids ratio of 0.12 and 1.5 kg of powder.

No.	Sieve fraction (μm)	t = 3 min	t = 5 min	t = 10 min	t = 15 min
1	< 250	0.149	0.145	0.138	0.138
2	$300 - 355$	0.147	0.143	0.138	0.138
3	$420 - 500$	0.147	0.143	0.135	0.135
4	$500 - 600$	0.145	0.140	0.133	0.129
5	$850 - 1000$	0.138	0.135	0.129	0.126
6	$1180 - 1400$	0.137	0.133	0.127	0.121

Table A.12: Fractional binder content of granules for target binder-to-solids ratio of 0.12 with 1.5 kg of powder.

No.	Sieve fraction (μm)	t = 3 min	t = 5 min	t = 10 min	t = 15 min
1	< 250	6.4	8.7	9.1	11.1
2	$250 - 300$	12.5	10.0	10.9	12.5
3	$300 - 355$	9.0	13.1	11.2	13.3
4	$355 - 420$	-	12.9	11.5	13.0
5	$420 - 500$	8.5	12.6	11.6	12.9
6	$500 - 600$	8.8	12.1	11.7	9.9
7	$600 - 710$	8.8	12.4	11.6	9.9
8	$710 - 850$	9.5	12.4	11.6	12.5
9	$850 - 1000$	9.5	12.6	11.7	12.3
10	$1000 - 1180$	8.5	12.0	11.9	11.7
11	$1180 - 1400$	8.6	12.0	12.1	10.1
12	$1400 - 1700$	7.9	12.1	12.3	9.4

Table A.13: Normalised GSD for binder-to-solids ratio of 0.11 and 1.75 kg of powder.

No.	Sieve fraction (μm)	t = 3 min	t = 5 min	t = 10 min	t = 15 min
1	< 250	0.719	0.688	0.581	0.481
2	$250 - 300$	0.101	0.091	0.100	0.097
3	$300 - 355$	0.020	0.021	0.025	0.021
4	$355 - 420$	0.015	0.014	0.013	0.015
5	$420 - 500$	0.014	0.014	0.013	0.016
6	$500 - 600$	0.012	0.012	0.011	0.013
7	$600 - 710$	0.010	0.013	0.010	0.010
8	$710 - 850$	0.002	0.011	0.018	0.020
9	$850 - 1000$	0.100	0.002	0.200	0.210
10	$1000 - 1180$	0.002	0.013	0.027	0.112
11	$1180 - 1400$	0.003	0.003	0.002	0.003
12	$1400 - 1700$	0.002	0.002	0.001	0.003

Table A.14: Granule porosity for binder-to-solids ratio of 0.11 and 1.75 kg of powder.

No.	Sieve fraction (μm)	t = 3 min	t = 5 min	t = 10 min	t = 15 min
1	< 250	0.142	0.138	0.133	0.136
2	$300 - 355$	0.141	0.137	0.133	0.136
3	$420 - 500$	0.140	0.136	0.129	0.132
4	$500 - 600$	0.137	0.132	0.128	0.126
5	$850 - 1000$	0.132	0.128	0.125	0.122
6	$1180 - 1400$	0.130	0.127	0.122	0.119

Table A.15: Fractional binder content of granules for target binder-to-solids ratio of 0.11 with 1.75 kg of powder.

No.	Sieve fraction (μm)	t = 3 min	t = 5 min	t = 10 min	t = 15 min
1	< 250	-	8.7	9.1	11.1
2	$250 - 300$	7.5	10.0	10.9	12.5
3	$300 - 355$	8.6	13.1	11.2	13.3
4	$355 - 420$	7.7	12.9	11.5	13.0
5	$420 - 500$	-	12.6	11.6	12.9
6	$500 - 600$	9.7	12.1	11.7	9.9
7	$600 - 710$	8.7	12.4	11.6	9.9
8	$710 - 850$	9.0	12.4	11.6	12.5
9	$850 - 1000$	9.4	12.6	11.7	12.3
10	$1000 - 1180$	-	12.0	11.9	11.7
11	$1180 - 1400$	-	12.0	12.1	10.1
12	$1400 - 1700$	10.1	12.1	12.3	9.4

Table A.16: Normalised GSD for binder-to-solids ratio of 0.13 and 1.5 kg of powder.

No.	Sieve fraction (μm)	t = 5 min	t = 10 min	t = 15 min
1	< 250	0.157	0.124	0.091
2	$250 - 300$	0.042	0.034	0.028
3	$300 - 355$	0.016	0.020	0.022
4	$355 - 420$	0.019	0.013	0.014
5	$420 - 500$	0.031	0.047	0.044
6	$500 - 600$	0.027	0.027	0.022
7	$600 - 710$	0.081	0.120	0.053
8	$710 - 850$	0.072	0.118	0.027
9	$850 - 1000$	0.128	0.135	0.095
10	$1000 - 1180$	0.089	0.054	0.028
11	$1180 - 1400$	0.060	0.038	0.016
12	$1400 - 1700$	0.075	0.043	0.019
13	$1700 - 2360$	0.074	0.052	0.025
14	$2360 - 2800$	0.027	0.024	0.034
15	$2800 - 3350$	0.024	0.022	0.046
16	$3350 - 4000$	0.019	0.023	0.046
17	$4000 - 4750$	0.020	0.012	0.050
18	> 4750	0.038	0.092	0.342

Table A.17: Normalised GSD for binder-to-solids ratio of 0.14 and 1.5 kg of powder.

No.	Sieve fraction (μm)	t = 5 min	t = 10 min	t = 15 min
1	< 250	0	-	-
2	$250 - 300$	0.001	-	-
3	$300 - 355$	0.001	-	-
4	$355 - 420$	0.002	-	-
5	$420 - 500$	0.002	-	-
6	$500 - 600$	0.002	-	-
7	$600 - 710$	0.004	-	-
8	$710 - 850$	0.004	0.022	-
9	$850 - 1000$	0.003	-	-
10	$1000 - 1180$	0.006	-	-
11	$1180 - 1400$	0.008	-	-
12	$1400 - 1700$	0.012	-	-
13	$1700 - 2360$	0.030	-	-
14	$2360 - 2800$	0.028	-	-
15	$2800 - 3350$	0.042	-	-
16	$3350 - 4000$	0.060	0.010	-
17	$4000 - 4750$	0.102	0.040	-
18	> 4750	0.692	0.929	1

* Sieve fractions (1-15) were combined in this size range at t = 10 min.

** For sieve fractions (1-17) there were no granules in this size range at t = 15 min.

Table A.18: Normalised GSD for binder-to-solids ratio of 0.13 and 1.75 kg of powder.

No.	Sieve fraction (μm)	t = 5 min	t = 10 min	t = 15 min
1	< 250	0.189	0.081	0.051
2	$250 - 300$	0.026	0.024	0.017
3	$300 - 355$	0.019	0.012	0.010
4	$355 - 420$	0.015	0.016	0.011
5	$420 - 500$	0.028	0.023	0.020
6	$500 - 600$	0.033	0.030	0.028
7	$600 - 710$	0.046	0.036	0.035
8	$710 - 850$	0.060	0.054	0.048
9	$850 - 1000$	0.086	0.082	0.068
10	$1000 - 1180$	0.082	0.109	0.109
11	$1180 - 1400$	0.098	0.114	0.120
12	$1400 - 1700$	0.082	0.100	0.118
13	$1700 - 2360$	0.099	0.134	0.137
14	$2360 - 2800$	0.038	0.046	0.052
15	$2800 - 3350$	0.034	0.040	0.043
16	$3350 - 4000$	0.029	0.039	0.041
17	$4000 - 4750$	0.015	0.027	0.029
18	> 4750	0.021	0.033	0.063

Table A.19: Normalised GSD for binder-to-solids ratio of 0.14 and 1.75 kg of powder.

No.	Sieve fraction (μm)	t = 5 min	t = 10 min	t = 15 min
1	< 250	0.045	-	-
2	$250 - 300$	-	-	-
3	$300 - 355$	-	-	-
4	$355 - 420$	-	-	-
5	$420 - 500$	-	-	-
6	$500 - 600$	-	-	-
7	$600 - 710$	-	0.028	-
8	$710 - 850$	-	-	0.012
9	$850 - 1000$	-	-	-
10	$1000 - 1180$	0.006	-	-
11	$1180 - 1400$	-	-	-
12	$1400 - 1700$	-	-	-
13	$1700 - 2360$	0.015	0.002	-
14	$2360 - 2800$	0.016	0.008	-
15	$2800 - 3350$	0.038	0.032	-
16	$3350 - 4000$	0.063	0.064	0.021
17	$4000 - 4750$	0.123	0.105	0.094
18	> 4750	0.694	0.760	0.874

* For sieve fractions (2-9) and (11-12) there were no granules corresponding to t = 5 min.

** Sieve fractions (1-12) were combined corresponding to t = 10 min.

*** Sieve fractions (1-15) were combined corresponding to t = 15 min.

Appendix B

Population Balance Model

B.1 Determination of Mechanistic Kernel Parameters

In this section, an outline is given for the procedure adopted in this study for determining the adjustable parameters present in the model expressions for the considered granulation phenomena. In addition, a suggested method is given which proposes that an optimisation criterion be used in determining these unknown parameters.

The model that has been developed for the granulation process incorporates mechanistic descriptions of nucleation, aggregation and breakage along-with an empirical relationship for consolidation. The method adopted in determining the sensitivity of the adjustable parameters, pertaining to each of the considered rate processes was based on examination of the magnitude of the changes in the output variable (i.e., particle size). This was computed using a finite difference approximation and is defined in Equation B.1 in which small perturbations are made to the parameters required to be determined for different time instances. This process is repeated for each perturbation and for each of the parameters under consideration.

$$\frac{\partial y(t)}{\partial x_i} \approx \frac{\mathbf{y}(t;\mathbf{x}+\delta x_i)-\mathbf{y}(t;\mathbf{x})}{\delta x_i} \tag{B.1}$$

Here, y is the output variable, $\mathbf{x} = [A_0\ c_1\ A\ c]^T$ is the vector of the parameters under consideration (i.e., A_0 corresponds to the parameter present in the nucleation kernel. c_1 corresponds to the parameter present in the aggregation kernel and so on so forth). x_i is

the *ith* element of $\mathbf{x}$.

The minimisation of the sum of squared errors ($\Phi(\mathbf{x})$) is used as the optimisation criterion and is defined in Equation B.2.

$$\Phi\mathbf{x} = \sum_{t=1}^{N_t}\sum_{i=1}^{N_s}(N_{t,i} - \hat{N}_{t,i}(x))^2 \tag{B.2}$$

Here $N_{t,i}$ and $\hat{N}_{t,i}$ are the experimental and model predicted values for the number of particles in size class i at a time instant of t. N_s is the maximum number of particle size classes and N_t is the total number of time instances used for sampling the vector of unknown parameters x. The criterion given in Equation B.2 is based on minimising the sum of squared errors between the model prediction and the measured output quantity obtained from experimental measurements. Solving this optimisation problem, (whereby the aim is to minimise the objective function and the overall sum of squared error) can be performed by using the sequential quadratic programming (SQP) method. Providing an initial value for the parameters of vector $\mathbf{x}$ will be an important first step and information providing engineering insight to the process will aid in this regard in addition to literature values as a guide if available. Testing the sensitivity of the objective function on each of the initial parameter values before commencing optimisation can be performed by perturbing each value separately by an arbitrarily small value such as 1% and observing the difference in the objective function for whether it is greater than the optimisation tolerance (e.g. 1×10^{-3}.

Appendix C

Numerical Method for Multi-dimensional Population Balance Models

A FORTRAN code was written in order to simulate the three-dimensional population balance model accounting for granule consolidation, aggregation and nucleation. In solving the three-dimensional population balance model, a hierarchical solution strategy is employed that explicitly casts the population balance in terms of the underlying sub-rate processes i.e., nucleation, aggregation and consolidation (Immanuel and Doyle III, 2005). The technique involves the discretisation of the system domain with respect to the three aforementioned internal coordinate axes followed by the recasting of the population balance into finite volumes. In this finite volume scheme, the population balance equation in Equation 2.10 may be re-written into its discrete form, as shown in Equation C.1 for the case with aggregation and consolidation as the granulation phenomena.

$$\frac{dF'_{i,j,k}}{dt} + \left(\frac{F'_{i,j,k}}{\triangle g_k}\right)\frac{dg}{dt}\Big|_{g_k} - \left(\frac{F'_{i,j,k+1}}{\triangle g_{k+1}}\right)\frac{dg}{dt}\Big|_{g_{k+1}} =$$
$$\frac{1}{2}\int_{s'=s_{nuc}}^{s-s_{nuc}}\int_{l'=0}^{l}\int_{g'=0}^{g}\beta(s', s-s', l', l-l', g', g-g')F'(s', l', g', t)$$
$$\times F'(s-s', l-l', g-g', t)ds'dl'dg'$$
$$- F'(s,l,g,t)\int_{s'=s_{nuc}}^{s_{max}}\int_{l'=0}^{l_{max}}\int_{g'=0}^{g_{max}}\beta(s', s, l', l, g', g)$$
$$\times F'(s', l', g', t)ds'dl'dg' \qquad \text{(C.1)}$$

Here $F'(i,j,k) = \int_{s=s_i}^{s_{i+1}}\int_{l=l_j}^{l_{j+1}}\int_{g=g_k}^{g_{k+1}} F(s,l,g)\,ds\,dl\,dg$. s_i is the value of the solid volume at the upper end of the i^{th} bin along the solid volume axis. l_j is the value of the liquid volume at the upper end of the j^{th} bin along the liquid volume axis. g_k is the value of the gas volume at the upper end of the k^{th} bin along the gas volume axis. In addition, β is the aggregation kernel and $\triangle g_k$ is the size of the k^{th} gas bin with respect to the gas volume axis.

In the solution of the finite volume population balances, a decomposition solution framework known as the hierarchical two-tier algorithm is employed (see Figure 2.6), wherein the various rate processes of nucleation, aggregation, consolidation, etc., are accounted individually at each time step while marching forward in time. Firstly, the population balance is written in terms of a number distribution by volume since the volume of the granules remain conserved during size changing mechanisms (e.g. aggregation) (Verkoeijen et al., 2002). Based on the finite volume discretisation of the particle population (the particles residing in each finite volume bin may be regarded as sub-populations of the whole particle population), the particle density within each finite volume bin is assumed to be uniform, allowing for the preprocessing and a priori calculations of time independent portions of the kernels and the computation-intensive integrals in Equation C.1 (Immanuel and Doyle III, 2003a, 2005). With these simplifying model assumptions, the population balance may be reduced to a set of coupled non-linear ordinary differential equations. At each time step, the contribution of each sub-rate process, i.e., nucleation, aggregation and growth are evaluated over the time interval. This step corresponds to the first tier of the

two-tier algorithm. In the second tier, the cumulative effect on the PSD is calculated.

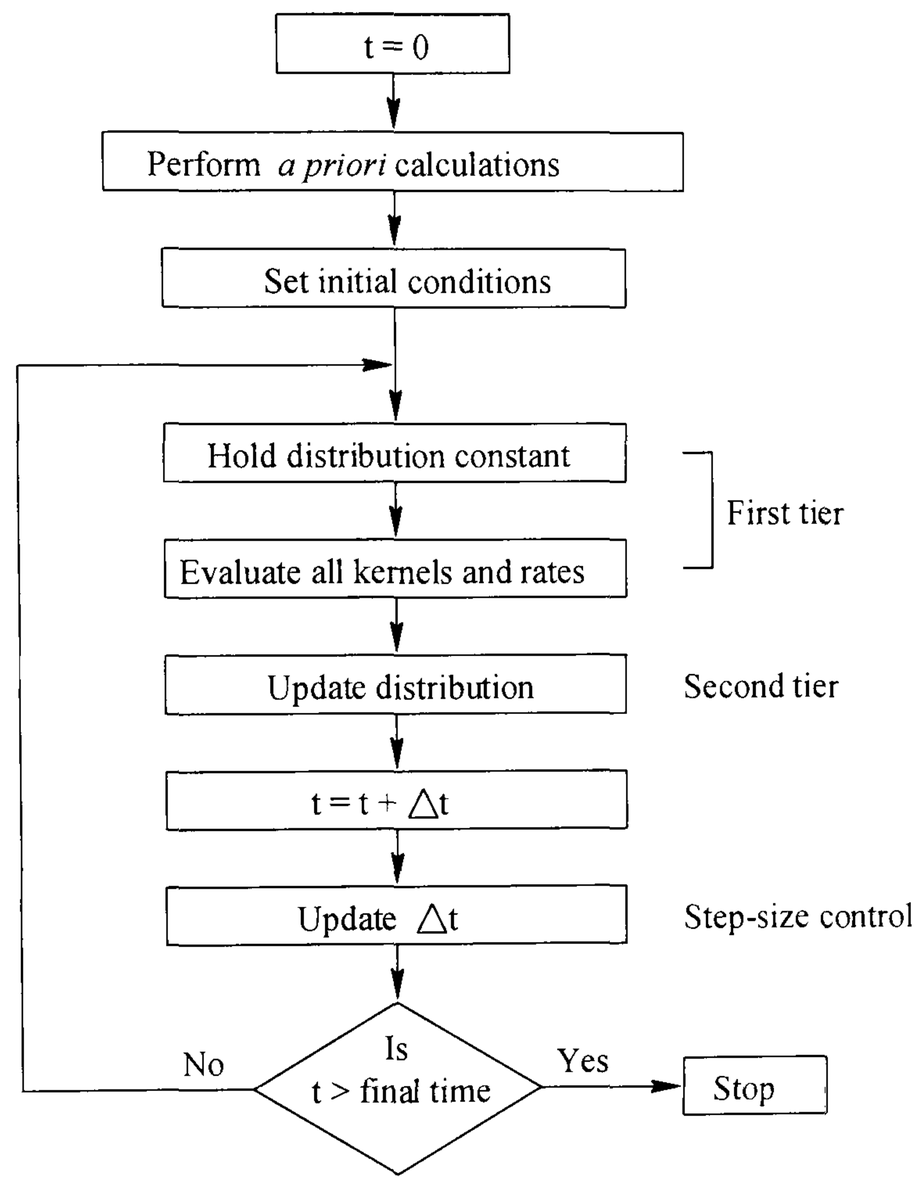

Figure C.1: Schematic representation of the hierarchical two-tier algorithm (Immanuel and Doyle III, 2003a).